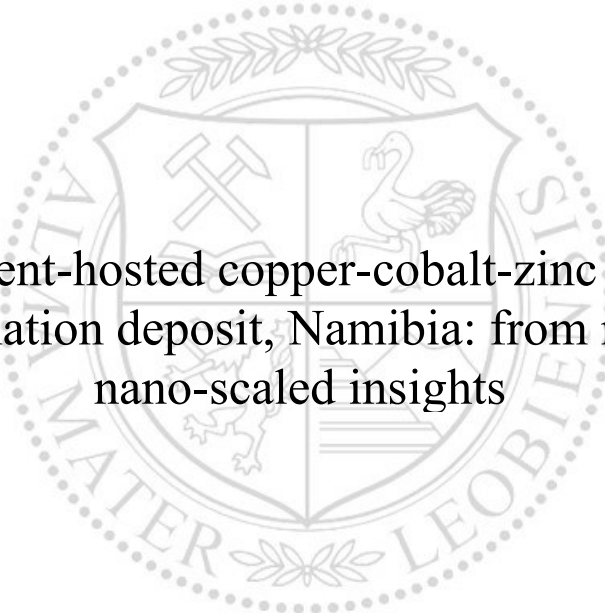




Chair of Geology and Economic Geology

Doctoral Thesis



The sediment-hosted copper-cobalt-zinc Dolostone
Ore Formation deposit, Namibia: from macro- to
nano-scaled insights

Viktor Bertrandsson Erlandsson M.Sc. B.Sc.

July 2023



MONTANUNIVERSITÄT LEOBEN

www.unileoben.ac.at

AFFIDAVIT

I declare on oath that I wrote this thesis independently, did not use other than the specified sources and aids, and did not otherwise use any unauthorized aids.

I declare that I have read, understood, and complied with the guidelines of the senate of the Montanuniversität Leoben for "Good Scientific Practice".

Furthermore, I declare that the electronic and printed version of the submitted thesis are identical, both, formally and with regard to content.

Date 19.06.2023

Signature Author

Viktor Bertrandsson Erlandsson

Acknowledgments

There are many people I would like to show my gratitude towards. Their support and involvement made my research possible and straight off led me to be a better and more competent researcher. Firstly, I have to say thank you to the company Gecko Namibia, who welcomed our cooperation on the Dolostone Ore Formation (DOF) project. Much gratitude to the exploration team, Rainer Ellmies, Kaarnia Ndalulilwa, Victoria Haukongo, Gideon Kalumbu, Matilde Uushona, Agripine Shinyemba, and all on-site technicians, whom all enabled the field campaign in Namibia and made the sampling campaign a truly fantastic experience. It is a cherished memory for life.

My uttermost appreciation and gratefulness to my supervisor Frank Melcher and my mentor Thomas Meisel, for taking me under their wings for my PhD journey. Their insights and guidance molded and elevated my approach and understanding of geochemistry. Also Phillip Gopon who has guided me and enabled me to enhance my skills of interpreting mineral data and additional mentoring. Through them, my eyes have been opened to the true wonder and curiosity that is mineral geochemistry. I must also thank all the colleagues of the MUL Department of Applied Geosciences and Geophysics and the Chair of General and Analytical Chemistry. So many helpful people whom made my time as a PhD student and LA-ICP-MS operator both fun and educational. With a special thank you to Daniela Ringhofer, Johann Raith, and Gerd Rantisch, who all were vital parts of the research group on the DOF project. An additional thank you for the hard work of the sample preparators Marie-Luise Harmsen, Ivaylo Martinov and Maik Zimmermann, along with the EPMA assistance from Maik Zimmermann.

Additional gratitude goes to Etienne Skrzypek at Universität Graz (Austria) and Martin Whitehouse, Heejin Joen, and Kerstin Lindén at the NordSIMS laboratory, Stockholm (Sweden) for their contributions to analyses and sample preparation. None of this work would ever been accomplished without the constant support from my family and friends, whom all kept encouraging me to complete my PhD. Lastly, I cannot leave out the international colleagues that I have collaborated with on several different projects: Aleš Šoster, Krzysztof Foltyn, and Milos Velojic. Thank you for everything our collaborations have given me.

Abstract

Although sediment-hosted Cu-Co deposits are significant sources of Cu and the most important sources of Co, very little work has been done on them using laser ablation inductively coupled mass spectrometry (LA-ICP-MS). LA-ICP-MS has proven to be a useful tool in deciphering formation processes for a range of sulfides and their ore-forming processes, especially when complemented with additional analytical techniques. In the pursuit of better the understanding of sediment-hosted Cu-Co deposits, this work investigates the recently discovered Cu-Co-Zn Dolostone Ore Formation (DOF) deposit in northwestern Namibia, by a multi-method geochemical approach. The DOF deposit is situated within the Kaoko Belt and is hosted in calcareous siltstones of the Ombombo Subgroup, which is part of the Neoproterozoic Damara Supergroup, and is the first recognized Co deposit in Namibia. Although hosted in an analogous tectonic setting and stratigraphic position to the sediment-hosted Cu-Co deposits of the Central African Copperbelt, little is known on the genesis of the DOF deposit. This study applies optical microscopy, electron beam techniques, LA-ICP-MS, and atom probe tomography to gain insights into the ore-forming processes responsible for the DOF deposit on a macro-, to micron-, and nano-scale. Additionally, monazite dating and sulfide sulfur isotopes were carried out to attain additional information on the genesis of the DOF deposit.

The DOF deposit's metal enrichment shows a bell curve-like distribution in e.g. Cu, Co, and Zn. The peak concentration of this metal enrichment is referred to as the Main DOF horizon, whilst the lower concentrations are known as the Wider DOF horizon. The Main DOF horizon is also characterized by an alteration mineral assemblage of stilpnomelane, siderite, and ankerite. The sulfide mineralogy of the DOF deposit is relatively simple, with dominant sulfides being pyrite, pyrrhotite, cobaltpentlandite, chalcopyrite, sphalerite, and linnaeite. Linnaeite and cobaltpentlandite are the main Co-bearing mineral in the DOF, although pyrite was shown to contain oscillatory zonation wherein high concentrations of Co can be found (up to 10 wt%). Linnaeite occurs as euhedral crystals in nodules and clusters, partially broken down, whilst cobaltpentlandite occurs as exsolution-like inclusions in both pyrite and pyrrhotite. Galena, cobaltite, and pentlandite occur as accessory phases. Sulfides occur in six types of mineralization styles in the DOF deposit: (1) disseminated; (2) polysulfide cluster aggregates; (3) polysulfide nodules; (4) veins, both sulfide- and gangue-dominated; (5) mineralized pressure shadows; and (6) "Events", which is a locally applied term for mineralization that occurs within vein- and/or slump-like structures that portray both ductile and brittle textures. Additionally, framboidal pyrite occurs throughout the stratigraphy, but is almost completely absent from the Main DOF horizon.

Pyrite, pyrrhotite, sphalerite, and chalcopyrite from these six mineralization styles were analyzed by LA-ICP-MS for their trace element composition. The trace elements show two main populations of sulfides between the mineralization style, in particular in regards to sphalerite and chalcopyrite, where disseminated, nodule, cluster, and "Event" sulfides group together (Group 1), whilst vein and pressure shadow sulfides group (Group 2). This is interpreted as evidence for at least two main stages of ore-formation. The fact that sphalerite and chalcopyrite both overgrow the iron-sulfides and linnaeite in the Group 1 mineralization styles indicates that the Cu-Zn mineralization post-dates the iron-sulfide formation. The linnaeite, which is only found within Group 1 mineralization styles, was suggested to have formed through pyrite decomposition and Co remobilization from the pyrite, through changes in oxygen and/or sulfur

fugacity. The cobaltpentlandite inclusions within the iron-sulfides of Group 1, were an intermediate product of this process. The Ga-Ge-In-Mn-Fe in sphalerite geothermometer indicated formation temperatures of $>310 \pm 50$ °C, for both sulfide groups, linking the ore formation to the Damara Orogeny.

Additional sulfide trace element data was acquired from sediment-hosted Cu(-Co) deposits from the Central African Copperbelt and the Polish Kupferschiefer, to enable a deposit-type comparison of the DOF. Random Forest analyses were used to investigate similarities and differences between the metallogenic Cu(-Co) districts, which showed that the sulfide trace elements vary greatly between the districts, which is most probably due to different metal sources in the basement or the detrital material from each basin's basement. This was also evident as the African districts shared more similarities to each other than to the Polish Kupferschiefer, which is reasonable as they are hosted in analogous tectonic settings and stratigraphies.

Zusammenfassung

Die Mineralchemie der Sulfide in wirtschaftlich bedeutenden sedimentgebundenen Cu-Co-Lagerstätten wurde bisher kaum mittels Laserablation - induktiv gekoppelter Plasmamassenspektrometrie (LA-ICP-MS) untersucht. LA-ICP-MS hat sich als nützliches Werkzeug zur Entschlüsselung von Bildungsprozessen für Sulfidlagerstätten erwiesen, insbesondere wenn die Methode durch zusätzliche Analysetechniken ergänzt wird. Um ein besseres Verständnis der sedimentgebundenen Cu-Co-Lagerstätten zu erreichen, wurde die kürzlich entdeckte Cu-Co-Zn-Lagerstätte der Dolostone Ore Formation (DOF) im Nordwesten Namibias mit einem geochemischen Ansatz untersucht. Die DOF-Lagerstätte liegt im Kaoko-Gürtel und ist an kalkhaltige Siltsteine der Ombombo-Untergruppe gebunden, welche Teil der neoproterozoischen Damara-Supergruppe ist. Die DOF ist die erste bekannte Co-Lagerstätte in Namibia. Obwohl sie sich in einer tektonischen Umgebung und stratigraphischen Position analog zu den sedimentgebundenen Cu-Co-Lagerstätten des zentralafrikanischen Kupfergürtels befindet, ist wenig über die Entstehung der DOF-Lagerstätte bekannt. Optische Mikroskopie, Elektronenstrahltechniken, LA-ICP-MS und Atomsondentomographie wurden genutzt, um die genetischen Prozesse bei der Lagerstättenbildung zu entschlüsseln. Dazu wurden die Proben im Mikrometer- und Nanomaßstab untersucht. Zusätzlich wurden Monazit-Datierungen und Schwefel-Isotopenuntersuchungen an Sulfidmineralen durchgeführt.

Die Metallanreicherung in der DOF-Lagerstätte zeigt eine glockenkurvenartige Verteilung von z.B. Cu, Co und Zn. Die Zone mit der höchsten Metallkonzentration wird als „Main-DOF“ bezeichnet, während der „Wider-DOF“-Horizont durch geringere Konzentrationen charakterisiert ist. Die Main-DOF ist durch eine Alterationsmineralogie aus Stilpnomelan, Siderit und Ankerit gekennzeichnet. Die Sulfidmineralogie der DOF ist relativ einfach, mit den vorherrschenden Sulfiden Pyrit, Pyrrhotit, Kobaltpentlandit, Chalkopyrit, Sphalerit und Linnaeit. Linnaeit und Kobaltpentlandit sind die wichtigsten Co-haltigen Minerale in der DOF. Pyrit weist eine oszillierende Zonierung auf, in der hohe Konzentrationen an Co gefunden werden können (bis zu 10 Gew.-%). Linnaeit tritt als idiomorphe Körner in teilweise deformierten Knollen und Clustern auf, während Kobaltpentlandit in Form entmischungsähnlicher Einschlüsse sowohl in Pyrit als auch in Pyrrhotin vorkommt. Galenit, Kobaltit und Pentlandit treten als Nebenphasen auf. Sulfide kommen in der DOF-Lagerstätte in sechs Typen vor: (1) disseminiert; (2) Polysulfid-Cluster-Aggregate; (3) Polysulfidknollen; (4) Adern, die sowohl von Sulfid als auch von Gangart dominiert sein können; (5) mineralisierte Druckschatten; und (6) „Events“, ein lokal verwendeter Begriff für Mineralisation, die innerhalb ader- und/oder slump-ähnlicher Strukturen auftritt, welche sowohl duktile als auch spröde Texturen aufweisen. Darüber hinaus kommt in der gesamten Stratigraphie Framboidpyrit vor, der jedoch in der Main-DOF fast vollständig fehlt.

Pyrit, Pyrrhotin, Sphalerit und Chalkopyrit wurden mittels LA-ICP-MS auf ihre Spurenelementzusammensetzung analysiert. Die Spurenelemente zeigen zwei Haupttypen von Sulfiden. Bei Sphalerit und Chalkopyrit werden disseminierte Sulfide, Knollen-, Cluster- und „Ereignis“-Sulfide zusammengefasst (Gruppe 1), während Ader- und Druckschattensulfide getrennt gruppiert werden (Gruppe 2). Dies wird als Beweis für mindestens zwei Hauptstadien der Erzbildung interpretiert. Nachdem Sphalerit und Chalkopyrit die Eisensulfide und Linnaeit in den Mineralisierungstypen der Gruppe 1 überwachsen und verdrängen, muss die Cu-Zn-Mineralisation nach der Eisensulfidbildung entstanden sein. Linnaeit, der nur in Gruppe 1

Mineralisationen vorkommt, entstand durch Pyritzersetzung und Co-Remobilisierung aus dem Pyrit. Die Kobaltpentlandit-Einschlüsse in den Eisensulfiden der Gruppe 1 stellen ein Zwischenprodukt dieses Prozesses dar. Das Ga-Ge-In-Mn-Fe-in-Sphalerit-Geothermometer zeigt für beide Sulfidgruppen Bildungstemperaturen von $>310 \pm 50$ °C an, was die Erzbildung mit der Damara-Orogenese in Verbindung bringt.

Zusätzliche Spurenelementdaten wurden aus sedimentgebundenen Cu(-Co)-Lagerstätten aus dem zentralafrikanischen Kupfergürtel und dem polnischen Kupferschiefer erfasst, um einen Vergleich der Lagerstättentypen mit der DOF zu ermöglichen. Mithilfe von Random-Forest-Analysen wurden Ähnlichkeiten und Unterschiede zwischen den metallogenetischen Cu(-Co)-Bezirken untersucht. Dabei zeigte sich, dass die Sulfidspurenelemente zwischen den Bezirken stark variieren, was höchstwahrscheinlich auf unterschiedliche Metallquellen im Basement zurückzuführen ist. Dies wurde auch dadurch deutlich, dass die afrikanischen Bezirke untereinander mehr Ähnlichkeiten aufwiesen als mit dem polnischen Kupferschiefer, was durch die analoge tektonische und stratigraphische Position bedingt sein kann.

Abbreviations

$\delta^{34}\text{S}$	Delta 34/32 sulfur isotopes
APT	Atom probe tomography
BSR	Bacterial sulfate reduction
CACB	Central African Copperbelt
Ccp	Chalcopyrite
DOF	Dolostone Ore Formation
EBSA	Electron backscattered diffraction
EDS	Energy-dispersive spectrometer
EPMA	Electron probe micro-analyzer
FIB	Focused ion beam
KCB	Katanga Copperbelt
LA-ICP-MS	Laser ablation inductively coupled plasma mass spectrometry
Lin	Linnaeite
MORB	Mid-ocean ridge basalt
OIB	Ocean island basalt
Po	Pyrrhotite
Py	Pyrite
SEM	Scanning electron microscope
SIMS	Secondary ion mass spectrometry
Sph	Sphalerite
SSHCD	Stratiform sediment-hosted copper deposit
SSHC(C)D	Stratiform sediment-hosted copper(-cobalt) deposit
SSHCCD	Stratiform sediment-hosted copper-cobalt deposit
TSR	Thermochemical sulfate reduction
WDS	Wavelength-dispersive spectrometer
ZCB	Zambian Copperbelt

Overview

1.	Introduction.....	1
1.1	State of the Art	1
1.2	Research Objectives and Work Packages.....	2
1.3	Geological Aspects of the Dolostone Ore Formation.....	4
	References.....	17
2.	Publications	21
2.1.	List of Included Publications	21
2.2.	My Contribution to the Included Publications	22
2.3.	List of Additional Publications	22
3.	Dissertation Outline	23
	Publication I.....	26
	Publication II.....	68
	Publication III.....	89
	Publication IV.....	142
5.	Summary and Conclusions	183
	Appendix 1.....	185
	List of conference abstracts authored during the time of the PhD	185
	Appendix 2.....	187
	Drill core sample list	187
	Appendix 3.....	195
	List of prepared sample and analytical methods used.....	195

1. Introduction

1.1 State of the Art

The demand for cobalt (Co) is exponentially increasing due to its usage in a wide range of high-tech applications, especially in the current renewable energy “green revolution” where Co is a crucial component of electrical batteries. Already in 2018, around 49% of the produced Co goes into electric-car batteries (Alves Dias et al. 2018). Approximately 68% of global Co production comes from SSHCCDs in the Congolese CACB (European Commission 2020; USGS 2020), and Co is currently listed as a “critical metal” for both the European Union (European Commission 2023) and the USA (USGS 2022). The increasing need of Co and its status as a critical metal, means that finding new sources Co is crucial for the future of a high-tech, renewable society. As the vast majority of mined Co comes from SSHCCDs, it is a reasonable starting point for the pursuit of new Co-bearing deposits.

Geochemical exploration in 2012 led to the discovery a Co and Cu anomaly now known as the DOF in northwestern Namibia (Ellmies 2018). Since the discovery of the DOF mineralization, large-scaled exploration drilling (2017-2019) was carried out to better constrain the extent of the DOF mineralization (Ellmies 2019). From the exploration, the DOF was determined to have an indicated and inferred resource of 225.5 Mt, with ore grades of 0.43 % Cu, 0.12 % Co, and 0.54 % Zn (Celsius Resources Limited 2021). The DOF is currently the first, and only, promising Co prospect in Namibia (Ellmies 2019). This said, very little is known about the geological aspects of the DOF. Only one academic study had previously been done on the DOF deposits, in the form of a Msc thesis by Allen (2016). That study did a lot of work on the host rocks and rigorous surface mapping of the study area. The focus on the actual sulfide mineralization was lesser, partially due to the limited amount of drill core, and this is where this PhD project carried on, as many questions were still unanswered.

Although the DOF shares several characteristics of the SSHCCDs in the CACB, e.g., hosted in coeval and similar sedimentary succession; several aspects differ greatly, such as the lack of evaporites in the Kunene Zone (Miller 2008; Miller 2013). Unlike most shale-hosted SSHC(C)Ds (Hitzman et al. 2005), the DOF does not occur in the “first-reductant shale”, which further complicates the geological model (Ellmies 2018). Due to these complicating factors, no concrete metallogenic model has been made for the DOF deposit so far. Understanding the formation processes responsible for ore deposits is important for local exploration, but also for regional and global exploration.

This PhD project seeks to expand the understanding of SSHC(C)Ds through a multi-method geochemical approach. The project focuses on the sediment-hosted Cu-Co-Zn DOF deposit, situated in the Kunene area of northwestern Namibia. In the scope of this study a multitude of analytical methods were applied on the mineralization, including SEM-EDS, EPMA, EBSD, APT, LA-ICP-MS, and SIMS, to help constrain the mode of Co (and other metals) occurrence and the geological formation processes involved in creating the DOF. Through these analytical techniques we view the mineralization at a macroscopic-, to microscopic-, and down to an atomic-scale.

1.2 Research Objectives and Work Packages

The ultimate aim of this PhD research project is to produce a feasible metallogenic model for the Cu-Co-Zn DOF deposit and place it in the regional geological setting of Namibia along with comparing it to other, more well-known, Cu(-Co) stratiform sediment-hosted deposits of Africa (i.e., the CACB) and the world (e.g., the Polish and German Kupferschiefer).

This study applied a multi-method in-situ geochemical approach, focusing on the sulfide minerals, to help answer the main research objectives:

- (1) Generate a metallogenic model for the Cu-Co DOF deposit.
- (2) How does the DOF compare to other well-known sediment-hosted Cu(-Co) deposits?

These research objectives will be answered through six work-packages (in accordance to the procedures of planning a PhD project at the Montanuniversität Leoben, Austria) that reflect different useful methods:

I. Field Work and sampling campaign

The project started with three weeks of fieldwork in Namibia (March 2019). Key outcrops of the different lithologies were visited along with extensive sampling of the available drill core from the company. Seeing outcrops are a key part for understanding the geology and relationship between units. These outcrops were not widely sampled due to the intense oxidation and supergene alteration conditions at the surface (Figure 1). Fortunately, we were granted access to the drill cores after an extensive exploration campaign by Gecko Namibia. Six drill holes were examined (Figure 2). Detailed logging and sampling was made of sections around the mineralized horizon. These samples are the focus of this study as they contain fresh sulfide mineralization and gangue minerals.

II. Petrography of the sulfide mineralization and associated gangue minerals

A combination of reflected- and transmitted-light optical microscopy along with SEM will be used to identify and differentiate mineral phases and textures. This is a vital step to understand the paragenetic relationship between sulfides and associated gangue phases, and to deduce the relative timing of the Cu-Co-Zn mineralization at the DOF deposit.

III. Sulfide trace element analysis by LA-ICP-MS

Trace element contents of sulfides are a powerful tool in deciphering genetic aspects of sulfide mineralizations (e.g., Cook et al. 2009; Frenzel et al. 2016; Duran et al. 2019; Hu et al. 2021). Certain trace element incorporations have been shown to be related to physicochemical parameters, which can then be used to help constrain the formation conditions of the sulfide mineralization. Furthermore, this will also expand the trace element database of sediment-hosted deposits, something that is at a very limited state in the current literature. Hence, this work package will fill a large gap in the research on sulfide geochemistry.

IV. Stable S Isotopes

Variations in $\delta^{34}\text{S}$ isotopes ($\text{S}^{34}/\text{S}^{32}$) of sulfides provide valuable data to better understand the source of S in the sulfides. Sulfur isotopes are commonly used in ore geology research and aid in

the understanding the mineralization processes, as two main question of ore deposits are what the source of both metals and sulfur is. Due to the complex results of the $\delta^{34}\text{S}$ isotopes analysis, this data is only presented briefly in the section “*Geological Aspects of the Dolostone Ore Formation*” in chapter “1. Introduction” of this dissertation, as the interpretation of this data is still being prepared for publication.

V. Atom probe tomography

This work package was added during the span of the PhD foremost due the discovery of extremely Co-rich sphalerite in the DOF deposit (by LA-ICP-MS), something that until now had not been recognized in scientific literature. Work Package “*V Atom Probe Tomography*” utilizes state-of-the-art techniques to better the understanding of Co (a critical metal) incorporation into sphalerite. Wherein we gained significant insights for the main research question of the PhD research, concerning the formation processes responsible for the current occurrence of the Co-mineralization of the DOF deposit.

VI. Geochronology

Geochronology is a vital tool when trying to deduce the genesis of a mineral deposit, when applicable, as many geological factors can interfere with radiometric dating. The biggest problem with dating sediment-hosted deposits is the lack of datable associated minerals. After petrographic studies of the mineral assemblage of the DOF stratigraphy, monazite was the best candidate for dating the mineralization. Monazite was observed to occur in close association with the DOF mineralization. It occurs both in the host rock and within veins. Due to the close mineralization-association, along with the fact that monazite U-Pb dating can be done with an EMPA, it was decided to target monazite to attain an age constrain.

Unfortunately, the monazite U-Pb dating was not successful in dating the mineralization. The only successful monazite ages reflected (1) detrital and (2) metamorphic ages. Due to this, this data is only presented briefly in the section “*Geological Aspects of the Dolostone Ore Formation*” in chapter “1. Introduction” of this dissertation.

It is worth noting that this PhD project was accompanied by a parallel PhD project by Daniela Ringhofer (previously Wallner), where each project focused on different aspects and methods to investigate the DOF deposit. Whilst my project focused on abovementioned work-packages; D. Ringhofer’s project comprised methods such as EPMA, extensive sulfide petrography, Raman spectrometry of graphite for geothermometry, and combining petrography with the drill core assay database to generate a geochemical key to transform the database into lithological units and eventually generate an ore deposit model. Work-package “*I. Field Work and sampling campaign*” was done together, as both PhD projects used the collected samples. Although, D. Ringhofer’s project was a vital part of the overall DOF research project, the work presented within this thesis was done by me. Research contributions by D. Ringhofer (i.e., Wallner) are referenced accordingly, e.g., compiling the geological DOF map (Figure 2) and coauthor in “*Publication I*”.

1.3 Geological Aspects of the Dolostone Ore Formation

As detailed description of the regional geological setting and local geology of the DOF deposit is covered in Publication I (Bertrandsson Erlandsson et al. 2022), this part of the dissertation will focus on aspects that have not been covered in the following publications.

Field work and sampling

The project was initiated with a field campaign in northwestern Namibia, where scarce DOF outcrops were visited (Figure 1A) and drill cores were sampled. Surface outcrops were not suitable for the aim of this project, due to intense oxidation and supergene alteration, which can be seen for tens of meters in the drill cores (Figure 1B-C). All drill core sampling was done in, observably, unoxidized, fresh drill core, to attain intact sulfide mineralization and host rock. Six boreholes were sampled (marked out in Figure 2). The sampled boreholes were chosen to have an E-W spread, with an approximate spacing of 3 km. Drill core samples were taken based on borehole geochemistry assays, to attain samples from varying degrees of mineralized rocks, including as barren rocks as well for reference materials. Full drill core sample list can be found in Appendix 2 and prepared samples with analytics can be found in Appendix 3.

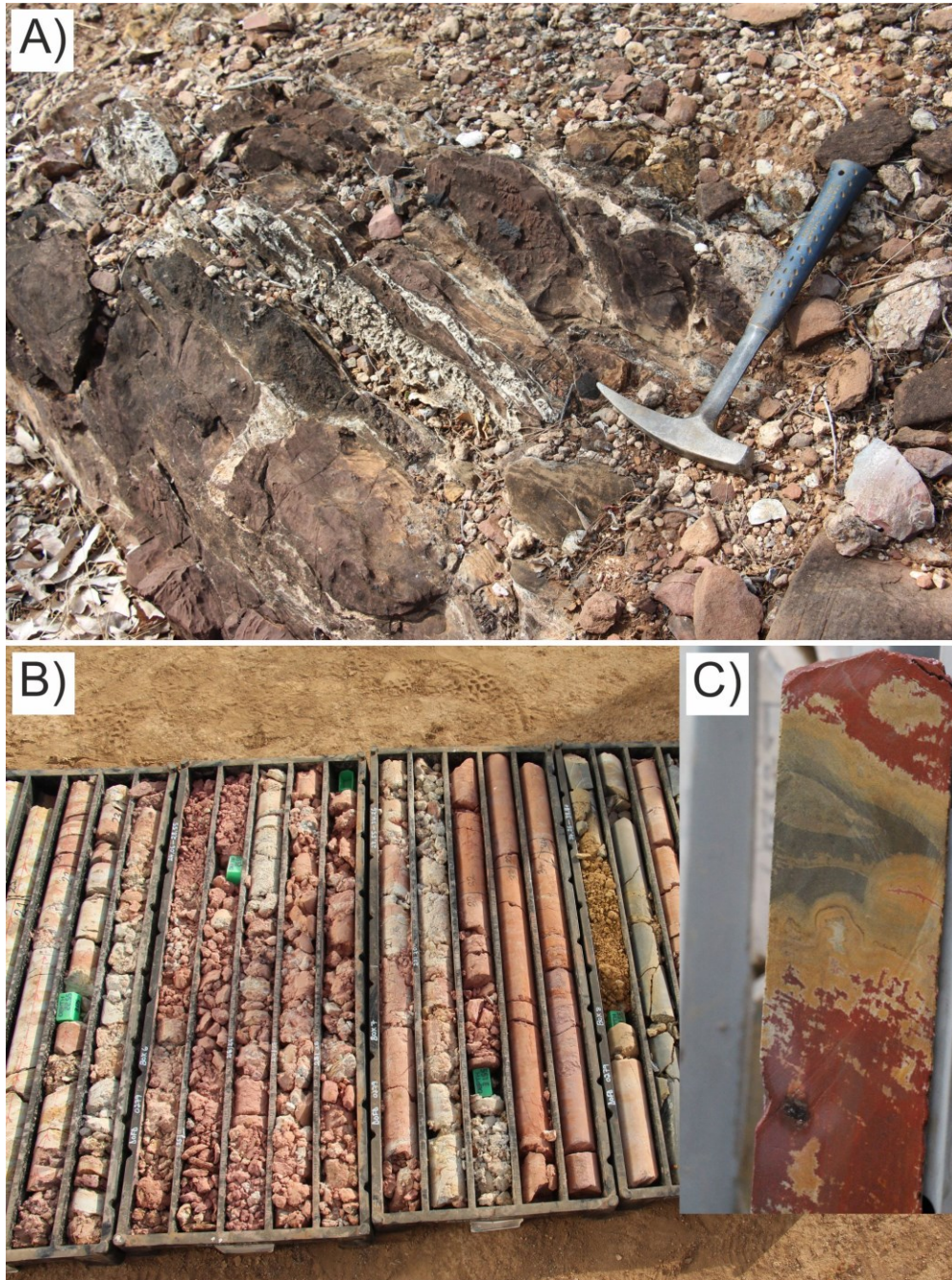


Figure 1. Examples of surface and near-surface exposures of the DOF. A) Rare surface outcrop of the DOF mineralization. B) Intensely oxidized drill core from the upper parts of the borehole. C) Halfed drill core portraying the deep weathering of the upper rocks.

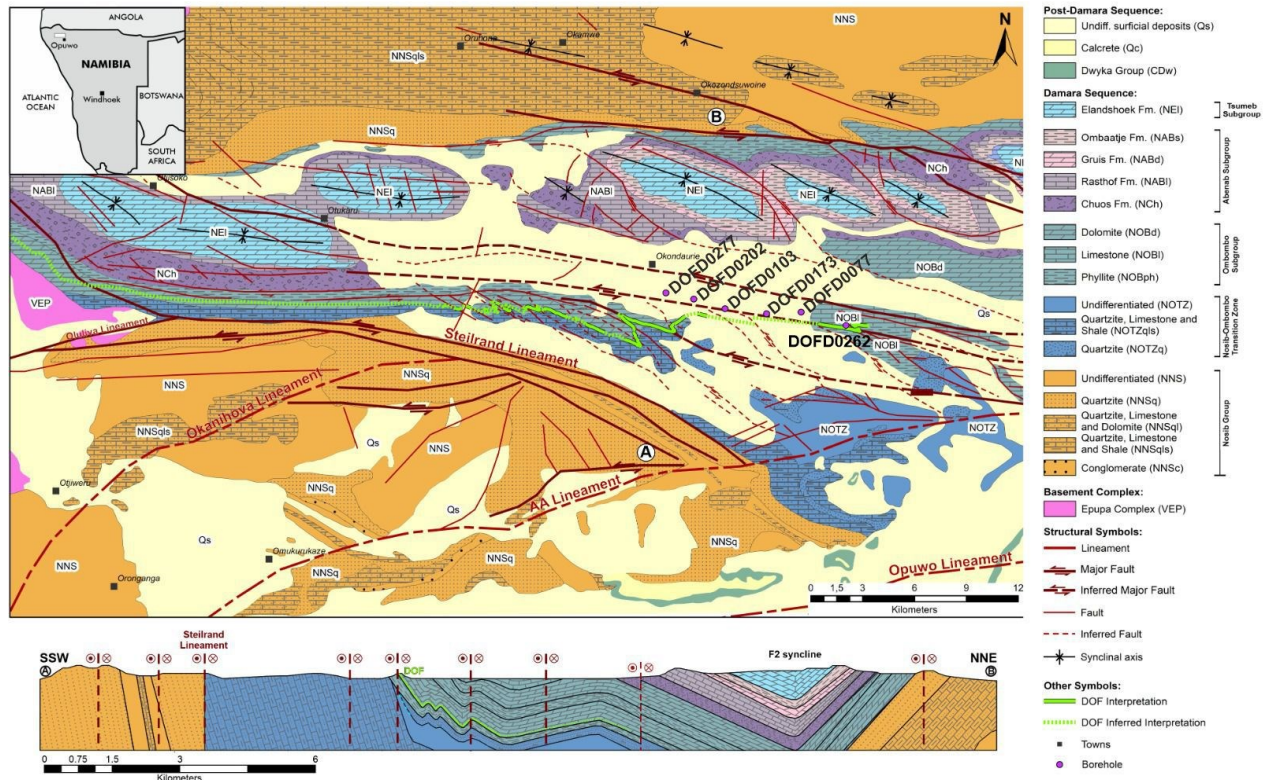


Figure 2. Geological map of the DOF study area; with the DOF horizon and sampled boreholes marked out. Schematic cross section from A to B in map. The map and cross section was made by Wallner et al. (2022), after data compiled from: Schreiber et al. (2011), Allen (2016), African Mining Capital Pty Ltd (2019), Blood (2019), Celsius Resources LTD (2019), Ellmies (2019). Published in Bertrandsson Erlandsson et al. (2022). Borehole DOFD0262 was added herein.

Geochemical aspects from exploration whole rock data

Through access to the drill core whole rock database from the exploration campaign by Gecko Namibia, several curious aspects of the DOF can be seen. One interesting feature of the DOF mineralization is its bell curve-like ore grade distribution into the hanging wall, but with a very sharp footwall contact (Figure 3). From this, two ore horizons have been distinguished, the Main DOF and the Wider DOF; the Main DOF shows a magnitude higher concentration of e.g., Co, Cu, and Zn, compared to the Wider DOF (Figure 3). Although there are minor amounts of host rock-hosted chalcopyrite and sphalerite mineralization (e.g., disseminations and mineralized nodules) in the Wider DOF, the main reason for delineating the Wider DOF is mineralized veins. These veins are typically gangue-dominated (quartz-carbonate) and contain chalcopyrite, sphalerite, and accessory amounts of galena. This is evident from the CaO peaks in Figure 3 (and drop in K₂O and Na content), which can be seen to correlate with the marked epigenetic structures (breccias/veins/Events). It seems like the two ore horizons occur within a section between two domains of breccias, veins, and/or “Events”, suggesting a link between the ore formation and these structures. These structures are believed to postdate the Main DOF mineralization, formed during a late-orogenic mineralization stage (Bertrandsson Erlandsson et al. 2022).

Basic core logging was done during the sampling campaign, where the main host rock type was determined to be argillite (Figure 3), which primarily seems to be siltstones, with lesser shales

and lenses of sandstones. Although no distinct carbonate units were identified during the core logging, later SEM-ESD analyses have shown that these are carbonate bearing, with dolomite in the Wider DOF and siderite-ankerite within the Main DOF horizon (Bertrandsson Erlandsson et al. 2022). Noticeable dips in K_2O and Na correlate with elevated CaO and drill core sections with major breccias, veins, and/or “Events” (Figure 3), suggesting these elements to correlate well with carbonate content. This shows that indeed the major lithology is argillite, with perhaps one carbonate horizon around 910 m, which marks the start of the Main DOF horizon. The argillites of the unmineralized rocks and Wider DOF contain predominately K-feldspar, plagioclase, quartz, dolomite, muscovite, biotite, and chlorite with lesser amounts of apatite, monazite, and rutile.

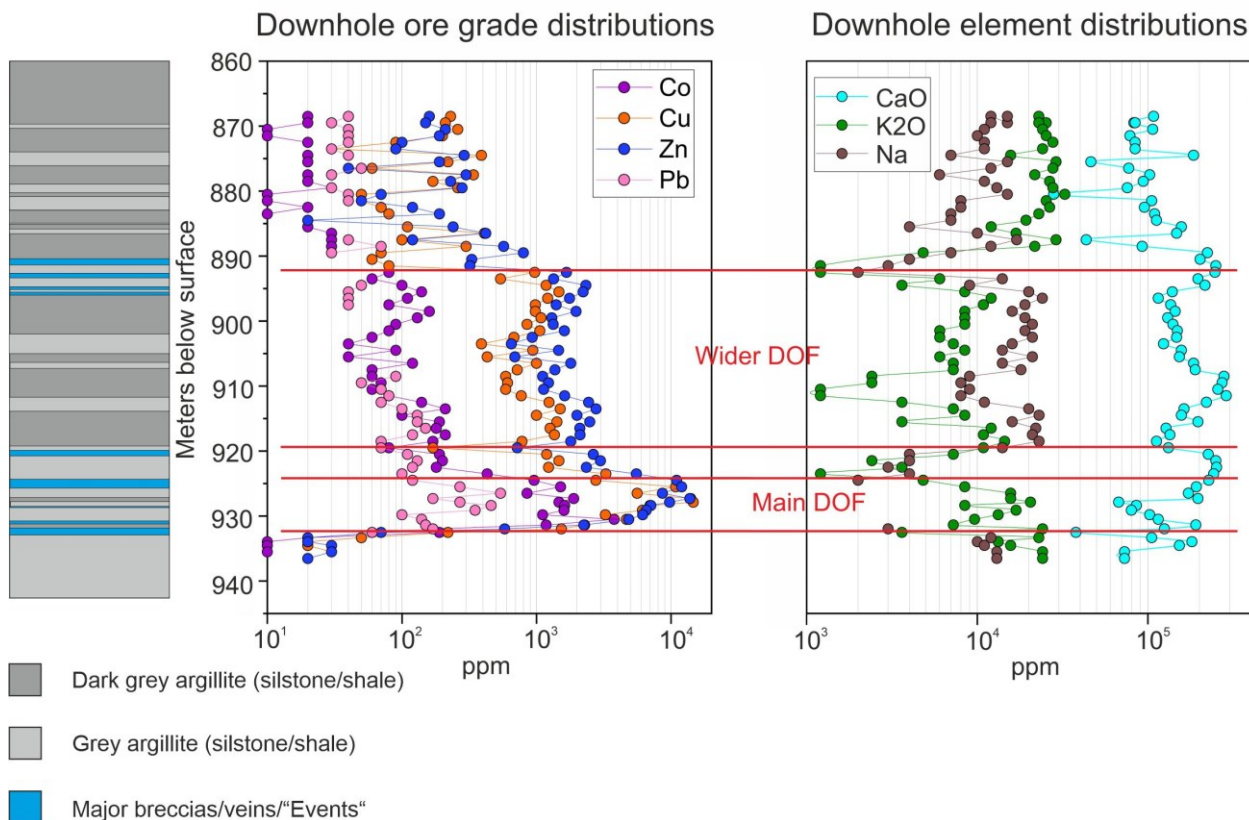
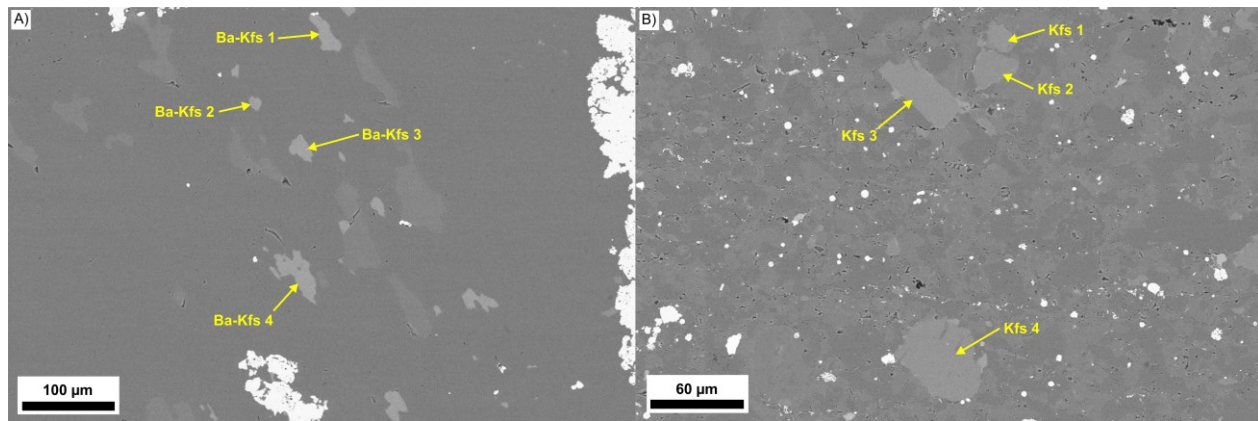


Figure 3. Schematic stratigraphic column from basic core logging during the field campaign. Additionally, downhole Co, Cu, Zn, and Pb grades and CaO, K_2O , and Na distributions, from exploration drill core assays. The Main and Wider DOF ore horizons are marked in red. Only major veins, breccias, and “Events” are marked as unit in the stratigraphic column. Note that depth is drill core length, not adjusted for the drilling angle. Representative example from exploration borehole DOFD0277.

Besides the high Cu-Co-Zn content, the DOF horizon is also characterized by lower, but varying, K concentrations, and no Na (Figure 3). The low Na content in the Main DOF is due to the lack of e.g., plagioclase within the Main DOF. Plagioclase occurs within the Wider DOF and the unmineralized host rock. K-feldspar has been identified in both the wider-DOF host rock and in the unmineralized host rock but is not found in the Main DOF host rock. In the Main DOF, K is primarily hosted in stilpnomelane (Bertrandsson Erlandsson et al. 2022). Whilst host rock K-feldspar shows BaO-concentrations <1 wt% (Figure 4A), Ba-rich K-feldspar is found in veins within

both the Main and Wider DOF horizons (Figure 4B), where also accessory barite crystals have been identified. High Ba concentrations in K-feldspar have been linked to acidic, Cl-rich basinal brines/evaporitic brines (Pal and Chaudhuri 2016). This would suggest that similar fluids may have been involved in the DOF mineralization, where acidic alteration led to the removal of K and Ba. These fluids would also have been Cl-rich and thus carried Cu, Co, and Zn that was precipitated as the Main DOF mineralization. The removed K and Ba would later be precipitated as Ba-rich K-feldspar and stilpnomelane and accessory barite in veins. Stilpnomelane and siderite has yet only been identified within the host rock of the Main DOF horizon and seems to be the best indicators for the hydrothermal alteration associated with the high-grade ore-forming fluids.



Analysis	Al ₂ O ₃	SiO ₂	K ₂ O	BaO	Analysis	Al ₂ O ₃	SiO ₂	K ₂ O	BaO
Ba-Kfs 1	18.03	63.35	15.65	2.97	Kfs 1	18.12	65	16.32	0.57
Ba-Kfs 2	16.88	68.20	12.01	2.90	Kfs 2	18.05	66.00	15.82	0.13
Ba-Kfs 3	19.48	64.33	12.88	3.30	Kfs 3	16.71	65.95	16.83	0.51
Ba-Kfs 4	20.89	64.23	11.69	3.19	Kfs 4	17.88	65.78	15.8	0.55

Figure 4. SEM-EDS analyses of K-feldspar (Kfs) in sample 277-12, which contains an example of the pressure shadow mineralization style within the Wider DOF. A) Ba-rich K-feldspar from the gangue mineral assemblage within a pressure shadow. B) Detrital K-feldspar from the host rock of the Wider DOF.

In situ sulfur isotopes of sulfides (Work package IV)

Sulfide $\delta^{34}\text{S}$ analyses were planned as a Work Package in the scope of this thesis, and were carried out but are currently in preparation for publication. Therefore, brief results will be presented herein.

Sulfur isotope analyses were carried out at the NordSIM laboratory in Stockholm, Sweden. An ims 1280 Cameca secondary ion mass spectrometer (SIMS) was used to measure ^{34}S and ^{32}S in pyrite, pyrrotite, chalcopyrite and sphalerite from the six aforementioned mineralization styles. Pyrite, pyrrotite and chalcopyrite were measured under similar instrumental conditions. Spot size was 10 microns, resulting in a ~ 200 nm deep crater, with a beam current of 1 nA. A 12-cycle acquisition time was used, i.e., 1.22 min acquisition time per spot measurement. Due to crystallographic effects of sphalerite, analytical settings had to be changed. A spot size of 20 microns was used for sphalerite analyses, with a beam current of 0.2 nA. The acquisition time was increased to a 24-cycle, i.e. 4.44 min. To correct for instrumental drift, reference materials were analyzed after 5 unknowns, and after a while, after every 6 unknown measurements. Analyses of sulfides were

made from the nodule and cluster mineralization styles in the Main DOF horizon, and from the “Event” mineralization style (for details on mineralization styles see Publication I, Bertrandsson Erlandsson et al 2022). These are what are referred to as “Main DOF” mineralization in this section of the dissertation. Additionally, $\delta^{34}\text{S}$ measurements of framboidal pyrite were done as a reference of syn-sedimentary $\delta^{34}\text{S}$.

Pyrite, typically framboidal pyrite, formed through BSR in an open water system tends to prefer light sulfur, resulting in highly negative $\delta^{34}\text{S}$ (Jensen 1967; Ohmoto and Rye 1979; Seal 2006). Such values were measured in framboidal pyrites from the unmineralized host rock (mean -14.08 ‰) and in the Main DOF (mean -14.15 ‰; Table 1; Figure 5). The Main DOF Cu-Zn mineralization (cluster and nodule mineralization styles) shows a mean $\delta^{34}\text{S}$ signature of 0.16 ‰, -1.11 ‰, and 1.41 ‰ for pyrite, chalcopyrite, and sphalerite respectively (Table 1). With similar $\delta^{34}\text{S}$ values around 0, the Main DOF mineralization is significantly different from the framboidal pyrite values (Figure 5); this suggests that an additional S source was involved in the formation of the DOF deposit. The general lack of framboidal pyrite within the Main DOF horizon has been interpreted such that framboidal pyrite was overgrown and replaced during the DOF mineralization (Bertrandsson Erlandsson et al. 2022). This would suggest that there may be a component of inherited S isotopes, but they are evidently overshadowed by the later, more significant, influx of S. A rare Main DOF sample containing framboidal pyrite was analyzed and showed similar $\delta^{34}\text{S}$ values to that of the rest of the framboidal pyrites (Figure 5). This later S would have formed through TSR, as the sulfide formation temperatures (>310 °C; Bertrandsson Erlandsson et al. 2022) were too high for BSR.

It is unlikely that the persisting framboidal pyrite was a sufficient source for the total S responsible for the DOF mineralization, and therefore the $\delta^{34}\text{S} \sim 0$ ‰ signature most likely reflects the original source. A sulfide $\delta^{34}\text{S}$ around 0 is typically attributed to magmatic fluids and associated igneous rocks, such as MORB and OIB (e.g., Ohmoto and Rye 1979; Huston 1997; Shanks 2001; Seal 2006). The trace element composition of sulfides from SHC(C)Ds have been suggested to be heavily influenced by the metal source, e.g. underlying basement rocks or eroded sediments therefrom (Bertrandsson Erlandsson et al. *in review*). The source of the metals for the DOF deposit is believed to include mafic rocks, due to the affinity of Co to mafic rocks, or magmatic-associated Co-deposits in the basement (Bertrandsson Erlandsson et al. *in review*). The ~ 0 $\delta^{34}\text{S}$ value of the Main DOF sulfides may therefore similarly reflect a magmatic (mafic?) source from, for example, the basement, such as the Kunene Igneous Complex or associated magmatic basement rocks to the north of the DOF (see the following section “Monazite Pb-U-Th dating (Work package VI)” for an more in-depth discussion on source materials.

Table 1. Statistical summary of in situ $\delta^{34}\text{S}$ of sulfides from the DOF deposit. Abbreviations: N = number of analyses; HR = unmineralized host rock.

Ore Horizon	Mineralization Style	Mineral	N	Mean	Min	Max
Main DOF	Cluster	Py	32	0.16	-1.81	1.50
		Ccp	16	-1.11	-3.27	0.20
		Sph	7	1.41	-0.01	2.14
	Event	Po	32	-0.86	-3.59	1.39
		Ccp	32	-0.27	-3.16	2.00
		Sph	32	0.80	0.12	2.16
HR	Framboidal	Py	8	-14.15	-21.32	20.69
	Framboidal	Py	13	-14.08	-21.32	25.83

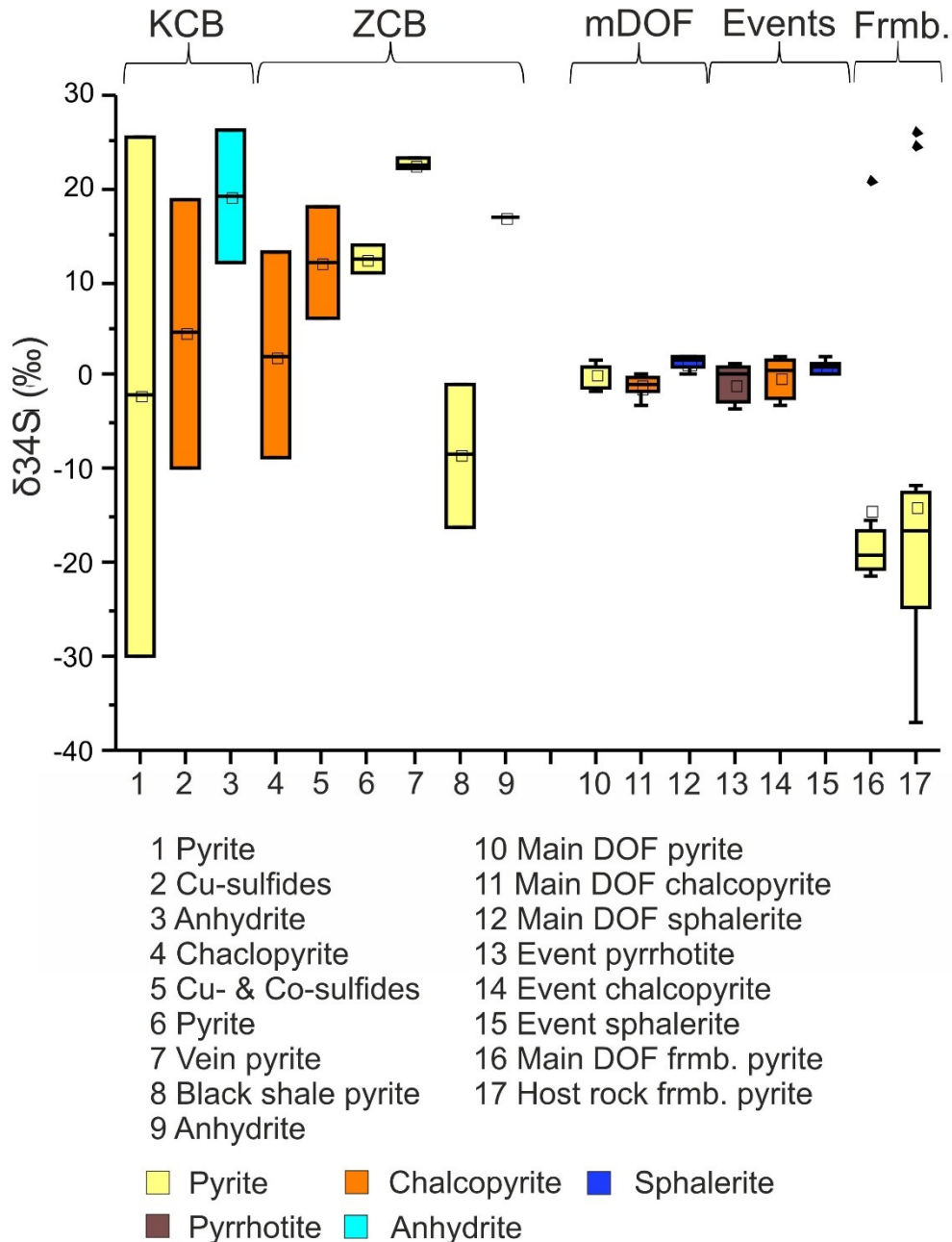


Figure 5. $\delta^{34}\text{S}$ isotopes of KCB, ZCB, and DOF sulfides. Due to the limitation of raw data, KCB and ZCB ranges are based on min and max values. DOF data has been subdivided into cluster and nodule data from the Main DOF horizon (mDOF), "Events", and framboidal pyrite (Frmb.). KCB deposits include Kamoto, Kambove-Ouest, Luiswishi, Etoile, and Ruashand (data from Lerouge et al. 2004). ZCB deposits include Konkola (Sweeney et al. 1986) and Nchanga (McGowan et al. 2006). Abbreviations: KCB = Katanga Copperbelt; ZCB = Zambian Copperbelt; mDOF = Main DOF horizon; Frmb. = framboidal pyrite.

Pyrrhotite, chalcopyrite, and sphalerite from the Event mineralization style from eastern and western boreholes were measured; sphalerite was only analyzed from the western borehole sample. These measurements show an E-W trend of more negative $\delta^{34}\text{S}$ values to the East (Figure 6). The similar $\delta^{34}\text{S}$ of pyrrhotite and chalcopyrite (and sphalerite) is interpreted as inherited S, as the pyrrhotite is being replaced by chalcopyrite and sphalerite (Figure 7). This is in agreement with the paragenesis of Bertrandsson Erlandsson et al. (2022) and Bertrandsson Erlandsson et al. (2023), which both suggest that the Main DOF Cu-Zn mineralization is associated with replacement of preexisting iron-sulfides (pyrite and/or pyrrhotite). The exact mechanism behind this E-W trend is still unexplained and requires further investigation.

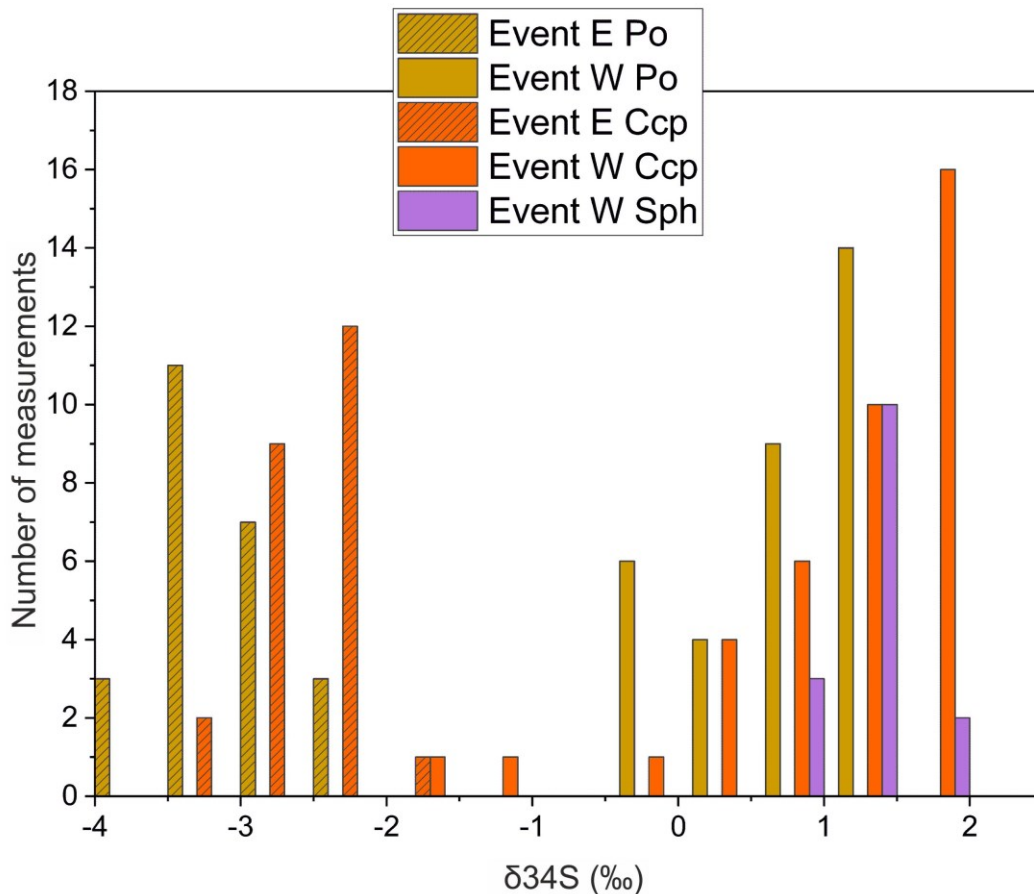


Figure 6. $\delta^{34}\text{S}$ isotope values from DOF sulfides from eastern and western Event mineralizations.

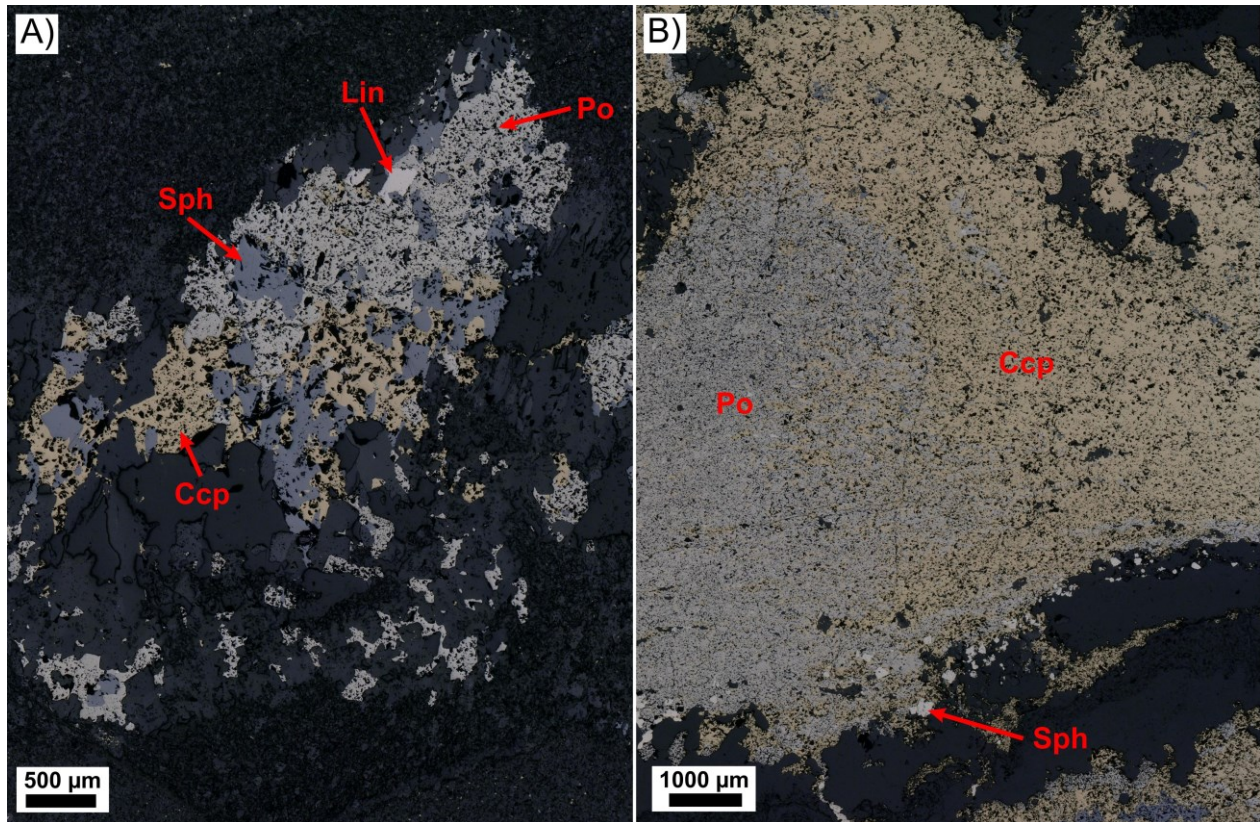


Figure 7. Reflected light micrographs of DOF Event mineralizations, with Pb-Zn mineralization replacing pyrrhotite. A) Western Event mineralization, from borehole 277. B) Eastern Event mineralization, from borehole 077.

Monazite Pb-U-Th dating (Work package VI)

In situ EPMA monazite Pb-U-Th dating was attempted in the scope of this PhD project to bracket the age of mineralization. As it did not yield results reliable enough for interpretation, the data is briefly presented herein.

Monazite was found in accessory amounts in both the host rock and in association with sulfide mineralization. When associated with the sulfide mineralization, the monazite occurs both as inclusions within sulfides and growing around sulfides, suggesting a strong association. Monazite also occurs within sulfide-bearing veins. It was based on these indications of the monazite being strongly associated with mineralization, that monazite was targeted for dating.

Quantitative analyses of monazite were performed at the University of Graz using a JEOL JXA-8530F Plus EPMA equipped with five wavelength-dispersive spectrometers (radius of the Rowland circle = 140 mm). Operating conditions were 15 kV accelerating voltage, 150 nA beam current and 1 μm beam diameter. The X-ray lines, counting times and calibration materials used for each mineral are listed in Table 2. Interference corrections include those of Y on $\text{PbM}\alpha$ and $\text{PbM}\alpha$, and those of Th on $\text{PbM}\alpha$ and $\text{UM}\alpha$; correction factors are listed in Table 3. Matrix correction follows the method of Bence and Albee (1968) with α -factors after Kato (2005).

Table 2. Settings for EPMA analyses of monazite - Elements and X-ray lines (JXA-8530F Plus, University of Graz).

Element	X-ray line	Analyzing crystal	Bkg position (mm)		Counting time (s)		Calibration material	Detection limit (wt%)
			+	-	Peak	Bkg		
Ca	K α	PETJ	1.5	-2.2	80	40	Plagioclase	0.02
S	K α	TAP	1.8	-6.8	80	40	Barite	0.08
Y	L α	TAP	1.3	-1.4	50	25	YPO ₄	0.03
Si	K α	TAP	3.5	-1.3	60	30	Plagioclase	0.03
P	K α	TAP	1.9	-2.6	20	10	CePO ₄	0.11
Al	K α	TAP	5	-5	10	5	Garnet	0.05
U	M α	PETL	4.2	-1.8	200	100	U metal	0.02
Th	M α	PETL	3.3	-2.9	20	10	Th metal	0.05
Pb	M α	PETH	4.3	-9.5	200	100	PbCrO ₄	0.014
Th	M α	PETH	2.3	-3.3	20	10	Th metal	0.05
La	L α	LIF	2.1	-1.9	20	10	LaPO ₄	0.19
Ce	L α	LIF	2.6	-3.6	10	5	CePO ₄	0.26
Pr	L β	LIF	0.7	-1.5	30	15	PrPO ₄	0.25
Nd	L β	LIF	4.8	-5.6	30	15	NdPO ₄	0.22
Sm	L β	LIF	1.2	-0.7	30	15	SmPO ₄	0.22
Gd	L β	LIF	0.9	-0.7	40	20	GdPO ₄	0.19
Dy	L α	LIF	0.8	-3.1	40	20	DyPO ₄	0.12

Notes: Analyzed at 15 kV, 150 nA, 1 μ m beam diameter. Average detection limit at 3 σ for the corresponding oxide (in wt%).

Table 3. Settings for EMP analyses of monazite - Interference correction factors (JXA-8530F Plus, University of Graz).

Interfering line	Interference position	Factor	Calibration material
YL α 1 (Mnz/Th-U phases)	PK α 1	0.0585	YAG garnet
YL α 1 (Mnz/Th-U phases)	PbM α 1	0.0053	YAG garnet
ThM α 1 (Mnz/Th-U phases)	UM α 1	0.0131	Th metal
ThM α 1 (Mnz/Th-U phases)	PbM α 1	0.0009	Th metal

Ninety-three spot analyses were made in eight different DOF polished sections. Out of the 93 spot analyses, only 53 analyses yielded an age >0 Ma. The vast majority of these 53 measurements had error equal to, or greater than, the calculated age (e.g. Figure 8A). The poor outcome is due to low concentrations of Pb, U, and Th in the monazites. Only 16 measurements yielded ages where the error was less than half the calculated age (Table 4). It seems the younger samples are more problematic with errors, and hence these ages should be seen as age indicators, rather than robust and reliable ages. The two oldest ages, 1,924 +/- 7 Ma and 1,652 +/- 10 Ma, have very small errors and may thus be viewed with more reliability.

Monazite can form under a wide range of geological settings, from diagenesis to hydrothermal fluids and metamorphism (e.g., Milodowski and Zalasiewicz 1991; Foster and Parrish 2003; Schandl and Gorton 2004), and can be found as detrital phases in sediments (Morton and Hallsworth 1999). Multiple formation occurrences of monazite seem to be present in the DOF (Figure 8; Table 4). The two oldest ages (1,924 ± 7 Ma and 1,652 ± 10 Ma) reflect detrital monazite, originating from basement rocks. Detrital zircons from magmatic paragneisses of the Epupa Complex (northwest of the DOF study area) have been dated to between 2,075 and 1,820 Ma, which may be related to arc magmatism during the 2,000 ± 200 Ma Eburnian event (Jung et al. 2015). This would be the best fit for a source for the 1,924 ± 7 Ma detrital DOF monazite. Magmatic zircons from migmatites and detrital zircons from paragneisses in the Orue Unit of the Epupa Complex have ages of 1,696 ± 19 and 1,660 ± 14 Ma respectively (Seth et al. 2003; Brandt et al. 2021), which is in good agreement with the 1,652 ± 10 Ma monazite from the DOF. Hence, the two oldest monazite ages obtained from the DOF host rocks very likely indicate a sediment source originating from the Epupa Complex to the northwest.

The 940 – 802 Ma ages (Tonian – Neoproterozoic) align with the suggested age of deposition for the lower Damara Supergroup sediments (e.g. Nosib Group; Miller 2008), and would suggest reworking of the Nosib Group sediments where diagenetic monazite was redeposited into the Ombombo Group. The final group of ages, 501 – 339 Ma, all have very high errors and are most probable attributed to late-orogenic monazite formation. The end phase of the Damara Orogeny has been dated to ~490 Ma (e.g., Singletary et al. 2003), which seems to be the most reasonable fit for the youngest monazite population measured at the DOF. Late-orogenic monazite can be seen overgrowing earlier, e.g. diagenetic, cores (Figure 8D). Such monazites are often orientated along the host rock schistosity.

Goscombe et al. (2003) suggest three main phases of orogenesis in the Kaoko Belt (herein referred to as KP1-3). KP1 is a thermal phase and resulted in partial melting, quartz veins, and granitoid formation (Seth et al. 1998; Goscombe et al. 2003), but is not believed to have affected the Kunene Zone (Goscombe et al. 2003) wherein the DOF deposit is situated. Peak metamorphism of the Kaoko Belt occurred during the transpressional phase KP2 and led to pervasive foliation in the Kaoko Belt, although no transpressional textures are observed in the Kunene Zone (Goscombe et al. 2003). KP3 is defined by N-S shortening, which is believed to have been most intense at the northern (Kunene Zone) and southern (Ugab Zone) ends of the Kaoko Belt (Goscombe et al. 2003). This phase led to upright, E- to ESE-trending, open folds along with reactivation of preexisting shear zones (e.g., the Sesfontein shear zone) and the formation of new retrograde ESE-trending shear zones in the Kunene Zone (Goscombe et al. 2003). The KP3 shortening phase has been dated

to have cooled to ~ 350 °C at around 499 ± 11 and 490 ± 11 Ma (Ahrendt et al. 1983). Foster et al. (2009) suggest that rapid exhumation, related to orogenic collapse at < 500 Ma, were a contributing factor to the shear zone reactivation.

Only two of the vein-hosted monazites yielded suitable ages: 501 ± 195 and 339 ± 152 Ma. These were both euhedral to subhedral monazite crystals within quartz-carbonate veins, which compared to the very irregular, anhedral host rock-hosted monazites (Figure 8), are believed to have formed hydrothermally together with the hosting vein. These ages would be part of the earliest population, related to the late-orogenic shortening phase (KP3) which would be in agreement with the interpretations of Bertrandsson Erlandsson et al. (2022). Pegmatites in the Costal Terrane, to the west of the Eastern Foreland (see Figure 1 in Publication I, Bertrandsson Erlandsson et al. 2022, for the tectonostratigraphic zones of the Damara Orogen), have been dated to the KP3 (Goscombe et al. 2005), which further supports the conclusion of the quartz-rich veining in the DOF being related to the late KP3 orogenic phase. The age of the main DOF horizon mineralization is thus still unknown.

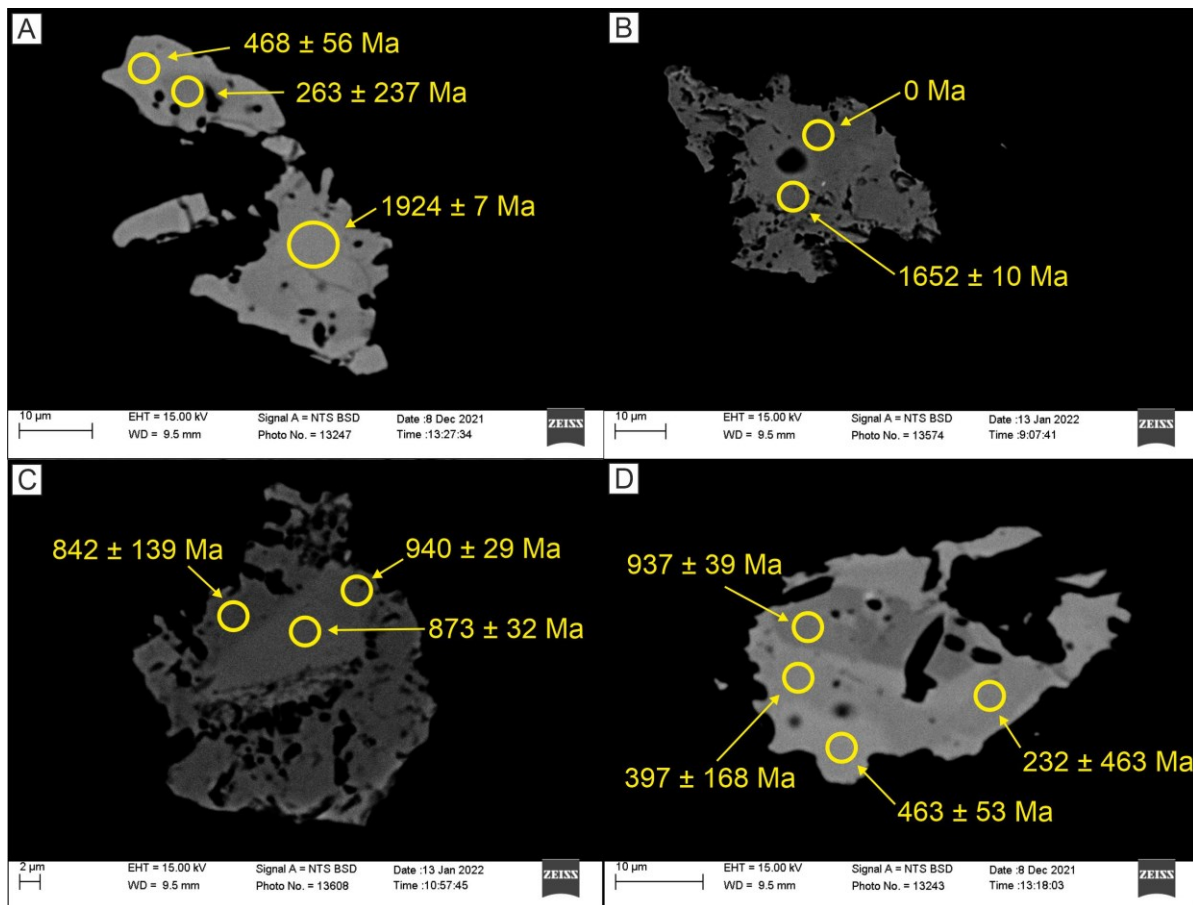


Figure 8. SEM-BSE images showing four dated monazite with respective calculated Pb-U-Th ages. Monazite sample as seen in Table 4: A) Sample 173-24-1_E; B) 202-1-1_B; C) 202-1-1_G1; D) 173-24-1_D. All these monazites are host rock-hosted.

Table 4. Calculated Pb-U-Th monazite ages, with errors less than half the calculated age. Sorted by calculated ages.

Sample	Age (Ma)	+/-
173-24-1_E-1	1924	7
202-1-1_B2	1652	10
202-1-1_G1-1	940	29
173-24-1_D1	937	39
202-1-1_G1-2	873	32
202-1-1_G1-3	842	139
202-1-1_C	802	75
262-27-1_Fx-2	501	195
202-1-1_H	482	116
173-24-1_E-3	468	56
173-24-1_D4	463	53
077-31-M4	408	192
173-24-1_D2	397	168
262-27-1_E3	344	166
262-27-1_E2	340	157
262-27-1_Fx-1	339	152

References

African Mining Capital Pty Ltd (2019): Structures: Geophysical Interpretation. Lithologies 1:1M Geology.

Ahrendt, H.; Behr, H.-J.; Clauer, N.; Hunziker, J. C.; Porada, H.; Weber, K. (1983): The Northern Branch: Depositional Development and Timing of the Structural and Metamorphic Evolution within the Framework of the Damara Orogen. In H. Martin, F. W. Eder (Eds.): Intracontinental Fold Belts. Berlin, Heidelberg: Springer Berlin Heidelberg, pp. 723–743.

Allen, N.K. (2016): Structurally controlled Cu-Zn-(Co-Pb) mineralization in the Neoproterozoic Ombombo Subgroup, Kaokoland, Namibia. Master Thesis. Colorado School of Mines.

Alves Dias, P.; Blagoeva, D.; Pavel, C; Arvanitidis, N. (2018): Cobalt: demand-supply balances in the transition to electric mobility. In Publications Office of the European Union 10, p. 97710.

Bence, A.E.; Albee, A.L. (1968): Empirical correction factors for the electron microanalysis of silicates and oxides. In The Journal of Geology 76 (4), pp. 382–403.

Bertrandsson Erlandsson, V.; Foltyn, K.; Muchez, P.; Rantitsch, G.; Ellmies, R.; Melcher, F. (in review, submitted on 2023-05-19). Sulfide geochemistry in sediment-hosted Cu(-Co) metallogenic districts: LA-ICP-MS analyses of chalcopyrite, sphalerite, and pyrite. Mineralium Deposita.

Bertrandsson Erlandsson, V.; Gopon, P.; Waldl, H.; Misch, D.; Ellmies, R.; Melcher, F. (2023): Sphalerite as a non-traditional critical metal source: Correlative microscopy (EPMA, EBSD, and APT) of cobalt-enriched sulfides from the sediment-hosted copper-cobalt Dolostone Ore Formation deposit, Namibia. In Frontiers in Earth Science 11, p. 1171859.

Bertrandsson Erlandsson, Viktor; Wallner, Daniela; Ellmies, Rainer; Raith, Johann G.; Melcher, Frank (2022): Trace element composition of base metal sulfides from the sediment-hosted Dolostone Ore

Formation (DOF) Cu-Co deposit in northwestern Namibia: Implications for ore genesis. In *Journal of Geochemical Exploration*, p. 107105.

Blood, J. (2019): Proposed Opuwo Cobalt Mining Project: Final Scoping Report: Opuwo, Kunene Region, Namibia.

Brandt, S.; Klemd, R.; Xie, H.; Bobek, P. (2021): Unravelling the PTt history of three high-grade metamorphic events in the Epupa Complex, NW Namibia: Implications for the Paleoproterozoic to Mesoproterozoic evolution of the Congo Craton. In *American Journal of Science* 321 (1-2), pp. 235–296.

Celsius Resources LTD (2019): Building an Extensive Cobalt Resource in Namibia.

Celsius Resources Limited (2021): ASX Release 1 July 2021 Celsius doubles mineral resource at Opuwo cobalt-copper project.

Cook, N.J.; Ciobanu, C.L.; Pring, A.; Skinner, W.; Shimizu, M.; Danyushevsky, L.V. et al. (2009): Trace and minor elements in sphalerite: A LA-ICPMS study. In *Geochimica et Cosmochimica Acta* (73), Article 16, pp. 4761–4791.

Duran, C.J.; Dubé-Loubert, H.; Pagé, P.; Barnes, S.-J.; Roy, M.; Savard, D. et al. (2019): Applications of trace element chemistry of pyrite and chalcopyrite in glacial sediments to mineral exploration targeting: Example from the Churchill Province, northern Quebec, Canada. In *Journal of Geochemical Exploration* (196), pp. 105–130.

Ellmies, R. (2018): Extensive stratiform Cu-Co-mineralisation at Okondaurie, Kunene Region. Unpublished Internal Report, Kunene Resources (Pty) Ltd.

Ellmies, R. (2019): Cobalt-copper and vanadium-chromium horizons in the Upper Ombombo Formation: A new mineral province in Kunene region? Geological Society of Namibia. Windhoek, Namibia.

European Commission (2020): Communication from the Commission to the European Parliament, the Council, the Economic and Social Committee and the Committee of the Regions. Critical Raw Materials Resilience: Charting a Path towards greater Security and Sustainability. Edited by European Commission. Brussels, Belgium.

European Commission (2023): Study on the Critical Raw Materials for the EU 2023 – Final Report. Edited by European Commission. Available online at https://single-market-economy.ec.europa.eu/sectors/raw-materials/areas-specific-interest/critical-raw-materials_en.

Foster, D.A.; Goscombe, B.D.; Gray, D.R. (2009): Rapid exhumation of deep crust in an obliquely convergent orogen: The Kaoko Belt of the Damara Orogen. In *Tectonics* (28), Article 4, 1-24.

Foster, G.; Parrish, R.R. (2003): Metamorphic monazite and the generation of PTt paths. In *Geological Society, London, Special Publications* 220 (1), pp. 25–47.

Frenzel, M.; Hirsch, T.; Gutzmer, J. (2016): Gallium, germanium, indium, and other trace and minor elements in sphalerite as a function of deposit type—A meta-analysis. In *Ore Geology Reviews* (76), pp. 52–78.

Goscombe, B.D.; Gray, D.R.; Armstrong, R.A.; Foster, D.A.; Vogl, J. (2005): Event geochronology of the Pan-African Kaoko Belt, Namibia. In *Precambrian Research* (140), Article 3, 1203-1241.

Goscombe, B.D.; Hand, M.; Gray, D.R.; Mawaby, J.O. (2003): The Metamorphic Architecture of a Transpressional Orogen: the Kaoko Belt, Namibia. In *Journal of Petrology* (44).

Hitzman, M.W.; Kirkham, R.; Broughton, D.; Thorson, J.; Selley, D. (2005): The sediment-hosted stratiform copper ore system. In *Economic Geology* (100).

Hu, Y.; Wei, C.; Ye, L.; Huang, Z.; Danyushevsky, L.; Wang, H. (2021): LA-ICP-MS sphalerite and galena trace element chemistry and mineralization-style fingerprinting for carbonate-hosted Pb-Zn deposits: Perspective from Early Devonian Huodehong deposit in Yunnan, South China. In *Ore Geology Reviews*, p. 104253.

Huston, D.L. (1997): Stable isotopes and their significance for understanding the genesis of volcanic-hosted massive sulfide deposits: a review.

Jensen, M.L. (1967): Sulfur isotopes and mineral genesis. In: Barnes, H., Wiley, J., Sons (Eds.), *Geochemistry of Hydrothermal Ore Deposits*, New York. 143, p. 165.

Jung, S.; Kröner, A.; Hauff, F.; Masberg, P. (2015): Petrogenesis of Synorogenic diorite-granodiorite-granite complexes in the Damara Belt, Namibia: Constraints from U–Pb zircon ages and Sr–Nd–Pb isotopes. In *Journal of African Earth Science* (101), pp. 253–265.

Kato, T. (2005): New accurate Bence-Albee α -factors for oxides and silicates calculated from the PAP correction procedure. In *Geostandards and Geoanalytical Research* 29 (1), pp. 83–94.

Lerouge, C.; Cailteux, J.; Kampunzu, A.B.; Milési, J.P.; Fléhoc, C. (Eds.) (2004): Preliminary sulfur isotope data of the Luiswishi ore deposit, DRC. 20th Colloquium on African Geology: Abstracts, Orléans, 2–7 June 2004: BRGM.

McGowan, R.R.; Roberts, S.; Boyce, A. J. (2006): Origin of the Nchanga copper–cobalt deposits of the Zambian Copperbelt. In *Mineralium Deposita* (40), Article 6-7, p. 617.

Miller, R. McG. (2008): *The Geology of Namibia*. 2nd ed. Windhoek, Namibia: Geological Survey.

Miller, R. McG. (2013): Comparative Stratigraphic and Geochronological Evolution of the Northern Damara Supergroup in Namibia and the Katanga Supergroup in the Lufilian Arc of Central Africa. In *Geoscience Canada* (40), Article 2, pp. 118–140.

Milodowski, A.E.; Zalasiewicz, J.A. (1991): Redistribution of rare earth elements during diagenesis of turbidite/hemipelagite mudrock sequences of Llandovery age from central Wales. In *Geological Society, London, Special Publications* 57 (1), pp. 101–124.

Morton, A.C.; Hallsworth, C.R. (1999): Processes controlling the composition of heavy mineral assemblages in sandstones. In *Sedimentary Geology* 124 (1-4), pp. 3–29.

Ohmoto, H.; Rye, R.O. (1979): *Isotopes of Sulfur and Carbon*. In: Barnes, H., Wiley, J., Sons (Eds.), *Geochemistry of Hydrothermal Ore Deposits*, New York.

Pal, D.C.; Chaudhuri, T. (2016): Radiation damage-controlled localization of alteration haloes in albite: Implications for alteration types and patterns vis-à-vis mineralization and element mobilization. In *Mineralogy and Petrology* 110, pp. 823–843.

Schandl, E.S.; Gorton, M.P. (2004): A textural and geochemical guide to the identification of hydrothermal monazite: criteria for selection of samples for dating epigenetic hydrothermal ore deposits. In *Economic Geology* 99 (5), pp. 1027–1035.

Schreiber, U.M.; Milner, S.C.; Goscombe, B.G. (2011): *Geological map of Namibia : 1:250 000 geological series: Sheet 1812 Opuwo*.

Seal, R.R. (2006): Sulfur isotope geochemistry of sulfide minerals. In *Reviews in mineralogy and geochemistry* (61), Article 1, pp. 633–677.

Seth, B.; Armstrong, R.A.; Brandt, S.; Villa, I.M.; Kramers, J.D. (2003): Mesoproterozoic U–Pb and Pb–Pb ages of granulites in NW Namibia: reconstructing a complete orogenic cycle. In *Precambrian Research* (126), Article 1-2, pp. 147–168.

Seth, B.; Kröner, A.; Mezger, K.; Nemchin, A.A.; Pidgeon, R.T.; Okrusch, M. (1998): Archaean to Neoproterozoic magmatic events in the Kaoko belt of NW Namibia and their geodynamic significance. In *Precambrian Research* (92), Article 4, pp. 341–363.

Shanks, W.C., III. (2001): Stable isotopes in seafloor hydrothermal systems: vent fluids, hydrothermal deposits, hydrothermal alteration, and microbial processes. In *Reviews in mineralogy and geochemistry* 43 (1), pp. 469–525.

Singletary, S.J.; Hanson, R.E.; Martin, M.W.; Crowley, James L.; Bowring, Samuel A.; Key, Roger M. et al. (2003): Geochronology of basement rocks in the Kalahari Desert, Botswana, and implications for regional Proterozoic tectonics. In *Precambrian Research* 121 (1-2), pp. 47–71.

Sweeney, M.; Turner, P.; Vaughan, D.J. (1986): Stable isotope and geochemical studies in the role of early diagenesis in ore formation, Konkola Basin, Zambian copper belt. In *Economic Geology* (81), Article 8, pp. 1838–1852.

USGS (2020): Mineral commodity summaries 2020. DOI: 10.3133/mcs2020.

USGS (2022): 2022 Final List of Critical Minerals. Notices. Vol. 87, No. 37. U.S. Geological Survey, Department of the Interior. Available online at <https://www.usgs.gov/news/national-news-release/us-geological-survey-releases-2022-list-critical-minerals>.

Wallner, D.; Bertrandsson Erlandsson, V.; Raith, J.; Rantitsch, G.; Melcher, F.; Ellmies, R. (2022): Mineralogical and Geochemical Characterization of the Dolostone Ore Formation, Kunene Region, Namibia. (Poster). Leoben, Austria, 2022.

2. Publications

2.1. List of Included Publications

The following publications have been written in the scope of resolving the aforementioned research questions of this PhD dissertation:

- I. Trace element composition of base metal sulfides from the sediment-hosted Dolostone Ore Formation (DOF) Cu–Co deposit in northwestern Namibia: Implications for ore genesis
Viktor Bertrandsson Erlandsson, Daniela Wallner, Rainer Ellmies, Johann G. Raith, Frank Melcher
Journal of Geochemical Exploration, 243 (2022) 107105
- II. Sphalerite as a non-traditional critical metal source: Correlative microscopy (EPMA, EBSD, and APT) of cobalt-enriched sulfides from the sediment-hosted copper-cobalt Dolostone Ore Formation deposit, Namibia.
Viktor Bertrandsson Erlandsson, Philip Gopon, Helene Waldl, David Misch, Rainer Ellmies, Frank Melcher
Frontiers in Earth Science, 11 (2023) 1171859
- III. Sulfide geochemistry in sediment-hosted Cu(-Co) metallogenic districts: LA-ICP-MS analyses of chalcopyrite, sphalerite, and pyrite
Viktor Bertrandsson Erlandsson, Krzysztof Foltyn, Philippe Muechez, Gerd Rantitsch, Rainer Ellmies, Frank Melcher
Mineralium Deposita, (submitted on 2023-05-19) MIDE-D-23-00105
- IV. New perspective on trace element (Re, Ge, Ag) hosts in the Cu-Ag Kupferschiefer deposit, Poland: Insight from a LA-ICP-MS trace element study
Krzysztof Foltyn, **Viktor Bertrandsson Erlandsson**, Władysław Zygo, Frank Melcher, Jadwiga Pieczonka
Ore geology Reviews, 143 (2022) 104768

2.2. My Contribution to the Included Publications

	Conception and planning ¹	Experiments	Analysis and interpretation	Manuscript preparation ¹
Publication I	95 %	100 %	90 %	90 %
Publication II	70 %	85 %	80 %	90 %
Publication III	90 %	100 %	70 %	80 %
Publication IV	15 %	80 %	30 %	10 %

2.3. List of Additional Publications

The following publications have coauthored and published during the timespan of the PhD, but were unrelated to the research questions of the PhD project:

Alves, F.E.A., Silva-Alves, G.P., Neumann, R., Neto, A.V.C., Brando-Soares, M., **Bertrandsson Erlandsson, V.** (in review, submitted on 2023-07-06). Native W, W-Ni Native Alloy, and Ag-Cu-Ni-Zn Native Alloys in the Oxidized Section of the Zona Basal Polymetallic Occurrence, Quadrilátero Ferrífero Mining District, Southeast Brazil. *American Mineralogist*.

Melcher, F., **Bertrandsson Erlandsson, V.**, Gartner, V., Henjes-Kunst, E., Raith, J., Rantitsch, G., Onuk, P., Henjes-Kunst, F., Potočnik Krajnc, B., Šoster, A. (in print). Carbonate-hosted “Alpine-type” lead-zinc deposits in the Eastern and Southern Alps – trace element geochemistry and isotopic data of sulphides. IAEG (Irish Association for Economic Geology) 50th Anniversary Conference.

Šoster, A., **Bertrandsson Erlandsson, V.**, Velojić, M., Gopon, P. (2023) Ultraviolet-photoluminescence and trace element analyses in Ga-rich sphalerite from the Djebel Gustar Zn-Pb deposit, Algeria. *Ore Geology Reviews*. Doi: <https://doi.org/10.1016/j.oregeorev.2023.105474>.

Steiner, T. M.C., **Bertrandsson Erlandsson, V.**, Šajn, R., Melcher, F. (2022). Preliminary chemical and mineralogical evaluation of tailing materials from base metal sulfide deposits in Serbia and North Macedonia. *Geologia Croatica*.

Velojić, M., **Bertrandsson Erlandsson, V.**, Melcher, F., Onuk, P., Jelenković, R., Cvetković, V. (2022). Trace elements in pyrite from the Čukaru Peki porphyry Cu–high-sulfidation deposit, Serbia: implications for ore evolution in a polyphase hydrothermal system. *Geologia Croatica*.

Foltyn, K., **Erlandsson, V. B.**, Kozub-Budzyń, G. A., Melcher, F., & Piestrzyński, A. (2020). Indium in polymetallic mineralisation at the Gierczyn mine, Karkonosze-Izera Massif, Poland: results of EPMA and LA-ICP-MS investigations. *Geological Quarterly*, 64(1), 74-85.

¹ Supervision not included

Şengün, F., **Erlandsson, V. B.**, Hogmalm, J., & Zack, T. (2019). In situ Rb-Sr dating of K-bearing minerals from the orogenic Akçaabat gold deposit in the Menderes Massif, Western Anatolia, Turkey. *Journal of Asian Earth Sciences*, 185, 104048.

3. Dissertation Outline

This PhD dissertation includes four articles, of which three have been published and one has been submitted. Three of these articles are first-authored and the fourth is second-authored.

With these publications, this thesis has been divided into two parts:

Part 1 – Sulfide trace element geochemistry: applications for ore genesis of the Cu-Co-Zn Dolostone Ore Formation deposit

The first part of this thesis focuses on the geochemistry, coupled with a range of microscopy methods, of the sulfides to deduce genetic and formation aspects of the DOF deposit. This led to constraining the paragenetic sequence of the DOF deposit, with several stages responsible for sulfide mineralization, ranging from syn-sedimentary pyrite to syn- and late-orogenic hydrothermal deformation and vein formation.

This part includes the following published articles (publication numbers are from the aforementioned section “2.1 List of Included Publications”):

Publication I: Bertrandsson Erlandsson, V., Ellmies, R., Raith, J.G., Wallner, D., & Melcher, F. (2022). Trace element composition of base metal sulfides from the sediment-hosted Dolostone Ore Formation (DOF) Cu-Co deposit in northwestern Namibia: Implications for ore genesis. *Journal of Geochemical Exploration*. 243: 107105.

Publication II: Bertrandsson Erlandsson, V., Gopon, P., Waldl, H., Misch, D., Ellmies, R., & Melcher, F. (2023). Sphalerite as a non-traditional critical metal source: correlative microscopy (EPMA, EBSD, APT) of cobalt hyper-enriched sphalerite from the sediment-hosted copper-cobalt Dolostone Ore Formation (DOF) deposit, Namibia. *Frontiers in Earth Science: special issue “Ore Formation and Critical Metal Deposits: Geological Contribution to the Clean Energy Transition”*. 11:1171859. doi: 10.3389/feart.2023.1171859.

Part 2 – Holistic perspectives of Dolostone Ore Formation deposit to other sediment-hosted Cu(-Co) deposits

One of the main aims of this PhD project was to put the DOF deposit in a more holistic perspective. This was done by comparing characteristic trace element trends of the sulfides from the DOF to two world-class sediment-hosted Cu(-Co) districts, the CACB and Kupferschiefer. Sulfide trace elements from the Polish Kupferschiefer were published by Foltyn et al. (2022), aka. Publication IV, this data was combined with Publication I and novel data from the DOF and CACB in the submitted Publication III. Publication III gives a holistic perspective on the DOF deposit and leads into the metal source for sediment-hosted Cu(-Co) deposits.

This part includes the following published articles (publication numbers are from the aforementioned section “2.1 List of Included Publications”):

Publication III: **Bertrandsson Erlandsson, V.**, Krzysztof Foltyn, Philippe Muchez, Gerd Rantitsch, Rainer Ellmies, Frank Melcher (submitted 19-05-2023). Sulfide geochemistry in sediment-hosted Cu(-Co) metallogenic districts: LA-ICP-MS analyses of chalcopyrite, sphalerite, and pyrite. *Mineralium Deposita*.

Publication IV: Foltyn, K., **Erlandsson, V. B.**, Zygo, W., Melcher, F., & Pieczonka, J. (2022). Newperspective on trace element (Re, Ge, Ag) hosts in the Cu-Ag Kupferschiefer deposit, Poland: Insight from a LA-ICP-MS trace element study. *Ore Geology Reviews*, *143*, 104768.

**4. Part 1 – Sulfide trace element
geochemistry: applications for ore genesis
of the Cu-Co-Zn Dolostone Ore Formation
deposit**

Publication I

Trace element composition of base metal sulfides from the sediment-hosted Dolostone Ore Formation (DOF) Cu–Co deposit in northwestern Namibia: Implications for ore genesis

Viktor Bertrandsson Erlandsson¹, Daniela Wallner¹, Rainer Ellmies², Johann G. Raith¹, Frank Melcher¹

¹Montanuniversität Leoben, Department of Applied Geosciences and Geophysics, Leoben, Austria

²Gecko Namibia, Swakopmund, Namibia

Journal of Geochemical Exploration, 243 (2022) 107105

The publication version in this thesis is the final version, which was accepted and published.

Abstract

The Dolostone Ore Formation (DOF) copper-cobalt mineralization is a recently discovered sediment-hosted deposit in Neoproterozoic low-grade metamorphosed carbonates and fine-grained siliciclastics in the Pan-African Kaoko Belt in Namibia. Six mineralization styles have been identified in the DOF. They comprise both brittle and ductile (micro)textures and include sulfides occurring in disseminations, clusters, nodules, pressure shadows, veins and the locally termed “DOF event”.

Laser ablation inductively coupled plasma mass spectrometry (LA-ICP-MS) in situ trace element analyses of base metal sulfides (sphalerite, chalcopyrite, pyrite and pyrrhotite) show distinct groupings of the mineralization styles. Sphalerite and chalcopyrite from the dissemination, cluster and nodule mineralization styles show similar trace element composition trends (e.g., Fe, Co, Ni, Se, Cd for sphalerite and Co, Ni, Se and Bi for chalcopyrite) that differ from vein and pressure shadow sphalerite and chalcopyrite which group together. Pyrite compositions in cluster and nodule types show a similar trace element grouping in elements such as Co, Ni, As, Se, Sb, Tl and Pb. In contrast, pyrites from pressure shadows and veins show a decoupling in elements such as Se, Sb, Tl and Pb, that grouped together in the aforementioned pyrite mineralization styles. Ge-Ga-In-Mn-Fe in sphalerite (GGIMFis) geothermometry indicates that the sphalerite (and associated sulfides) from all mineralization styles crystallized at temperatures at or above 310 ± 50 °C. This temperature range corresponds with the regional metamorphism induced by the Damaran orogeny. Thus, the DOF copper-cobalt mineralization is related to, or at least strongly overprinted by, Damaran metamorphism and deformation.

Trace element differences in the sphalerite-chalcopyrite groupings reveal that the vein and pressure shadows mineralization styles were formed at lower temperatures than the other ones but still above the GGIMFis closing temperature of 310 ± 50 °C. Evidence is vacant for a typical low-temperature, early sediment-hosted copper mineralization. This work demonstrates the strength of using trace elements for deducing the ore-forming system of polyphase sulfide deposits.

Keywords: copper-cobalt, sediment-hosted deposits, trace element, sulfides, LA-ICP-MS, Namibia

1. Introduction

Sediment-hosted copper deposits (SHCD) are one of the largest sources for Cu in the world (Mudd et al. 2013), especially when considering that they are more or less restricted to supergiant deposits hosted in just three sedimentary basins namely the Permian Zechstein Basin with the Polish and German Kupferschiefer, the Neoproterozoic Katangan Basin hosting the Central African Copperbelt (CACB) which stretches across Zambia and the Democratic Republic of Congo, and the Russian Paleoproterozoic Kodaro-Udokan Basin (Hitzman et al. 2010). The CACB alone accounted for around 10 % of the global Cu production in 2019 (USGS 2020). Besides being a globally significant source for copper, SHCDs constitute the number one source of cobalt, namely from the CACB. In 2019, the Democratic Republic of Congo and Zambia stood for 68 % of the global Co production (European Commission 2020; USGS 2020). Cobalt is increasingly becoming more relevant in the strive towards a fossil fuel-free future, as 49 % of the world’s Co is used in the production of batteries (Alves Dias et al. 2018) and new significant sources of cobalt are sought

after as the European Commission has classified cobalt as a critical raw material (European Commission 2020).

Stratiform sediment-hosted copper deposits characteristically form in transgressional rift-basin environments, where the basement and the basal clastic red bed rift sediments are commonly believed to be the source for the metals (Hitzman et al. 2005). Mafic minerals from e.g. subaerial volcanics, have been shown to contain substantial concentrations of Cu that may be released from the minerals during weathering and diagenesis (Walker 1989). Subaerial volcanics are commonly found within the red bed sediments and have therefore been proposed as a source of the Cu for SHCDs (e.g. Hitzman et al. 2005; Metcalfe et al.; Brown 1992; Haynes 1986). The metals were leached and transported by oxidizing, near neutral pH brines which predominantly precipitate sulfides due to reduction when interacting with a redox boundary, typically host rocks rich in organic matter or mobile hydrocarbons (Hitzman et al. 2005). Dating the exact age of SHCD mineralization is difficult and complex. It is now widely agreed upon that ore genesis is a multi-stage process which spans over a long time, from early diagenesis, through basin inversion with even the later stages of orogenesis (basin closure) resulting in ore remobilization and a final mineralization stage (Mambwe et al. 2019; Brems et al. 2009; Dewaele et al. 2006; Hitzman et al. 2005).

Plenty of LA-ICP-MS trace element data has been published and summarized from a wide range of base metal sulfides and deposit types (e.g. sphalerite: Cook et al. (2009), Pfaff et al. (2011), Ye et al. (2011), Cook et al. (2012), Murakami and Ishihara (2013), Belissont et al. (2014), Lockington et al. (2014), Frenzel et al. (2016); chalcopyrite: George et al. (2016), George et al. (2018), Duran et al. (2019); pyrite and/or pyrrhotite: Campbell and Ethier (1984), Large et al. (2007), Thomas et al. (2011), Winderbaum et al. (2012), Ingham et al. (2014), Large et al. (2014), Gregory et al. (2015), Liu et al. (2018), Conn et al. (2019); and galena: George et al. (2015)). One common feature of all aforementioned data sets is the lack of trace element data for SHCDs. Only recently has this been acknowledged and data on the Polish Kupferschiefer (Foltyn et al. 2022) and the Kalahari Copper Belt (Kelepile et al. 2020) have been published.

The DOF is a recently discovered copper-cobalt mineralization hosted in low-grade metamorphosed dolomitic marlstones, and to a lesser extent argillaceous carbonates, of the Neoproterozoic Ombombo Subgroup metasediments in the Kunene region of northwestern Namibia and has the potential of becoming Namibia's first Co mine (Ellmies 2013). The DOF mineralization currently has an indicated and inferred mineral resource of 225.5 Mt with grades of 0.12 % Co, 0.43 % Cu and 0.54 % Zn (Celsius Resources Limited 2021). Although of very large tonnage, the DOF Co-Cu-mineralization remains up until today the only known cobalt deposit in Namibia. Within this study, we present trace element data trends and partitioning between sphalerite, chalcopyrite, pyrite and pyrrhotite, and discuss the pervasive effects of regional Damaran metamorphism on the SHCD Dolostone Ore Formation and its impact on ore formation and sulfide geochemistry, hoping to expand the understanding of the formation processes behind these economically significant SHCDs.

2. Geological Setting

2.1 Regional geology of the Dolostone Ore Formation mineralization

The sediment-hosted Cu-Co(-Zn-Pb) Dolostone Ore Formation (DOF) mineralization was first recognized in 2012. Exploration of the DOF mineralization started in 2013 by Kunene Resources, and was progressed in Joint Ventures with First Quantum Minerals (FQM) and later Celsius Resources. The DOF mineralization is hosted in dolomitic argillaceous marlstones and argillaceous carbonates within the Neoproterozoic Ombombo Subgroup of the Damara Supergroup sediments (Hoffmann et al. 2002; Allen 2016). The Damara Supergroup represents a typical rift basin-carbonate platform sedimentary environment, starting at its base with basal fluvial clastic red bed sediments of the Neoproterozoic Nosib Group (up to 5 km thick; Porada 1989), which represent the rift environment with dominantly arkosic to feldspathic sandstones and with lesser conglomerates. These clastic sediments were deposited from around 850 Ma in predominantly NE-trending half grabens within the 595 – 550 Ma Kaoko Belt. The Nosib Group unconformably overlies the Pre-Damara, Paleoproterozoic basement (Miller 2008; Allen 2016; Guj 1970), i.e. the 1861 to 1758 Ma Epupa gneisses (Kröner et al. 2010) in the DOF area.

Following the clastic rift sediments of the Nosib Group is the Otavi Group, dominated by cyclically deposited marine carbonates and siliciclastics. In the Kunene region (Kunene Zone) the Otavi Group comprises three subgroups: the Ombombo, Abenab and Tsumeb Subgroups (from oldest to youngest). The Ombombo Subgroup comprises carbonates and siliciclastics with a thickness between 1.6 and 2.8 km in the study area. Within the Northern Platform and the Northern Margin Zone (Fig. 1), the Ombombo Subgroup is subdivided into the Beesvlakte, Devede and Okakuyu Formations (Hoffman and Halverson 2008; Miller 2008). This subdivision has not been confirmed for the Kunene Zone (Fig. 1); though mapping by Allen (2016) shows that the local DOF basin displays facies changes from west to east, with an easterly increase in the thickness and content of carbonate relative to the siliciclastic component of the underlying siltstones. This is believed to correspond with a deepening of the basin towards the east. The existence of east-dipping syn-sedimentary faults has been proposed by Allen (2016), and may be related to the eastward deepening of the basin.

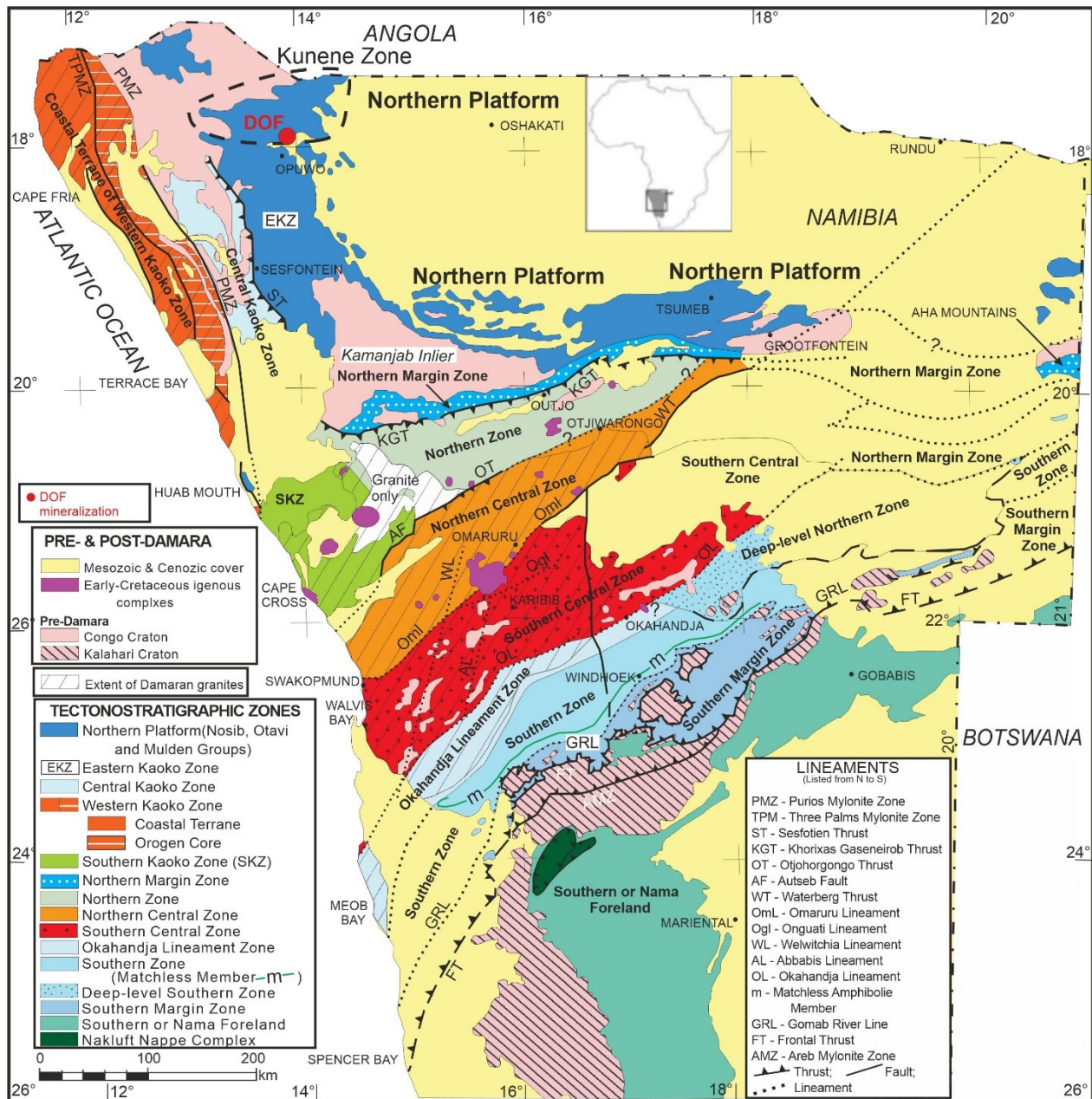


Fig. 1. Map showing main tectonostratigraphic zones of the Damara Orogen and the Kunene Zone (modified after Miller 2013 and references therein) with the DOF (Dolostone Ore Formation) Cu-Co mineralization marked within the Kunene Zone of the Eastern Kaoko Zone (EKZ) in the Eastern Foreland.

The DOF horizon occurs within the upper part of the Ombombo Group, several kilometers above the red beds of the Nosib Group (Fig. 2) and a flysch-like sedimentation of calcareous and carbonaceous siliciclastic sediments of the lower and middle parts of the Ombombo Formation. The sediment sequence hosting the DOF horizon comprises calcareous and carbonaceous shale, shale, siltstone, silty dolostone and dolostone. Carbonaceous horizons occur widely in the footwall and hanging wall of the DOF and are not specific to the DOF. Arkosic silty sandstones and calcareous silty sandstones have also been mapped in the sediment package hosting the DOF. The carbonate rocks have been interpreted as pelagic carbonates (Allen 2016). Together with the

shales and siltstones, they were deposited in a low energy environment on the basin slope. Sub-grabens within the slope facies may have served as the depositional environment for the sandstone, i.e. as channel deposits. The varying degree of carbonate content within the siliciclastic rocks is due to variations in pelagic carbonate sedimentation and diagenesis, which is common for sedimentary rocks at the continental slope (Allen 2016). Organic matter occurs throughout the entire Ombombo Formation (Allen 2016).

The Abenab and Tsumeb Subgroups overlay the Ombombo Subgroup (Fig. 2). Both start with basal glacial diamictites associated with the Sturtian glaciation (Chuos Formation diamictite) and the Marinoan glaciation (Ghuab Formation diamictite), and each with subsequent transgressive cap carbonates (the Rasthof/Berg Aukas Formations and Maieberg Formation/Keilberg Member respectively; Hoffmann and Prave 1996, Hoffman 2011). Widespread diagenetic dolomitization of Otavi Group limestone is common, especially along the margins of the different sub-basins. The Mulden Group is the youngest group of the Damara Supergroup and typically comprises flysch sediments (Miller 2008).

The Damara Supergroup (Fig. 2) was proposed to be a coeval analogue to the Katanga Supergroup in the Central African Copperbelt by Miller (2013), the locality of a range of world-class sediment-hosted Cu-Co deposits. This is based on correlations of the sedimentary basin successions with the Sturtian and Marinoan glacial sediments acting as direct datum markers. The two Supergroups have also been shown to have been affected by similar deformation during the Pan-African orogeny (Miller 2013). However, one of the key differences between these Neoproterozoic sedimentary successions is the lack of widespread evaporites in the Kaoko Belt (Miller 2008, 2013).

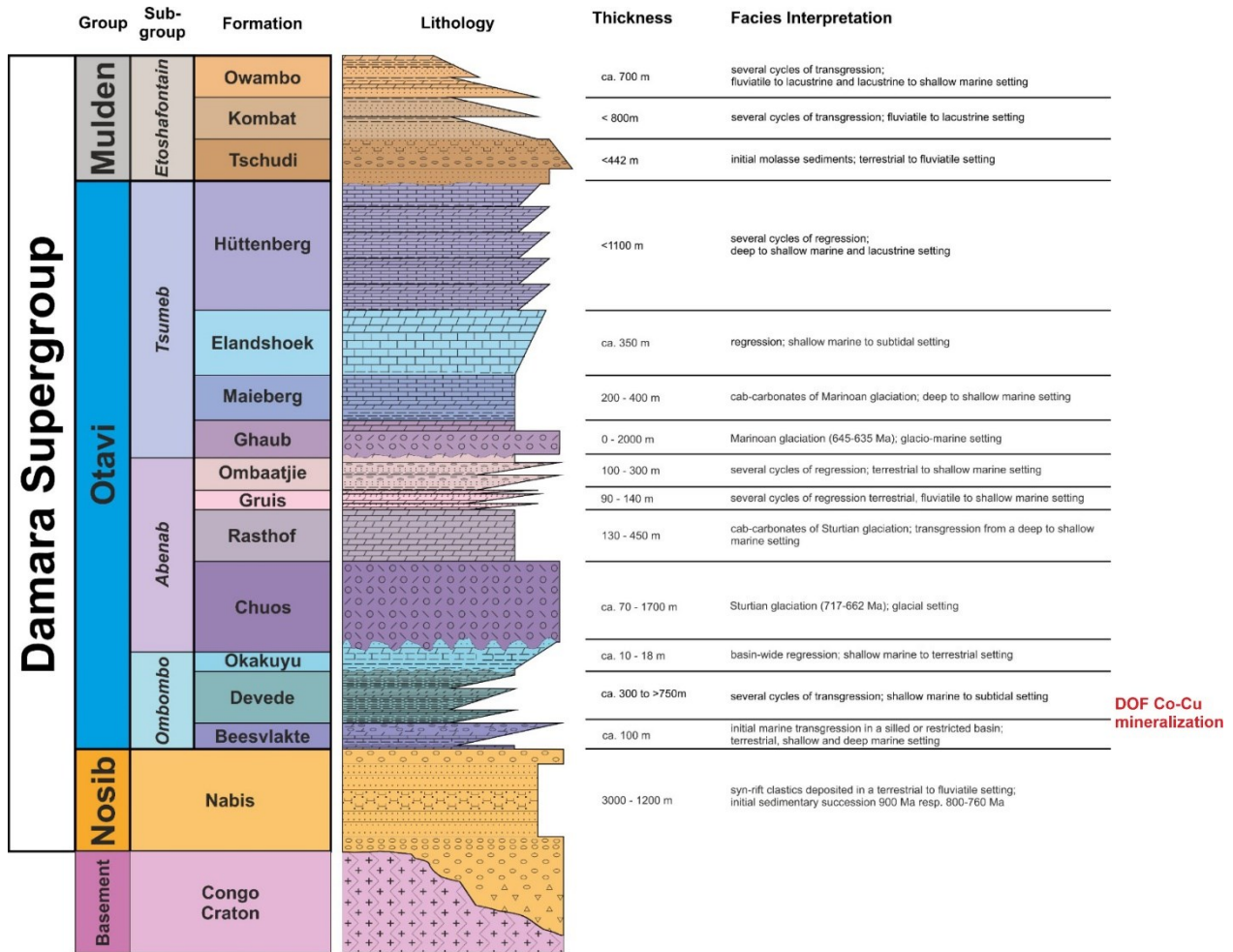


Fig. 2. Generalized stratigraphic column of the Damara Supergroup related to the study area and the Kaoko Belt. Compiled after Martin (1965), Hedberg (1979), SACS (1980), Hoffmann and Prave (1996), Miller (1997), Hoffmann et al. (2004), Miller (2008), Hoffman and Halverson (2008), Hood et al. (2015) and Hoffman et al. (2021). With the proposed location of the Co-Cu DOF mineralization marked out.

2.2 Deformational history of the Kaoko Belt

The orogenesis of the Kaoko Belt comprises two main phases, the Kaoko Phase (590—535 Ma) and the Damara Phase (555—505 Ma), both part of the Damara orogeny (Goscombe et al. 2017; Goscombe et al. 2003). The Kaoko Belt is considered a classic example of an oblique transpressional orogenic belt and is the result of the collision of the Congo, Kalahari and Rio De La Plata cratons (Goscombe et al. 2017; Porada 1989; Prave 1996; Trompette 1997). The Kaoko phase starts at around 590 Ma with the W over E obduction of the Coastal Terrane onto the western margin of the Congo Craton (Fig. 1). Between 580—560 Ma the main transpressional phase of the Kaoko Phase occurred, associated with emplacement of syn-kinematic granitoids. The transpressional phase comprised both wrench-type and classical shortening deformation. Northwest-southeast strike-slip shear zones developed after around 550 Ma, which marks the final stage of the initial transpressional Kaoko Phase (Goscombe et al. 2017; Goscombe et al. 2005; Konopásek et al. 2005; Goscombe et al. 2003; Hoffman, et al. 1998; Seth et al. 1998).

The onset of NNW-SSE shortening during the Damaran Phase, at approximately 530–525 Ma, marks the termination of the Kaoko Phase and results in reactivation of Kaoko Belt shear zones and pegmatite formation, accompanied by rapid exhumation and reactivation of preexisting shear zones at temperatures of around 300 °C (Foster et al. 2009; Goscombe et al. 2005). Prolonged Damaran N-S shortening resulted in E-W buckling of the Kaoko Belt shear zones along with emplacement of a second generation of pegmatites at around 515 Ma (Goscombe et al. 2005). At around 508–505 Ma, the stress field changed back to E-W across the Kaoko Belt with subsequent E-W shortening and N-S extension. This final stage of the Kaoko Belt was accompanied by a post-kinematic thermal pulse and in situ melting, resulting in a third generation of pegmatite (Goscombe et al. 2017).

Goscombe et al. (2005) subdivided the Kaoko Belt into four major tectono-metamorphic zones from E to W: the Eastern Foreland (referred to as the Eastern Kaoko Zone by some authors, e.g. Miller 2008), External Nappe Zone, Orogen Core and the Coastal Terrain (Fig. 1). These zones are discriminated based on differences in ages of events, style of the deformation and metamorphic response, which were controlled by two major shear zones, the Three Palms Mylonite Zone (TPMZ) and the Purros Mylonite Zone (PMZ), along with the Sesfontein Thrust (ST) in the east (Fig. 1). There is a general decrease in metamorphic grade and deformation eastwards. Temperature estimates based on host rock assemblages suggest that the regional metamorphism in the eastern Kaoko Belt (east of the Sesfontein Thrust) did not exceed 400 °C (Guj 1970).

The Eastern Foreland hosting the DOF is characterized by the lowest degree of Damaran metamorphism (sub-greenschist facies metamorphism) of carbonate platform to molasse sediments. Deformation in the Eastern Foreland is expressed as km-scale upright, open to close cylindrical folds, box folds and ramp anticlines subsequent to E-W coaxial shortening (Goscombe et al. 2003; Guj 1970). It is the last shortening phase of the Kaoko Belt (590 – 535 Ma) that is primarily responsible for these structures of the Eastern Foreland and in particular in the Kunene Zone. The earlier transpressional phases of the western and central Kaoko Belt had minimal impact on the Kunene Zone of the Eastern Foreland (Goscombe et al. 2003).

The Damara Supergroup sediments unconformably overly the Paleoproterozoic basement of the Congo Craton which in the Eastern Foreland has not been reworked during the Damara orogeny. The E-W shortening phase of the belt also led to the development of a network of steep discontinuous thrusts, such as the Sesfontein Thrust, which marks the western margin of the Eastern Foreland or “Eastern Domain” (Guj 1970). In the Eastern Foreland shortening structures developed like progressively tightening of folds, late-stage crenulation and low-grade metamorphism during the late progressive transpressional stage of the Kaoko Phase, when the Sesfontein Thrust formed (Goscombe et al. 2017). During the final shortening phase of the Kaoko Belt evolution, ESE-trending shear zones developed in the Kunene Zone of the Eastern Foreland (Fig. 3) (Goscombe 1999).

2.3 Geology of the Dolostone Ore Formation Cu-Co mineralization

The DOF is defined by a Cu-Co-Zn-Pb-Fe-Mn enrichment within the Ombombo Subgroup deposited in the Ombazu Trough. The Ombazu Trough is a NW-SE trending basin (Ellmies 2018) that formed during early rifting (ca. 900 – 757 Ma; Miller 2013) of the metamorphic basement

rocks of the Epupa Complex (Hedberg 1979). Hosted in a siltstone-shale-carbonate succession, the DOF mineralization is considered as a typical stratiform sediment-hosted Cu mineralization that has been mapped over a strike length of at least 43 km by geologists of the exploration companies Celsius Resources and Namibia Critical Metals (Ellmies, 2018). The E-W trending ore horizon dips generally to the north with a dip in the east at 35-40° and 60-70° in the west. The Cu-Co mineralization is still open at depth under the carbonate rocks in the north and seems to stretch across most of the Ombazu Trough. The DOF mineralization is hosted within the lower Ombombo Subgroup of the Damara Supergroup sediments (Hoffmann et al. 2002; Allen 2016). It is herein suggested that the DOF horizon is hosted within mixed carbonate-siliciclastics of the Beesvlakte Formation (Fig. 2). This is based on the mapping by Allen (2016) who shows the proximity to the underlying Nosib Group, as well as the identification of overlying dolostones that are in accordance with the Devede Formation as previously described by Miller (2013), although this remains indecisive as the DOF horizon is stratigraphically situated several kilometers above the Nosib Group. It is important to note that the Damara Supergroup sequence in the Kunene area may not be directly comparable to that of the Ombazu Trough. We can only conclude with certainty that the DOF is hosted within the upper part of the at least 8 km thick Ombombo Subgroup, between the clastic sediments of the Nosib Group and below the Sturtian diamictites of the Chuos Subgroup.

The thickness of the mineralized horizon varies between <1 and 15 m. The DOF horizon generally shows a thickening trend eastwards, which is believed to correspond with a change in host lithologies and deepening of basin (Ellmies 2018). The main ore horizon commonly exhibits a sharp footwall contact, whilst the hanging wall contact is gradual, portrayed as a bell-shaped zone with decreasing ore grade. This zone is referred to as the wider-DOF horizon. Iron is strongly enriched in the DOF horizon and is evident in the gangue mineralogy; the main DOF horizon host rock contains stilpnomelane, ankerite and siderite along with the sulfides.

The Ombombo Subgroup in the DOF area (Fig. 3) displays upright, tight to open WNW-trending folds, which occur at a 500 m to km-scale. In the central DOF area these folds have a steeper northern plunge at around 25–32°, but locally these folds have a less steep plunge at on average 9°. This folding phase is coeval with formation of an axial plane WNW-trending cleavage within the rocks. The penetrative cleavage predominantly is outlined by chlorite and white mica. The WNW cleavage is well developed within most of the different rock types. Fold S-asymmetry and WNW plunge is proposed to have formed during NNE-side up, sinistral shearing associated with shortening to the SSW. At least two sets of high angle to bedding parallel veins are suggested to have formed during this deformation event. The first are WNW-trending, concordant to the cleavage. The second set of veins are NNE-trending, perpendicular to fold and cleavage trends. This set of veins is suggested to have formed perpendicular to extension. Banded, bedding parallel veins are proposed to have formed due to bedding slip, either predating or syngenetic with early Damaran deformation. A later E-W shortening phase resulted in further faulting (Allen 2016). Due to the folded nature of the DOF horizon (Fig. 3), it is believed that the main mineralization predates the large-scale regional folding.

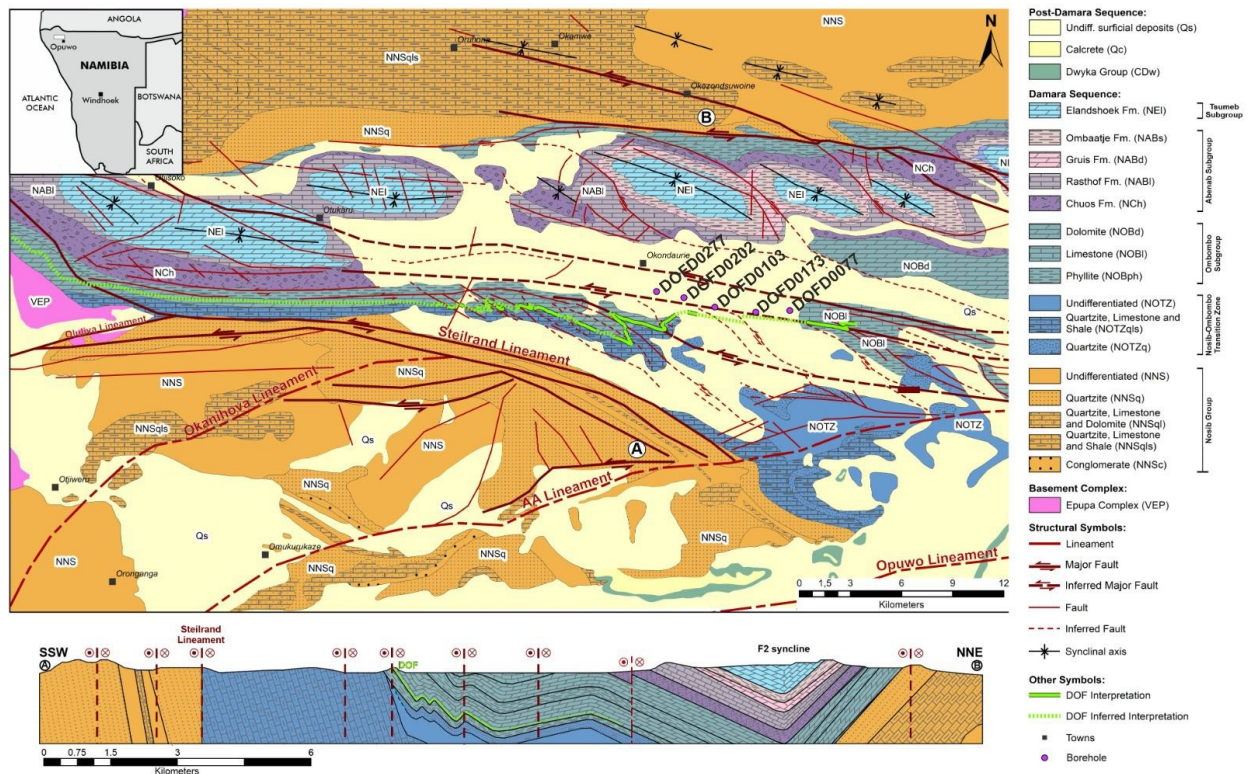


Fig. 3. Geological map showing the DOF mineralization area and boreholes in the southern Kunene Zone of the Eastern Foreland. The map and cross section have been compiled by Wallner et al. (2022) from the following sources: Geological Survey of Namibia (Schreiber et al. 2011) and Allen (2016); the extent of the Nosib-Ombombo Transition Zone (NOTZ) according to Ellmies (2019) and Allen (2016); the extent of the DOF according to Celsius Resources LTD (2019) and Blood (2019); position and orientation of faults after African Mining Capital Pty Ltd (2019). The schematic geological cross-section (marked A - B) is based on additional data by Celsius Resources LTD (2019) and Ellmies (2019).

3. Sampling and Analytical Methods

3.1 Sample description

Nine polished resin mounts and two polished thick-sections (ca. 100 μm) from five different boreholes (Fig. 3) were prepared and subsequently analyzed by LA-ICP-MS. Samples used in this study were collected from exploration drill cores of Celsius Resources. The boreholes were selected to get a spread of approximately 2 km apart. Rare outcrops of mineralized rock are intensely oxidized, covered by calcrete and therefore not of use for chemical analysis of sulfides. Petrographic descriptions herein, of both host rock and mineralization styles, are primarily based on the samples analyzed with LA-ICP-MS. Samples were described and investigated by reflective light microscopy along with a Zeiss Evo MA 10 SEM coupled with a Bruker Quantax EDX detector.

3.2 Laser ablation inductively coupled plasma mass spectrometry (LA-ICP-MS)

In situ LA-ICP-MS spot analyses were performed utilizing an ESI NWR213 Nd:YAG laser ablation system coupled to an Agilent 8800 triple quadrupole ICP-MS, at the Department of Applied Geosciences and Geophysics, Montanuniversität Leoben, Austria. Sulfides were ablated with a spot size diameter of 50 μm with laser fluency set to 5 J/cm², at a 10 Hz repetition rate. Helium was used as the carrier gas with a flow rate of 0.75 L/min. A 30 sec pre-ablation background

collection was done, followed by 60 sec of laser ablation and data acquisition. Individual ablation cycles were followed by a 30 sec delay for cell wash-out.

The in-house sphalerite matrix-matched sinter pressed powder pellet reference material MUL-ZnS1 (Onuk et al. 2017) was used as external standard for the quantification of the element concentrations of sphalerite and iron-sulfides. Sulfur was used as internal standard. The USGS pressed powder polysulfide reference material MASS-1 (Wilson et al. 2002) was used as a secondary standard for quality control of the analysis run. The MASS1 was used as the external standard for the quantification of Te, Au, Tl and Hg in sphalerite and iron-sulfides, as the reference material MUL-ZnS-1 is not suitable for these elements. The MASS-1 was used as external standard and Cu as internal standard for chalcopyrite analyses. Both reference materials were analyzed periodically (every 20 spots) for instrumental drift correction. Masses analyzed were: ^{34}S , ^{51}V , ^{52}Cr , ^{55}Mn , ^{57}Fe , ^{59}Co , ^{60}Ni , ^{63}Cu , ^{67}Zn , ^{71}Ga , ^{74}Ge , ^{75}As , ^{82}Se , ^{95}Mo , ^{107}Ag , ^{111}Cd , ^{115}In , ^{118}Sn , ^{121}Sb , ^{125}Te , ^{197}Au , ^{201}Hg , ^{205}Tl , ^{208}Pb and ^{209}Bi . Data reduction was performed in the Lolite 4 software (Paton et al. 2011). Limits of detection were calculated by the 'Howell et al. 2010' method within the lolite software.

Laser ablation spots were carefully positioned to avoid inclusions, microcracks or other visible impurities that could interfere with the measured data. In general, inclusions were abundant in several of the sulfide phases analyzed such as 'chalcopyrite disease' in sphalerite and Co-sulfide inclusions within the iron-sulfides. Host rock contamination is also a relatively common problem during laser ablation of minerals from sediment-hosted deposits. Thus, interferences in the acquired time-count signal are inevitable. This was also taken into consideration when representative sections of the time-count signal were selected for the data reduction, but could not be completely avoided. All $\mu\text{g/g}$ values reported in this text are median values, if not noted otherwise. Median values were used to minimize the impact of outliers; this is preferable as this type of geochemical data is bound to be skewed by inclusions. P95 and P5 values are reported rather than minimum and max values, due to the presence of extreme outlier values.

4. Results

4.1 Petrography of the DOF mineralization styles

Sulfide mineralization in the DOF mineralization can be subdivided into six mineralization styles: (1) disseminated, (2) cluster, (3) nodule, (4) pressure shadow, (5) vein, and (6) event (Fig. 4). The "event style" is a local term for soft-sediment-like or slump-like structures that occur throughout the footwall of the mineralized stratigraphy, but are intensely mineralized within the DOF horizon. The nodule style was subdivided into two styles, nodule and pressure shadow. This was done as microscopic textures revealed distinct differences. The nodule style has an apparent sedimentary texture. Pressure shadow style is named due to its sigmoidal clast texture, with distinct pressure shadow tails around a core clast.

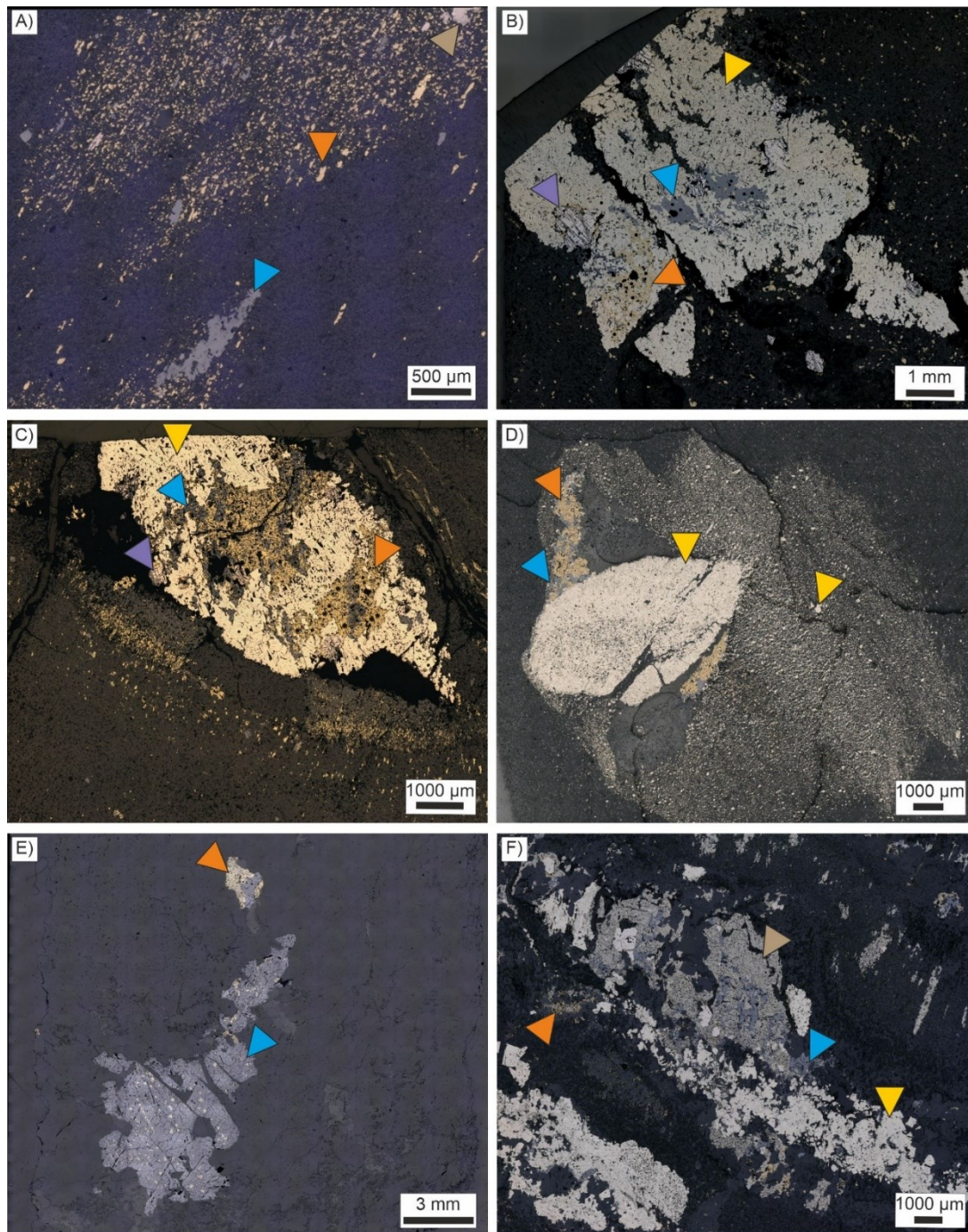


Fig. 4. Plane polarized light reflective light micrographs of the different mineralization styles of the DOF mineralization: A) Disseminated chalcopyrite, sphalerite and pyrrhotite. B) Polysulfide cluster with pyrite, chalcopyrite, sphalerite and linnaeite mineralization. C) Ellipsoidal polysulfide nodule with pyrite, chalcopyrite, sphalerite and linnaeite. D) Chalcopyrite-sphalerite pressure shadow style mineralization around a central pyrite core and surrounded by a halo of fine-grained disseminated pyrite. E) Quartz-carbonate veinlet with sphalerite-chalcopyrite. F) "Event" mineralization style with pyrite, pyrrhotite, sphalerite and chalcopyrite.

4.1.1 Disseminated

Disseminated mineralization (Fig. 4A) is the most pervasive style within the DOF mineralization. Pyrite and pyrrhotite are the major sulfides that can occur as disseminations within the major DOF ore horizon(s) as well as in the country rocks. Disseminated framboidal and euhedral pyrite is widespread outside the main ore horizon(s). Disseminations vary in size from a few μm to over 50 μm , although they tend to be smaller than 30 μm . As the grain size of the sulfide dissemination of the DOF is mostly below 50 μm , less LA-ICP-MS spots were possible for this style. Disseminated sphalerite and chalcopyrite occur as both unoriented, anhedral intergrowths and as elongated, subhedral aggregates either unoriented or elongated along foliations and/or matrix lamination. Idioblastic linnaeite or grimmite (Ni-linnaeite, NiCo_2S_4) crystals occasionally occur disseminated in the host rock matrix. Linnaeite is most commonly enclosed in iron-sulfides and not freely disseminated.

4.1.2 Cluster

Clusters refer to irregular aggregates of sulfides dominantly comprised of either pyrite or pyrrhotite (Fig. 4B). Pyrrhotite has only been recognized to occur in the disseminated, cluster and event mineralization styles. When pyrrhotite occurs in disseminations or clusters, it is without pyrite. The shape of the clusters is irregular with uneven contacts to the host rock matrix. The sulfides in the clusters often contain inclusions of host rock and gangue minerals. Sphalerite and chalcopyrite occur in the clusters as coarser grained, anhedral crystals and may overgrow/replace the iron sulfides. Chalcopyrite also forms rims around idioblastic linnaeite crystals within the clusters (Fig. 5A). Unoriented stilpnomelane laths and siderite are also associated with the sulfides in the clusters (Fig. 5A). Linnaeite occurs as euhedral crystals and commonly contains inclusions of galena. Pseudomorphic replacement of linnaeite by the iron-sulfides has also been observed. Pyrrhotite often contains abundant Co-sulfide "inclusions" (Fig. 5B). These Co-sulfide phases visually resemble exsolution flames, similar to pentlandite flames in pyrrhotite in magmatic Ni ores (e.g. Ramdohr 1969). SEM-EDS analyses of this phase suggests that it is either jaipurite $[\text{CoS}]$ or cobaltpentlandite $[\text{Co}_9\text{S}_8]$, but other non-identified phases containing additional Cu and Ni have also been found, indicating a complex mineralogy in the Co-Ni-Cu-S system. Accessory cobaltite has been identified within linnaeite-bearing clusters. Small (1 – 10 μm) monazite grains have also been documented.

4.1.3 Nodule

Sulfide aggregates in the DOF mineralization of ellipsoidal shape and mm sized are referred as nodules. They are predominantly comprised of coarse-grained pyrite (Fig. 4C). They have uneven contact boundaries to the host rock matrix and in some cases develop into augen-like textures (Fig. 4C). Iron carbonates and stilpnomelane laths are observed within the nodules and both, siderite and ankerite, may form rims around some nodules. Host rock minerals can be found within the nodule matrix. Commonly, sphalerite and chalcopyrite occur as coarser grained interstitial phases in the core of the pyrite nodules (Fig. 4C). Chalcopyrite also forms rims around idioblastic linnaeite and linnaeite is partly enclosed by pyrite (with or without a chalcopyrite rim) and by the host rock matrix. Chalcopyrite rims have been identified along the edges where linnaeite is in direct contact to the host rock matrix. The pyritic nodule matrix contains the aforementioned Co-S inclusions.

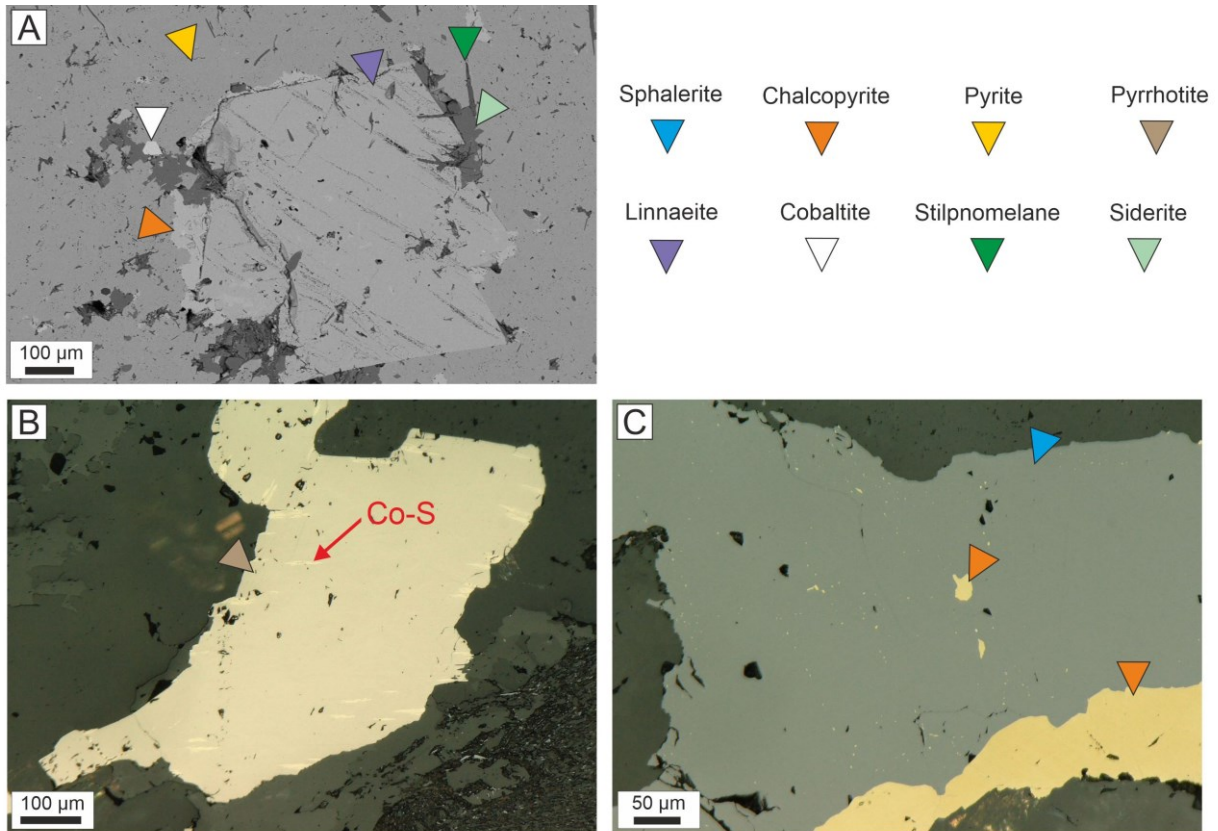


Fig. 5. A) SEM-BSE micrograph showing an idioblastic linnaeite crystal with a rim of chalcopyrite hosted in pyrite of cluster style mineralization. Stilpnomelane and siderite are also found within this cluster. B) Reflected light micrograph showing pyrrhotite with flame-like Co-S phase. C) Reflected light micrograph of coexisting chalcopyrite and sphalerite, the latter with minute chalcopyrite inclusions (“chalcopyrite disease”).

4.1.4 Pressure shadow

The pressure shadow mineralization style is characterized, and separated texturally from the nodule style, by the presence of distinct tails developed as pressure shadows around iron-sulfide aggregates (Fig. 4D). Pyrite is the dominant sulfide in this type. The central clast itself is composed entirely of pyrite, whilst sphalerite and chalcopyrite are situated within the pressure shadow tails. The whole pressure shadow clast is surrounded by a halo containing disseminated pyrite. The grain size of the disseminated pyrite and mineralization intensity in these halos decrease away from the pressure shadow clast. The ellipsoidal pyrite clast is rotated (sub)perpendicular to the host rock laminations or foliation. Accessory sphalerite and chalcopyrite can be found enclosed within the central pyrite clast. The pressure shadow central clast contain abundant dolomite inclusions. What looks to be relict framboidal textures can also be seen in the pyrite core. The pressure shadow tail comprises sphalerite and chalcopyrite along with gangue minerals, principally quartz with subordinate Fe-dolomite and accessory K-feldspar. The interstitial sphalerite and chalcopyrite are intergrown and sphalerite displays minute chalcopyrite inclusions (“chalcopyrite disease”; Fig. 5C).

4.1.5 Veins

Veins and veinlets occur throughout the stratigraphy and can be either sulfide-bearing or quartz-dominated, with varying amounts of hydrothermal Fe-dolomite and K-feldspar (Fig. 4E). Occasionally, albite occurs in the veins. The thickness of veinlets varies from some millimeters to several centimeters; locally even decimeters thick veins are observed. There are certainly several generations of veins as some veins are sub- to parallel to the host rock laminations or foliation whilst other veins crosscut any host rock layering at high angle. Folded veins also occur in the stratigraphy adding to the structural complexity. Accessory galena has been identified to occur interstitially between the gangue minerals in some veins. Sphalerite and chalcopyrite occur together in the veins and the sphalerite commonly contains chalcopyrite inclusions. Pyrite is euhedral to subhedral and may contain enclosed sphalerite and chalcopyrite, or it is present within the vein gangue minerals. Sphalerite and chalcopyrite are anhedral and interstitial between the gangue minerals. Interesting to note is that no cobalt phase has yet been identified within any of the veins. However, the occurrence of accessory pentlandite has been confirmed, containing between 1 and 2 wt% Co.

4.1.6 DOF Event

The so-called “event” mineralization style comprises enigmatic structures within the DOF stratigraphy. They display both ductile and brittle features that are mineralized and non-mineralized. The DOF events resemble both soft-sediment deformational structures, such as slumps, but also crack-seal veins with incorporated host rock. The dominant sulfide of the event style mineralization varies from pyrite and pyrrhotite-dominated to chalcopyrite-dominated. Pyrite and pyrrhotite have only been observed coexisting within the event mineralization style, where pyrrhotite is the dominant iron-sulfide (Fig. 4F). The amount of pyrite varies, but pyrrhotite is always the dominant iron sulfide. Pyrite often occurs enclosed in pyrrhotite. Sphalerite and chalcopyrite are commonly associated and are often intergrown. Sphalerite, chalcopyrite and pyrrhotite all show anhedral, interstitial growth textures, whilst pyrite tends to form more subhedral to euhedral crystals. Cobalt occurs as both idiomorphic linnaeite and as Co-sulfide inclusions within the iron-sulfides. Accessory galena has been identified in the event-style mineralization too.

All these different mineralization styles are dominantly hosted in calcareous siltstones. Mineralization of the main DOF horizon is hosted in siltstones dominated by stilpnomelane and subordinate Fe-dolomite and quartz, which defines the main DOF host rock. Carbonate rich lithologies more commonly host veins and event style mineralization rather than disseminations, clusters and nodules; although veins also occur in the clastic rocks. The host rock matrix is moderately mineralized containing framboidal pyrite along with minor disseminated, anhedral sphalerite and chalcopyrite, except the main DOF horizon where framboidal pyrite is absent. This suggests that the mineralizing fluids migrated through a large portion of the hosting sedimentary succession, but were focused in what is referred to as the main DOF horizon.

4.2 Base metal geochemistry

Element compositions of the analyzed sulfide phases (sphalerite, chalcopyrite, pyrite and pyrrhotite) within one sample are relatively homogeneous. Sample-internal variations occur mostly for elements where inclusions are common. These inclusions are in most cases either gangue minerals or other sulfide-phases (such as chalcopyrite in sphalerite or Co-S flames in iron-sulfides). Sphalerite-chalcopyrite intergrowths are evident from samples of every mineralization style. As mentioned previously, the LA-ICP-MS data has been scrutinized to remove obvious inclusions of phases. Aspects such as multiple generations, zonations and other internal heterogeneities makes the data evaluation process delicate and complicated. For example, V, Cr and Mn are commonly enriched in the LA-ICP-MS data; this is predominantly due to, suggestively, host rock inclusions. Laser ablation-ICP-MS analyses of other sediment-hosted sulfides, carried out by the lead author, show that host rock gangue minerals commonly occur intergrown in the sulfides in this type of deposits. Due to this, much of the spot analyses had to be neglected when calculating averages. Other elements that share similar problematics of occurring as inclusions are Cu, Zn, and Pb.

4.2.1 Sphalerite geochemistry

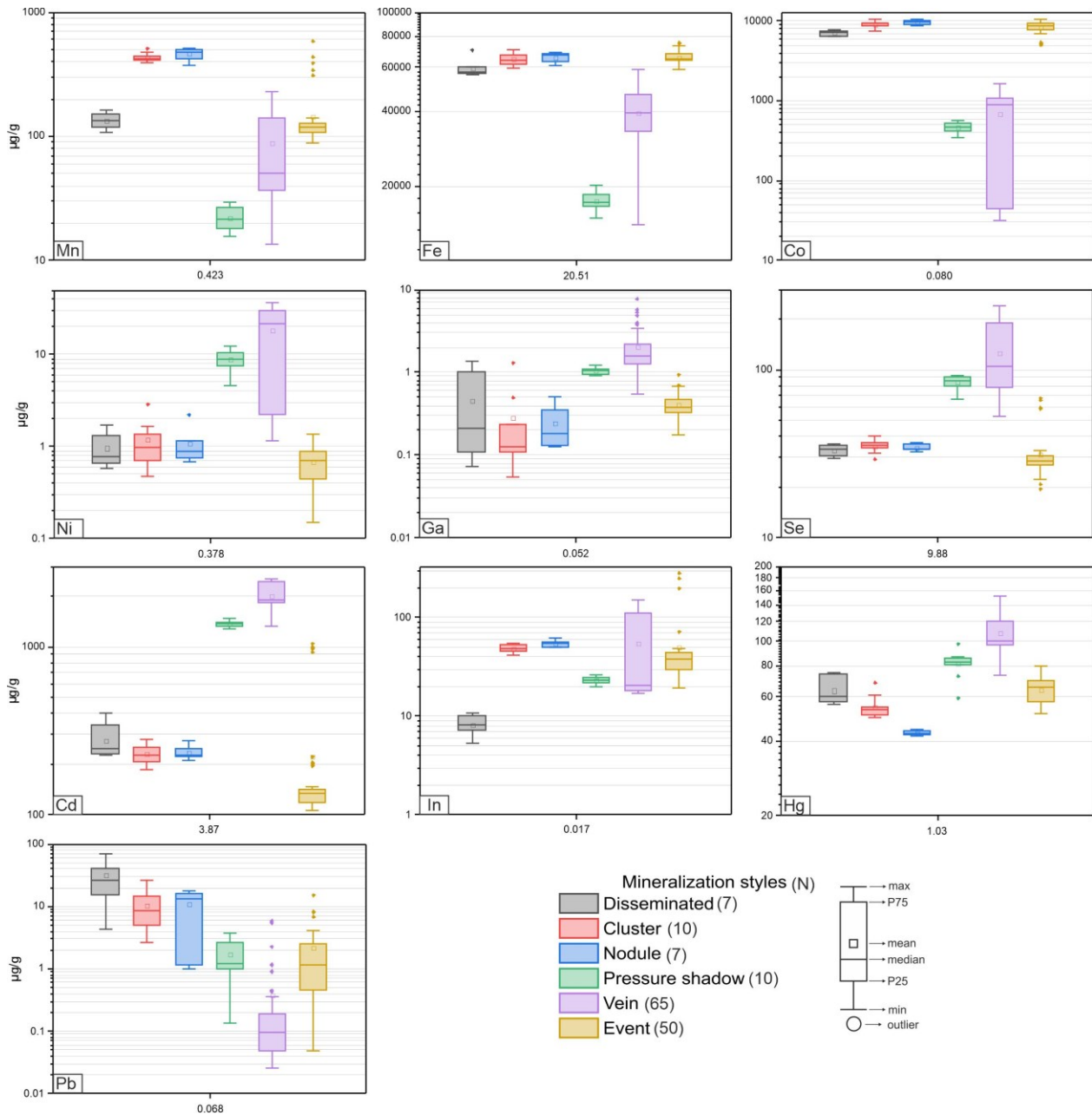


Fig. 6. Box and whisker plots of LA-ICP-MS trace element results for sphalerite from the different mineralization styles. Average detection limit (in $\mu\text{g/g}$) for each element is shown below appropriate plot.

Sphalerite in the DOF carries significant contents of minor and trace elements, especially of Fe, Mn, Co, Ni, Se, and occasionally of In and Cd. It also exhibits low contents of Ga, Ge, As, Ag, Sn, Sb (Table 1). Similar concentration ranges were observed between (1) the disseminated, cluster, nodule and event; and (2) the pressure shadow and vein mineralization styles, for most of the elements that show significant variation; i.e. Mn, Fe, Co, Ni, Ga, Ge, Se, Cd and Hg concentrations (Fig. 6). We will henceforth refer to these two groupings as sphalerite-chalcopyrite groups 1 and 2 (SC1 & SC2). The vein style concentrations often show a larger range that could be due to the

simplistic categorization of the veins. Sphalerite group 1 shows elevated concentrations of Mn, Fe, Co and Pb, whilst being depleted in Ni, Ga, Se, Cd and Hg, compared to sphalerite group 2. Uniform higher Fe concentrations are seen in disseminated, cluster, nodule and event (SC1) style sphalerite (median 5.6 to 6.7 wt%). The pressure shadow style has significantly lower Fe concentrations of median 1.7 wt%. Vein style sphalerite shows intermediate Fe concentrations with median 3.9 wt%.

Two populations of Co in sphalerite concentration ranges were identified in the mineralization styles: higher median values of 7290 to 9829 $\mu\text{g/g}$ Co were detected in disseminated, cluster, nodule and event (SC1) sphalerite and lower median values of 465 to 890 $\mu\text{g/g}$ Co in vein and pressure shadow sphalerite. Disseminated sphalerite has a median Co concentration of 7290 $\mu\text{g/g}$; cluster sphalerite has a median Co concentration of 9263 $\mu\text{g/g}$; nodule sphalerite has a median Co concentration of 9829 $\mu\text{g/g}$; pressure shadow sphalerite has a median Co concentration of 465 $\mu\text{g/g}$; vein sphalerite has a median Co concentration of 890 $\mu\text{g/g}$; and event sphalerite has a median Co concentration of 8630 $\mu\text{g/g}$. Sphalerite from both groups show Co to be incorporated in solid solution or as nano-inclusions, based off the smooth time-resolved LA-ICP-MS count signals (Fig. 7). Nickel concentrations in sphalerite are inverted to Co. Low Ni-sphalerite is seen in the disseminated, cluster, nodule and event styles (median 0.79 to 0.97 $\mu\text{g/g}$), all values being just above the average detection limit of 0.38 $\mu\text{g/g}$. In contrast, pressure shadow and vein sphalerite show higher Ni concentrations. Pressure shadow style sphalerite contains a median 8.8 $\mu\text{g/g}$ of Ni. Vein style sphalerite shows a range of concentrations, P5 1.5 $\mu\text{g/g}$ and P95 35 $\mu\text{g/g}$ Ni, with a median of 22 $\mu\text{g/g}$.

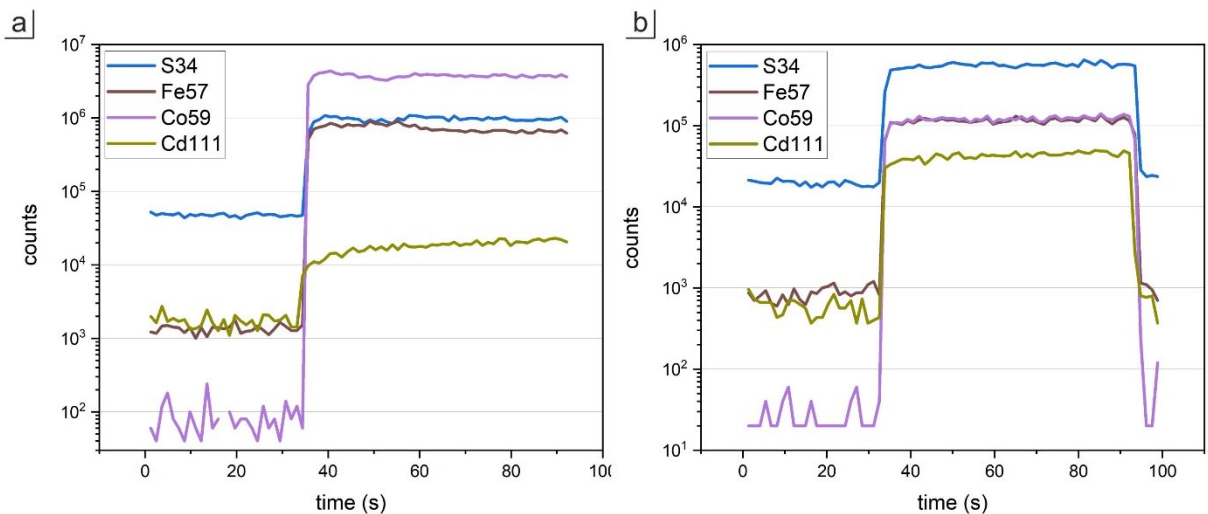


Fig. 7. Time-resolved LA-ICP-MS count signals of selected masses for: a) Co-rich, cluster sphalerite. b) Co-poor, vein sphalerite; note different scale on y-axes.

All DOF sphalerite are affected by “chalcopyrite disease”, evident from ore microscopy and the time-resolved count signals from the LA-ICP-MS analyses (Fig. 8), resulting in more erratic Cu signals during the analysis. The most obvious chalcopyrite inclusions have been removed from the data set. Due to this, Cu concentrations vary greatly and can range from tens to thousands of $\mu\text{g/g}$ within one mineralization style.

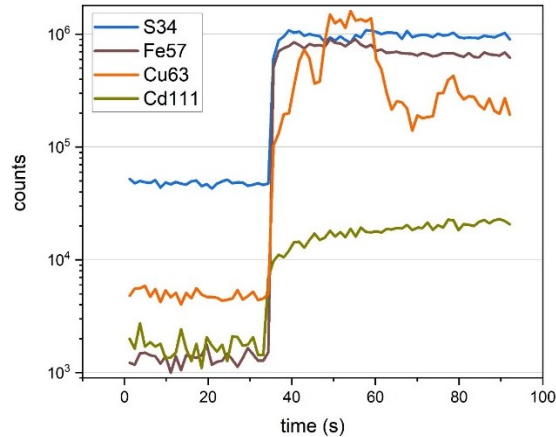


Fig. 8. Time-resolved LA-ICP-MS count signals of selected masses showing copper (Cu^{63}) inclusions in sphalerite, associated with chalcopyrite inclusions.

Both Ga and Ge concentrations are low in sphalerite from all mineralization styles, with the highest Ga concentrations being just above $1 \mu\text{g/g}$ in pressure shadow and vein sphalerite and Ge being below $1 \mu\text{g/g}$ in all styles. Cadmium concentrations show two distinct populations. The low Cd sphalerite population comprises dissemination (median $249 \mu\text{g/g}$), cluster, nodule and event (sphalerite group 1), with median Cd of $134 - 226 \mu\text{g/g}$. The pressure shadow and vein style (sphalerite group 2) makes up the high-end Cd concentration population with median 1369 and $1883 \mu\text{g/g}$ respectively. Indium shows a different trend than the aforementioned elements, where the disseminated sphalerite is decoupled from the In range of the cluster, nodule and event mineralization styles. Sphalerite from the disseminated style contains the lowest In concentrations of all styles, whilst cluster and nodule sphalerite contain the highest median In concentrations. Several elements were measured below detection limit (or just above it) of the ICP-MS in sphalerite from each of the mineralization styles: V, Cr, As, Mo, Sb, Te, Tl, and Au (Table 1).

Table 1. Statistical summary of LA-ICP-MS analyses of sphalerite from the different mineralization styles.

	Disseminated						Cluster					
	Median	P5	P95	N	n	DL	Median	P5	P95	N	n	DL
V	<0.70	<0.70	0.11	3	2	0.070	0.075	<0.050	0.12	6	1	0.050
Cr	<0.38	<0.38	<0.38	4	4	0.38	<0.37	<0.37	<0.37	6	6	0.37
Mn	133	109	159	5	0	0.32	423	399	496	9	0	0.41
Fe	5.8*	5.6*	6.7*	7	0	17	6.4*	6.1*	6.9*	10	0	16
Co	7290	6485	7768	7	0	0.10	9263	7944	10568	10	0	0.076
Ni	0.79	0.61	1.6	7	0	0.33	0.97	0.57	2.3	10	0	0.28
Cu	893	863	1550	3	0	2.1	519	353	631	5	0	1.8
Ga	0.21	0.085	1.3	7	0	0.059	0.13	0.066	0.94	10	0	0.046
Ge	<0.14	<0.14	0.76	7	0	0.15	<0.15	<0.15	0.44	10	6	0.15
As	<0.64	<0.64	<0.64	6	6	0.64	0.71	<0.61	1.0	10	2	0.61
Se	33	30	36	7	0	7.1	35	30	39	10	0	5.8
Mo	<0.073	<0.073	<0.073	7	7	0.073	<0.0053	<0.0053	<0.0053	9	9	0.053
Ag	0.87	0.43	1.6	7	0	0.020	0.63	0.32	0.94	10	0	0.020
Cd	249	229	382	7	0	3.9	226	193	275	10	0	3.7
In	8.1	5.9	11	7	0	0.018	48	42	55	10	0	0.020
Sn	<0.46	<0.46	1.0	7	4	0.46	0.73	<0.42	1.6	10	2	0.42
Sb	<0.12	<0.12	0.27	7	6	0.12	<0.10	<0.10	<0.10	10	10	0.10
Te	<0.22	<0.22	0.37	7	5	0.22	<0.20	<0.20	0.21	10	8	0.20
Au	na			na	na		na			na	na	
Hg	60	57	75	7	0	0.90	53	50	65	10	0	0.99
Tl	0.033	<0.023	0.24	7	3	0.023	<0.022	<0.022	0.062	10	5	0.022
Pb	26	6.4	64	5	0	0.22	8.7	3.6	21	10	0	0.24
Bi	2.1	0.37	4.9	7	0	0.019	0.78	0.37	2.1	10	0	0.017

	Nodule						Pressure shadow					
	Median	P5	P95	N	n	DL	Median	P5	P95	N	n	DL
V	<0.080	<0.080	<0.080	2	2	0.080	<0.064	<0.064	<0.064	10	10	0.064
Cr	<0.41	<0.41	<0.41	5	5	0.41	<0.65	<0.65	<0.65	10	10	0.65
Mn	476	385	506	6	0	0.41	21	16	29	10	0	0.61
Fe	6.7*	6.2*	6.9*	7	0	18	1.7*	1.5*	2.0*	9	0	20
Co	9829	8791	10539	7	0	0.12	465	375	559	10	0	0.08
Ni	0.89	0.71	1.9	7	0	0.39	8.8	5.3	12	9	0	0.48
Cu	524	146	2349	5	0	1.8	408	127	973	10	0	2.2
Ga	0.18	0.13	0.47	6	0	0.044	1.1	0.92	1.2	10	0	0.060
Ge	<0.20	<0.20	0.49	7	4	0.20	0.39	<0.26	0.50	10	0	0.26
As	<0.66	<0.66	1.1	7	4	0.66	<0.83	<0.83	<0.83	9	9	0.83
Se	34	33	37	7	0	6.8	87	71	92	10	0	11.2
Mo	<0.061	<0.061	<0.061	7	7	0.061	<0.092	<0.092	<0.092	10	10	0.092
Ag	0.49	0.14	0.91	7	0	0.034	0.30	0.11	0.59	10	0	0.031
Cd	226	216	267	7	0	4.1	1369	1294	1446	10	0	5.0
In	55	49	60	7	0	0.023	23	21	26	10	0	0.012
Sn	0.79	<0.45	3.2	7	1	0.45	<0.31	<0.31	<0.31	9	9	0.31
Sb	<0.12	<0.12	<0.12	7	7	0.12	<0.11	<0.11	<0.11	9	9	0.11
Te	<0.25	<0.25	<0.25	7	7	0.25	<0.33	<0.33	<0.33	10	10	0.33
Au	na			na	na		<0.026	<0.026	<0.026	10	10	0.026
Hg	43	42	44	7	0	0.90	83	65	93	10	0	0.80

Tl	<0.022	<0.022	0.063	7	4	0.022	<0.023	<0.023	<0.023	9	9	0.023
Pb	13	1.1	17	7	0	0.21	1.2	0.29	3.5	9	0	0.066
Bi	0.77	0.062	1.9	7	0	0.015	<0.013	<0.013	<0.013	9	9	0.013

	Vein						Event					
	Median	P5	P95	N	n	DL	Median	P5	P95	N	n	DL
V	<0.07	<0.07	<0.07	65	65	0.07	<0.068	<0.068	<0.068	47	45	0.068
Cr	<0.62	<0.62	<0.62	65	65	0.62	<0.61	<0.61	<0.61	47	47	0.61
Mn	51	19	220	65	0	0.39	119	91	368	50	0	0.45
Fe	3.9*	1.5*	5.4*	65	0	21	6.2*	6.0*	7.3*	50	0	21
Co	890	38	1258	65	0	0.066	8630	5186	9947	50	0	0.089
Ni	22	1.5	35	65	0	0.39	0.71	<0.37	1.1	50	0	0.37
Cu	67	28	277	60	1	3.0	194	52	614	36	0	3.3
Ga	1.6	0.86	4.9	65	0	0.053	0.38	0.26	0.65	50	0	0.053
Ge	0.52	0.21	1.4	65	0	0.21	<0.25	<0.25	0.31	50	46	0.25
As	<0.72	<0.72	<0.72	65	65	0.72	<0.62	<0.62	0.93	50	26	0.62
Se	104	55	224	65	0	10	28	22	59	50	0	11
Mo	<0.066	<0.066	<0.066	65	65	0.066	<0.061	<0.061	<0.061	50	50	0.061
Ag	0.26	0.12	1.0	65	1	0.026	0.60	<0.028	3.1	50	3	0.028
Cd	1883	1370	2520	65	0	3.8	134	110	981	50	0	3.9
In	21	17	148	65	0	0.017	38	23	140	50	0	0.015
Sn	<0.46	<0.46	1.1	65	37	0.46	<0.40	<0.40	0.88	50	36	0.40
Sb	<0.11	<0.11	<0.11	65	65	0.11	<0.10	<0.10	<0.10	50	50	0.10
Te	<0.30	<0.30	<0.30	65	65	0.30	<0.30	<0.30	<0.30	50	49	0.30
Au	<0.020	<0.020	<0.020	65	65	0.020	<0.028	<0.028	<0.028	50	50	0.028
Hg	101	88	144	65	0	1.0	65	53	73	50	0	1.2
Tl	<0.022	<0.022	<0.022	65	65	0.022	<0.020	<0.020	<0.020	50	49	0.020
Pb	0.10	<0.063	1.2	64	19	0.063	1.2	<0.067	7.9	44	4	0.067
Bi	<0.014	<0.014	0.02	64	54	0.014	0.15	0.03	1.3	49	1	0.013

All concentrations are reported in $\mu\text{g/g}$, except * which are reported in wt%. The median values are all calculated with 1/2 of the measurement's detection limit when the measurement is below the detection limit. Reported detection limits (DL) are median values from all individual analysis detection limits of each mineral and mineralization style. Major elements are not reported as LA-ICP-MS set up is fine-tuned for trace elements. N: number of individual LA-ICP-MS analyses; n: number of analyses below detection limit (bdl); na: not analyzed.

4.2.2 Chalcopyrite geochemistry

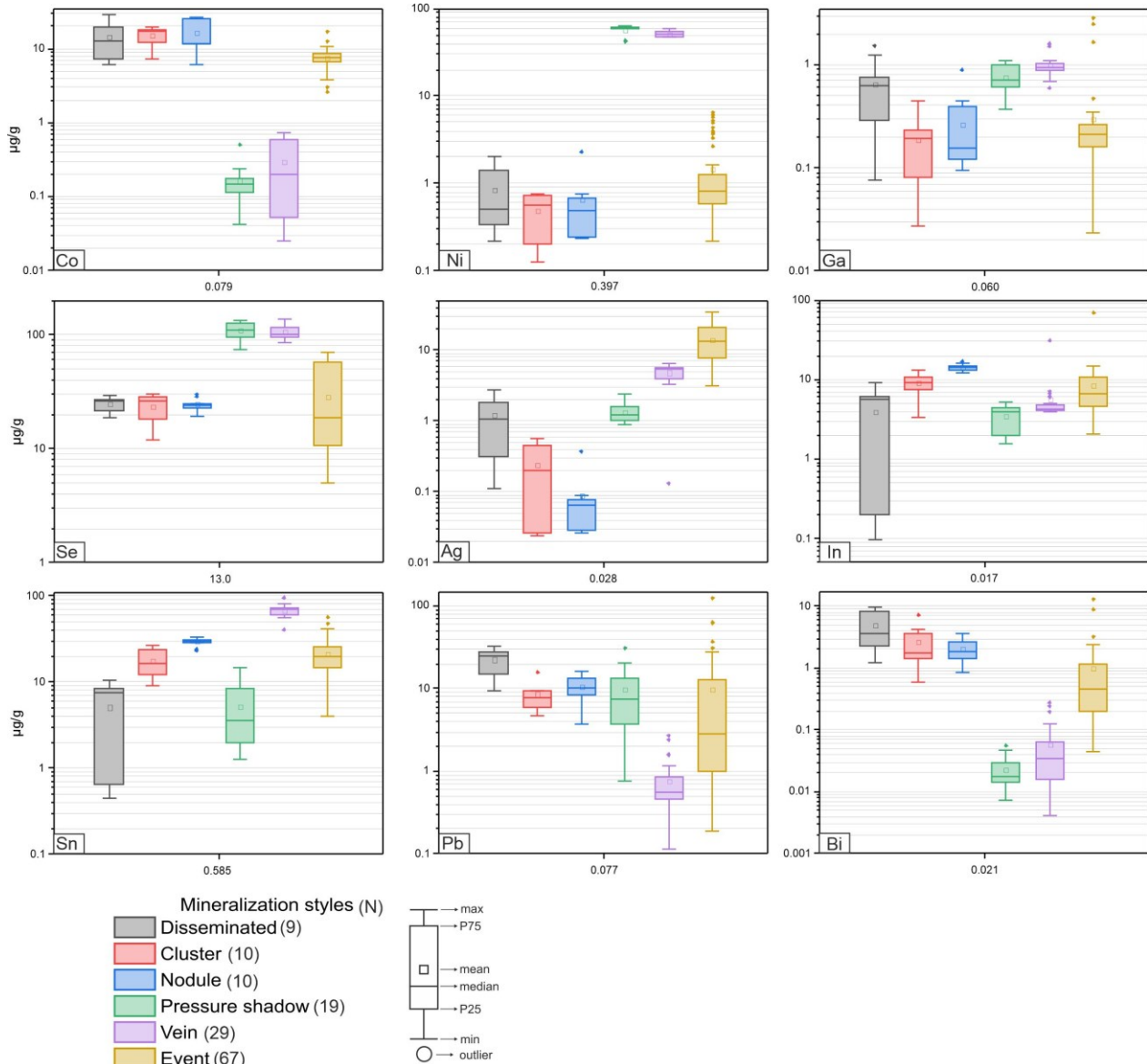


Fig. 9. Boxplots of LA-ICP-MS trace element results of chalcopyrite from the different mineralization styles. Average detection limit for the element is shown below appropriate plot.

Chalcopyrite in the DOF generally contains lower trace elements than sphalerite. The most abundant elements in chalcopyrite are Ni, Co, Zn, Se, In, Sn and Pb. A similar grouping to that of sphalerite mineralization styles (SC1 & SC2) can be seen in chalcopyrite (Fig. 9). Chalcopyrite from the disseminated, cluster and nodule styles, group together in a first group (SC1), whilst on the other hand chalcopyrite from pressure shadow and vein styles define a second group (SC2). There are exceptions to this grouping as well, e.g., Sn. Chalcopyrite from the events mineralization style is similar to group 1, but shows a greater spread in element concentrations. The disseminated chalcopyrite also shows a significant range in values for certain elements (e.g., Ag, In and Sn). This is due to the existence of two populations of chalcopyrite, based off the aforementioned trace element content, depending on the sample (see single spot concentration data in Supplementary

Materials 1). Cobalt and Bi are the only elements significantly enriched within the SC1 group (disseminated, cluster, nodule and often event), and the SC1 group chalcopyrite contain lower concentrations of Ni, Ga, Se and Ag compared to the second group (SC2). Several elements are below detection limits in chalcopyrite from all the mineralization styles, e.g. As, Mo, Cd and Au.

Table 2. Statistical summary of LA-ICP-MS analyses of chalcopyrite from the different mineralization styles.

	Disseminated						Cluster					
	Median	P5	P95	N	n	DL	Median	P5	P95	N	n	DL
V	0.46	<0.15	2.4	4	2	0.15	0.57	0.16	1.7	7	1	0.14
Cr	1.5	<0.74	6.8	9	3	0.74	<0.71	<0.71	6.7	9	6	0.71
Mn	3.0	3.0	3.0	1	0	0.57	7.1	4.3	9.1	4	0	0.48
Co	13	6.4	26	7	0	0.11	17	8.7	19	4	0	0.087
Ni	0.50	<0.45	2.0	8	3	0.45	0.57	<0.33	0.76	5	2	0.33
Zn	249	217	314	6	0	55	371	313	485	6	0	55
Ga	0.62	0.11	1.4	9	1	0.094	0.19	<0.079	0.37	8	2	0.079
Ge	0.70	<0.24	1.0	9	1	0.24	0.64	0.35	4.8	10	0	0.21
As	<0.64	<0.64	<0.64	8	8	0.64	<0.79	<0.79	<0.79	8	8	0.79
Se	26	20	29	9	0	11	26	14	30	10	0	9.2
Mo	<0.12	<0.12	<0.12	9	8	0.12	<0.088	<0.088	<0.088	8	8	0.088
Ag	1.1	0.17	2.7	9	0	0.040	0.20	<0.048	0.54	10	3	0.048
Cd	<6.0	<6.0	<6.0	9	9	6.0	<3.4	<3.4	<3.4	10	10	3.4
In	5.6	0.13	9.0	9	0	0.031	9.3	5.1	12	10	0	0.027
Sn	7.5	<1.1	9.8	9	4	1.1	17	10	26	10	0	0.89
Sb	<0.16	<0.16	0.41	9	8	0.16	<0.15	<0.15	<0.15	10	10	0.15
Te	0.56	<0.38	1.6	9	2	0.38	0.52	0.37	0.76	10	0	0.30
Au	<0.041	<0.041	0.12	9	7	0.041	<0.028	<0.028	0.039	10	8	0.028
Hg	<2.3	<2.3	7.0	9	6	2.3	5.0	2.8	8.2	9	0	1.6
Tl	0.29	<0.045	1.8	9	2	0.045	0.082	<0.043	0.38	8	3	0.043
Pb	25	11	31	6	0	0.12	7.9	4.9	14	6	0	0.14
Bi	3.7	1.5	9.6	8	0	0.054	1.8	0.95	5.9	10	0	0.029

	Nodule						Pressure shadow					
	Median	P5	P95	N	n	DL	Median	P5	P95	N	n	DL
V	<0.12	<0.12	0.14	6	4	0.12	<0.10	<0.10	<0.10	19	17	0.10
Cr	<0.89	<0.89	1.7	10	8	0.89	<0.80	<0.80	<0.80	19	19	0.80
Mn	6.6	3.9	18	7	0	0.63	4.4	3.9	4.9	19	0	0.62
Co	12	7.1	26	5	0	0.13	0.15	<0.091	0.27	19	3	0.091
Ni	<0.48	<0.48	1.7	9	5	0.48	60	43	62	19	0	0.42
Zn	417	312	608	8	0	48	91	45	126	19	0	37
Ga	0.16	0.099	0.69	10	0	0.074	0.70	0.45	1.1	19	0	0.068
Ge	0.51	0.35	1.3	10	0	0.29	0.79	0.63	1.1	19	0	0.23
As	<0.67	<0.67	<0.67	10	10	0.67	<1.2	<1.2	<1.2	18	18	1.2
Se	24	20	29	10	0	13	111	78	132	19	0	16
Mo	<0.15	<0.15	<0.15	10	10	0.15	0.11	0.11	0.11	19	19	0.11
Ag	0.065	<0.047	0.25	10	3	0.047	1.2	0.89	1.9	19	0	0.032
Cd	<6.9	<6.9	<6.9	10	0	6.9	<4.6	<4.6	v	19	19	4.6
In	14	12	16	10	0	0.033	3.9	1.6	5.1	19	0	0.012
Sn	30	23	32	10	0	1.0	3.6	1.4	13	19	0	0.37
Sb	<0.21	<0.21	<0.21	10	10	0.21	0.30	<0.11	1.3	19	2	0.11
Te	0.64	<0.37	1.0	10	3	0.37	<0.42	<0.42	<0.42	19	19	0.42

Au	<0.039	<0.039	<0.039	10	10	0.039	<0.037	<0.037	<0.037	19	19	0.037
Hg	2.4	<2.0	3.1	10	4	2.0	2.3	1.3	3.8	19	1	0.94
Tl	<0.046	<0.046	0.16	9	6	0.046	<0.035	<0.035	<0.035	19	19	0.035
Pb	10	4.4	16	10	0	0.14	7.5	1.2	22	18	0	0.081
Bi	1.9	0.99	3.2	10	0	0.036	0.018	<0.015	0.048	19	6	0.015

	Vein						Event					
	Median	P5	P95	N	n	DL	Median	P5	P95	N	n	DL
V	<0.090	<0.090	<0.090	29	29	0.090	<0.080	<0.080	<0.080	60	54	0.080
Cr	<0.74	<0.74	<0.74	29	29	0.74	<0.70	<0.70	<0.70	66	66	0.70
Mn	4.4	4.2	4.8	29	0	0.56	4.5	4.2	5.1	58	0	0.51
Co	0.20	<0.074	0.72	29	8	0.074	7.6	3.5	10	54	1	0.065
Ni	50	47	57	29	1	0.36	0.81	0.43	5.2	63	4	0.37
Zn	313	177	449	18	0	30	384	252	597	59	0	27
Ga	0.95	0.72	1.6	28	0	0.056	0.21	<0.052	0.34	67	8	0.052
Ge	0.84	0.70	1.5	29	0	0.26	0.22	<0.19	0.52	67	28	0.19
As	<0.83	<0.83	<0.83	29	29	0.83	<0.85	<0.85	<0.85	67	67	0.85
Se	101	87	132	29	0	13	19	<13	66	67	17	13
Mo	<0.088	<0.088	<0.088	29	29	0.088	<0.077	<0.077	<0.077	67	67	0.077
Ag	5.4	3.3	6.2	29	0	0.027	13	3.4	24	67	0	0.023
Cd	<5.7	<5.7	9.4	28	15	5.7	<4.5	<4.5	<4.5	66	66	4.5
In	4.3	4.0	7.0	29	0	0.017	6.7	3.8	12	67	0	0.015
Sn	69	56	89	29	0	0.60	19	9.0	40	66	0	0.53
Sb	<0.12	<0.12	<0.12	29	29	0.12	<0.11	<0.11	0.23	65	56	0.11
Te	<0.26	<0.26	0.58	29	26	0.26	0.30	<0.28	1.8	65	30	0.28
Au	<0.029	<0.029	<0.029	29	29	0.029	<0.033	<0.033	<0.033	67	67	0.033
Hg	3.7	2.3	9.0	29	0	1.2	3.8	<1.1	9.2	67	3	1.1
Tl	<0.025	<0.025	<0.025	29	29	0.025	<0.023	<0.023	0.10	67	54	0.023
Pb	0.55	0.25	2.1	29	0	0.054	2.8	0.28	31	63	0	0.071
Bi	0.034	<0.021	0.22	29	10	0.021	0.45	0.086	2.4	63	0	0.016

The median values are all calculated with 1/2 of the measurement's detection limit when the measurement is below the detection limit. Reported detection limits (DL) are median values from all individual analyses detection limits of each mineral and mineralization style. Major elements are not reported as LA-ICP-MS set up is fine-tuned for trace elements. N: number of individual LA-ICP-MS analyses; n: number of analyses below detection limit (bdl); na: not analyzed.

4.2.3 Pyrite geochemistry

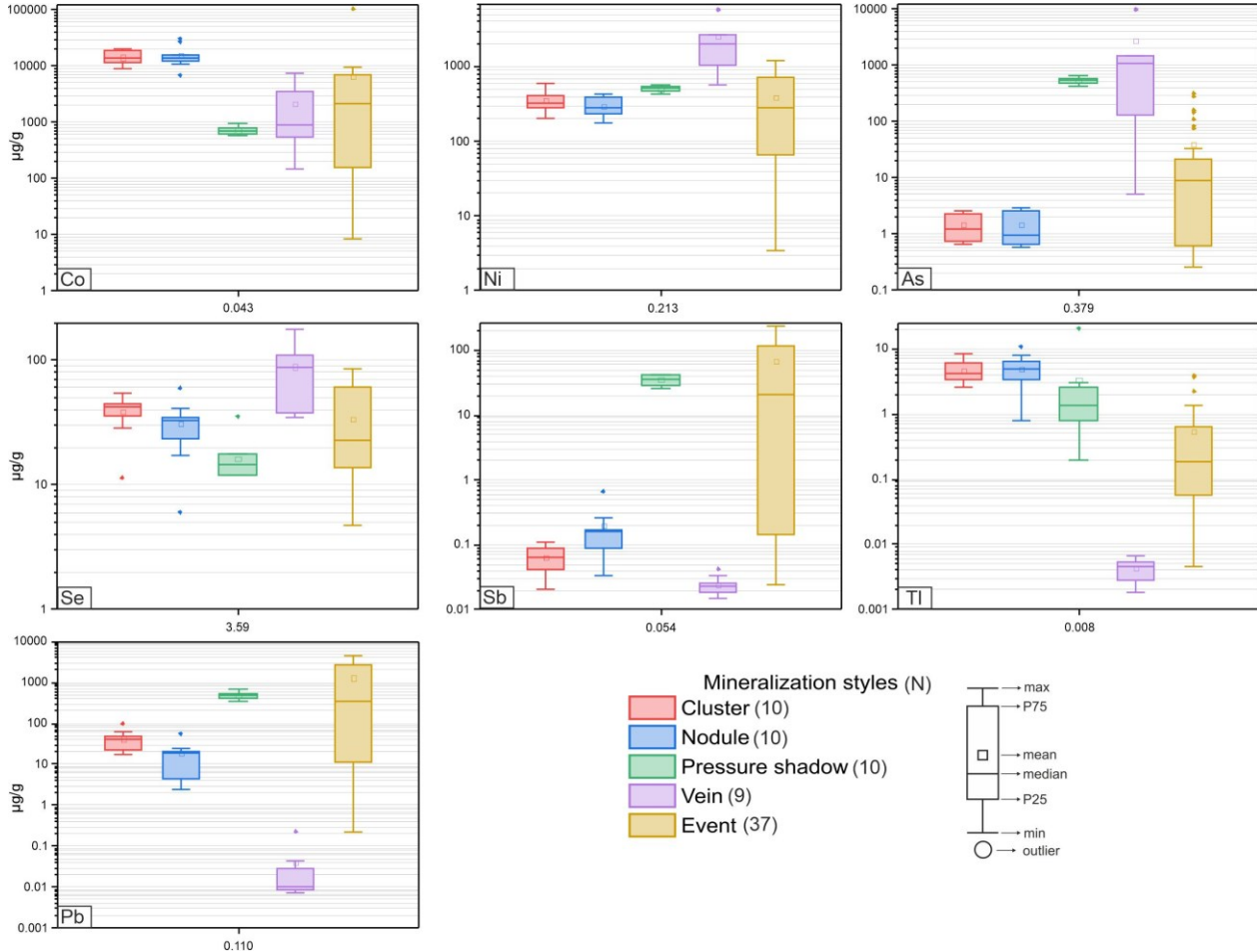


Fig. 10. Boxplots of LA-ICP-MS trace element results of pyrite from the different mineralization styles. Average detection limit for the element is shown below appropriate plot.

Pyrite in the DOF is highly enriched in Co over Ni and carries variable As, Se, Sb and Pb contents. Only cluster and nodule pyrite could clearly be grouped together as most element concentrations vary significantly between mineralization styles. Mineralization styles that grouped together in sphalerite and chalcopyrite, such as pressure shadow and vein styles, are distinctly decoupled in the pyrite analyses (e.g. Sb, Tl and Pb). It appears that (1) cluster and nodule pyrite data group together; (2) the pressure shadow and vein pyrites are noticeably decoupled in most cases; (3) event pyrites show a wide range in element concentrations, usually resulting in a median value intermediate to the two other pyrite groupings.

The previously mentioned Co-sulfide inclusions, a distinctive characteristic of the iron-sulfides in all mineralization styles (besides pressure shadow and veins), result in obvious problems when conducting LA-ICP-MS analyses. Time-resolved count signals clearly demonstrate the presence of Co-phase inclusions in the hosting iron-sulfide. Comparing high and low Co signals it is evident that there are at least iron-sulfides which are Co-poor. It is extremely difficult to determine if all high Co values are due to inclusions of Co-phases or if there is some zoning within the iron-sulfides. Pyrites from the cluster, nodule, pressure shadow and vein mineralization styles all show

lower, relatively similar median Ni concentrations (between 288 and 508 $\mu\text{g/g}$), whilst vein pyrites are strongly enriched in Ni with median 2056 $\mu\text{g/g}$. Just as with Co in pyrite, Ni shows a large range in values in both the vein and event styles, the event pyrites showing the greatest variation in Ni concentrations. The inverted Co-Ni trend seen in both sphalerite and chalcopyrite, where high Co correlates with low Ni and reverse, can also be seen in pyrites, although not as prominent. Just like Co in pyrite, Ni seems to be associated with the Co-phase inclusions, and thus skew the data to some degree.

Arsenic is the only element to clearly show the typical sphalerite-chalcopyrite grouping of the styles. Cluster and nodule pyrite contain the lowest As contents with median 1.2 and 0.97 $\mu\text{g/g}$ respectively. Event pyrites have higher As contents of median 9.0 $\mu\text{g/g}$, but with a large range between P5 <0.39 and P95 194 $\mu\text{g/g}$. Pressure shadow and vein pyrites contain the highest As concentrations with median 556 and 1045 $\mu\text{g/g}$ respectively. Selenium concentrations show a scattered range between the mineralization styles with no distinct grouping. The pressure shadow and vein styles show decoupled median values. Both the vein and event style pyrites have a relatively large range of concentrations, compared to the other styles, and show overlapping (Fig. 10).

Antimony concentrations show the most drastic variations between the different mineralization styles (Fig. 10). Cluster, nodule and vein pyrites show Sb contents just around (and below) the detection limits. Pressure shadow pyrites show significantly higher Sb concentrations, with the highest median value of 36 $\mu\text{g/g}$ and thus showing a decoupling between pressure shadow and vein concentrations. One population of event pyrite has Sb contents below the detection limit (<0.055 $\mu\text{g/g}$) and up to maximum 0.46 $\mu\text{g/g}$, whilst another event pyrite population has Sb contents ranging between 4.9 and 196 $\mu\text{g/g}$. Cadmium is the only element that is below detection limits in pyrites from each mineralization style. The vein style pyrites are exceptionally trace element-poor; V, Cr, Mo, Ag, Cd, In, Au, Hg and Tl all show below detection limit measurements, along with In, Sn and Sb yielding only one value each, the rest being below the limits of detection. A general depletion in redox sensitive elements such as V, Cr, Mo and Sb is observed in some of the mineralization styles.

Table 3. Statistical summary of LA-ICP-MS analyses of pyrite from the different mineralization styles.

	Cluster					
	Median	P5	P95	N	n	DL
V	0.29	0.10	0.43	4	0	0.031
Cr	0.25	<0.17	0.39	4	1	0.17
Mn	33	11	48	7	0	0.18
Co	13831	9759	19394	10	0	0.056
Ni	321	217	537	9	0	0.21
Cu	5.7	<01.2	69	7	3	1.2
Zn	na			na	na	
Ga	0.14	0.074	0.64	10	0	0.025
Ge	0.56	0.30	1.3	10	0	0.077
As	1.2	0.67	2.5	8	0	0.23
Se	42	19	54	10	0	3.0
Mo	<0.043	<0.043	0.069	8	7	0.043
Ag	0.54	0.41	1.5	9	0	0.0094

Cd	<1.7	<1.7	<1.7	10	10	1.7
In	<0.021	<0.021	0.030	10	5	0.021
Sn	0.69	0.40	1.4	10	0	0.19
Sb	0.066	<0.055	0.11	9	4	0.055
Te	0.32	0.14	0.68	10	0	0.11
Au	na			na	na	
Hg	<0.36	<0.36	1.1	10	8	0.36
Tl	4.2	2.8	7.6	10	0	0.0080
Pb	42	18	85	9	0	0.066
Bi	1.7	0.68	2.7	10	0	0.0081

Pressure shadow

	Median	P5	P95	N	n	DL
V	2.6	0.86	4.5	10	0	0.035
Cr	4.5	2.1	6.8	10	0	0.28
Mn	110	86	274	10	0	0.29
Co	698	594	908	10	0	0.040
Ni	508	439	570	10	0	0.24
Cu	317	159	489	10	0	2.0
Zn	119	27	1125	10	0	5.0
Ga	0.43	0.18	1.2	10	0	0.031
Ge	0.20	<0.12	0.54	10	0	0.12
As	556	418	633	10	0	0.42
Se	15	12	28	10	0	4.3
Mo	5.8	0.22	10	10	0	0.044
Ag	2.4	1.7	3.4	10	0	0.016
Cd	<2.2	<2.2	<2.2	10	10	2.2
In	0.011	<0.0073	0.093	10	3	0.0073
Sn	0.25	<0.15	0.48	10	2	0.15
Sb	36	27	43	10	0	0.057
Te	1.7	0.98	2.0	10	0	0.18
Au	0.046	<0.017	0.064	10	1	0.017
Hg	0.88	0.46	1.7	10	0	0.33
Tl	1.3	0.25	13	10	0	0.012
Pb	490	367	624	10	0	0.086
Bi	6.7	4.9	7.8	10	0	0.0059

Event

	Median	P5	P95	N	n	DL
V	0.058	<0.022	0.21	24	3	0.022
Cr	<0.27	<0.27	0.83	29	20	0.27
Mn	11	9.4	16	17	0	0.18
Co	1694	33	8844	30	0	0.033
Ni	297	6.4	970	29	0	0.22
Cu	48	<0.96	163	32	9	0.96
Zn	<4.8	<4.8	6.9	29	26	4.8
Ga	0.052	0.027	0.61	36	0	0.019
Ge	0.34	<0.095	0.63	36	3	0.095
As	9.0	<0.39	194	36	3	0.39

Se	23	6.4	73	37	0	3.7
Mo	0.29	<0.025	1.4	34	10	0.025
Ag	0.61	0.15	2.1	37	3	0.010
Cd	<1.5	<1.5	<1.5	35	35	1.5
In	0.0087	<0.0065	0.14	35	14	0.0065
Sn	<0.21	<0.21	1.0	37	18	0.21
Sb	20	<0.055	196	37	6	0.055
Te	0.32	<0.11	1.4	37	12	0.11
Au	<0.011	<0.011	0.067	37	19	0.011
Hg	0.71	<0.52	1.3	36	13	0.52
Tl	0.18	0.017	2.5	37	1	0.0071
Pb	353	0.56	3707	36	0	0.23
Bi	0.71	0.034	9.6	36	0	0.0099

The median values are all calculated with 1/2 of the measurement's detection limit when the measurement is below the detection limit. Reported detection limits (DL) are median values from all individual analyses detection limits of each mineral and mineralization style. Major elements are not reported as LA-ICP-MS set up is fine-tuned for trace elements. N: number of individual LA-ICP-MS analyses; n: number of analyses below detection limit (bdl); na: not analyzed.

4.2.4 Pyrrhotite geochemistry

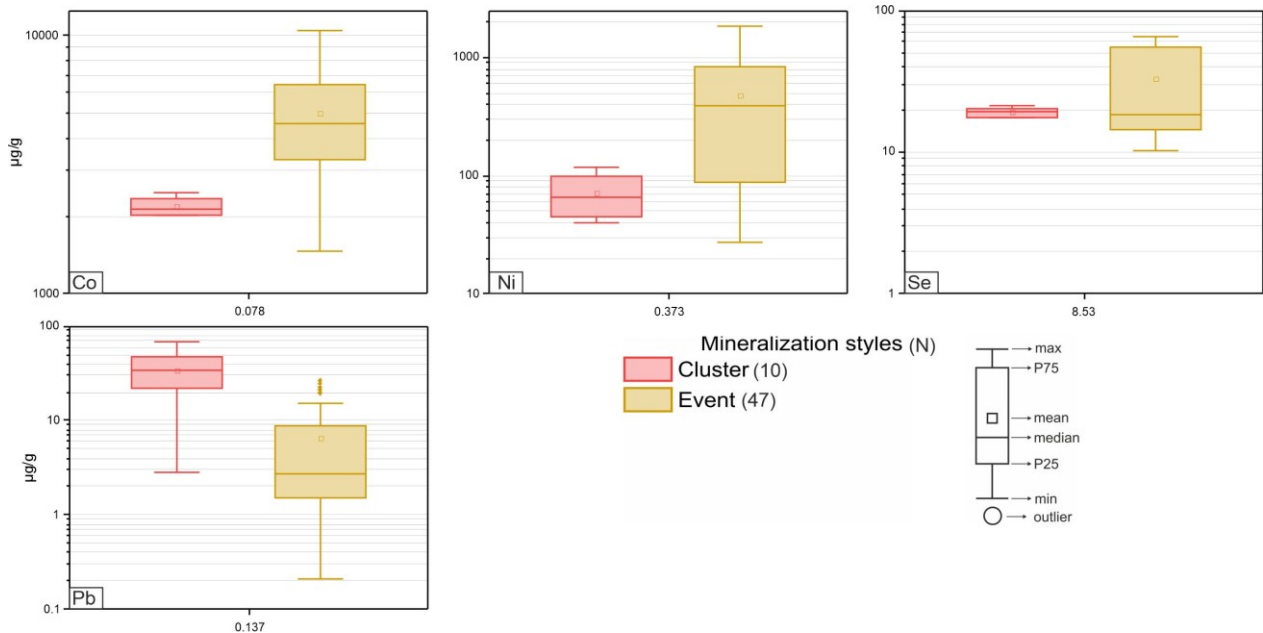


Fig. 11. Boxplots of LA-ICP-MS trace element results of pyrrhotite from the different mineralization styles. Average detection limit for the element is shown below appropriate plot.

Pyrrhotite was only recognized in the disseminated, cluster and event mineralization styles; the disseminated pyrrhotite was too fine-grained to analyze by LA-ICP-MS and could thus not be included in this study. DOF pyrrhotites are relatively poor in trace elements, with only Mn, Co, Ni, Zn, Se, Hg (in event pyrrhotite), Pb and Bi showing concentrations above 1 µg/g. Trace element concentrations show greater ranges in event pyrrhotite than in cluster pyrrhotites (Fig. 11). Cobalt in cluster pyrrhotites is lower than in event pyrrhotite, a reversed relationship to cluster and event

pyrites, where Co is enriched in the cluster pyrite compared to event pyrite. Arsenic, In, Sn, Sb, Te, Hg and Tl are either below detection limits or just above, meaning that their analyses should be considered with caution.

Table 4. Statistical summary of LA-ICP-MS analyses of pyrrhotite from the different mineralization styles.

	Cluster						Event					
	Median	P5	P95	N	n	DL	Median	P5	P95	N	n	DL
V	0.15	<0.060	0.67	10	2	0.060	<0.056	<0.056	0.15	46	35	0.056
Cr	<0.33	<0.33	0.64	10	6	0.33	<0.54	<0.54	0.67	46	42	0.54
Mn	12	7.9	31	7	0	0.32	10	5.8	15	44	0	0.40
Co	2.1*	2.0*	2.4*	4	0	0.13	4.5*	1.7*	9.0*	46	0	0.073
Ni	66	42	111	4	0	0.29	389	46	1142	46	0	0.40
Cu	<2.2	<2.2	73	5	3	2.2	<2.4	<2.4	<2.4	38	32	2.4
Zn	na			na	na		<8.3	<8.3	<8.3	40	39	8.3
Ga	0.10	0.066	0.21	9	1	0.045	<0.040	<0.040	0.088	46	25	0.040
Ge	0.20	0.15	0.29	10	0	0.14	<0.19	<0.19	0.50	47	18	0.19
As	<0.53	<0.53	1.0	10	6	0.53	<0.64	<0.64	0.79	47	42	0.64
Se	19	17	21	10	0	5.4	18	12	58	46	0	8.9
Mo	<0.055	<0.055	<0.055	10	10	0.055	<0.052	<0.052	<0.052	47	47	0.052
Ag	0.46	0.063	1.0	10	0	0.020	0.91	0.16	3.2	47	2	0.022
Cd	<3.1	<3.1	<3.1	10	10	3.1	<3.2	<3.2	<3.2	46	46	3.2
In	0.036	<0.033	0.15	10	5	0.033	<0.017	<0.017	<0.017	45	39	0.017
Sn	<0.35	<0.35	<0.35	10	9	0.35	<0.38	<0.38	<0.38	47	47	0.38
Sb	<0.089	<0.089	<0.089	10	9	0.089	<0.093	<0.093	<0.093	47	47	0.093
Te	0.33	<0.21	0.61	10	1	0.21	<0.24	<0.24	0.57	47	35	0.24
Au	na			na	na		<0.024	<0.024	<0.024	47	47	0.024
Hg	<0.63	<0.63	<0.63	10	10	0.63	0.50	<0.92	1.0	46	41	0.92
Tl	<0.016	<0.016	0.058	10	5	0.016	<0.021	<0.021	0.065	46	45	0.021
Pb	34	3.2	61	10	0	0.15	2.7	0.56	23	42	2	0.11
Bi	3.6	0.24	5.5	10	0	0.016	0.41	0.029	1.9	44	1	0.016

The median values are all calculated with 1/2 of the measurement's detection limit when the measurement is below the detection limit. Reported detection limits (DL) are median values from all individual analyses detection limits of each mineral and mineralization style. Major elements are not reported as LA-ICP-MS set up is fine-tuned for trace elements. N: number of individual LA-ICP-MS analyses; n: number of analyses below detection limit (bd); na: not analyzed.

5. Discussion

5.1 Base metal sulfide trace elements compositions

Sphalerite from the disseminated, cluster, nodule and event types contains exceptional trace element concentrations. Cobalt concentrations between 7290 – 9829 µg/g (disseminated, cluster, nodule and event styles) are extreme for sphalerite and are among the highest values reported so far (Frenzel et al. 2016; Cook et al. 2009). In contrast, cadmium concentrations in sphalerite from the same mineralization styles show unusually low concentrations, 134 – 249 µg/g, whilst the pressure shadow and vein sphalerite show more typical, although still relatively low, Cd concentrations (1369 and 1883 µg/g respectively). Both Co and Cd may occur in sphalerite by substitution of the divalent Fe²⁺ (Co²⁺ and Cd²⁺) along with other divalent elements such as Mn²⁺ (Cook et al. 2009). The solid solution or nano-inclusions of both Co and Cd is furthermore demonstrated in the time-resolved count signals from the LA-ICP-MS analyses (Fig. 7). To better

understand the incorporation of Co in sphalerite one would need to deploy a technique such as atom probe tomography (APT), as done with invisible gold in pyrites from Carlin-type gold deposits (Gopon et al. 2019). However, this does not explain the low Cd concentrations seen in most DOF sphalerite. In addition, Cd is mostly below detection limits in the other associated sulfides, which indicates that the ore-forming fluid for this sphalerite population, and associated sulfides, was poor in Cd.

5.1.1 Grouping of the DOF mineralization styles

The similar trace element concentrations in certain mineralization styles allow to distinguish genetic stages (Fig. 12). Sphalerite and chalcopyrite show similar trends in the different mineralization styles, where the disseminated, cluster, nodule and event sphalerite and chalcopyrite (group SC1) and the pressure shadow and vein styles (group SC2) group together. Cluster and nodule pyrite group together, similar to the SC1 group, whilst on the other hand, pressure shadow and vein pyrite are decoupled in several of the trace elements, e.g., Ni, Se, Sb, Tl, Pb (Fig. 10). Event pyrite shows a wide range of element concentrations and no distinct group affiliation. These observations suggest that pyrite along with sphalerite and chalcopyrite formed during separate stages. Nodule and cluster pyrite is proposed to have a similar genetic stage to the sphalerite and chalcopyrite of the SC1 group. As pyrites are found in veins, it is reasonable to suggest that vein pyrites formed along the SC2 group. Thus, pressure shadow pyrite would have formed in an additional stage due to their trace element composition decoupling from vein pyrite.

The wide range in trace element compositions of the different mineralization styles may be due to the simplified categorization of the mineralization styles. The event style is perhaps the most enigmatic style found in the DOF mineralization. Veins in sediment-hosted copper deposits have formed during multiple genetic stages both in the Central African Copperbelt, e.g. Brems et al. (2009), and in the Kupferschiefer, e.g. Jowett (1987). Therefore, a similar, thorough investigation of the DOF veins would be required to fully understand and subdivide the vein and event mineralization styles, which is outside the scope of this study. The same applies for the DOF events that may comprise several genetic stages and seem to have an origin stretching from early soft sediment deformation to late brittle deformation and hydrothermal overprint. Although veins are not very significant to the Co mineralization, as Co (linnaeite) is hosted in the clusters, nodules and events of the DOF, their sphalerite and chalcopyrite contents significantly contribute to the sediment-hosted Cu and Zn mineralization.

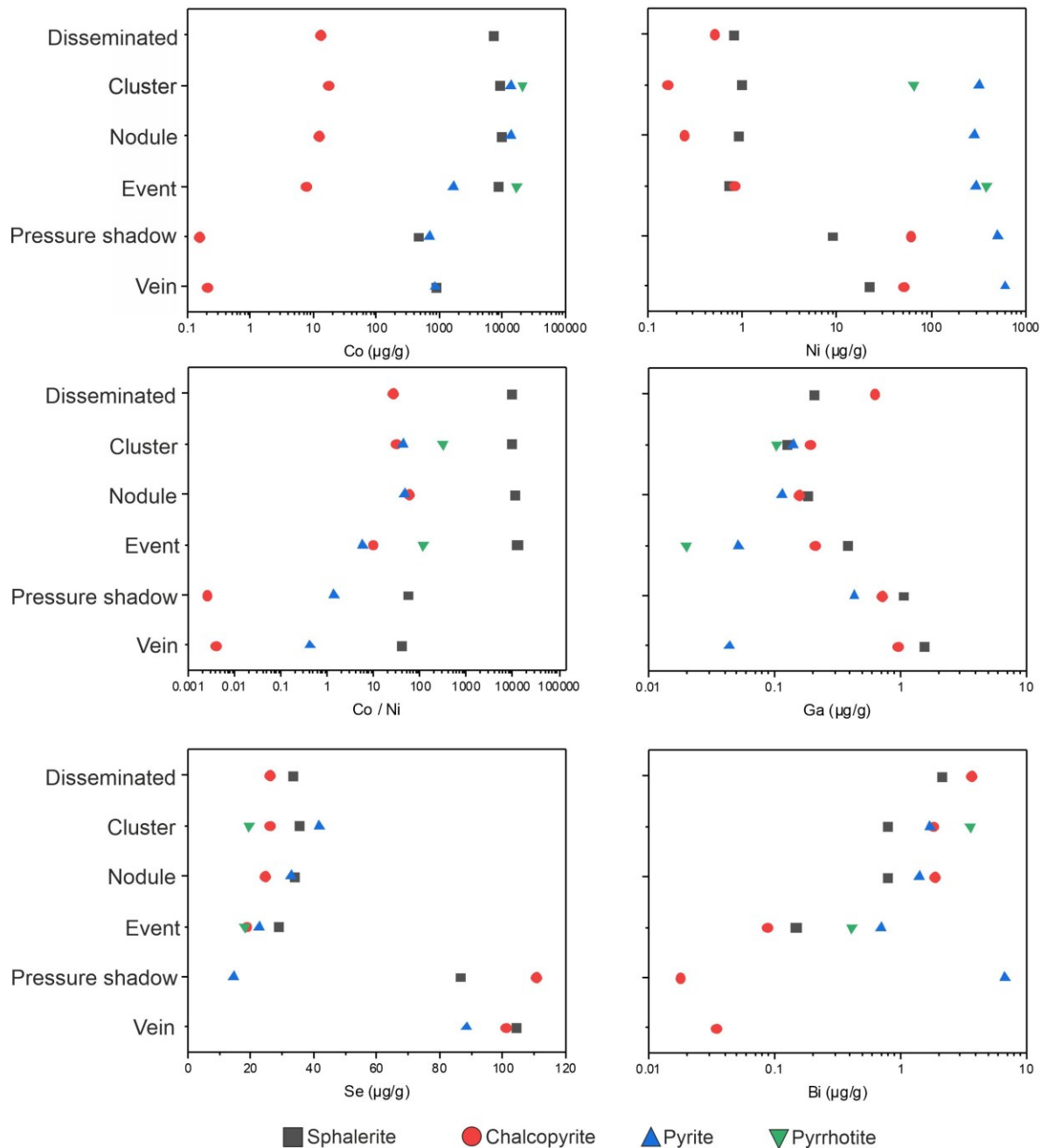


Fig. 12. Scatter plots displaying median distribution of selected elements between sphalerite, chalcopyrite, pyrite and pyrrhotite from the six mineralizations styles of the DOF mineralization.

5.2 Host preference of trace elements in coexisting iron-sulfides and its implications for ore paragenesis

Pyrite and pyrrhotite are only found to coexist within the event mineralization where the trace element distribution in these two iron-sulfides can be compared. In all other mineralization styles, the iron sulfide is either pyrite or pyrrhotite. Event pyrites are enriched in Cu, As, Sb, Tl and Pb, in comparison to event pyrrhotite. Gallium, Ge, and Mo tend to be slightly enriched in the event pyrites, although these elements occur in lower concentrations close to detection limits.

Concentrations of Mn, Co, Ni, Se, and Ag are shown to be relatively similar in both iron-sulfides within the event mineralization style. Both are Zn-poor, with most spots below detection limits.

Both sphalerite and chalcopyrite are associated and intergrown with pyrrhotite in the events style mineralization. Occasionally, galena is part of this association. The fact that the event pyrrhotite is depleted in elements such as Cu and Pb, compared to the event pyrite, could suggest that these elements were released from pre-existing event pyrites to locally form new phases, such as chalcopyrite and galena, along with the pyrrhotite during a remobilization event. Large et al. (2007) showed that trace elements such as Cu, Zn, Ag, Au, Te and Pb were all depleted in metamorphic pyrites compared to earlier diagenetic and hydrothermal pyrite from a sediment-hosted Au deposit. Large et al. (2007) proposed that these remobilized trace elements would preferentially partition into other sulfides rather than becoming incorporated in the recrystallized metamorphic pyrite. The release of Cu, Zn and Pb from pyrite during recrystallization at amphibolite facies metamorphism has been proposed by Conn et al. (2019) to result in the formation of sphalerite, chalcopyrite and galena at a millimeter to centimeter (occasionally meter) scale. This seems to agree with our observations of the event pyrite to pyrrhotite transformation, associated with formation of sphalerite, chalcopyrite and galena. Cobalt, Ni and Se contents do not show substantial changes in pyrite during amphibolite facies recrystallization (Conn et al. 2019), in agreement with the coexisting event iron-sulfide data of this study which show no significant difference in these elements. This is explained by Huston et al. (2016) and Large et al. (2007) by Co, Ni and Se being too tightly incorporated into the pyrite lattice, and thus remaining in the pyrite structure during metamorphism.

This supports the textural observations in the DOF events indicating that pyrite pre-dates pyrrhotite, sphalerite and chalcopyrite and may therefore have served as a source of Cu and Pb for these phases. Pyrite in the vein style is low in Cu and Zn. Although being associated with sphalerite and chalcopyrite, vein pyrite forms a discrete phase without the characteristically interstitial sphalerite and chalcopyrite, as is the case for the previously mentioned mineralization styles. Pressure shadow style pyrites are the only analyzed pyrites with elevated Cu and Zn contents. It is worth pointing out that the pyrite and sphalerite-chalcopyrite occupy two distinct domains of the pressure shadow clasts, pyrite being in the core and in the dissemination halo, whilst sphalerite and chalcopyrite are strictly situated within the pressure shadows of the pressure shadow clast. This could perhaps be related to the elevated Cu and Zn concentrations in the pressure shadow pyrite, compared to the other mineralization styles. The pressure shadow pyrite has been deformed but not significantly recrystallized, as remnant framboidal structures and host rock inclusions can be seen within the core. Perhaps the local metamorphic recrystallization was not sufficient to liberate the trace elements in the pressure shadow pyrite. As previously mentioned, Zn was not notably present in neither of the event iron-sulfides and thus requires another source for the recrystallized event sphalerite. The underlying Nosib Group red beds and/or basement rocks are believed to be the main source of the metals for the DOF Cu-Co mineralization, as is suggested for most other sediment-hosted Cu(-Co) deposits (e.g. Azaraien et al. 2017; van Wilderode et al. 2015 & Hitzman et al. 2005).

In the main DOF mineralization horizon sphalerite and chalcopyrite replace pre-existing framboidal pyrite. The latter is more common further away from the Co-Cu dominated zones. This

could explain the lack of disseminated pyrite within the main DOF ore horizon. It could also be possible that framboidal and euhedral pyrite, as well as pre-epigenetic Cu-Zn mineralization, were reworked into the different pyrites of this study during metamorphism. There is evidence of framboidal pyrite clusters showing different degrees of pyritic overgrowth in the less mineralized host rock along with relict framboidal textures in some ore horizon sulfides. A detailed study would be required to better understand the possible role of early sedimentary to diagenetic pyrite for the formation of the DOF Cu-Co mineralization, focusing on pyrite from the hanging and footwall that was unaffected by the mineralization. Additionally, Conn et al. (2019) concludes that trace elements (such as Cu, Zn and Pb) do not migrate far during metamorphic recrystallization. This raises the question if the main DOF horizons are associated to local deformation zones, rather than redox fronts that is the commonly accepted model for classic sediment-hosted copper deposits.

Discrimination of pyrite from different sources and ore deposits using Co/Ni ratios was proposed by Campbell and Ethier (1984). More recent discrimination study for hydrothermal and magmatic pyrite are based on Co/Sb and Se/As (Duran et al. 2015). Campbell and Ethier (1984) point out that the Co and Ni concentrations in pyrite reflect the availability of these elements in the ore-forming system and reflect their enrichment within a metallogenic province. Considering the DOF being a Co-mineralization, where Co has been significantly enriched, it is most reasonable that DOF pyrite Co and Ni concentrations would not be comparable to the general deposit types of which the discrimination plots are based off. Similar concerns are raised for the discrimination plot developed by Duran et al. (2015), as it is partly based on Co concentrations. The pressure shadow pyrite core is the only pyrite not directly associated with the main Co-mineralization and showing trace element compositions similar to typical sedimentary pyrite (Table 5), according to trace element ratios derived from a comprehensive study done on sedimentary pyrite by Gregory et al. (2015). This comparison of pyrite is more suitable as it uses more than only Co/Ni ratios. The different element ratios suggest that the pyrite core of the Cu-Zn pressure shadow mineralization is of sedimentary origin.

Table 5. Trace element ratios of DOF pressure shadow style core pyrite compared to typical ratios for sedimentary pyrite from an extensive review of the trace element composition of Archean to modern sedimentary/syngenetic to diagenetic pyrite by Gregory et al. (2015).

Ratio	DOF (After Gregory et al, 2015)		
	Pressure shadow	Ratios	% of dataset that are within the range
Co/Ni	1	< 2	91
Zn/Ni	0.2	< 10	83
Cu/Ni	1	< 2	89
As/Ni	1	< 10	93
Te/Au	780	< 1000	93
As/Au	12016	> 200	100
Ag/Au	51	> 2	100
Sb/Au	780	> 100	95
Bi/Au	145	> 1	95

5.3 Trace element partitioning of coexisting sulfides

The effects of metamorphism on sphalerite and chalcopyrite trace element composition is not yet well constrained. Cugerone et al. (2020) studied the behavior of trace elements in sphalerite during metamorphism below 400 °C, but could not draw any generally valid conclusions as the trace elements showed great heterogeneity and varied more depending on fluid source and deposit types. A handful of trace elements in sphalerite have been shown to correlate with formation temperature (Frenzel et al. 2016), where Mn, Fe and In increase whilst Ga and Ge decrease with temperature of formation. Cave et al. (2020) proposes that elements such as Ge, Ga, Cd and Sn are enriched in chemically remobilized sphalerite whilst depleted in Fe, Tl, Co, Bi, compared to the primary sphalerite. Cave et al. (2020) attributes this to higher mobility of e.g. Zn, Ge, Ga and Sn compared to Fe and Co during chemical remobilization, along with preferential partitioning of the depleted elements into co-crystallizing phases, i.e. ferroan-dolomite and galena in their study. This strongly suggests that pressure shadow and vein sphalerite (and associated phases) are the result of a later remobilization event, as elements enriched in SC2 sphalerites include Cd, Ga, and Ge, whilst being depleted in Fe and Co. The remaining elements mentioned by Cave et al. (2020) show no difference and are all very low, around and below detection limits.

The findings of Frenzel et al. (2016) and Cave et al. (2020) may seem contradictory, but it is important to note that Frenzel et al. (2016) strictly looked at the correlation between aforementioned elements and the formation temperature of host sphalerite, whilst the observations of Cave et al. (2020) focus on relative changes in sphalerite trace element composition due to the effects of subsequent recrystallization. Therefore, one may further speculate that not only are the SC2 sphalerite and chalcopyrite formed from pre-existing base metal sulfides, but also at lower temperatures than the SC1 group, as SC2 sphalerites are depleted in elements such as Mn, Fe and In and at the same time relatively enriched in Ga and Ge.

Elements such as Ga, In and Sn may get enriched in chalcopyrite during metamorphic recrystallization, as chalcopyrite is otherwise a relatively unfavored host for these trace elements in co-crystallizing base metal sulfides at lower temperatures (George et al. 2018; George et al. 2016). Several studies have examined the preferential partitioning of trace elements in co-crystallizing sulfides. Indium concentrations do show variability in DOF chalcopyrites, with pressure shadow and vein chalcopyrites containing relatively less In, along with one population of disseminated chalcopyrite which is In-poor. Thus, the SC2 (pressure shadow and vein) chalcopyrite may have formed at lower temperatures than the SC1 chalcopyrites. George et al. (2018) suggest that co-crystallizing sphalerite and chalcopyrite will have similar Cd:Zn ratios when formed under constant physiochemical conditions. The complete absence of Cd in DOF chalcopyrite makes this assessment impossible to test. Obviously the ore forming system of the DOF mineralization was Cd depleted, as SC1 sphalerite is extremely to moderately Cd-poor.

It was attempted to apply the Ga-Ge-In-Mn-Fe (GGIMF) sphalerite geothermometer (Frenzel et al. 2016) using the element concentrations in sphalerite from each mineralization style. Calculated temperatures from all mineralization styles fall within or above 310 ± 50 °C (see data set in Supplementary Material 2), which is regarded as the closing temperature of this geothermometer (Frenzel et al. 2016), suggesting that all DOF sphalerite formed at higher

temperatures. This is in agreement with the proposed trace element remobilization model derived from the event pyrites and the subsequent recrystallization of sphalerite, chalcopyrite, galena and pyrrhotite. Hence, the GGIMF thermometer is not applicable to sediment-hosted Cu-Co mineralization in the DOF. Nevertheless the geochemical differences seen in sphalerite and chalcopyrite all advocate that the SC2 assemblage formed at lower temperatures than the SC1 assemblage, even though both groups formed at temperatures above 310 ± 50 °C. Host rock assemblages suggest that the regional metamorphism in the eastern domain of the Kaoko Belt could not have exceeded 400 °C (Guj 1970). This is in agreement with the presence of stilpnomelane in the main DOF horizon, as stilpnomelane has been shown to only be stable to $\sim 430 - 470$ °C (Miyano and Klein 1989).

5.4 Sulfide mineral paragenesis

Four major sulfide-forming stages can be deduced: (1) syngenetic/diagenetic, (2) metamorphic stage I, (3) metamorphic stage II and (4) remobilization/late orogenic (Fig. 13). (1) Framboidal pyrite (Pyrite 1) in the hanging wall and footwall carbonaceous siliciclastic host rocks of the DOF ore horizon is the only evidence for a pre-metamorphic sulfide generation. The absence of disseminated pyrite in the main DOF ore horizon(s) is explained by later replacement of disseminated pyrite by base metal sulfides (dominantly sphalerite and chalcopyrite). The pressure shadow pyrite core is proposed to have formed during this stage as well, along with pyritic overgrowths on framboids during diagenesis. (2) Coarse-grained euhedral pyrites in the hanging wall and footwall host rocks indicate that regional metamorphism affected the whole sedimentary package. During this metamorphic stage I cluster, nodule and primary event pyrite 2 formed. (3) During ongoing Damaran metamorphism the stage II pyrites liberated trace elements (e.g. Zn, Cu, Pb) which were mobilized to contribute to the formation of discrete phases such as sphalerite, chalcopyrite and galena, all growing interstitially to the pyrite or pyrrhotite in the DOF events. However, the mineralizing hydrothermal fluids must have been derived from an additional metal-rich (Co, Cu, Zn & Pb) source to form the main Co-mineralization. Thus metamorphic element liberation would not be the sole source of the Co, Cu, Zn & Pb, but rather contributed to the elements necessary for the base metal sulfide formation. It is in this stage that the event pyrrhotite forms as well, growing interstitially to the other base metal sulfides. The presence of pyrrhotite, rather than pyrite, indicates either lower fO_2 conditions or higher metal/S during mineralization of the main ore stage. (4) During subsequent stage 4, Zn and Cu, along with Fe, was remobilized to form sphalerite and chalcopyrite in the pressure shadow clast tails and in the different types of veins. Trace element compositions of sphalerite from these different stages suggest that Stage 4 occurred at relatively lower temperatures yet still above 310 ± 50 °C (the approximate closure temperature of the GGIMF thermometer), suggestively during retrograde metamorphism.

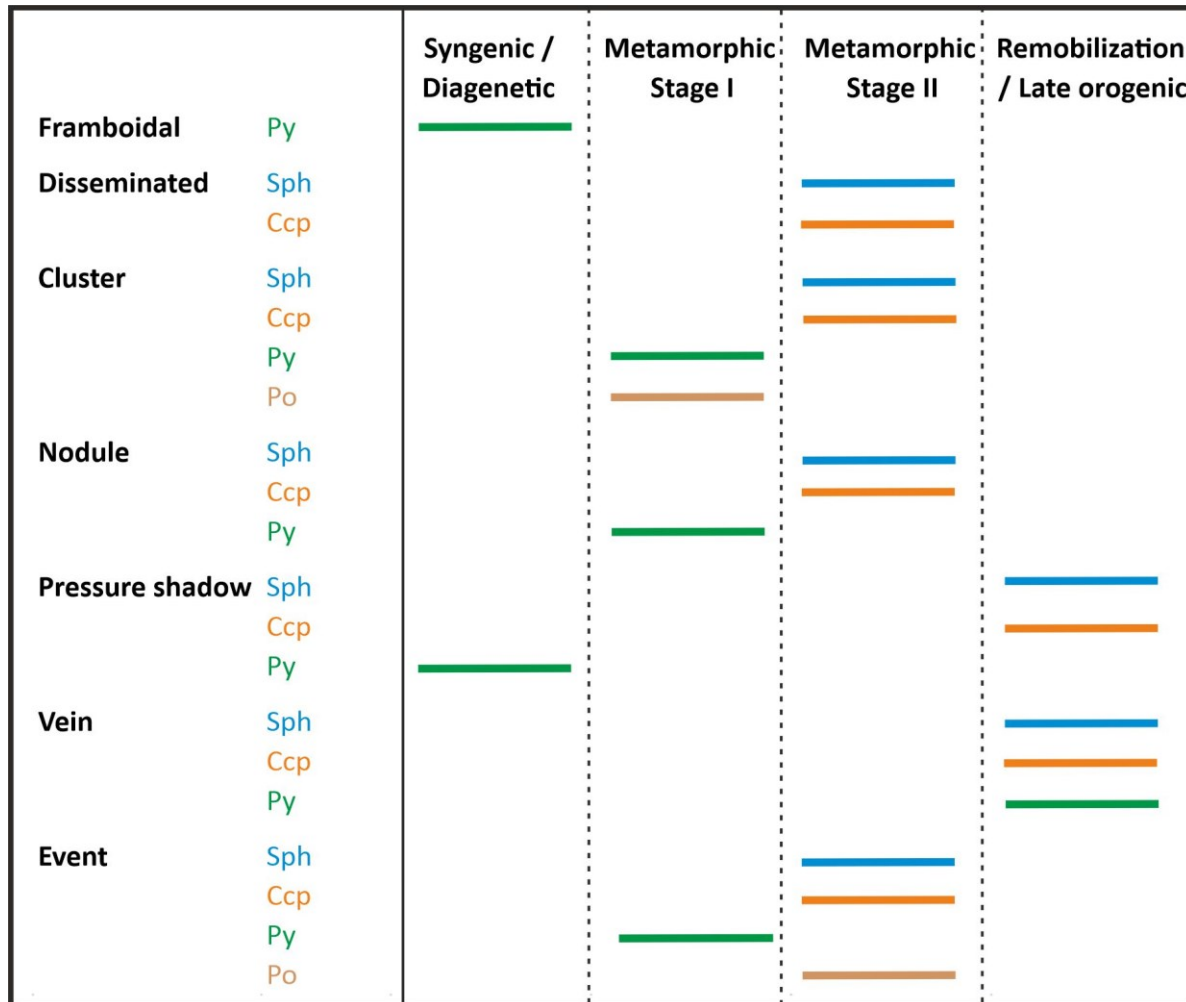


Fig. 13. Proposed paragenesis of DOF sulfides based of trace element compositions and textural relationships. Abbreviations: Py = pyrite; Sph = sphalerite; Ccp = chalcopyrite; Po = pyrrhotite.

6. Conclusions

Micro-textural observations and trace element patterns of the DOF base metal sulfides sphalerite, chalcopyrite and Fe sulfides demonstrate that the sediment-hosted Cu-Co mineralization hosted within Neoproterozoic sediments in the Kunene region in NW Namibia was significantly influenced by metamorphism during the Damaran Orogeny. This study demonstrates that the DOF mineralization, if not formed directly during the metamorphic event, was at least strongly affected which resulted in three stages of base metal sulfide formation subsequent to initial syngenic to diagenetic pyrite (Fig. 13). The nature of the DOF outcropping over 43 km strike length as a single, strongly stratiform mineralization within the upper part of the 8 km thick succession of calcareous and carbonaceous sedimentary rocks of the Ombombo Formation cannot be explained by the principle of a “first reductant”. The mineralization is likely structurally controlled by an early orogenic slump in the Ombazu Trough or thrust structure that remains to be defined by detailed structural studies in future.

Petrographic observations together with trace element data demonstrate that the Dolostone Ore Formation mineralization is the product of four main stages of sulfide formation (Fig. 13). Syn-

sedimentary to diagenetic pyrite (stage 1) is omnipresent within the sediments hosting the DOF Cu-Co mineralization. These pre-ore pyrites were later overprinted or recrystallized during the first metamorphic stage (stage 2) that was then followed by the second metamorphic main Cu-Zn mineralization stage (stage 3). These stages resulted in the formation of the disseminated, cluster, nodule and “event” mineralization styles. Late-orogenic ductile-to-brittle deformation resulted in the formation of pressure shadow mineralization and veins (stage 4).

It remains uncertain when cobalt, the main element of economic interest, was introduced into the mineralizing system. But lack of Co in stage 4 sulfides (and as a discrete phase) indicates that Co was not significantly remobilized during this late stage. Co-phases are also lacking in the earliest stage when disseminated framboidal pyrite formed. However, due to analytical limitations (too small grain size) it is unknown how much Co is in the early framboidal pyrites. Sphalerite and chalcopyrite of Stages 2 and 3 both are enriched in Co. They are associated with discrete Co-phases, such as linnaeite, and therefore are the main stages of Co-mineralization of the DOF. Stages 2 and 3 may have been contemporaneous and linked to the introduction of Co. As cobalt is not believed to be significantly remobilized from pyrite during metamorphic recrystallization, a different, earlier source of Co is necessary, such as the underlying Nosib Group red beds or the basement rocks.

Acknowledgement

A big gratitude is given to the exploration team of Gecko Namibia who helped us during the fieldwork and sample collection of this study, with a special mention to Kaarina Ndalulilwa for organization of drill cores and sample shipment. Marie-Luise Harmsen and Maik Zimmermann for their excellent sample preparation. The authors would also like to express appreciation to Thomas Meisel for the insightful discussions on the errors and misrepresentation of geochemical data. Final thanks go to the anonymous reviewers and their comments that resulted in significant improvements of this paper.

Supplementary material

The Supplementary Material for this article can be found online at:

<https://www.sciencedirect.com/science/article/pii/S0375674222001637#da0005>

References

- African Mining Capital Pty Ltd (2019): Structures: Geophysical Interpretation. Lithologies 1:1M Geology.
- Allen, N. K. (2016): Structurally controlled Cu-Zn-(Co-Pb) mineralization in the Neoproterozoic Ombombo Subgroup, Kaokoland, Namibia. Master Thesis. Colorado School of Mines.
- Alves Dias, Patricia; Blagoeva, Darina; Pavel, Claudiu; Arvanitidis, Nikolaos (2018): Cobalt: demand-supply balances in the transition to electric mobility. In Publications Office of the European Union 10, p. 97710.
- Azaraien, H.; Shahabpour, J.; Aminzadeh, B. (2017): Metallogenesis of the sediment-hosted stratiform Cu deposits of the Ravar Copper Belt (RCB), Central Iran. In Ore Geology Reviews (81), pp. 369–395.
- Belissant, R.; Boiron, M.-Ch.; Luais, B.; Cathelineau, M. (2014): LA-ICP-MS analyses of minor and trace elements and bulk Ge isotopes in zoned Ge-rich sphalerites from the Noailhac–Saint-Salvy deposit

(France): Insights into incorporation mechanisms and ore deposition processes. In *Geochimica et Cosmochimica Acta* (126), pp. 518–540.

Blood, J. (2019): Proposed Opuwo Cobalt Mining Project: Final Scoping Report: Opuwo, Kunene Region, Namibia.

Brems, D.; Muchez, Ph; Sikazwe, O.; Mukumba, W. (2009): Metallogeneses of the Nkana copper–cobalt south orebody, Zambia. In *Journal of African Earth Sciences* (55), Article 3-4, pp. 185–196.

Brown, A. C. (1992): Sediment-hosted stratiform copper deposits. In *Geoscience Canada* (19), Article 3, pp. 125–141.

Campbell, F. A.; Ethier, V. G. (1984): Nickel and cobalt in pyrrhotite and pyrite from the Faro and Sullivan orebodies. In *The Canadian Mineralogist* (22), Article 3, pp. 503–506.

Cave, Bradley; Lilly, Richard; Hong, Wei (2020): The Effect of Co-Crystallising Sulphides and Precipitation Mechanisms on Sphalerite Geochemistry: A Case Study from the Hilton Zn-Pb (Ag) Deposit, Australia. In *Minerals* 10 (9), p. 797.

Celsius Resources Limited (2021): ASX Release 1 July 2021 Celsius doubles mineral resource at Opuwo cobalt-copper project.

Celsius Resources LTD (2019): Building an Extensive Cobalt Resource in Namibia.

Conn, C. D.; Spry, P. G.; Layton-Matthews, D.; Voinot, A.; Koenig, A. (2019): The effects of amphibolite facies metamorphism on the trace element composition of pyrite and pyrrhotite in the Cambrian Nairne Pyrite Member, Kanmantoo Group, South Australia. In *Ore Geology Reviews* (114), p. 103128.

Cook, N. J.; Ciobanu, C. L.; Brugger, J.; Etschmann, B.; Howard, D. L.; Jonge, M. D. de et al. (2012): Determination of the oxidation state of Cu in substituted Cu-In-Fe-bearing sphalerite via μ -XANES spectroscopy. In *American Mineralogist* (97), Article 2-3, pp. 476–479.

Cook, N. J.; Ciobanu, C. L.; Pring, A.; Skinner, W.; Shimizu, M.; Danyushevsky, L. V. et al. (2009): Trace and minor elements in sphalerite: A LA-ICPMS study. In *Geochimica et Cosmochimica Acta* (73), Article 16, pp. 4761–4791.

Cugerone, A. Cenk-Tok, B.; Muñoz, M.; Kouzmanov, K.; Oliot, E.; Motto-Ros, V.; Le Goff, E. (2020): Behavior of critical metals in metamorphosed Pb-Zn ore deposits: example from the Pyrenean Axial Zone. In *Mineralium Deposita*, pp. 1–21.

Dewaele, S.; Muchez, Ph.; Vets, J.; Fernandez-Alonzo, M.; Tack, L. (2006): Multiphase origin of the Cu–Co ore deposits in the western part of the Lufilian fold-and-thrust belt, Katanga (Democratic Republic of Congo). In *Journal of African Earth Sciences* (46), Article 5, pp. 455–469.

Duran, C. J.; Barnes, S-J; Corkery, John T. (2015): Chalcophile and platinum-group element distribution in pyrites from the sulfide-rich pods of the Lac des Iles Pd deposits, Western Ontario, Canada: Implications for post-cumulus re-equilibration of the ore and the use of pyrite compositions in exploration. In *Journal of Geochemical Exploration* 158, pp. 223–242.

Duran, C. J.; Dubé-Loubert, H.; Pagé, P.; Barnes, S.-J.; Roy, M.; Savard, D. et al. (2019): Applications of trace element chemistry of pyrite and chalcopyrite in glacial sediments to mineral exploration targeting: Example from the Churchill Province, northern Quebec, Canada. In *Journal of Geochemical Exploration* (196), pp. 105–130.

Ellmies, R. (2013): Extensive stratiform Cu-Co-mineralisation discovered. internal company reports of Kunene Resources Namibia.

Ellmies, R. (2018): Extensive stratiform Cu-Co-mineralisation at Okondaurie, Kunene Region. Internal “Living Document”, Kunene Resources (Pty) Ltd.

Ellmies, R. (2019): Cobalt-copper and vanadium-chromium horizons in the Upper Ombombo Formation: A new mineral province in Kunene region? Geological Society of Namibia. Windhoek, Namibia.

European Commission (2020): Communication from the Commission to the European Parliament, the Council, the Economic and Social Committee and the Committee of the Regions. Critical Raw Materials

Resilience: Charting a Path towards greater Security and Sustainability. Edited by European Commission. Brussels, Belgium.

Foltyn, Krzysztof; Bertrandsson Erlandsson, Viktor; Zygo, Władysław; Melcher, Frank; Pieczonka, Jadwiga (2022): New perspective on trace element (Re, Ge, Ag) hosts in the Cu-Ag Kupferschiefer deposit, Poland: insight from a LA-ICP-MS trace element study. In *Ore Geology Reviews*, p. 104768.

Foster, D. A.; Goscombe, B. D.; Gray, D. R. (2009): Rapid exhumation of deep crust in an obliquely convergent orogen: The Kaoko Belt of the Damara Orogen. In *Tectonics* (28), Article 4, 1-24.

Frenzel, M.; Hirsch, T.; Gutzmer, J. (2016): Gallium, germanium, indium, and other trace and minor elements in sphalerite as a function of deposit type—A meta-analysis. In *Ore Geology Reviews* (76), pp. 52–78.

George, L. L.; Cook, N. J.; Ciobanu, C. L. (2016): Partitioning of trace elements in co-crystallized sphalerite–galena–chalcopyrite hydrothermal ores. In *Ore Geology Reviews* (77), pp. 97–116.

George, L. L.; Cook, N. J.; Ciobanu, C. L.; Wade, B. P. (2015): Trace and minor elements in galena: A reconnaissance LA-ICP-MS study. In *American Mineralogist* (100), Article 2-3, pp. 548–569.

George, L. L.; Cook, N. J.; Crowe, B. B. P.; Ciobanu, C. L. (2018): Trace elements in hydrothermal chalcopyrite. In *Mineralogical Magazine* (82), Article 1, pp. 59–88.

Gopon, Phillip; Douglas, James O.; Auger, Maria A.; Hansen, Lars; Wade, Jon; Cline, Jean S. et al. (2019): A nanoscale investigation of Carlin-type gold deposits: An atom-scale elemental and isotopic perspective. In *Economic Geology* 114 (6), pp. 1123–1133.

Goscombe, B. D. (1999): Geological report on magnetic and radiometric anomalies mapped in the region south of the Kunene Igneous Complex, Namibia. Company exploration reports, Geological Survey of Namibia.

Goscombe, B. D.; Foster, D. A.; Gray, D. R.; Wade, B.; Marsellos, A.; Titus, N. P. (2017): Deformation correlations, stress field switches and evolution of an orogenic intersection: The Pan-African Kaoko-Damara orogenic junction, Namibia. In *Geoscience Frontiers* (8), pp. 1187–1232.

Goscombe, B. D.; Gray, D. R.; Hand, M. (2005): Extrusional Tectonics in the Core of a Transpressional Orogen; the Kaoko Belt, Namibia. In *Journal of Petrology* (46), Article 6, pp. 1203–1241.

Goscombe, B. D.; Hand, M.; Gray, D. R. (2003): Structure of the Kaoko Belt, Namibia: progressive evolution of a classic transpressional orogen. In *Journal of Structural Geology* (25), Article 7, pp. 1049–1081.

Gregory, D. D.; Large, R. R.; Halpin, J. A.; Baturina, E. L.; Lyons, T. W.; Wu, S. et al. (2015): Trace element content of sedimentary pyrite in black shales. In *Society of Economic Geologists Special Publication* 16 (110), Article 6, pp. 1389–1410.

Guj, P. (1970): The Damara Mobile Belt in the south-western Kaokoveld South West Africa. PhD Thesis. University of Cape Town / Precambrian Research Unit, Cape Town, South Africa.

Haynes, D. W. (1986): Stratiform copper deposits hosted by low-energy sediments; II, Nature of source rocks and composition of metal-transporting water. In *Economic Geology* 81 (2), pp. 266–280.

Hedberg, R. M. (1979): Stratigraphy of the Ovamboland Basin, South West Africa. University of Cape Town / Precambrian Research Unit. Department of Geology.

Hitzman, M. W.; Kirkham, R.; Broughton, D.; Thorson, J.; Selley, D. (2005): The sediment-hosted stratiform copper ore system. In *Economic Geology* (100).

Hitzman, M. W.; Selley, D.; Bull, S. (2010): Formation of sedimentary rock-hosted stratiform copper deposits through Earth history. In *Economic Geology* (105), Article 3, pp. 627–639.

Hoffman, P. F. (2011): Glaciogenic and associated strata of the Otavi carbonate platform and foreslope, northern Namibia: evidence for large base-level and glacioeustatic changes. In G. Shields-Zhou, G. P. Halverson, E. Arnaud (Eds.): *The Geological Record of Neoproterozoic Glaciations*. 36th ed. London: Geological Society of London.

Hoffman, P. F.; Halverson, G. P. (2008): Otavi Group of the western Northern Platform, the Eastern Kaoko Zone and the western Northern Margin Zone. In R. McG. Miller (Ed.): *The Geology of Namibia: Neoproterozoic to Lower Palaeozoic*. 2nd ed. Windhoek, Namibia: Geological Survey (2), 13-69–13-136.

Hoffman, P. F.; Halverson, G. P.; Schrag, D. P.; Higgins, J. A.; Domack, E. W.; Macdonald, F. A. et al. (2021): Snowballs in Africa: sectioning a long-lived Neoproterozoic carbonate platform and its bathyal foreslope (NW Namibia). In *Earth-Science Reviews* (219), p. 103616. DOI: 10.1016/j.earscirev.2021.103616.

Hoffman, P. F., Kaufman, A. J., Halverson, G. P., Schrag, D. P. (1998): Comings and goings of global glaciations on a Neoproterozoic tropical platform in Namibia. 8(5), 1-9. *GSA today*.

Hoffmann, K.-H.; Condon, D. J.; Bowring, S. A.; Crowley, J. L. (2004): U-Pb zircon date from the Neoproterozoic Ghaub Formation, Namibia: Constraints on Marinoan glaciation. In *Geology* (32), Article 9, pp. 817–820.

Hoffmann, K.-H.; Prave, A. R. (1996): A preliminary note on a revised subdivision and regional correlation of the Otavi Group based on glaciogenic diamictites and associated cap dolostones. In *Communications of the geological survey of Namibia* (11), pp. 77–82.

Hoffmann, K.-H.; Rabie, L.; Menge, G. (2002): *Geological Map of Namibia 1:250,000. Sheet 1712 "Swartbooisdrift"*. Windhoek, Namibia: Ministry of Mines and Energy, Directorate Geological Survey of Namibia.

Hood, A. v. S.; Wallace, M. W.; Reed, C. P.; Hoffmann, K.-H.; Freyer, E. E. (2015): Enigmatic carbonates of the Ombombo Subgroup, Otavi Fold Belt, Namibia: A prelude to extreme Cryogenian anoxia? In *Sedimentary Geology* (324), pp. 12–31.

Huston, D. L.; Mernagh, T. P.; Hagemann, S. G.; Doublier, M. P.; Fiorentini, M.; Champion, D. C. et al. (2016): Tectono-metallogenic systems - The place of mineral systems within tectonic evolution, with an emphasis on Australian examples. In *Ore Geology Reviews* (76), pp. 168–210.

Ingham, E. S.; Cook, N. J.; Cliff, J.; Ciobanu, C. L.; Huddleston, A. (2014): A combined chemical, isotopic and microstructural study of pyrite from roll-front uranium deposits, Lake Eyre Basin, South Australia. In *Geochimica et Cosmochimica Acta* (125), pp. 440–465.

Jowett, E. C. (1987): Formation of sulfide-calcite veinlets in the Kupferschiefer Cu-Ag deposits in Poland by natural hydrofracturing during basin subsidence. In *The Journal of Geology* (95), Article 4, pp. 513–526.

Kelepile, Tebogo; Betsi, Thierry Bineli; Franchi, Fulvio; Shemang, Elisha (2020): Partitioning and distribution of silver in sediment-hosted Cu-Ag deposits: Evidence from the Ghanzi-Chobe Belt portion of the Kalahari Copper Belt. In *Ore Geology Reviews* 124, p. 103663.

Konopásek, J.; Kröner, S.; Kitt, S. L.; Passchier, C. W.; Kröner, A. (2005): Oblique collision and evolution of large-scale transcurrent shear zones in the Kaoko belt, NW Namibia. In *Precambrian Research* (136), Article 2, pp. 139–157.

Kröner, A.; Rojas-Agramonte, Y.; Hegner, E.; Hoffmann, K.-H.; Wingate, M. T.D. (2010): SHRIMP zircon dating and Nd isotopic systematics of Palaeoproterozoic migmatitic orthogneisses in the Epupa Metamorphic Complex of northwestern Namibia. In *Precambrian Research* 183 (1), pp. 50–69.

Large, R. R.; Halpin, J. A.; Danyushevsky, L. V.; Maslennikov, V. V.; Bull, S. W.; Long, J. A. et al. (2014): Trace element content of sedimentary pyrite as a new proxy for deep-time ocean-atmosphere evolution. In *Earth and Planetary Science Letters* (389), pp. 209–220.

Large, R. R.; Maslennikov, V. V.; Robert, F.; Danyushevsky, L. V.; Chang, Z. (2007): Multistage sedimentary and metamorphic origin of pyrite and gold in the giant Sukhoi Log deposit, Lena gold province, Russia. In *Economic Geology* (102), Article 7, pp. 1233–1267.

Liu, Z.; Shao, Y.; Zhou, H.; Liu, N.; Huang, K.; Liu, Q. et al. (2018): Major and trace element geochemistry of pyrite and pyrrhotite from stratiform and lamellar orebodies: implications for the ore genesis of the Dongguashan copper (gold) deposit, eastern China. In *Minerals* (8), Article 9, p. 380.

Lockington, J. A.; Cook, N. J.; Ciobanu, C. L. (2014): Trace and minor elements in sphalerite from metamorphosed sulphide deposits. In *Mineralogy and Petrology* (108), Article 6, pp. 873–890.

Mambwe, P.; Muchez, P.; Lavoie, S.; Kipata, L.; Dewaele, S. (2019): Evidence for late Lufilian orogenic mineralizing fluids at the Kamalondo Cu-Co deposit (Tenke Fungurume, Democratic Republic of the Congo). In *Society for Geology Applied to Mineral Deposits (Ed.): Life with Ore Deposits on Earth. Volume: 1: Advances in Understanding Hydrothermal Processes. The 15th SGA Biennial Meeting. Glasgow, Scotland, 27-30 August*, pp. 287–290.

Martin, H. (1965): *The Precambrian geology of South West Africa and Namaqualand*. Cape Town, South Africa: Precambrian Research Unit, University of Cape Town.

Metcalf, R.; Rochelle, C. A.; Savage, D.; Higgo, J. W. (1994): Fluid-rock interactions during continental red bed diagenesis: implications for theoretical models of mineralization in sedimentary basins. In *Geological Society London Special Publications* (78), Article 1, pp. 301–324.

Miller, R. McG. (1997): The Owambo Basin of northern Namibia. In R. C. Selley (Ed.): *Sedimentary Basins of the World: African Basins*, vol. 3. Amsterdam: Elsevier, pp. 237–317.

Miller, R. McG. (2008): *The Geology of Namibia*. 2nd ed. Windhoek, Namibia: Geological Survey.

Miller, R. McG. (2013): Comparative Stratigraphic and Geochronological Evolution of the Northern Damara Supergroup in Namibia and the Katanga Supergroup in the Lufilian Arc of Central Africa. In *Geoscience Canada* (40), Article 2, pp. 118–140.

Miyano, Takashi; Klein, Cornelis (1989): Phase equilibria in the system $K_2O-FeO-MgO-Al_2O_3-SiO_2-H_2O-CO_2$ and the stability limit of stilpnomelane in metamorphosed Precambrian iron-formations. In *Contributions to Mineralogy and Petrology* 102 (4), pp. 478–491.

Mudd, Gavin M.; Weng, Zhehan; Jowitt, Simon M. (2013): A detailed assessment of global Cu resource trends and endowments. In *Society of Economic Geologists Special Publication* 16 108 (5), pp. 1163–1183.

Murakami, H.; Ishihara, S. (2013): Trace elements of Indium-bearing sphalerite from tin-polymetallic deposits in Bolivia, China and Japan: A femto-second LA-ICPMS study. In *Ore Geology Reviews* (53), pp. 223–243.

Onuk, P.; Melcher, F.; Mertz-Kraus, R.; Gäbler, H.-E.; Goldmann, S. (2017): Development of a Matrix-Matched Sphalerite Reference Material (MUL -ZnS-1) for Calibration of In Situ Trace Element Measurements by Laser Ablation-Inductively Coupled Plasma-Mass Spectrometry. In *Geostandards and Geoanalytical Research* (41), Article 2, pp. 263–272.

Paton, C.; Hellstrom, J.; Paul, B.; Woodhead, J.; Hergt, J. (2011): Iolite: Freeware for the visualisation and processing of mass spectrometric data. In *Journal of Analytical Atomic Spectrometry* (26), Article 12, pp. 2508–2518.

Pfaff, K.; Koenig, A.; Wenzel, T.; Ridley, I.; Hildebrandt, L. H.; Leach, D. L.; Markl, G. (2011): Trace and minor element variations and sulfur isotopes in crystalline and colloform ZnS: Incorporation mechanisms and implications for their genesis. In *Chemical Geology* (286), Article 3-4, pp. 118–134.

Porada, H. (1989): Pan-African rifting and orogenesis in southern to equatorial Africa and eastern Brazil. In *Precambrian Research* (44), Article 2, pp. 103–136.

Prave, A. R. (1996): Tale of three cratons: tectonostratigraphic anatomy of the Damara Orogen in northwestern Namibia and the assembly of Gondwana. In *Geology* (24), pp. 1115–1118.

Ramdohr, P. (1969): *The ore minerals and their intergrowths*. Oxford, New York: Pergamon Press (International series of monographs on earth sciences.).

SACS (1980): *Stratigraphy of South Africa, Handbook 8. Part 1: Lithostratigraphy of the Republic of South Africa, South West Africa/Namibia and the Republics of Bophuthatswana, Transkei and Venda*. Pretoria, South Africa: Geological Survey.

Seth, B.; Kröner, A.; Mezger, K.; Nemchin, A. A.; Pidgeon, R. T.; Okrusch, M. (1998): Archaean to Neoproterozoic magmatic events in the Kaoko belt of NW Namibia and their geodynamic significance. In *Precambrian Research* (92), Article 4, pp. 341–363.

Thomas, H. V.; Large, R. R.; Bull, S. W.; Maslennikov, V.; Berry, R. F.; Fraser, R. et al. (2011): Pyrite and pyrrhotite textures and composition in sediments, laminated quartz veins, and reefs at Bendigo gold mine, Australia: Insights for ore genesis. In *Economic Geology* (106), Article 1, pp. 1–31.

Trompette, Roland (1997): Neoproterozoic (~ 600 Ma) aggregation of Western Gondwana: a tentative scenario. In *Precambrian Research* 82 (1-2), pp. 101–112.

USGS (2020): Mineral commodity summaries 2020. DOI: 10.3133/mcs2020.

van Wilderode, J.; Debruyne, D.; Torremans, K.; Elburg, M. A.; Vanhaecke, F.; Muchez, P. (2015): Metal sources for the Nkana and Konkola stratiform Cu–Co deposits (Zambian Copperbelt): Insights from Sr and Nd isotope ratios. In *Ore Geology Reviews* 97 (127-138).

Walker, T. R. (1989): Application of diagenetic alterations in redbeds to the origin of copper in stratiform copper deposits. Geological Association of Canada.

Wallner, D.; Bertrandsson Erlandsson, V.; Raith, J.; Rantitsch, G.; Melcher, F.; Ellmies, R. (2022): Mineralogical and Geochemical Characterization of the Dolostone Ore Formation, Kunene Region, Namibia. (Poster). Leoben, Austria, 2022.

Wilson, S. A.; Ridley, W. I.; Koenig, A. E. (2002): Development of sulfide calibration standards for the laser ablation inductively-coupled plasma mass spectrometry technique. In *Journal of Analytical Atomic Spectrometry* (17), Article 4, pp. 406–409.

Winderbaum, L.; Ciobanu, C. L.; Cook, N. J.; Paul, M. Metcalfe, A.; Gilbert, S. (2012): Multivariate analysis of an LA-ICP-MS trace element dataset for pyrite. In *Mathematical Geosciences* (44), Article 7, pp. 823–842.

Ye, L.; Cook, N. J.; Ciobanu, C. L.; Yuping, L.; Qian, Z.; Tiegeng, L. et al. (2011): Trace and minor elements in sphalerite from base metal deposits in South China: a LA-ICPMS study. In *Ore Geology Reviews* (39), Article 4, pp. 188–217.

Publication II

Sphalerite as a non-traditional critical metal source: Correlative microscopy (EPMA, EBSD, and APT) of cobalt- enriched sulfides from the sediment-hosted copper-cobalt Dolostone Ore Formation deposit, Namibia

**Viktor Bertrandsson Erlandsson¹, Phillip Gopon¹, Helene Waldl²,
David Misch¹, Rainer Ellmies³, Frank Melcher¹**

¹Montanuniversität Leoben, Department of Applied Geosciences and Geophysics, Leoben,
Austria

²Christian Doppler Laboratory for Advanced Coated Cutting Tools, Montanuniversität Leoben,
Leoben, Austria

³Gecko Namibia, Swakopmund, Namibia

Frontiers in Earth Science, 11 (2023) 1171859

The publication version in this thesis is the final version, which was accepted and published.

Abstract

Sphalerite from the sediment-hosted Dolostone Ore Formation (DOF) Cu-Co-Zn deposit, in northwestern Namibia, has previously been shown to contain extremely high concentrations of the critical metal Co (up to 1 wt%). These concentrations are the highest reported in sphalerite to date, and the how and why of sphalerite being able to incorporate such high concentrations of Co are poorly constrained. We use correlative electron microprobe microanalysis, electron backscattered diffraction, and atom probe, to reconstruct the likely incorporation mechanisms and modes of occurrence of such high Co concentrations in natural sphalerite.

While over twenty samples were studied, the comprehensive analytical workflow was executed on one representative sample to gain a detailed understanding of Co enrichment. The sulfides of the studied sample are: Co-rich pyrite, chalcopyrite, Co-rich sphalerite, linnaeite, cobaltpentlandite, and cobaltite, mentioned in order of abundance. Detailed petrography of these sulfides indicates that they formed through three stages during the main Cu-Co-Zn ore stage of the DOF. Cobalt was initially contained in pyrite that grew during Ore Stage 1 and was later affected by oxidizing fluids (Ore Stage 2). This led to remobilization and growth of linnaeite ($\text{Co}^{2+}\text{Co}^{3+}_2\text{S}_4$). A later change in $f\text{O}_2$ (Ore Stage 3) led to the breakdown of linnaeite and the further growth of accessory cobaltite along with the Co-rich sphalerite and chalcopyrite. The hyper-enriched Co-sphalerite then is the last major sink for Co in the DOF deposit.

A low Fe and Co, and high Zn sub-grain boundary network within the Co-rich sphalerite was identified by EPMA and EBSD. This sub-grain network is believed to have formed during a later, secondary metamorphic stage (Cu-Zn(-Pb) Ore Stage 4), which developed during ductile deformational mineralization styles such as pressure shadows and veins. Our APT data reconstructions show no evidence for Co-inclusions within the Co-sphalerite and spatial ion correlation analyses of the data suggest that Co occurs in the sphalerite through simple substitution of Zn. This study demonstrates that sphalerite may contain significant concentrations of the Co through simple substitution, potentially representing an important non-traditional Co source in future critical metal exploration.

Keywords: cobalt, sphalerite, Dolostone Ore Formation, substitution mechanisms, EBSD, atom probe tomography

1 Introduction

The increasing complexity of technologies related to communication, mobility, renewable energy, etc., poses a great demand for an increasingly complex set of raw materials (for our society). Cobalt is one of those increasingly sought-after critical metals due to its crucial role in large storage capacity batteries. Approximately 49 % of the world's Co goes into the production of electric-car batteries (Alves Dias et al. 2018), while as of 2019 the Central African Copperbelt (CACB) is responsible for approximately 68 % of the global Co production (European Commission 2020; USGS 2020). This combination of importance and source limitation led to Co being identified as a critical raw material by the EU and US authorities (European Commission 2020; USGS 2022). Sphalerite has been shown to have the potential to host a wide range of minor and trace elements, including several critical elements such as Co, Ge, Ga, In, and Sb (e.g. Frenzel et al. 2016; Lockington et al. 2014; Cook et al. 2009). Analyses of sphalerite from different ore

deposit types have demonstrated that deposit-specific enrichment of certain critical elements occurs. For example, Ga and Ge in carbonate-hosted Pb-Zn deposits (Liu et al. 2022; Bonnet et al. 2016; Frenzel et al. 2016; Marsh et al. 2016), while In is commonly enriched in polymetallic vein deposits (Foltyn et al. 2020; Frenzel et al. 2016; Murakami and Ishihara 2013). Sphalerites from sediment-hosted Cu-Co deposits have not yet been well studied in regards to trace elements, with the DOF sphalerite being one of the first examples of hyper-enrichment in such styles of mineralizations (Bertrandsson Erlandsson et al. 2022).

While Fe^{2+} has been shown to readily substitute for Zn^{2+} in sphalerite (1 - 10 wt%; Frenzel et al. 2016; Lockington et al. 2014; Cook et al. 2009), Co^{2+} has only been recognized to occur in comparably minor concentrations of hundreds to just above thousands of $\mu\text{g/g}$ in sphalerite despite their similar ionic radii (e.g. Cook et al. 2009; Intiomale and Oosterbosch 1974). The highest Co concentrations in sphalerite have been reported in the sediment-hosted Dolostone Ore Formation (DOF) Cu-Co mineralization in northwestern Namibia (up to 1.5 wt%; Bertrandsson Erlandsson et al. 2022). These findings spark the question as to why and how such abnormally high Co concentrations may be incorporated. While the laser ablation inductively coupled mass spectrometry technique (LA-ICP-MS) that was used in the original study is able to quickly and precisely measure trace elements, the large analytical spot size (typically 20 – 100 μm) does not allow for a detailed understanding of the incorporation mechanisms.

A combination of electron microprobe microanalysis (EPMA), electron backscattered diffraction (EBSD), and atom probe tomography (APT) was applied to achieve a better understanding of how Co occurs within the deposit, is distributed within the individual crystals, and how it is distributed at the atomic scale specifically in sphalerite. EPMA enables higher resolution mapping of major and minor elements in the sphalerite to see if Co is homogeneously distributed throughout the Co-rich sphalerite crystals, whilst APT allow to investigate if Co occurs as nano-inclusions or homogeneously distributed within the lattice. The application of APT has recently shown to be a powerful tool to determine the distribution of e.g. Cu and Ge in sphalerite (Fougerouse et al. 2023). The techniques established by Gojon et al. (2019) may be used to visualize the atomic scale associations between the major, minor, and trace elements are used to elucidate if a coupled or simple substitution mechanism is responsible for the high Co concentrations in the DOF sphalerite crystals.

2 Geological Setting

2.1 Regional Geology

The Dolostone Ore Formation (DOF) mineralization is hosted in the Ombombo Subgroup of the Neoproterozoic Damara Supergroup (Allen 2016). The Damara Supergroup sediments represent a succession from a rift basin to carbonate platform, starting with fluvial siliciclastics, grading into marine shales, siltstones and carbonates. The basal Nosib Group sediments were deposited in grabens formed during the break-up of Rodinia and are comprised of arkosic and felspathic sandstones with some interbedded conglomerates that uncomfortably overly the Paleoproterozoic basement (Allen 2016; Miller 2008; Porada 1989; Guj 1970). Overlying the Nosib Group is the Ombombo Subgroup, the basal member of the Otavi Group, composed of cyclical marine fine-grained siliciclastics and carbonates. Within the DOF area, the Ombombo Subgroup sediments are predominantly composed of calcareous shales and siltstones, interbedded with

minor sandstones, and carbonates (Allen 2016; Hoffman and Halverson 2008; Miller 2008). The Ombombo Subgroup is overlain by the Abenab Subgroup, which in the DOF area is present as the Chuos Formation diamictite and Rasthof Formation cap-carbonates (Allen 2016; Hoffmann and Prave 1996; Hoffman 2011).

The DOF mineralization is tectonostratigraphically situated within the Eastern Foreland Zone within the Kaoko Belt, which is the NE-SW trending branch of the metamorphic belts formed during the Damara orogeny (Goscombe et al. 2005). The Kaoko Belt formed through two main orogenic phases, the 590 – 535 Ma Kaoko Phase and the 555 – 505 Ma Damara Phase (Goscombe et al. 2017; Goscombe et al. 2003). The Eastern Foreland Zone represents the lowest grade metamorphic rocks within the Kaoko Belt, with temperature estimates ranging from 300 – 400 °C (Foster et al. 2009; Guj 1970).

2.2 Geology of the Dolostone Ore Formation mineralization

The sediment-hosted DOF is a Cu-Co-Zn mineralization horizon within a siltstone-shale carbonate succession of the Ombombo Subgroup in the NW-SE trending Ombazu Trough (Figure 1). The mineralized DOF horizon is traced for at least 43 km along strike and dips 35 – 70° to the north with a thickness of <1 – 15 m. The variation in dip is due to folding caused by the Damaran orogeny (Bertrandsson Erlandsson et al. 2022). The main sulfides of the DOF mineralization are in order of abundance: pyrite, chalcopyrite, sphalerite, pyrrhotite, and linnaeite with minor cobaltpentlandite and accessory galena and cobaltite (Bertrandsson Erlandsson et al. 2022). The main Co(-Cu-Zn) mineralization is hosted in altered siltstones that are predominately comprised of stilpnomelane, ankerite to Fe-dolomite, siderite, and quartz, with lesser amounts of white mica and chlorite. Ore Stage one mineralization resulted in more classical sediment-hosted mineralization styles, with disseminated sulfides, pyrite nodules, and polysulfide clusters (see Bertrandsson Erlandsson et al. 2022 for full description of the mineralization stages). There is a fourth mineralization style which is attributed to Ore Stage one, referred to as “DOF events”; these are vein-like features that show both brittle and ductile textures and are believed to have been affected by both main mineralization stages (Bertrandsson Erlandsson et al. 2022). Stage one was initially divided into two sub-stages (metamorphic stage I & II) by Bertrandsson Erlandsson et al. (2022), where pyrite was proposed to pre-date the Cu and Zn mineralization of Ore Stage one. Ore Stage one is responsible for the main Co-mineralization but can be texturally subdivided into three separate stages (Figure 3), which will be further discussed herein.

Ore Stage two is dominated by vein-type mineralization and sulfide mineralization within pressure-shadows and lacks substantial Co-phases (see Bertrandsson Erlandsson et al. 2022 for full description of the mineralization stages). Not only are discrete Co-phases predominantly attributed to the Ore Stage one mineralization, but also Ore Stage one pyrite, chalcopyrite and sphalerite show elevated Co concentrations compared to the Co-poor Ore Stage two sulfides. Sphalerite from Ore Stage one contains between 5,186 – 10,568 µg/g Co, compared to 38 – 1,258 µg/g Co in Ore Stage two sphalerite (Bertrandsson Erlandsson et al. 2022). Sulfides from both stages commonly occur intergrown, with sphalerite frequently containing chalcopyrite inclusions (Figure 3B). The sphalerite geothermometer by Frenzel et al. (2016) yielded sphalerite formation temperatures above the closing temperature of the geothermometer (i.e. 310 ± 50 °C) suggesting that ore-formation was linked to the regional Damaran metamorphism (Bertrandsson Erlandsson

et al. 2022). The Co-rich sphalerite investigated in this study is from the Ore Stage one cluster mineralization style (Figure 3). Organic matter is widely present within the DOF Ombombo Formation (Allen 2016) and framboidal pyrite is omnipresent in the DOF stratigraphy, with the exception of within the main Co(-Cu-Zn) DOF mineralization (Bertrandsson Erlandsson et al. 2022).

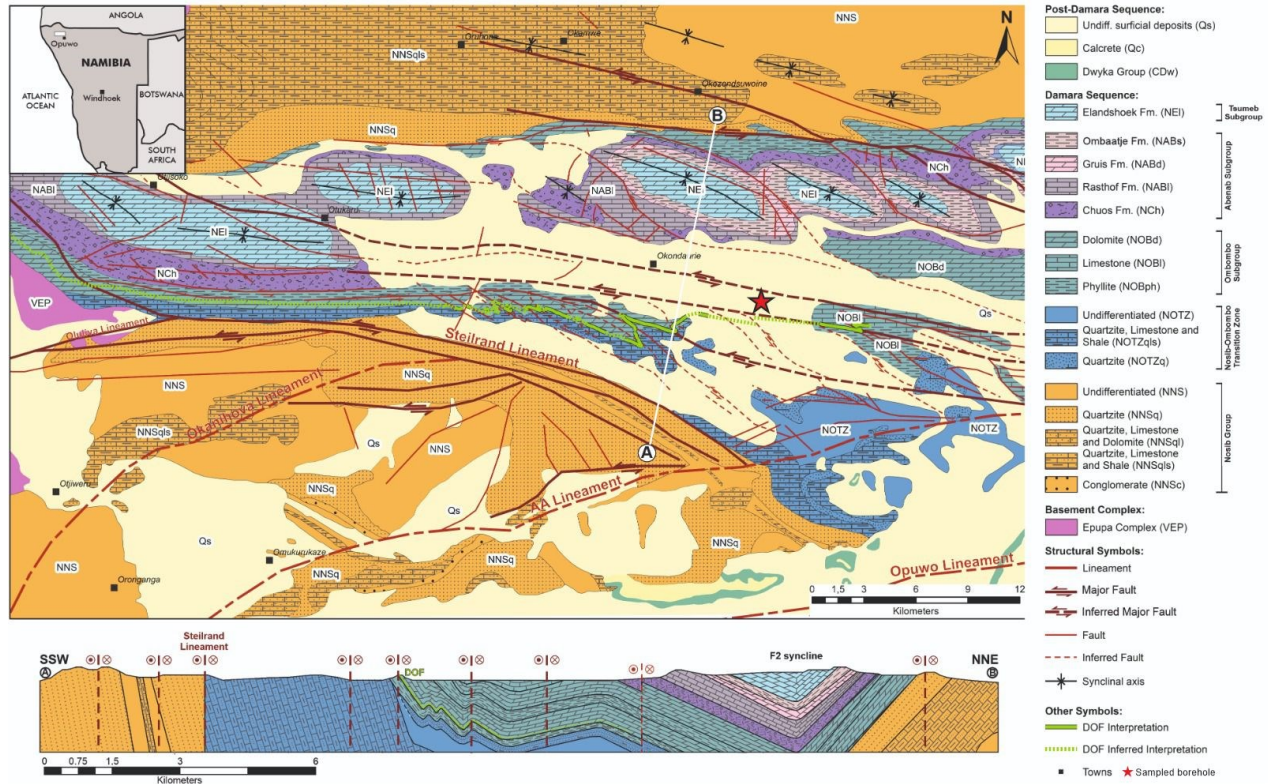


Figure 1. Local geological map and schematic geological cross-section (from the A and B symbols on the map) of the Dolostone Ore Formation (DOF) Co-Cu-Zn mineralization (modified after Bertrandsson Erlandsson et al. 2022; and references therein). The borehole from which the investigated sample is from is marked out with a red star.

3 Methods

3.1 Sample selection

Over twenty samples were looked at to obtain a general understanding of the sphalerite occurrences in the different mineralization styles and to find sphalerite samples with the highest Co concentration for our study. The polished mount selected for further EPMA and APT characterization was chosen as it contained 1) the sphalerite with the highest Co concentrations (Bertrandsson Erlandsson et al., (2022) (Bertrandsson Erlandsson et al. 2022), 2) relatively large sphalerite crystal sizes (for EPMA), and 3) sphalerite that appears to be a significant source of Co from this ore stage (see Section 5.1). The selected sphalerite comes from the ‘polysulfide cluster’ mineralization style, but as discussed in the introduction all mineralization styles are part of the same overarching ore-forming stage (Bertrandsson Erlandsson et al. 2022).

3.2 EPMA

A JEOL Superprobe JXA 8200 EPMA at the Department of Applied Geosciences and Geophysics (Montanuniversität Leoben, Austria) was utilized for element mapping. The instrument is equipped with five wavelength-dispersive (WDS) and one energy dispersive (EDS) spectrometers. The WDS spectrometers were used to measure Cu, Cd, Fe, Co, and Zn whilst the EDS detector measured S, Ni, and As. The crystals used for each WDS element were: Cu on TAP, Cd on PETJ, Fe on LIF, Co and Zn on LIFH. All elements were measured with a 50 ms dwell time per pixel. Mapping was conducted using the stage scan mode with a 15.0 keV and 100 nA electron-beam.

3.3 EBSD

EBSD measurements were carried out using a FEI Versa 3D Dual Focused Ion Beam FE-SEM with a Kamera: Symmetry S3 detector at the Department of Materials Science (Montanuniversität Leoben, Austria). The EBSD measurements were conducted with a 20 keV electron-beam. Scan parameters used a phase cubic standard and 500 nm step size in beam scanning mode. Grain dilatation clean-up was applied on the data, an iterative method which considers neighboring grains to reassign unidentified points (Edax 2022).

3.4 Atom probe tomography

3.4.1 FIB-SEM

Sample preparation for APT analyses was done using the general procedures set out in Thompson et al. (2007), as well as the procedures for site specific preparation of geologic materials set out in Gojon et al. (2019a). One 3 x 30 µm wedge-shaped liftout was taken from a Co-rich sphalerite from a sample from the cluster mineralization style. Sample preparation was done with a FEI Versa 3D Dual Focused Ion Beam FE-SEM equipped with a focused ion beam (FIB) and micromanipulator at the Department of Materials Science, Montanuniversität Leoben. The position of the lift-out location was chosen with great care, due to the intricate “network” feature that was identified during EPMA mapping (Supplementary Materials A). The liftout was targeted to include a portion of the low Fe/Co network as well as the ‘bulk’ high Co sphalerite. Ten needle shaped samples were prepared from slices from this one lift-out bar. Successful APT data was only attained from sample section M9 and M11 of the liftout.

3.4.2 APT

APT analyses were carried out using a CAMECA LEAP 5000 XR at the Department of Materials Science (Montanuniversität Leoben, Austria). Measurements were performed in laser assisted mode with a 355 nm UV laser. This instrument has a ~52 % ion detection efficiency and analysis conditions were as follows: stage temperature 50K; 125 Hz pulse frequency; 40-80pJ laser pulse energy; detection rate of 0.005 average ions per pulse. Initial run conditions were taken from the successful analysis of iron sulfide in Gojon et al. (2022a), and were further modified and improved based on how the previous needle shaped specimen ran/fractured. Two out of four samples fractured prior to the acquisition of a statistically meaningful number of ions. This fracture yield is comparable to the fracture yields reported in Fougereuse et al. (2016), Gojon et al. (2022a), and Gojon et al. (2019b), etc for similar sulfide minerals. Reconstruction of the APT datasets was conducted using the specimen-profile mode in the IVAS software (v3.8.12). Ranging the data was also done using the IVAS software, but the AtomProbeLab Matlab script (London 2019) was used

to calculate concentrations due to its improved complex peak overlap solver (compared to the IVAS software; see Gopon et al. 2022b for further details).

Spatial correlation graphs of the elements were generated using the ‘Local Chemistry’ function in the 3Depict software (Haley 2018) by using the “.pos” and range files generated in IVAS (see Gopon et al. 2019b for further details). The local correlation plots show the concentration of a specific element within a defined volume surrounding every ion of a pre-defined target element; e.g. the concentration of Zn surrounding each Co ion. We plot both as relative numbers, as this function does not allow the more rigorous overlap correction of London (2019). The relative, rather than the absolute, difference is the important point (i.e. that there is a shift in the peaks or not). In our case, we defined the ‘Local Chemistry’ as a 3 nm sphere surrounding each target ion. This analysis is conducted for both the actual dataset as well as the same dataset with the ion IDs randomly reassigned, in order to approximate that matrix composition, i.e. what the data should look like if the ions were completely randomly distributed. These plots show relative comparisons and are meant for investigating trends rather than absolute concentrations.

As the laser incident side of insulating materials tends to have higher count rates, the incident side appears to have a higher concentration of major elements (Gault et al. 2012). This had the effect of creating a double peak in our spatial correlation graphs for the major elements, one from each half of the data. This was most clear in the Zn and S APT data (Figure 2), which should not vary this drastically in a pure sphalerite sample. Because of this single-laser induced data artifact, the data was split into two regions of interests (ROIs), to be able to carry out spatial correlation analyses properly. Spatial correlation plots of these two ROIs showed the same trends, and thus using the ROIs was deemed more suitable than the complete APT dataset with the laser-induced artifacts (Supplementary Materials B). It should be noted that the ‘double peak’ shown in Figure 2 was only present when comparing the spatial correlation between minor and major elements, and no artifacts were observed when comparing minor to minor or minor to trace elements. However, for consistency sake the opposite-laser incident side ROI of all datasets were used for all spatial correlation plots.

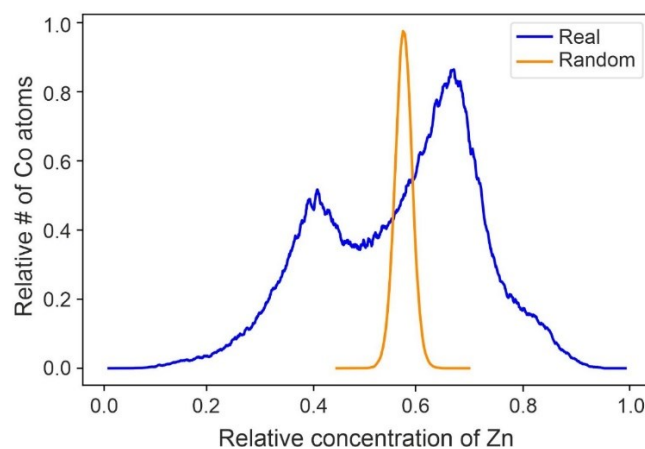


Figure 2. Spatial correlation plot of Zn ions surrounding Co ions from the full APT dataset. Two distinct peaks are visible, which is due to the varying Zn concentrations in the dataset consequent of the single-laser induced artifact.

4 Results

4.1 Petrographic observations

Point counting confirmed the relative abundance of the sulfides with 9.1 % pyrite, 5.3 % chalcopyrite, 1.0 % sphalerite, and 0.7 % linnaeite in the investigated polished section. Euhedral to subhedral linnaeite is predominantly found enveloped by Ore Stage 1 pyrite (Figure 3) and commonly rimmed by chalcopyrite within the host pyrite. Sphalerite contains abundant chalcopyrite inclusions. Sphalerite was noted to overgrow linnaeite in some areas (Figure 3). Both sphalerite and chalcopyrite can be seen overgrowing the host pyrite, but also occur disseminated within the stilpnomelane-ankerite-siderite host rock. There are rare occurrences where linnaeite occurs independently of pyrite within the host rock. The linnaeite in the cluster and nodule mineralization styles exhibits a crisscross-like texture, reminiscent of exsolution textures (Figure 3). This texture is not present in all of the DOF linnaeite, e.g. from the vein-like “DOF event” mineralization style (Bertrandsson Erlandsson et al. 2022). Accessory cobaltite can be seen in the vicinity and overgrowing some of the linnaeite crystals. The entire polysulfide cluster appears “fractured” with sulfide aggregates and pieces being dispersed into the host rock matrix. Sphalerite and chalcopyrite within the larger clusters seem to be aligned with the host rock schistosity, i.e. in the direction in which the cluster minerals are fractured. Disseminated chalcopyrite can be seen following and wrapping around the ripped-apart pyrite aggregates. Euhedral siderite within the host pyrite cluster was previously described by Bertrandsson Erlandsson et al. (2022), but more detailed petrography shows sphalerite and chalcopyrite overgrowing and around euhedral siderite crystals.

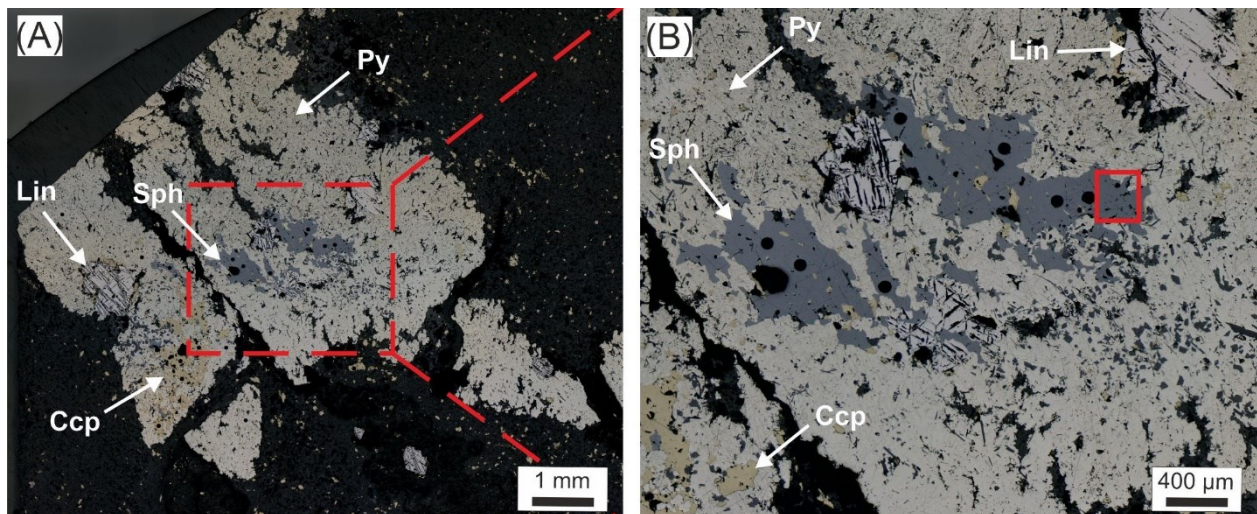


Figure 3. Reflective light micrographs of the cluster mineralization style of the DOF containing the Co-rich sphalerite investigated in this study. (A) Overview micrograph of the cluster mineralization. (B) Close up micrograph with a solid red square indicating the targeted area investigated within this study. Shown here is also the sphalerite clearly replacing pyrite and linnaeite. Round black holes in the sphalerite are laser ablation pits.

4.2 Micron-scaled element distribution in DOF sphalerite

Element maps by EPMA of Co-rich sphalerite show homogeneously distributed elements (S, Fe, Co, Ni, Cu, Zn, and Cd) within individual sphalerite crystals, however a network enriched in Zn and deficient in Fe and Co was observed between the crystals (Figure 4). To save space Figure 4 shows

only the Fe, Zn, and Co signals; all other elements (S, Ni, Cu, and Cd) are shown in Supplementary Materials C. Higher concentrations of Fe can be seen dotting the high Zn network (Figure 4), these Fe spots correlate with Cu (Supplementary Materials C) and represent chalcopyrite inclusions in the sphalerite. The sample liftout area is free from visible chalcopyrite inclusions. The other measured elements show no obvious compositional difference between the sphalerite crystals and the high Zn network (Supplementary Materials C). EBSD mapping reveals several sub-grains and sub-grain boundaries within the sphalerite crystal (Figure 4) that correlate well with the high Zn network identified in the EPMA element maps. These sub-grains show moderate misorientation angles to each other with the bulk of the sphalerite crystals having similar orientation angles, with a low degree of misorientation between them.

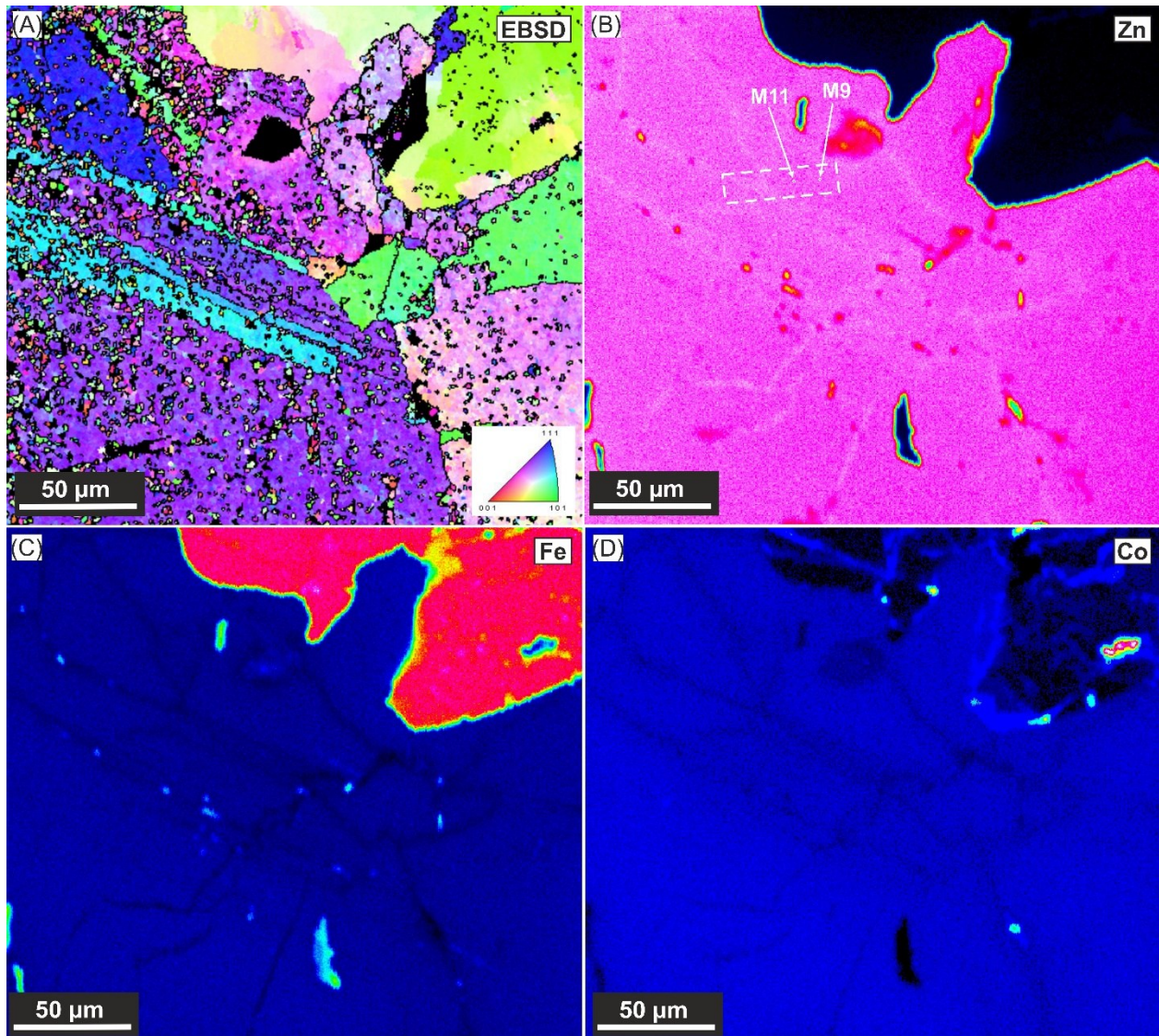


Figure 4. SEM-EBSD grain misorientation map over the investigated area (A). EPMA element maps of the same area as A, showing Zn, Fe, and Co distributions (B – D respectively). Position of the two successful APT samples are marked out in (B), within dashed lines making the liftout bar.

4.3 Atom-scale element distribution in DOF sphalerite

Four needle-shaped specimens were prepared from the Co-rich sphalerite, of which two APT data sets were successfully obtained (see Supplementary Materials D for a mass spectra example). The APT needle shaped sample reconstruction obtained from the Co-rich sphalerite shows homogeneously distributed S, Zn, Mn, Fe, Co, and Cd, with no visible evidence for nano-inclusions (Figure 5). AtomProbeLab Matlab script calculations yielded a sphalerite trace element composition of 4.3 at% Fe, 0.70 at% Co, 179 ppm Mn, 103 ppm Cd, 44 ppm Se, and 35 ppm In (Supplementary Materials E).

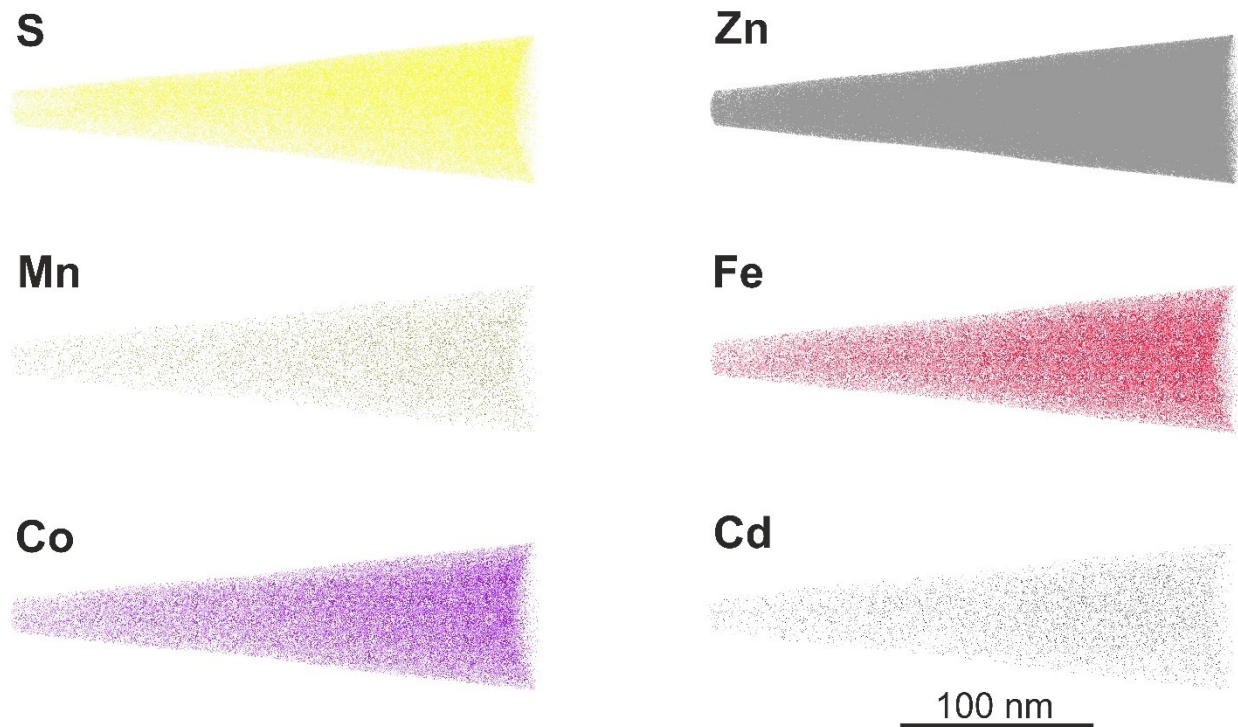


Figure 5. APT data reconstruction of Co-rich sphalerite needle shaped specimens, showing S, Zn, Mn, Fe, Co and Cd ions.

The spatial ion correlation analyses of local concentrations of Zn ions around Co, Fe, Mn, and Cd ions show that the real data curves have a shift to the left of the randomized data showing an anticorrelation between the minor and trace elements and Zn (Figure 6). As a reminder these spatial correlation plots show the relative concentrations of a specific element in a predefined volume (here 3nm sphere) surrounding a target element. These are plotted as normalized and smoothed lines where each point on the line is the relative number of target ions that occurs at a specific concentration of the specified element. This analysis is then repeated for a randomized version of the same data to approximate the matrix compositions/distribution if the target and specified element were randomly distributed (see Methods section 3.4.2 for further details). An anticorrelation between the target and specified element can then be inferred when the real data curve is shifted to the left of the randomized data curve. The shift to the left of the real vs randomized data with Zn as the target ion implies that there is less Zn surrounding the other ion, than if all ions were randomly distributed. If ions were randomly distributed, there would be no link between the compared ions in regards to element incorporation and substitution (e.g. for Co

and In. Figure 7D). A positive correlation (real data curve shifted to the right of the randomized curve), would imply that, in this example, there is an increased amount of Zn surrounding another ion. Hence, there is more Zn where there is more e.g. Co, compared to randomly distributed elements. Spatial ion correlation plots of Fe, Mn, Cd and In surrounded by Co were also made to look at the relationship between Co and the other minor and trace elements (Figure 7). The real data curves of Fe, Mn, and Cd show a shift to the left compared to the randomized data, indicating an anticorrelation between these elements and Co. The real data curve of In does not show notable shift compared to the randomized data curve, indicating that In is distributed randomly in relation to Co.

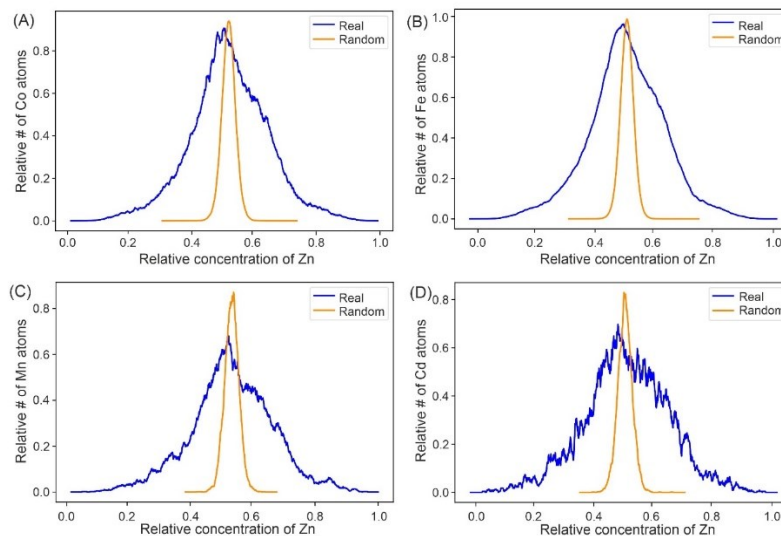


Figure 6. Local concentration of Zn surrounding Co, Fe, Mn, and Cd ions (A-D respectively), the most abundant minor and trace elements. Y-axis shows the relative number of Co, Fe, Mn, and Cd ions that are surrounded by a relative concentration of Zn.

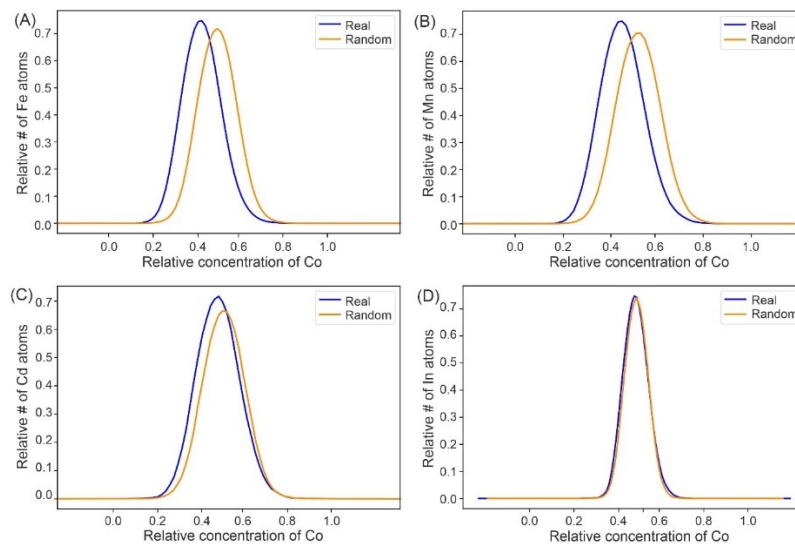


Figure 7. Local concentration of Co surrounding each Fe, Mn, Cd, and In ions (A-D respectively). Y-axis shows the relative number of Fe, Mn, Cd, and In ions that are surrounded by a relative concentration of Co.

5 Discussion

5.1 Local mobilization and redistribution of cobalt in the DOF mineralization

In the DOF mineralization, linnaeite is present as a stoichiometric Co-phase; in addition, associated sulfides also contain elevated concentrations of Co (Bertrandsson Erlandsson et al. 2022). It is considered crucial to understand the reason for the widespread Co-enrichment in sphalerite, and why Co is not just hosted in the linnaeite. Detailed petrographic observations and interpretations reveal a refined paragenetic sequence of the Co-bearing sulfides in the DOF deposit. Multiple hydrothermal stages lead to a complex Co mobilization and redistribution from earlier sulfides to newly formed sulfides, through a range of physicochemical changes.

5.1.1 Oxidizing conditions as prerequisites for linnaeite formation in the sediment-hosted DOF deposit

Based on petrographic and mineral-chemical investigation, the Cu and Zn, that is associated with the main Co stage, postdates the linnaeite in Ore Stage one, as sphalerite is seen overgrowing the linnaeite (Figure 3). As chalcopyrite partly occurs as rims around euhedral linnaeite, and intergrown with sphalerite, it is reasonable to conclude that the main Co stage Cu and Zn mineralization occurred later than the formation of linnaeite. This main Co stage was previously subdivided into two sub-stages (Co stage and Cu-Zn stage) by Bertrandsson Erlandsson et al. (2022) based on the crosscutting relationship of the sphalerite/chalcopyrite and linnaeite. However, further petrographic investigation shows three stages (Co-bearing pyrite, linnaeite growth, formation of Co-bearing sphalerite/chalcopyrite). The timing of linnaeite formation was still unclear, but is addressed in this study with better petrographic evidence. Hydrothermal alteration of other magmatic sulfides such as pyrrhotite-pentlandite-chalcopyrite by lower temperature fluids (e.g. 150 – 200 °C) has been shown to result in replacement and formation of a pyrite-millerite-chalcopyrite assemblage (Holwell et al. 2017). Cobalt and nickel have been shown to act similarly during hydrothermal alteration of magmatic minerals (Tuba et al. 2014), and thus it can be assumed that replacement processes could form Co-phases (e.g. linnaeite) in much the same way that Ni-phases (pentlandite) can form from the breakdown of pyrite and millerite (Holwell et al. (2017). Furthermore, it has been shown that linnaeite can form at low temperatures (< 150 °C) through replacement of preexisting cobaltpentlandite (Co,Ni)₉S₈, (Xia et al. 2008).

Our petrographic observations combined with the experimental evidence, suggest that the original DOF Co mineralization formed Co-rich pyrite (Ore Stage one). This pyrite is seen enveloping most of the linnaeite crystals (Figure 3), and it appears that the linnaeite grew at the expense of the Co-rich pyrite. The remobilizing of Co from Co-rich pyrite into linnaeite most likely happened during the greenschist facies overprinting that affected the DOF mineralization (Ore Stage two; Bertrandsson Erlandsson et al. 2022). As 66 % of the Co occurs as Co³⁺ in linnaeite (Co²⁺Co³⁺₂S₄), the physiochemical conditions of Ore Stage two must have been more oxidizing than in Ore Stage one where Co is most likely present as Co²⁺ in pyrite. The presence of euhedral siderite within and around the host pyrite cluster, and associated nodule mineralization style (Bertrandsson Erlandsson et al. 2022) points towards an additional decrease in fS₂, as fS₂ has been shown to be the major reason for pyrite → siderite transformation (Qiu et al. 2021). Diagenetic siderite formation after sedimentary framboidal pyrite has also been described by McKay et al. (1995) due to either the influx of oxidized meteoric water or bicarbonate formation

as a result of sulfate reduction related to the framboidal pyrite formation on the expense of organic carbon. The carbonate production may also have formed during methanogenesis of organic matter during continued burial to the methanogenic zone (McKay et al. 1995), which is an oxidizing process that would tie in with the formation of the DOF linnaeite. Hence, the hydrothermal fluid responsible for the linnaeite, and siderite, formation of Ore Stage two must have been oxidizing.

5.1.2 Formation of cobalt-rich sphalerite and associated accessory cobalt-phases

The linnaeite often appears “eaten up”, and in the vicinity of linnaeite sphalerite (and chalcopyrite) are present, suggesting that linnaeite was no longer stable and started breaking down. During breakdown, the Co moved into sphalerite that was growing by the partial replacement of pyrite and linnaeite and influx of Cu and Zn (Ore Stage three). The decomposition of linnaeite is also supported by the presence of cobaltpentlandite inclusions within the host pyrite and accessory subhedral cobaltite overgrowing linnaeite (Results 4.1 & Bertrandsson Erlandsson et al. 2022). Thermodynamic stability modeling of Co-S-O and Co-S-O-As has demonstrated that decreasing fS_2 and/or fO_2 conditions will result in the transformation of linnaeite → cobaltpentlandite → cobaltite (Vasyukova and Williams-Jones 2022; Williams-Jones and Vasyukova 2022). As sphalerite and chalcopyrite formed during the decomposition of linnaeite, i.e. elevated rather than decreased fS_2 , it is more likely that a decrease in fO_2 is responsible for breakdown of linnaeite and the subsequent formation of sphalerite, chalcopyrite, cobaltpentlandite and cobaltite.

In our interpretation, the pyrite was the original host of Co, and the sphalerite (along with accessory cobaltite) being the ultimate Co sink. With linnaeite and cobaltpentlandite being a transitional ore stage that was only stable during a brief portion of the deposits P/T/t history (Figure 9), due to their decomposition. It is worth noting that pre-Co(-Cu-Zn) mineralization sedimentary-diagenetic pyrite has been reported to contain median 698 $\mu\text{g/g}$ Co (Bertrandsson Erlandsson et al. 2022), showing that Co was relatively abundant in all stages of sulfide-growth of the DOF deposit.

In summary, our proposed paragenetic sequence for the DOF mineralization is as follows:

- 1) Hydrothermal Co-bearing pyrite formed first (Ore Stage one).
- 2) The Co-bearing pyrite was later oxidized with Co remobilized to form linnaeite (and siderite; Ore Stage two).
- 3) A decrease in fO_2 led to the growth of cobaltpentlandite within the pyrite and eventually resulted in the formation of cobaltite, with sphalerite and chalcopyrite forming sometime during this last stage (Ore Stage three).

	Main Co-Cu-Zn ore-forming stage			Cu-Zn ore-stage Ore Stage 4
	Ore Stage 1	Ore Stage 2	Ore Stage 3	
Pyrite	██████████			██████████
Linnaeite		██████████		
Siderite		██████████		
Cobaltpentlandite		██████████		
Sphalerite		·· ████████ ··		██████████
Chalcopyrite		·· ████████ ··		██████████
Cobaltite			██████████	

Figure 8. Revised paragenetic sequence of the main Co(-Cu-Zn) ore-forming stage of the DOF deposit, along with the later, secondary Cu-Zn stage (modified after Bertrandsson Erlandsson et al., 2022). See text for more detailed description of the physiochemical conditions of each stage.

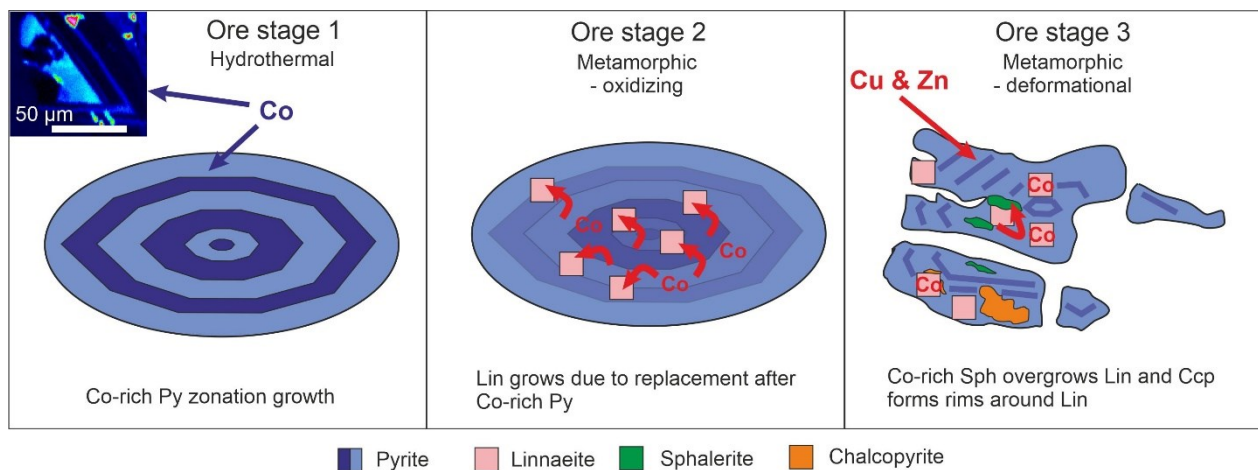


Figure 9. Schematic reconstruction of Co mobilization and redistribution between sulfides during the main Co(-Cu-Zn) DOF mineralization (Ore Stages 1-3), based on the polysulfide cluster mineralization of this study. The hydrothermal Ore Stage 1 introduced the majority of the Co in pyrite (indicated by blue shades in the figure), as seen in the inset EPMA Co map. Ore Stage 2 is defined by a change in redox state of the mineralizing system to more oxidized conditions, resulting in pyrite-hosted Co^{2+} to oxidize to Co^{3+} , and leading to the formation of linnaeite. The brittle deformational Ore Stage 3 saw redox states returning to Co^{2+} , which enabled the incorporation of Co in newly formed sphalerite. Schematic is based of the DOF cluster mineralization style seen in Figure 3. Abbreviations: Py = pyrite, Lin = linnaeite, Sph = sphalerite, Ccp = chalcopyrite.

5.2 Incorporation and substitution of cobalt, and other trace elements, in cobalt-rich sphalerite

As the Zn-rich network-feature revealed by the EPMA mapping correlates well with the sub-grains of the EBSD map (Figure 4), we interpreted this to be Zn-enriched and Co/Fe-deficient sub-grain boundaries. Due to the smooth count-time resolved LA-ICP-MS signals in sphalerite it is believed that the Co does not occur as large micro-inclusions of Co-bearing phases within the sphalerite, but either through substitution in the sphalerite crystal matrix or as nano-inclusions

(Bertrandsson Erlandsson et al. 2022). To differentiate between micro- / nano-inclusions or lattice bound Co, we need to look at the atomic-scale elemental distribution with the aid of an atom probe.

In order to elucidate the incorporation mechanism of Co into sphalerite (nano-inclusion or lattice bound) we applied atomic scale spatial correlation analyses of the elements in our APT datasets. The shift of the “real” curves in Figure 7 to lower concentrations compared to the randomized data, for Co, Fe, Mn, and Cd (Figure 6) to Zn, indicate that these elements have an anti-correlation with Zn. This is evidence for simple substitution of Zn by Co, Fe, Mn, and Cd in the DOF sphalerite. The anti-correlation between Fe, Mn, and Cd to Co (Figure 7) further supports that coupled substitution of Co with Fe, Mn, or Cd is not responsible for the elevated Co concentrations in the DOF sphalerite. Instead, all correlation plots indicate simple Co-Zn substitution as a viable mechanism to incorporate the high Co concentrations observed in the DOF sphalerite. Indium and Co show no shift and are therefore interpreted to occur independent of each other within the DOF sphalerite (Figure 7).

Our atomic scale observations of the incorporation of Co into sphalerite is in keeping with the expected incorporation mechanism based off the Goldschmidt Rules (Goldschmidt 1954). Ionic radius and charge of Zn^{2+} (0.60 Å) means that several similar sized 2+ ions would be expected to substitute for Zn in sphalerite (ZnS). Manganese²⁺ (0.66 Å), Fe²⁺ (0.63 Å), Co²⁺ (0.58 Å), and Cu²⁺ (0.57 Å) (Shannon 1976) all fall within the $\pm 15\%$ atomic radius “window” that support simple element substitution (Goldschmidt 1954). As Fe may commonly occur in wt% concentrations in sphalerite (e.g. Frenzel et al. 2016; Cook et al. 2009), where $\text{Zn}^{2+} \leftrightarrow \text{Fe}^{2+}$, so it might be expected that Co concentrations in sphalerite might be similarly high, if not higher. Experimental work by Becker and Lutz (1978) and Niu et al. (1990) showed that sphalerite-structured crystals can contain up to 40 mol% and 36.4 at% Co respectively at high temperatures. That the DOF sphalerite have the highest Co concentrations ever measured in natural samples (1.06 wt%), is therefore puzzling, as both the theory and the direct observation indicate that the incorporation of Co into sphalerite is not special, and that based on experiments and comparison with high Fe sphalerite, we should therefore expect to see Co concentrations in natural sphalerite regularly above the measured maximum. Possible explanations might be that in the experimentally grown sphalerite with >30 wt% Co, a different incorporation mechanism might be at play (possibly nano-inclusions), or that the concentration of Co is seldom high enough to warrant any phase to have higher than $\sim 1\%$ Co.

5.2.1 Sub-grain boundary formation and element remobilization

The majority of the sub-grain boundaries in the Co-rich sphalerite (Figure 4) broadly align with the foliation within the host rock as well the sense of fracture direction of the sulfide clusters. This suggests that these sub-grain boundaries formed during a later deformation event. The Co-poor sphalerite from DOF Ore Stage 4 is believed to have formed during this later deformational stage and aligns with the Co-poor sub-grain boundaries (Figure 4). It is interesting that the major element (Zn), rather than the trace/minor elements, is preferentially segregated to the sub-grain boundaries. This retention of trace elements and expulsion of the stoichiometric element is in contrast to the generally observed pattern of trace elements being segregated on grain boundaries that is commonly observed in silicates and sulfides (Gopon et al. 2022b; Fougereuse

et al. 2021; Cugerone et al. 2020; Dubosq et al. 2019; Fougrouse et al. 2019; Gopon et al. 2018; Marquardt and Faul 2018; etc.) and warrants further investigation. Cobalt in pyrite (incorporated through simple substitution) has been shown to be preferentially retained during metamorphic overprints compared to trace elements incorporated through coupled substitution (e.g. Conn et al. 2019; Huston et al. 2016; Large et al. 2007). While this might explain the retention of Co in sphalerite, it still does not explain the expulsion of the stoichiometric element (Zn).

6 Conclusions

Detailed petrographic observations have led to an updated paragenesis of the main Co(-Cu-Zn) ore stage of the DOF deposit, where three discrete stages are proposed (Ore Stage 1-3). Initial Co-rich pyrite clusters and nodules formed during Ore Stage one, forming the host for much of the later sulfides. The oxidizing properties of the hydrothermal fluid responsible for Ore Stage two resulted in the formation of linnaeite ($\text{Co}^{2+}\text{Co}^{3+}_2\text{S}_4$) by neocrystallization within the host pyrite. Lower $f\text{O}_2$ conditions later resulted in the transformation of linnaeite and pyrite into cobaltpentlandite \rightarrow cobaltite along with the formation of the Co-rich sphalerite and chalcopyrite. This portrays the local mobilization and redistribution of Co, from initial pyrite into the hyper-enriched Co-sphalerite that is unique of the DOF deposit.

EPMA and EBSD analyses revealed a sub-grain boundary network within the Co-rich sphalerite of Ore Stage three, which is depleted in both Fe and Co, and elevated in Zn compared to the bulk sphalerite sub-grains. These sub-grain boundaries are suggested to have formed during later deformation (Ore Stage four). This ore stage is responsible for the formation of a secondary Cu-Zn(-Pb) mineralization, barren of Co, expressed as pressure shadow and vein mineralization within the DOF deposit. The sphalerite from Ore Stage four is likewise poor in both Fe and Co, compared to the sphalerite of Ore Stage three.

The APT reconstructions of the needle-shaped specimens revealed Co to be homogeneously distributed within the Co-rich sphalerite sample, with no visually or statistically detectable micro- or nano-scaled Co-inclusions or clusters. Atomic scale spatial correlation analyses of the individual ions showed a negative correlation between Zn to both Fe and Co, suggesting that both elements occur in the sphalerite through substitution of Zn. Additional atomic spatial correlation analyses indicated a negative correlation between Fe and Co, indicating that these two elements occur independent of each other and thus represent simple substitution in the sphalerite crystal lattice. This study demonstrates the potential of natural sphalerite to easily incorporate significant quantities of Co, making it a potentially important unconventional source for Co and other critical metals.

Acknowledgments

The authors would like to thank the following: Maik Zimmermann, for allowing to use the electron microprobe laboratory of the Chair of Resource Mineralogy at the Montanuniversität Leoben and his time and effort in attaining the EPMA maps; Florian Altenberger, for the constructive discussions on writing and article publication; and Gerhard Hawranek, for help with the EBSD measurements. Thank you as well to Denis Fougrouse and Nigel John Cook for their helpful and constructive comments, which greatly improved the manuscript.

Supplementary material

The Supplementary Material for this article can be found online at:

<https://www.frontiersin.org/articles/10.3389/feart.2023.1171859/full#supplementary-material>

References

Allen, N. K. (2016): Structurally controlled Cu-Zn-(Co-Pb) mineralization in the Neoproterozoic Ombombo Subgroup, Kaokoland, Namibia. Master Thesis. Colorado School of Mines.

Alves Dias, Patricia; Blagoeva, Darina; Pavel, Claudiu; Arvanitidis, Nikolaos (2018): Cobalt: demand-supply balances in the transition to electric mobility. In Publications Office of the European Union 10, p. 97710.

Becker, W.; Lutz, H. D. (1978): Phase studies in the systems CoS₁bMnS, CoS₁bZnS, and CoS₁bCdS. In *Materials Research Bulletin* 13 (9), pp. 907–911.

Bertrandsson Erlandsson, Viktor; Wallner, Daniela; Ellmies, Rainer; Raith, Johann G.; Melcher, Frank (2022): Trace element composition of base metal sulfides from the sediment-hosted Dolostone Ore Formation (DOF) Cu-Co deposit in northwestern Namibia: Implications for ore genesis. In *Journal of Geochemical Exploration*, p. 107105.

Bonnet, Julien; Mosser-Ruck, Régine; Caumon, Marie-Camille; Rouer, Olivier; Andre-Mayer, Anne-Sylvie; Cauzid, Jean; Peiffert, Chantal (2016): Trace element distribution (Cu, Ga, Ge, Cd, and Fe) in sphalerite from the Tennessee MVT deposits, USA, by combined EMPA, LA-ICP-MS, Raman Spectroscopy, and crystallography. In *The Canadian Mineralogist* 54 (5), pp. 1261–1284.

Conn, C. D.; Spry, P. G.; Layton-Matthews, D.; Voinot, A.; Koenig, A. (2019): The effects of amphibolite facies metamorphism on the trace element composition of pyrite and pyrrhotite in the Cambrian Nairne Pyrite Member, Kanmantoo Group, South Australia. In *Ore Geology Reviews* (114), p. 103128.

Cook, N. J.; Ciobanu, C. L.; Pring, A.; Skinner, W.; Shimizu, M.; Danyushevsky, L. V. et al. (2009): Trace and minor elements in sphalerite: A LA-ICPMS study. In *Geochimica et Cosmochimica Acta* (73), Article 16, pp. 4761–4791.

Cugerone, Alexandre; Cenki-Tok, Bénédicte; Oliot, Emilien; Muñoz, Manuel; Barou, Fabrice; Motto-Ros, Vincent; Le Goff, Elisabeth (2020): Redistribution of germanium during dynamic recrystallization of sphalerite. In *Geology* 48 (3), pp. 236–241.

Dubosq, Renelle; Rogowitz, Anna; Schweinar, Kevin; Gault, Baptiste; Schneider, David A. (2019): A 2D and 3D nanostructural study of naturally deformed pyrite: assessing the links between trace element mobility and defect structures. In *Contributions to Mineralogy and Petrology* 174 (9), p. 72.

Edax (2022): Edax OIM Software Help.

European Commission (2020): Communication from the Commission to the European Parliament, the Council, the Economic and Social Committee and the Committee of the Regions. Critical Raw Materials Resilience: Charting a Path towards greater Security and Sustainability. Edited by European Commission. Brussels, Belgium.

Foltyn, K.; Erlandsson, V. B.; Kozub-Budzyń, G. A.; Melcher, F.; Piestrzyński, A. (2020): Indium in polymetallic mineralisation at the Gierczyn mine, Karkonosze-Izera Massif, Poland: results of EPMA and LA-ICP-MS investigations. In *Geological Quarterly* (64), Article 1, 000-000.

Foster, D. A.; Goscombe, B. D.; Gray, D. R. (2009): Rapid exhumation of deep crust in an obliquely convergent orogen: The Kaoko Belt of the Damara Orogen. In *Tectonics* (28), Article 4, 1-24.

Fougereuse, Denis; Cugerone, Alexandre; Reddy, Steven M.; Luo, Kai; Motto-Ros, Vincent (2023): Nanoscale distribution of Ge in Cu-rich sphalerite. In *Geochimica et Cosmochimica Acta*.

Fougereuse, Denis; Reddy, Steven M.; Aylmore, Mark; Yang, Lin; Guagliardo, Paul; Saxey, David W. et al. (2021): A new kind of invisible gold in pyrite hosted in deformation-related dislocations. In *Geology* 49 (10), pp. 1225–1229.

Fougerouse, Denis; Reddy, Steven M.; Kirkland, Christopher L.; Saxey, David W.; Rickard, William D.; Hough, Robert M. (2019): Time-resolved, defect-hosted, trace element mobility in deformed Witwatersrand pyrite. In *Geoscience Frontiers* 10 (1), pp. 55–63.

Fougerouse, Denis; Reddy, Steven M.; Saxey, David W.; Rickard, William D. A.; van Riessen, Arie; Micklethwaite, Steven (2016): Nanoscale gold clusters in arsenopyrite controlled by growth rate not concentration: Evidence from atom probe microscopy. In *American Mineralogist* 101 (8), pp. 1916–1919.

Frenzel, M.; Hirsch, T.; Gutzmer, J. (2016): Gallium, germanium, indium, and other trace and minor elements in sphalerite as a function of deposit type—A meta-analysis. In *Ore Geology Reviews* (76), pp. 52–78.

Gault, Baptiste; Moody, Michael P.; Cairney, Julie M.; Ringer, Simon P. (2012): *Atom probe microscopy*: Springer Science & Business Media.

Goldschmidt, Victor Moritz (1954): *Geochemistry*: LWW (2).

Gopon, P.; Douglas, J. O.; Wade, J.; Moody, M. P. (2019a): Complementary SEM-EDS/FIB-SEM sample preparation techniques for atom probe tomography of nanophase-FeO in apollo 16 regolith sample 61501, 22. In *Microscopy and Microanalysis* 25 (S2), pp. 2544–2545.

Gopon, P.; Douglas, James O.; Auger, Maria A.; Hansen, Lars; Wade, Jon; Cline, Jean S. et al. (2019b): A nanoscale investigation of Carlin-type gold deposits: An atom-scale elemental and isotopic perspective. In *Economic Geology* 114 (6), pp. 1123–1133.

Gopon, P.; Douglas, James O.; Meisenkothen, Frederick; Singh, Jaspreet; London, Andrew J.; Moody, Michael P. (2022a): Atom probe tomography for isotopic analysis: development of the 34S/32S system in sulfides. In *Microscopy and Microanalysis* (28(4)), 1127-1140.

Gopon, P.; Forshaw, J.; Waters, D.; & Wade, J. (Eds.) (2018): Pyroxene thermometry on single crystals of the Lewisian Complex, Scotland. EGU General Assembly Conference Abstracts.

Gopon, Phillip; Forshaw, Jacob B.; Wade, Jon; Waters, David J.; Gopon, Christine (2022b): Seeing through metamorphic overprints in Archean granulites: Combined high-resolution thermometry and phase equilibrium modeling of the Lewisian Complex, Scotland. In *American Mineralogist* 107 (8), pp. 1487–1500.

Goscombe, B. D.; Foster, D. A.; Gray, D. R.; Wade, B. (2017): Metamorphic response and crustal architecture in a classic collisional orogen: The Damara Belt, Namibia. In *Gondwana Research* (52), pp. 80–124.

Goscombe, B. D.; Gray, D. R.; Hand, M. (2005): Extrusional Tectonics in the Core of a Transpressional Orogen; the Kaoko Belt, Namibia. In *Journal of Petrology* (46), Article 6, pp. 1203–1241.

Goscombe, B. D.; Hand, M.; Gray, D. R. (2003): Structure of the Kaoko Belt, Namibia: progressive evolution of a classic transpressional orogen. In *Journal of Structural Geology* (25), Article 7, pp. 1049–1081.

Guj, P. (1970): *The Damara Mobile Belt in the south-western Kaokoveld South West Africa*. PhD Thesis. University of Cape Town / Precambrian Research Unit, Cape Town, South Africa.

Haley, D. (2018): 3Depict: Valued Point Cloud Visualisation and Analysis Software. Available online at <http://threedepict.sourceforge.net/>.

Hoffman, P. F. (2011): Glaciogenic and associated strata of the Otavi carbonate platform and foreslope, northern Namibia: evidence for large base-level and glacioeustatic changes. In G. Shields-Zhou, G. P. Halverson, E. Arnaud (Eds.): *The Geological Record of Neoproterozoic Glaciations*. 36th ed. London: Geological Society of London.

Hoffman, P. F.; Halverson, G. P. (2008): Otavi Group of the western Northern Platform, the Eastern Kaoko Zone and the western Northern Margin Zone. In R. McG. Miller (Ed.): *The Geology of Namibia: Neoproterozoic to Lower Palaeozoic*. 2nd ed. Windhoek, Namibia: Geological Survey (2), 13-69–13-136.

Hoffmann, K.-H.; Prave, A. R. (1996): A preliminary note on a revised subdivision and regional correlation of the Otavi Group based on glaciogenic diamictites and associated cap dolostones. In *Communications of the geological survey of Namibia* (11), pp. 77–82.

Holwell, David A.; Adeyemi, Zeinab; Ward, Laura A.; Smith, Daniel J.; Graham, Shaun D.; McDonald, Iain; Smith, Jennifer W. (2017): Low temperature alteration of magmatic Ni-Cu-PGE sulfides as a source for hydrothermal Ni and PGE ores: A quantitative approach using automated mineralogy. In *Ore Geology Reviews* 91, pp. 718–740.

Huston, D. L.; Mernagh, T. P.; Hagemann, S. G.; Doublier, M. P.; Fiorentini, M.; Champion, D. C. et al. (2016): Tectono-metallogenic systems - The place of mineral systems within tectonic evolution, with an emphasis on Australian examples. In *Ore Geology Reviews* (76), pp. 168–210.

Intiomale, M. M.; Oosterbosch, R. (1974): Géologie et géochimie du gisement de Kipushi, Zaïre. In *Annales de la Société géologique de Belgique*.

Large, R. R.; Maslennikov, V. V.; Robert, F.; Danyushevsky, L. V.; Chang, Z. (2007): Multistage sedimentary and metamorphic origin of pyrite and gold in the giant Sukhoi Log deposit, Lena gold province, Russia. In *Economic Geology* (102), Article 7, pp. 1233–1267.

Liu, K.; Cugerone, Alexandre; Zhou, Mei-Fu; Zhou, Jia-Xi; Sun, Guo-Tao; Xu, Jing et al. (2022): Germanium enrichment in sphalerite with acicular and euhedral textures: an example from the Zhulingou carbonate-hosted Zn (-Ge) deposit, South China. In *Mineralium Deposita*, pp. 1–23.

Lockington, J. A.; Cook, N. J.; Ciobanu, C. L. (2014): Trace and minor elements in sphalerite from metamorphosed sulphide deposits. In *Mineralogy and Petrology* (108), Article 6, pp. 873–890.

London, Andrew J. (2019): Quantifying uncertainty from mass-peak overlaps in atom probe microscopy. In *Microscopy and Microanalysis* 25 (2), pp. 378–388.

Marquardt, Katharina; Faul, U. H. (2018): The structure and composition of olivine grain boundaries: 40 years of studies, status and current developments. In *Physics and Chemistry of Minerals* 45 (2), pp. 139–172.

Marsh, Erin E.; Hitzman, Murray W.; Leach, David L. (2016): Critical elements in sediment-hosted deposits (clastic-dominated Zn-Pb-Ag, Mississippi Valley-type Zn-Pb, sedimentary rock-hosted Stratiform Cu, and carbonate-hosted Polymetallic Deposits): A review.

McKay, J. L.; Longstaffe, F. J.; Plint, AG (1995): Early diagenesis and its relationship to depositional environment and relative sea-level fluctuations (Upper Cretaceous Marshybank Formation, Alberta and British Columbia). In *Sedimentology* 42 (1), pp. 161–190.

Miller, R. McG. (Ed.) (2008): *The Geology of Namibia: Neoproterozoic to Lower Palaeozoic*. 2nd ed. Windhoek, Namibia: Geological Survey (2).

Murakami, H.; Ishihara, S. (2013): Trace elements of Indium-bearing sphalerite from tin-polymetallic deposits in Bolivia, China and Japan: A femto-second LA-ICPMS study. In *Ore Geology Reviews* (53), pp. 223–243.

Niu, C. M.; Kershaw, R.; Dwight, K.; Wold, A. (1990): The preparation and properties of cobalt-doped II–VI chalcogenides. In *Journal of Solid State Chemistry* 85 (2), pp. 262–269.

Porada, H. (1989): Pan-African rifting and orogenesis in southern to equatorial Africa and eastern Brazil. In *Precambrian Research* (44), Article 2, pp. 103–136.

Qiu, Zheng-Jie; Fan, Hong-Rui; Goldfarb, Richard; Tomkins, Andrew G.; Yang, Kui-Feng; Li, Xiao-Chun et al. (2021): Cobalt concentration in a sulfidic sea and mobilization during orogenesis: Implications for targeting epigenetic sediment-hosted Cu-Co deposits. In *Geochimica et Cosmochimica Acta* 305, pp. 1–18.

Shannon, R. D. (1976): Revised effective ionic radii and systematic studies of interatomic distances in halides and chalcogenides. In *Acta crystallographica section A: crystal physics, diffraction, theoretical and general crystallography* 32 (5), pp. 751–767.

Thompson, K.; Lawrence, D.; Larson, D. J.; Olson, J. D.; Kelly, T. F.; Gorman, B. (2007): In situ site-specific specimen preparation for atom probe tomography. In *Ultramicroscopy* 107 (2-3), pp. 131–139.

Tuba, Györgyi; Molnár, Ferenc; Ames, Doreen E.; Péntek, Attila; Watkinson, David H.; Jones, Peter C. (2014): Multi-stage hydrothermal processes involved in “low-sulfide” Cu (-Ni)-PGE mineralization in the

footwall of the Sudbury Igneous Complex (Canada): Amy Lake PGE zone, East Range. In *Mineralium Deposita* 49 (1), pp. 7–47.

USGS (2020): Mineral commodity summaries 2020. DOI: 10.3133/mcs2020.

USGS (2022): 2022 Final List of Critical Minerals. Notices. Vol. 87, No. 37. U.S. Geological Survey, Department of the Interior.

Vasyukova, O. V.; Williams-Jones, A. E. (2022): Constraints on the Genesis of Cobalt Deposits: Part II. Applications to Natural Systems. In *Economic Geology* 117 (3), pp. 529–544.

Williams-Jones, A. E.; Vasyukova, O. V. (2022): Constraints on the Genesis of Cobalt Deposits: Part I. Theoretical Considerations. In *Economic Geology* 117 (3), pp. 513–528.

Xia, Fang; Zhou, Jinwen; Brugger, Joël; Ngothai, Yung; O’Neill, Brian; Chen, Guorong; Pring, Allan (2008): Novel route to synthesize complex metal sulfides: hydrothermal coupled dissolution–reprecipitation replacement reactions. In *Chem. Mater.* 20 (8), pp. 2809–2817.

4. Part 2 – Holistic perspectives of the Dolostone Ore Formation deposit to other sediment-hosted Cu(-Co) deposits

Publication III

Sulfide geochemistry in sediment-hosted Cu(-Co) metallogenic districts: LA-ICP-MS analyses of chalcopyrite, sphalerite, and pyrite

Viktor Bertrandsson Erlandsson¹, Krzysztof Foltyn², Philippe Muchez³, Gerd Rantitsch¹, Rainer Ellmies⁴, Frank Melcher¹

¹Montanuniversität Leoben, Department of Applied Geosciences and Geophysics, Peter-Tunner-Straße 5, 8700 Leoben, Austria

²AGH University of Science and Technology, Faculty of Geology, Geophysics and Environmental Protection, Krakow, Poland

³KU Leuven, Department of Earth and Environmental Sciences, Leuven, Belgium

⁴Gecko Namibia, Swakopmund, Namibia

Mineralium Deposita, in review (submitted on 2023-05-19) MIDE-D-23-00105

The publication version in this thesis is the latest version, which currently is being reviewed.

Abstract

Stratiform sediment-hosted Cu deposits (SSHCDs) are a significant source of global Cu production and other important metal by-products. The Polish Kupferschiefer produces Ag, Au, Pt, Pd and Re as side products, whilst Co is one of most important metals extracted from the SSHCDs of the Central African Copperbelt. This study combines both novel and recently published laser ablation inductively coupled plasma mass spectrometry sulfide trace element data from three SSHCD districts, the Polish Kupferschiefer, the Central African Copperbelt, and the Namibian Dolostone Ore Formation, to constrain the differences and similarities between sediment-hosted Cu(-Co) districts. All the investigated districts exhibit mineralization disseminated within the host rock itself, and mineralization occurring within later epigenetic veins. Chalcopyrite, sphalerite, and pyrite trace element compositions vary significantly between the metallogenic districts and between different ore stages. Sulfide trace element compositions are more similar between the African districts, compared to the Polish Kupferschiefer. Random Forest analyses method discriminates SSHCDs based on trace element geochemistry. The sulfide trace element compositions compared to other deposit types and genetic discrimination diagrams show that the SSHCD sulfide data cluster separately from other deposit types. The variation in sulfide trace element composition between the three investigated SSHCD districts suggests that sulfide geochemistry is heavily related to the geology of the host basin and the underlying basement rocks, implying that the geological setting of individual basins strongly affect metal availability.

Keywords: sediment-hosted copper deposits, trace elements, LA-ICP-MS, sulfides, random forest classification

1. Introduction

Trace element analysis by laser ablation inductively coupled plasma mass spectrometry (LA-ICP-MS) has been widely applied to better understand ore-forming processes and to characterize several ore deposit-types, e.g. Mississippi Valley type (Hu et al. 2021), skarn (Chen et al. 2020), porphyry copper and epithermal (Franchini et al. 2015; Cook et al. 2016; Sykora et al. 2018; Velojić et al. 2022). Pyrite from sediment-hosted Au deposits (e.g., Large et al. 2007; Large et al. 2009) and sedimentary pyrite in general (e.g., Large et al. 2014; Gregory et al. 2015) have been widely investigated. Discrimination plots based on mineral geochemistry are useful to understand ore-forming systems. Cobalt versus Ni in pyrite plots were made by Campbell and Ethier (1984) to discriminate pyrite of sedimentary, volcanic or magmatic origins. Duran et al. (2015) used Se/As vs Co/Sb to distinguish hydrothermal and magmatic pyrite. Duran et al. (2019) later proposed a ternary Se-Ni-Cd discrimination diagram for chalcopyrite that separates chalcopyrite from hydrothermal and magmatic origins. Most recently, sphalerite discrimination plots have been suggested by Hu et al. (2021) to discriminate sphalerite from MVT deposits from “magmatic activity-related” sphalerite. Liu et al. (2022) additionally presented discrimination plots to separate sphalerite from MVT, skarn, VMS and SEDEX deposits.

Yet, stratiform sediment-hosted Cu and Cu-Co deposits (SSHCDs and SSHCCDs respectively) have until recently been absent from these studies. This point was recognized by Marsh et al. (2016), who concluded that there is “virtually no data on Ga concentrations” and “very little data” for Ge from SSHCDs, when summarizing significant Ga sources. Foltyn et al. (2022) presented LA-ICP-MS trace element data from sulfides from the Polish Kupferschiefer, which is the classic example of

sediment-hosted Cu. Sulfide trace element geochemistry was also used by Bertrandsson Erlandsson et al. (2022) to reconstruct a multi-stage, orogenic-associated, ore genesis for the sediment-hosted Dolostone Ore Formation Cu-Co deposit in northern Namibia. As ~68 % of the world's current Co production comes from the sediment-hosted deposits of the Central African Copperbelt (CACB), specifically the Congolese CACB, along with 10 % of global Cu production (USGS 2020), it is of high importance to include these deposit-types to improve the understanding of the trace element composition of the ore sulfides and distribution within different deposits.

This study aims therefore to investigate base metal sulfides (chalcopyrite, sphalerite and pyrite) using LA-ICP-MS from three sediment-hosted Cu(-Co) occurrences: the Polish Kupferschiefer, the CACB (with samples from both the Congolese and Zambian parts of the CACB) and the Dolostone Ore Formation in Namibia. This will be achieved by combining both novel and already published LA-ICP-MS data. Herein we use Random Forest (Breiman 2001) to classify the trace element datasets of chalcopyrite, sphalerite and pyrite from four stratiform sediment-hosted Cu(-Co) districts to constrain element characteristics between (1) the deposits themselves and (2) of sediment-hosted Cu(-Co) as a whole compared to other deposit types. As stratiform sediment-hosted Cu(-Co) deposits commonly comprise both a diagenetic hydrothermal mineralization stage and later epigenetic vein stage, we investigate the impact of mineralization generations on the trace element composition of the deposits. Additionally, the reason for variation in sulfide geochemistry will be discussed with a focus on the impact of varying metal sources for the different stratiform sediment-hosted Cu(-Co) districts.



Fig. 1 Location of the four stratiform sediment-hosted Cu deposits included in this study. DOF = Dolostone Ore Formation. Base map from Esri 2018.

2. Geological setting

2.1 The Polish Kupferschiefer

The Lubin-Głogów copper district in southwestern Poland (Appendix P3-1) is the classic example of the reduced-facies type (i.e. Kupferschiefer type) of stratiform sediment-hosted copper mineralization. The basement of the hosting Fore-Sudetic Homocline is composed of deformed Proterozoic to Pennsylvanian gneisses, schists, phyllites, granitoids, conglomerates, sandstones and mudstones (Tomaszewski 1978). They are overlain by Permian sediments following the final stages of the Variscan Orogeny (McCann et al. 2006). Extensive rift-related tectonics and related magmatic activity influenced the Cisuralian “Lower Rotliegend” beds composed of red-colored clastic sediments and bi-modal volcanics. The overlying “Upper Rotliegend” beds are terrestrial beds composed of aeolian sandstones interbedded with deposits of alluvial fans, braided rivers and playas (Karnkowski 1999; Kiersnowski and Buniak 2006; McCann et al. 2006). A post-Cisuralian Zechstein transgression reworked and redeposited the uppermost part of the Rotliegend forming the gray white “Weissliegend” sandstone (Glennie and Buller 1983).

In a typical Kupferschiefer profile, a thin (average 0.3 m-thick) layer of black, marine, shale represents the base of the succession. It was formed under euxinic bottom waters (Paul 2006). The Basal Limestone is a carbonate horizon up to 0.3 meters thick, locally present beneath the Kupferschiefer (Kłapciński 1971; Kłapciński and Peryt 2007). The Kupferschiefer is overlain by the Zechstein Limestone and is followed by the Lower Anhydrite, the Oldest Halite, and the Upper Anhydrite. In the areas of so-called “sandstone elevations”, which represent paleodunes, the Kupferschiefer is absent and Zechstein carbonates overlie the Weissliegend sandstone directly. The Cu-Ag sulfide mineralization occurs mainly as veinlets, dispersed disseminations, impregnations, coarse-grained aggregate nests and locally semi-massive ores in the contact zone between the Rotliegend and Zechstein Groups and is not restricted to the Kupferschiefer layer. It is found in the Weissliegend, the Basal Limestone, the Kupferschiefer and the Zechstein Limestone units. Geological resources of the copper ore deposit operated by KGHM in Fore-Sudetic Monocline are 1 552.28 Mt, of average grade of Cu 1.81 % and 53 g/t of Ag. The amount of metals in geological resources is over 28.11 Mt metallic Cu and over 82.05 thousand t of metallic Ag (PGI 2021).

The depositional age of the Kupferschiefer is 260 – 258 Ma (Menning et al. 2006; Peryt et al. 2012), while results of geochronological studies of mineralization range from the Guadalupian to the Early Triassic (Jowett et al. 1987; Nawrocki 2000; Alderton et al. 2016; Nawrocki 2017), Late Triassic (Mikulski and Stein 2015; Mikulski and Stein 2017), Late Triassic-Early Jurassic (Bechtel et al. 1999; Alderton et al. 2016) and Late Jurassic (Symons et al. 2011). Most authors agree that mineralization processes were long-term and took place in several stages (Wodzicki and Piestrzyński 1994; Michalik and Sawłowicz 2001; Blundell et al. 2003; Alderton et al. 2016). The main mineralizing process was the migration of low-temperature, oxidizing, metalliferous chloride brines sourced from paleo-depressions filled with Rotliegend red bed sediments, through the anoxic basal sediments of the Zechstein Group (Jowett 1986; Oszczepalski 1999). Blundell et al. (2003) has also suggested the basement as a possible metal source. Most of the Kupferschiefer polymetallic Cu–Ag ore deposits in Poland and Germany are spatially associated with an oxidized area known as “Rote Fäule” (Appendix P3-1). These transgressive, red-stained, hematitic footwall alteration zones are thought to be formed by secondary oxidation (e.g., Oszczepalski 1999)

resulting from the flow of oxidizing fluids through the Weissliegend sandstone and Kupferschiefer units, probably during diagenesis. Temperature estimates for the German Kupferschiefer suggest that the shale was affected by temperatures up to 130 °C (Bechtel et al. 1995). Whilst Speczik and Puttmann (1987) suggest that the mineralizing fluids sporadically exceeded 100 °C and that the higher recorded temperatures are the results of maturation events that post-date the main mineralization of the Polish Kupferschiefer. Epigenetic veins show fluid homogenization temperatures between 145 – 200 °C (Strengel-Martinez et al. 1993).

2.2 The Central African Copperbelt

The world-class Cu-Co deposits of the Central African Copperbelt (CACB) have a combined total pre-mining endowment of 166 Mt Cu (Taylor et al. 2013) with several deposits having average grades of 5 % Cu and 1 % Co (Hitzman et al. 2005). They occur in an area stretching over 400 km long and 100 km wide on both sides of the DR Congo and Zambian border. The deposits are hosted in Neoproterozoic sediments with an age between <880 Ma and 542 Ma (Armstrong et al. 2005; Master et al. 2005; Cailteux et al. 2018). The host-rock overlies a basement of metasedimentary and magmatic rocks (Van Wilderode et al. 2015). The Neoproterozoic sediments were deformed during the Pan-African Lufilian orogeny, dated between 560 and 530 Ma (Hanson et al. 1993; John et al. 2004). Although copper and cobalt mineralization occur at many stratigraphic levels in the Neoproterozoic Roan, Nguba and Kundelungu Groups (Mambwe et al. 2023), the ores are concentrated in the lower part of the Roan Group which forms the base of the Katanga Supergroup (Cailteux et al. 2005). The deposits are characterized by both stratiform and stratabound mineralization, but being restricted to a stratigraphic or lithological sequence (Cailteux et al. 2005; Dewaele et al. 2006). Numerous models have been proposed for the ore-forming processes in the Central African Copperbelt, ranging from a magmatic to syn-sedimentary, diagenetic and orogenic origin or a multiphase origin (for a review see Cailteux et al. 2005 and Selley et al. 2005). Compilation of all available data demonstrate that mineralization occurred over a protracted period that spanned diagenesis, basin inversion and metamorphism (Hitzman et al. 2012). Two main hypogene mineralization periods are proposed by El Desouky et al. (2010). The first phase occurred during diagenesis of the Neoproterozoic strata (Bartholomé et al. 1972) and the second near maximum burial and deformation (orogenesis) of the strata (Cailteux et al. 2005). Both in Zambia and in the DR Congo, the second main stage has been subdivided into successive mineralization substages ranging from the onset of folding, syn-folding to post-folding (Brems et al. 2009; Cailteux et al. 2018).

2.2.1 Congolese Luiswishi deposit

The Luiswishi Cu-Co ore deposit is located in the eastern part of the Congolese part of the Central African Copperbelt (hereafter referred to as KCB; Katanga Copperbelt; Appendix P3-1). Since this deposit has been already intensely studied (El Desouky et al. 2010 and references therein) and the two main mineralization stages recognized in the CACB are present in this deposit, it has been selected for the study of the geochemistry of sulfides from both stages. The ore at Luiswishi is concentrated in two formations of the Roan Group. They ore occurrences are termed the Lower and Upper Orebody and occur respectively in the Kamoto and Kambove Formations (Cailteux et al. 2005). Sulfides from the first mineralization phase occur disseminated in the host rock and together with gangue minerals such as quartz and dolomite in nodules and lenses (El Desouky et al. 2010). Analysis of fluid inclusions in these gangue minerals indicate the mineralizing fluid had

an intermediate salinity (5-12 eq. wt% NaCl) and a temperature between 115 and 220 °C (El Desouky et al. 2009). Sulfides from the second stage occur in nodules, veins and breccia. They precipitated from a high salinity (35-42 eq. wt% NaCl) and high temperature (>290 °C) fluid (El Desouky et al. 2009). Contained resources at Luiswishi show 200 000 t Cu at a grade of 2.5 % and 88 000 t Co at 1.1 % (Taylor et al. 2013).

2.2.2 Zambian Nchanga deposit

The Nchanga deposit, located in the Zambian part of the Central African Copperbelt (hereafter referred to as ZCB; Zambian Copperbelt; Appendix P3-1), has been thoroughly studied by (McGowan et al. 2003; McGowan et al. 2006). The current ore bodies are the result of basin inversion during the Lufilian orogeny (Molak 1995; McGowan et al. 2006) and therefore belong to the second main stage of mineralization in the Copperbelt. Also at Nchanga, a Lower and an Upper Orebody are present in the Lower Roan, which underwent lower greenschist facies metamorphism. Mineralization mainly occurs as disseminated, breccia-hosted, fracture-related and vein-hosted in coarser-grained quartzofeldspathic rocks (McGowan et al. 2003). At Nchanga, the sheared basement granite and the Roan cover occur interleaved due to thrusting of the basement- cover contact (Daly et al. 1984). In addition, the Roan sediments are intensely folded and the limbs of the tight folds are often replaced by a thrust (Swardt 1962). The Lower Ore body is controlled by a low-angle thrust fold and high-angle extensional structures in the basement (Daly et al. 1984; McGowan et al. 2003). The Upper Orebody is spatially associated with thrust-propagated fold hinge zones (McGowan et al. 2006). Metal-bearing fluids could have been derived from the deeper part of the basin and from the basement and the sulfide originated from thermochemical reduction at the site of deposition (McGowan et al. 2003). The mineralizing fluid had a high salinity (31-38 eq. wt% NaCl) and a minimum temperature of 140 – 180 °C (McGowan et al. 2006). The Nchanga deposit has a contained resource of >13 Mt Cu at grade of 3.24 % and >130 000 t Co at a grade of 0.03 (Taylor et al. 2013).

2.3 The Namibian Dolostone Ore Formation

The Dolostone Ore Formation (DOF) is a Cu-Co-Zn mineralization hosted in fine-grained siliciclastics and carbonates of the Ombombo Subgroup in the Neoproterozoic lower Damara Supergroup (Appendix P3-1; Allen 2016). The Damara Supergroup is a rift basin to carbonate platform succession with basal fluvial clastic red bed sediments (Nosib Group). The Nosib Group is predominately composed of arkosic to feldspathic sandstones that were deposited in half grabens (Guj 1970; Porada 1989; Miller 2008; Allen 2016). The Otavi Group overlies the Nosib Group and comprises cyclical marine carbonates and siliciclastics, with an upward increasing carbonate component. In the DOF area, the Otavi group is composed of carbonates, calcareous shales and siltstones (Hoffman and Halverson 2008; Miller 2008; Allen 2016). The DOF is situated within the Eastern Foreland Zone of the NE-SW trending Kaoko Belt (Goscombe et al. 2005). The eastern foreland experienced greenschist facies regional metamorphism during the Damaran Orogeny that resulted in folding and local shearing (Goscombe 1999; Goscombe et al. 2003; Goscombe et al. 2005). Temperature estimates of the regional metamorphism in the DOF area range between 300 – 400 °C (Guj 1970; Foster et al. 2009).

Ore mineralization occurs as disseminations, polysulfide nodules, and aggregates within the host rock itself along with vein-hosted and pressure shadow mineralization. Two main ore-forming

stages have been proposed: (1) syn-metamorphic Cu-Co-Zn mineralization and (2) late Cu-Zn(-Pb) vein and pressure shadow mineralization. Sulfide mineralization is dominantly composed of chalcopyrite, sphalerite and pyrite with subordinate linnaeite and pyrrhotite and minor to accessory galena and cobaltite (Bertrandsson Erlandsson et al. 2022). Bertrandsson Erlandsson et al. (2022) attributes the main ore formation to the Damaran Orogeny and the second main ore-forming stage to post orogenesis, based on sulfide trace element trends. Extensive exploration drilling has given the DOF the deposit an indicated and inferred resource of 225.5 Mt at ore grades of 0.043 % Cu, 0.12 % Co, and 0.54 % Zn (Celsius Resources Limited 2021).

3. Samples and analytical methods

3.1 Sampled deposits

Thirty-five samples from four sediment-hosted Cu(-Co) districts are included within this study (Table 1): eleven samples from the Polish Kupferschiefer; five samples from the Congolese Luiswishi deposit and two samples from the Zambian Nchanga deposit of the CACB; and fifteen samples from the Namibian DOF. LA-ICP-MS data from the Polish Kupferschiefer used herein was published by Foltyn et al. (2022), with additional newly acquired data for this study. Novel data was acquired from the KCB for this study. Trace element data of sulfides from the Namibian DOF was initially published by Bertrandsson Erlandsson et al. (2022), but is herein combined with additional samples analyzed for this study.

Samples were subdivided based on a simplified genetic division. Ore stage 1 sulfides represent sulfides occurring directly in the host rock itself, commonly expressed as dissemination and mineralized nodules. Stage 2 sulfides are predominantly vein-hosted and are believed to have formed later. Stage 1 mineralization typically formed during diagenesis, whilst stage 2 is more related to later hydrothermal events. There are caveats to this subdivision, such as that the degree of metamorphism is low at the Polish Kupferschiefer and that the DOF mineralization shows only metamorphic formation temperatures (Table 1). Hence, this simplification is predominantly made based on the mode of occurrence.

Table 1 Genetic parameters of the sediment-hosted copper deposits investigated in this study

SSHCD District		Age	Ore stages	Formation temperature
Deposit				
Polish Kupferschiefer		Guadalupian - Early Triassic ^A	1	80 – 140 °C ^{B,C}
		Triassic – Jurassic (?) ^D	2	100 – 200 °C ^{B,E}
CACB				
DRC	Luiswishi	816 ± 62 Ma ^F	1	115 – 220 °C ^G
		592–512 Ma ^H	2	270 – 385 °C ^G
Zambia	Nchanga	~583±24 Ma ^I	2	105 – 300 °C ^J
Kunene Namibia		~520 - 480 Ma	1	>310 – 400 °C ^{K,L,M}
	DOF	(uncertain) ^K	2	~310 °C ^K

Ore Stage 1 refers to sediment-hosted mineralization, related to diagenesis. Ore stage 2 refers to mineralization within epigenetic hydrothermal veins, typically orogenic (with the exception of the Polish Kupferschiefer), and accompanied by abundant gangue minerals such as quartz and carbonates. All formation temperatures are based on fluid inclusion data, except for the DOF deposit that is derived from sphalerite trace element composition and regional metamorphic temperatures, and Kupferschiefer stage 1 that is estimated based on stable isotopes and organic matter maturation. References may not always strictly relate to the investigated deposit, but rather the metallogenic district. Abbreviations: CACB = Central African Copperbelt, DOF = Dolostone Ore Formation, DRC = Democratic Republic of Congo. References: A = Alderton et al. (2016); B = Borg et al. (2012); C = Vaughan et al. (1989); D = Jowett (1987); E = Strengel-Martinez et al. (1993); F = Selley et al. (2005); G = El Desouky et al. (2009); H = Rainaud et al. (2005); I = Barra et al. (2004); J = McGowan et al. (2006); K = Bertrandsson Erlandsson et al. (2022); L = Foster et al. (2009); M = Guj (1970).

3.2 Laser ablation inductively coupled plasma mass spectrometry (LA-ICP-MS)

All LA-ICP-MS trace element analyses used in this study have been carried out at the Montanuniversität Leoben, Austria, using an ESI NWR213 Nd:YAG laser ablation system coupled to an Agilent 8800 QQQ ICP-MS. This makes the novel and previously published data directly comparable as the same instrument set up, and analytical conditions have been used. A 50 µm spot size is used with an on-mineral fluency of 2 – 3 J/cm² for the sulfides with a repetition rate of 10 Hz. Helium carrier gas was used at a 0.75 L/min flow rate in the laser ablation cell. Background values are collected during a 30-second pre-ablation laser warm-up, which is followed by 60 seconds dwell time when the laser is active. Each laser ablation cycle is separated by a 30-second washout period.

Isotopes analyzed are: ³⁴S, ⁵¹V, ⁵²Cr, ⁵⁵Mn, ⁵⁷Fe, ⁵⁹Co, ⁶⁰Ni, ⁶³Cu, ⁶⁷Zn, ⁷¹Ga, ⁷²Ge, ⁷³Ge, ⁷⁴Ge, ⁷⁵As, ⁸²Se, ⁹⁵Mo, ¹⁰⁷Ag, ¹¹¹Cd, ¹¹⁵In, ¹¹⁸Sn, ¹²¹Sb, ¹²⁵Te, ¹⁹⁷Au, ²⁰¹Hg, ²⁰⁵Tl, ²⁰⁸Pb, and ²⁰⁹Bi. Although Belissant et al. (2014) demonstrate that ⁷⁴Ge is the most suitable germanium mass for sulfide (sphalerite) analyses, due to the potential polyatomic interference of As-S species on all germanium isotopes, ⁷²Ge and ⁷³Ge were added in the element suite of this study to make sure

that the Ar-S interference is negligible. The software Lolite 4 (Paton et al. 2011) was utilized for data reduction. Detection limits were calculated using the 'Howell method' in the Lolite 4 software. Additionally, ^{24}Mg , ^{27}Al , ^{28}Si and ^{43}Ca were monitored during LA-ICP-MS analyses, but not quantified. This was done to determine the presence of gangue mineral inclusions within the measured sulfides and potential element associations to the gangue inclusions.

The USGS pressed powder polysulfide reference material MASS-1 (Wilson et al. 2002) was used as external standard for data quantification of chalcopyrite, with Cu as the internal standard. For sphalerite and pyrite data quantification, the sphalerite matrix-matched sinter pressed powder pellet reference material MUL-ZnS1 (Onuk et al. 2017) was used as external standard, with S as the internal standard. With the exceptions of concentration quantification of Te, Au, Tl and Hg in sphalerite and pyrite, the MASS-1 was used as the external standard for these elements as the MUL-ZnS1 is not suitable for quantification of these elements. To correct for instrumental drift and quality control during the analytical runs, both reference materials were regularly analyzed (every 20 spots). Sulfide minerals may exhibit heterogeneous trace element distributions (Cook et al. 2016), and thus 20 spot analyses per sulfide phase was sought after to get a representative dataset. Naturally, this is not always possible due to limiting factors such as quantity of sulfide phases in a sample and crystal sizes. All trace element concentration values herein are reported as $\mu\text{g/g}$, if not noted otherwise.

3.3 Statistical evaluation of trace element data

The LA-ICP-MS datasets have been subdivided into two major ore stages, to enable discussion on differences between the early and later stages of mineralization. Stage 1 refers generally to more truly sediment-hosted, sulfide dominated, mineralizations styles e.g., disseminations but also bedding-parallel sulfide veins and veinlets. Stage 2 mineralization is predominantly characterized as bedding cross-cutting, epigenetic, gangue-dominated (quartz or carbonate) veins. These epigenetic veins have formed paragenetically later than the sediment-hosted mineralization in all of the metallogenic districts (Jowett et al. 1987; El Desouky et al. 2010; Bertrandsson Erlandsson et al. 2022). Stages were disregarded for general comparison of the metallogenic districts, as the aim of this is to deduce broad scale similarities and differences between the metallogenic districts as a whole.

3.3.1 Random Forest classification

Binary Random Forest analyses (Breiman 2001) were applied on the trace element datasets to investigate element characteristics of the different sediment-hosted Cu(-Co) districts. The Random Forest analysis ranks each element on how well it distinguishes the two datasets, as this is indicated by the Gini value. The Gini value works as an index to define the best split threshold in the Random Forest decision trees at each node generated (Gregory et al. 2019). The higher the Gini value of an element is relative to another the more suitable the element is at discriminating the two datasets. Random Forest statistical evaluations were carried out in R (Development Core Team 2013) using the RandomForest package. Fifty spot measurements were used for comparisons to the Kupferschiefer dataset and 70 for the CACB-DOF comparison. Different sample sizes (minimum 29 data points) had to be used when carrying out the Random Forest analyses due to varying sample sizes of the separate datasets of the deposits and mineralization stages. Median values of each element of the separate datasets were inserted into missing cells.

Samples are picked at random to avoid overfitting. Each Random Forest dataset comparison was carried out five times to evaluate the impact of the random sample selection. Five hundred trees were generated each run with four variables tied at each of the splits. Random Forest analyses were carried out on sulfides from the Polish Kupferschiefer, KCB and Namibian DOF. Additionally, the trace element datasets for the KCB and DOF sulfides were separated into the two main ore forming stages. This was not done for the Polish Kupferschiefer, as the dataset is not large enough to make such a division whilst avoiding overfitting. The dataset for the ZCB deposit was too small to be included in the Random Forest analyses.

4. Results

4.1 Sulfide trace element composition of sediment-hosted Cu(-Co) deposits

4.1.1 Chalcopyrite trace element geochemistry

For Co, As, In, Sn, Sb, and Tl, chalcopyrite shows similar trace element ranges between the African districts compared to the Polish Kupferschiefer, (Fig. 2; Appendix P3-2). Cobalt, As, and Se show similar concentrations between all districts, with the exception of stage 2 Polish Kupferschiefer for As and stage 2 DOF for Co. Manganese shows a wide range within stage 1 chalcopyrite from each district, although not always higher median concentrations than stage 2 (e.g., the DOF). The Polish Kupferschiefer shows overall higher concentrations of Mn. Cobalt is relatively similar between the districts and their stages, but with stage 1 Kupferschiefer chalcopyrite having lower median concentration of 0.57 $\mu\text{g/g}$. Stage 1 DOF chalcopyrite shows the highest median Co concentrations (8.6 $\mu\text{g/g}$) whilst stage 2 DOF has the lowest median Co concentration (0.17 $\mu\text{g/g}$) of all districts. Nickel in chalcopyrite shows similar trends to Co, with relatively similar concentrations, but with stage 1 Polish Kupferschiefer and Stage 2 DOF chalcopyrite having elevated concentrations, in contrast to Co. Zinc concentrations generally show a wide range between the districts and within a mineralization stage, with the DOF stages and the ZCB chalcopyrite having the higher median concentrations (339 and 222 $\mu\text{g/g}$ respectively).

Chalcopyrite from the CACB districts shows higher Ga concentrations compared to the Polish Kupferschiefer and DOF, with the stage 2 KCB chalcopyrite having the highest median Ga concentration (70 $\mu\text{g/g}$). Stage 2 chalcopyrite shows slightly elevated concentrations compared to stage 1 of each district. Germanium concentrations are low with the KCB chalcopyrite having slightly higher concentrations, similar to Ga. Stage 2 Kupferschiefer chalcopyrite shows a wide range of Ge concentrations and has significantly higher median Ge concentrations than the other districts and stages (1,240 $\mu\text{g/g}$). Arsenic is only significantly higher in stage 2 Polish Kupferschiefer chalcopyrite (307 $\mu\text{g/g}$), but with a wide range of As concentrations. The African districts have relatively similar, lower, As concentrations. Selenium shows a minor range of concentrations between the different districts with stage 2 DOF chalcopyrite having the highest Se concentration (104 $\mu\text{g/g}$) and the ZCB having the lowest concentrations (<8.1 $\mu\text{g/g}$, below the limit of detection).

Both stages of the Polish Kupferschiefer have the highest Ag concentrations out of the districts, with stage 1 chalcopyrite containing the highest median Ag concentration of the two stages (57 $\mu\text{g/g}$). The CACB districts have low Ag content, with stage 1 KCB chalcopyrite having the lowest Ag concentrations (<0.057 $\mu\text{g/g}$, below detection limit). The African districts contain relatively similar In concentrations (between 4.3 and 31 $\mu\text{g/g}$), but the KCB chalcopyrite is slightly elevated

in In (19 and 31 $\mu\text{g}/\text{g}$, respectively for stage 1 and 2). Both Polish Kupferschiefer stages show lower In concentrations (1.5 and 0.37 $\mu\text{g}/\text{g}$, stage 1 and 2 respectively). Tin trends are similar to In, with similar concentrations between the African districts and stages (ranging from median 18 to 50 $\mu\text{g}/\text{g}$), whilst the Polish Kupferschiefer chalcopyrite displays lower Sn concentrations (1.8 and 1.6 $\mu\text{g}/\text{g}$, respectively for stage 1 and 2). Antimony concentrations show an inverse trend to that of In and Sn, with the Polish Kupferschiefer chalcopyrite containing the highest Sb content, stage 2 in particular with 30 $\mu\text{g}/\text{g}$. The African districts contain uniform Sb concentrations (below respective detection limits, around 0.12 $\mu\text{g}/\text{g}$, see Appendix P3-2) with the exception of stage 1 KCB chalcopyrite, which has a minimal higher median concentrations 0.44 $\mu\text{g}/\text{g}$ and displays a wide range (maximum 8.3 $\mu\text{g}/\text{g}$). Thallium concentrations have a similar trend to Sb with the Polish Kupferschiefer chalcopyrites having higher median concentrations of 1.5 and 0.60 $\mu\text{g}/\text{g}$; and relatively similar concentrations between the African districts, with stage 1 KCB slightly higher median Tl concentration (0.06 $\mu\text{g}/\text{g}$) and showing a wide range. Lead, in general, shares the trend of Sb and Tl, with the Kupferschiefer chalcopyrite having the highest median concentrations (137 and 153 $\mu\text{g}/\text{g}$, stage 1 and 2 respectively) and stage 1 KCB chalcopyrite displaying a wide range, the rest of the African deposits show a relatively large range of Pb concentrations. All of the investigated districts and stages show Cd, Te, and Au concentrations below respective detection limits in chalcopyrite (Appendix P3-2). Vanadium, As, and Mo occur below the respective detection limit in all districts and stages, with the exception of stage 1 Kupferschiefer chalcopyrite. Antimony and Tl occur at below detection limits in the African Cu-Co districts (Online Resource 2).

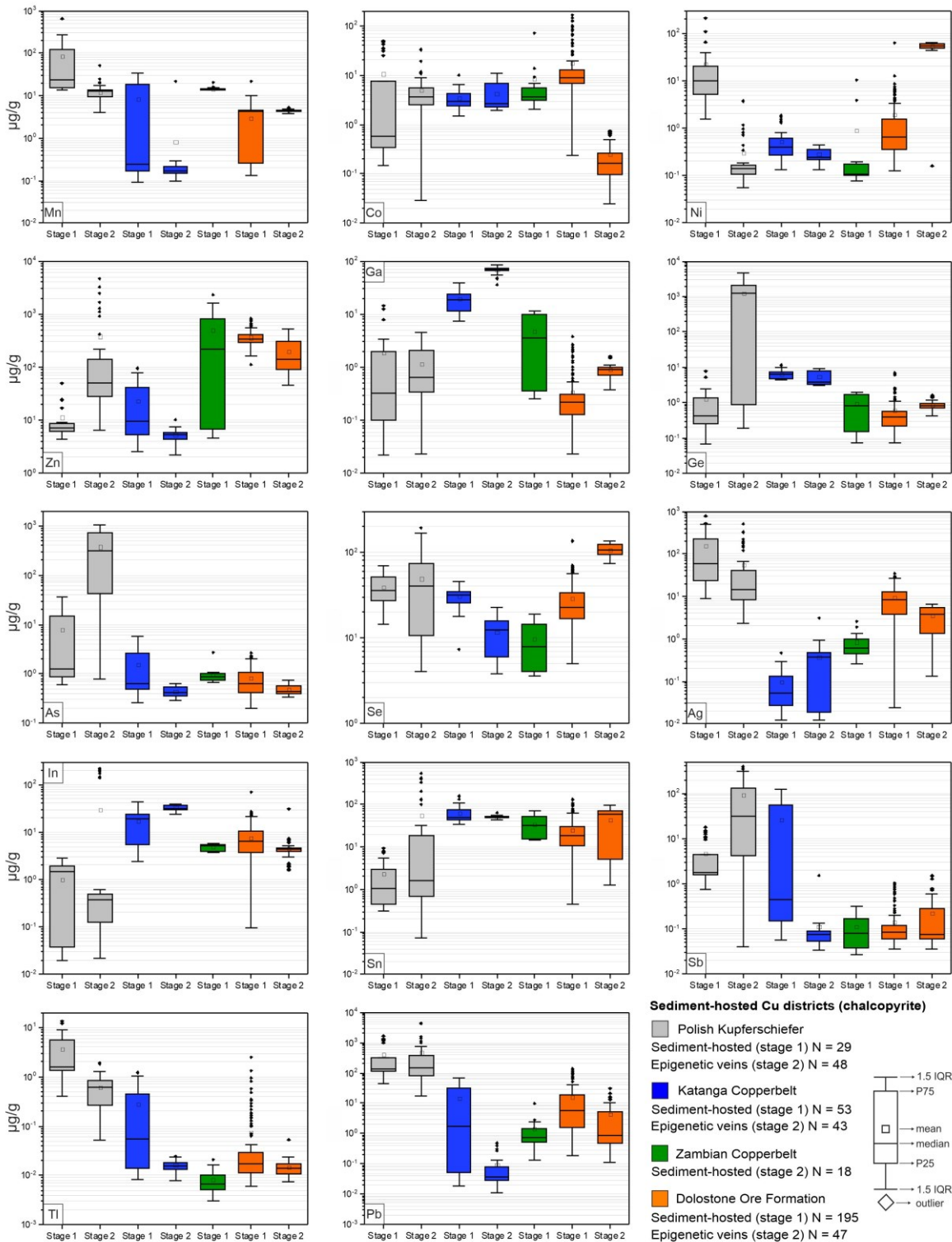


Fig. 2 Chalcopyrite trace element geochemistry of selected elements between the four investigated chalcopyrite-bearing deposits. Data for the Polish Kupferschiefer and ZCB is from Foltyn et al. (2022); the Dolostone Ore Formation is from this study and Bertrandsson Erlandsson et al. (2022). N = maximum number of LA-ICP-MS analyses for each group

4.1.2 Sphalerite trace element geochemistry

Sphalerite was only identified in samples from the Polish Kupferschiefer and the DOF. Trace element concentrations vary quite significantly both between the two deposits and between stages (Fig. 3). Kupferschiefer sphalerite generally shows elevated concentrations of Ge (stage 1 and 2 median values: 3.5 and 1.2 $\mu\text{g/g}$), Ag (33 and 2.7 $\mu\text{g/g}$), Cd (4,700 and 9,200 $\mu\text{g/g}$), Sn (3.6 and 1.2 $\mu\text{g/g}$), Tl (2.4 and 1.1 $\mu\text{g/g}$), and Pb (102 and 25 $\mu\text{g/g}$). DOF sphalerite has elevated concentrations of Mn (stage 1 and 2 median values: 201 and 44 $\mu\text{g/g}$), Fe (6.5 and 3.9 wt%), Co (8,672 and 799 $\mu\text{g/g}$), Se (28 and 99 $\mu\text{g/g}$), and In (34 and 21 $\mu\text{g/g}$). Inter-deposit differences with regards to mineralization stage 1 and 2 is evident in most of the elements (Fig. 3). Manganese, Fe, Ag, Sn, and Pb are all elevated in stage 1 sphalerite from both deposits, to their respective stage 2. Cadmium is the only element that is elevated in stage 2 sphalerite in both deposits. The most striking differences between the two districts are that Kupferschiefer sphalerite is Fe-poor whilst DOF sphalerite is Cd-poor. Vanadium, Cr, As, Te, Au, and Bi occur close to or at below detection limits in both deposits (Appendix P3-2).

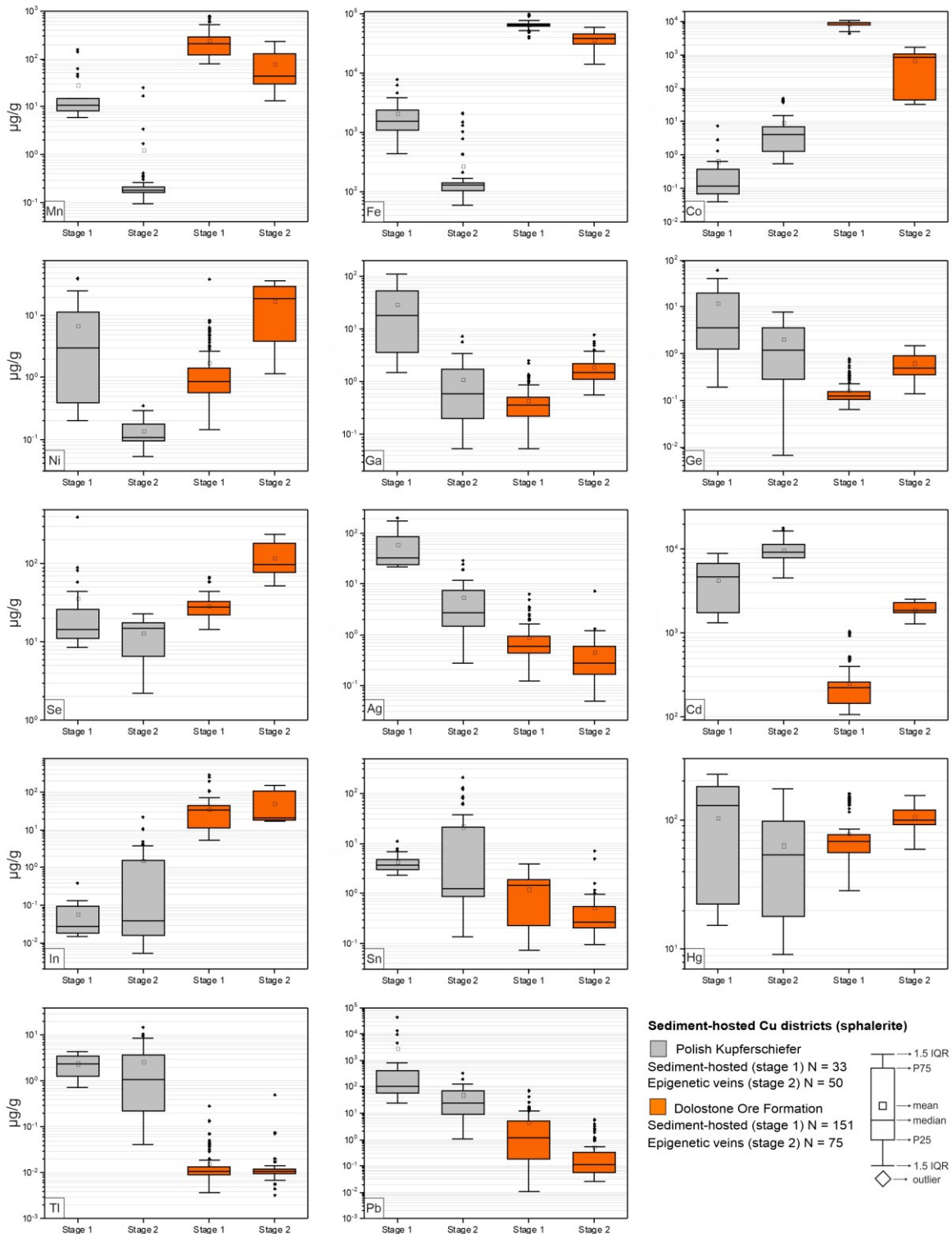


Fig. 3 Sphalerite trace element geochemistry of selected elements between the Polish Kupferschiefer and the Dolostone Ore Formation. Data for the Polish Kupferschiefer is from Foltyn et al. (2022) and this study; the Dolostone Ore Formation is from this study and Bertrandsson Erlandsson et al. (2022). N = maximum number of LA-ICP-MS analyses for each group

4.1.3 Pyrite trace element geochemistry

Pyrite associated with Cu mineralization was not identified in the Polish Kupferschiefer stage 2 and ZCB mineralizations. Pyrite trace element composition is most similar between the African Cu-Co districts than compared to the Polish Kupferschiefer (Fig. 4). Selenium is the only element present above detection limits in pyrite that shows relatively similar concentrations between all sediment-hosted Cu(-Co) districts, from median 10 $\mu\text{g/g}$ in the Polish Kupferschiefer to 55 $\mu\text{g/g}$ in the KCB stage 2 pyrite (Fig. 4). In the African districts, stage 1 pyrite is noticeably elevated in trace elements compared to stage 2 (e.g. Mn, Sn, Tl and Pb). Manganese is significantly elevated in stage 1 Polish Kupferschiefer pyrite (322 $\mu\text{g/g}$). Both stage 1 pyrites of the KCB and DOF are elevated in Mn compared to their stage 2. Cobalt occurs in significant concentrations in the sediment-hosted Cu-Co pyrites: stage 1 KCB = 8,480 $\mu\text{g/g}$, stage 2 KCB = 77,058 $\mu\text{g/g}$, stage 1 DOF = 12,432 $\mu\text{g/g}$, and stage 2 DOF = 3,699 $\mu\text{g/g}$. Nickel concentrations show a relatively more uniform median distribution between the KCB and DOF (175 – 634 $\mu\text{g/g}$), although stage 2 DOF pyrite exhibits a wide range of Ni concentrations to values below the limit of detection (0.23 $\mu\text{g/g}$). Polish Kupferschiefer has the lowest median Co and Ni concentration (91 & 25 $\mu\text{g/g}$ respectively), but stage 1 pyrite has significantly higher Cu concentrations (4,493 $\mu\text{g/g}$) compared to the other stages and districts. Stage 1 KCB pyrite also has elevated Cu concentrations (564 $\mu\text{g/g}$), stage 2 KCB pyrite has median 9.2 $\mu\text{g/g}$ Cu. Both DOF stages show similar median Cu concentrations (246 & 181 $\mu\text{g/g}$), but large ranges (Fig. 4).

Median As content of Polish Kupferschiefer and KCB pyrite is relatively similar, between 90 and 367 $\mu\text{g/g}$. DOF pyrite has significantly lower median As contents (0.6 & 5.2, stage 1 & 2 respectively), and stage 2 DOF does have a notably wider range of As content than stage 1 (Fig. 4). Median Sn occurs only above 1 $\mu\text{g/g}$ in the Polish Kupferschiefer and stage 1 KCB pyrite. Thallium is significantly elevated in the Polish Kupferschiefer pyrite (846 $\mu\text{g/g}$), whereas Tl in the African districts is just above 1 $\mu\text{g/g}$ or below the limit of detection. Lead in pyrite varies between the districts and stages (Fig. 4), where the Polish Kupferschiefer pyrite has the highest median concentration of 1.71 $\mu\text{g/g}$ and stage 2 KCB has noticeably the lowest Pb content (0.03 $\mu\text{g/g}$). Stage 2 DOF shows a very large range in Pb concentrations, compared to the overall range of the other districts, from below the detection limit (0.17 $\mu\text{g/g}$) to 29 $\mu\text{g/g}$. Median Sn, Tl and Pb are all higher in stage 1 pyrite compared to stage 2 pyrite in both the KCB and DOF (Fig. 4). Gallium, Te, and Au are reported just above their respective limit of detection in pyrite form all districts. Additionally, Mo, Cd, and Hg occur below or just above the detection limits within the KCB and DOF pyrites (Appendix P3-2).

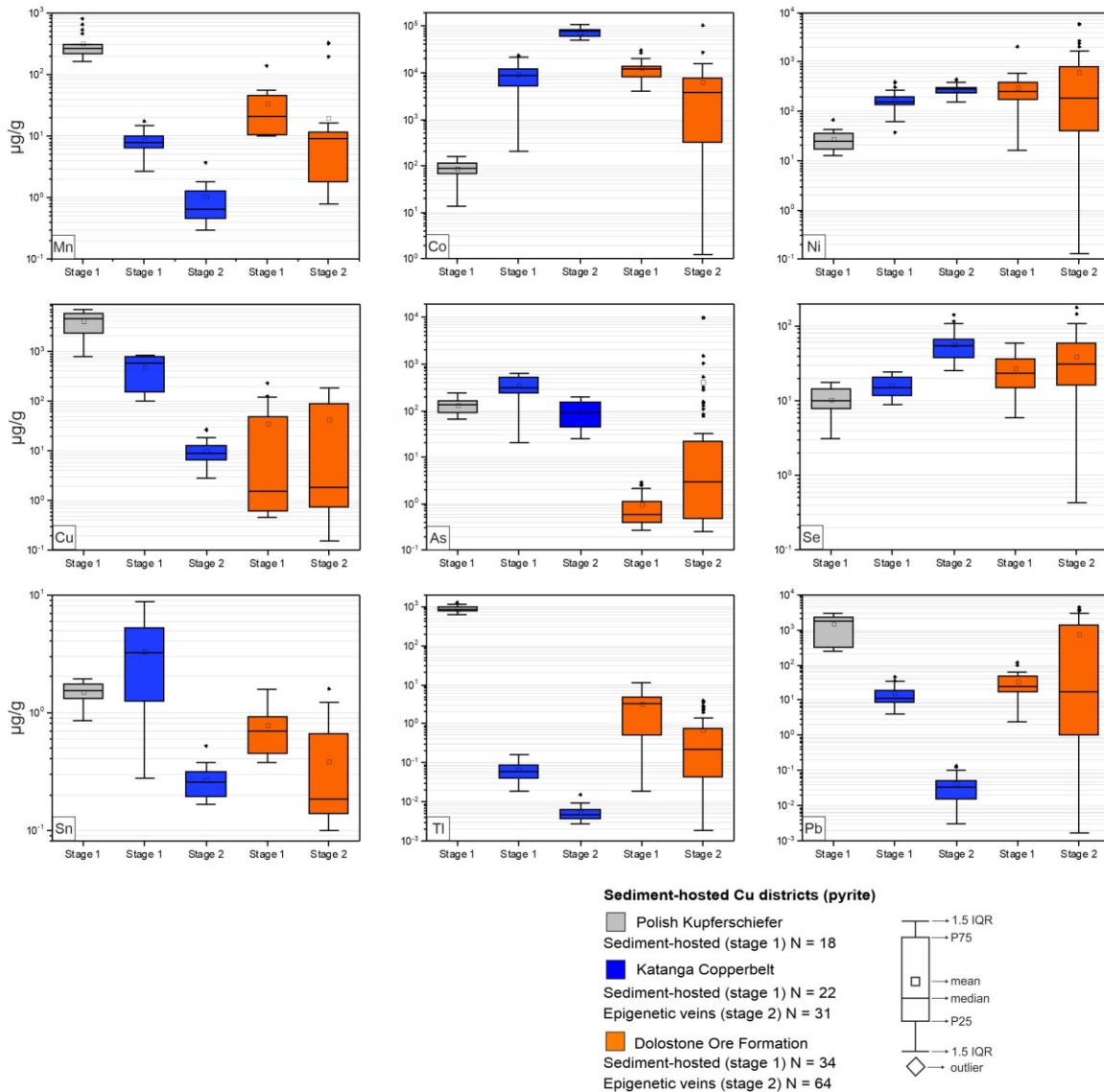


Fig. 4 Pyrite trace element geochemistry of selected elements from the Polish Kupferschiefer, Katanga Copperbelt and the Dolostone Ore Formation. Data for the Dolostone Ore Formation is from this study and Bertrandsson Erlandsson et al. (2022). N = maximum number of LA-ICP-MS analyses for each group

4.2 Random Forest analysis

Chalcopyrite is the only ore mineral that is found in all of the investigated metallogenic districts. However, chalcopyrite from the Nchanga deposit (ZCB) had to be excluded from the Random Forest statistics as the sample population is below 30. Random Forest analyses were done in pairs between the three remaining deposits (Appendix P3-3). Thallium, Sb, Pb, Mn, Zn, As, and In are the best discriminating elements for chalcopyrite between the Polish Kupferschiefer and the DOF. Gallium, Ge, Zn, Ag, S, In, Ni, and Pb are the best discriminating elements for chalcopyrite between the KCB and the DOF. Sphalerite was only identified in the Polish Kupferschiefer and the DOF, thus only these two deposits were compared. Iron, Cd, Tl, In, Co, Mn, Pb, and Ni indicate the most prominent discriminators for sphalerite between the two sphalerite-bearing deposits. Pyrite shows the most variance in the most significant elements but has some elements with high

decreased Gini values. Manganese, Ag, Tl, V, As, and Co are good discriminating elements between pyrite from the KCB and the DOF (Appendix P3-3).

4.3.1 Random Forest analyses of the DOF and the KCB by stage subdivision

Chalcopyrite from the two main ore stages of the KCB are discriminated best by Ga, Se, In, Sb, V, and Pb (Appendix P3-3). Selenium and Sb are elevated in stage 1, and Ga, In, Pb, and V in stage 2. Selenium, Co, Ni, Ga, and Bi are good discriminator elements for chalcopyrite from the two main ore stages of the DOF deposit (Appendix P3-3). Stage 1 DOF chalcopyrite is elevated in Co and Bi, whilst stage 2 is elevated in Se, Ni, and Ga. Cobalt, Cd, Se, Fe, Ge, and Ga are the best discriminator elements for sphalerite from the two main ore stages of the DOF deposit, where stage 1 sphalerite is elevated in Co and Fe, and stage 2 sphalerite in Se, Cd, Ga, and Ge.

5. Interpretations and discussion

Mixed analyses of the target sulfides and gangue phases (and other sulfides) are a common challenge in all analyzed deposits, as sulfides of sediment-hosted Cu(-Co) deposits commonly occur intergrown with the host rock gangue minerals. This results in high variability of number of data points per element in a sample set. Vanadium and Cr, for example, are commonly correlated with Si and Al count signals, attributed to Al-bearing silicates from the host rock that occur as inclusions within the sulfides (Fig. 5A). Correlation between Mn and Ca is also common. The Ca is attributed to carbonate inclusions, as carbonates are common gangue minerals in these types of deposits, thus this can explain higher Mn values in the dataset. As the investigated sulfides are from Cu-deposits, Cu-sulfides are widespread and commonly occur as inclusions within both pyrite and sphalerite (Fig. 5B). This explains the varying Cu concentrations in the sphalerite and pyrite, although effort has been made to omit obvious inclusions. Cobalt-phases may also occur as inclusions in especially pyrite, as pointed out in the DOF by Bertrandsson Erlandsson et al. (2022), but the pyrite from sediment-hosted Cu-Co deposits generally still shows high Co concentrations (Fig. 4). Cobalt-rich pyrite is well recognized in the KCB (Bartholomé et al. 1971), and thus serves to support the high Co concentrations measured in our sediment-hosted Co deposit pyrite. These observations should be taken into consideration when interpreting LA-ICP-MS analyses of sulfides from sediment-hosted Cu(-Co) deposits and working with data from them.

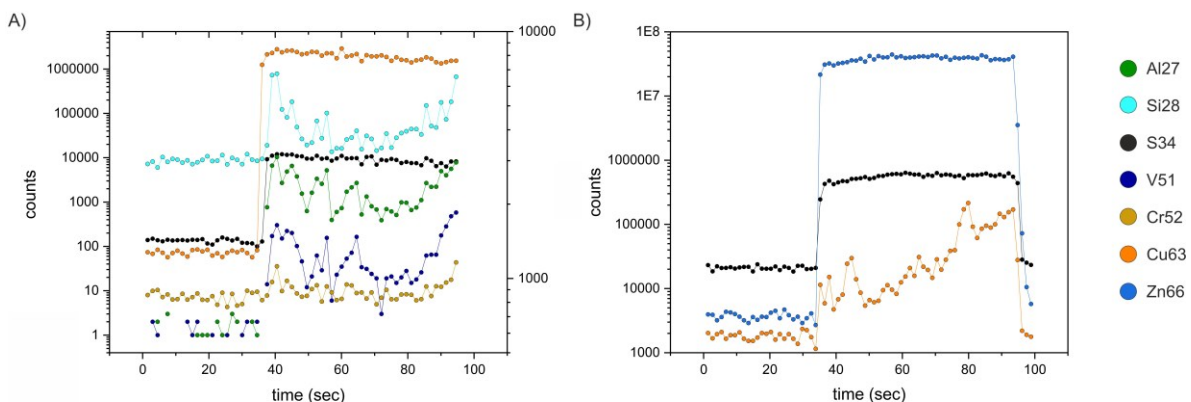


Fig. 5 Time-resolved count signals of inclusions in sulfides. A) Si-Al gangue phase inclusion in KCB chalcopyrite. Vanadium and Cr signals mirror those of Si and Al. Observe that the right-side Y-axis plots Si28 and Cr52. B) Cu-signal indicating Cu-bearing mineral inclusion in DOF sphalerite

5.1 Statistical approach to a trace element comparison of sediment-hosted Cu deposits

DOF stage 1 chalcopyrite was shown by Bertrandsson Erlandsson et al. (2022) to be Co-rich and Ni- and Se-poor. The DOF mineralization has exceptions to this rule, as Bertrandsson Erlandsson et al. (2022) proposed certain gangue-dominated veins or “DOF events” to be related to the first main Cu-Co stage. All the DOF stage 1 sulfides are characterized by elevated Co concentrations. In the case of the DOF data, genetic subdivision is based on Bertrandsson Erlandsson et al. (2022) and trace element composition of the sulfides, which was how the paragenetic stages of the DOF was made therein. For example, DOF stage 1 sphalerite is Fe- and Co-rich whilst being Ni- and Cd-poor. Stage 2 of the DOF comprises gangue-dominated veins and has been suggested to have formed during late-orogenic stages, after the Co mineralization (Bertrandsson Erlandsson et al. 2022).

5.1.1 Trace element characteristics of chalcopyrite from sediment-hosted Cu deposits

Random Forest analyses demonstrate that specific elements discriminate chalcopyrite from the Polish Kupferschiefer, KCB and DOF. Gallium and Ag in chalcopyrite are the best discriminators between the Polish Kupferschiefer and the KCB; Ga, Ge, and Zn in chalcopyrite between the KCB and DOF; Tl and In for Polish Kupferschiefer and the DOF (Fig. 6A). Gallium is the most prominent discriminator of the Luiswishi deposit of the KCB, with In and Sn being secondary discriminators (Fig. 6A). Silver being a distinguishing element for Polish Kupferschiefer chalcopyrite is reasonable as the Polish Kupferschiefer is one of the world’s largest producers of Ag from Cu ore (USGS 2020). Chalcopyrite is known to be able to host hundreds $\mu\text{g/g}$ of silver (George et al. 2018), suggesting that the Ag-bearing fluids not only formed discrete Ag-phases but also were incorporated into chalcopyrite.

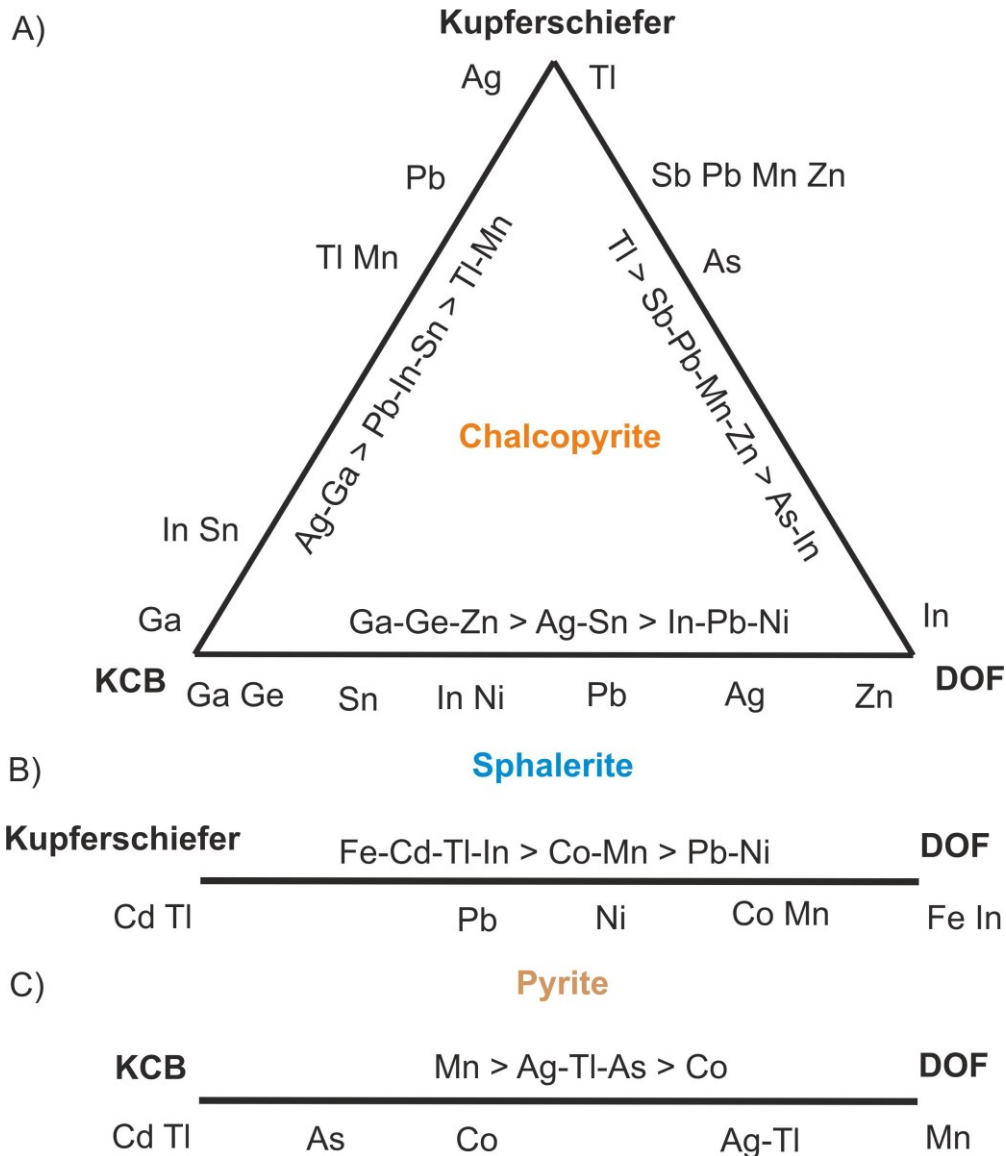


Fig. 6 Ternary diagram of deposit-defining elements, derived from Random Forest analyses, of A) chalcopyrite, B) sphalerite, and C) pyrite. The proximity of the element to the deposit name relates to a higher mean Gini value. Relative grouping of the elements, based on higher Gini values, are indicated by >. Abbreviations: KCB = Katanga Copperbelt; DOF = Dolostone Ore Formation

Silver distinguishes both DOF chalcopyrite from CACB chalcopyrite as well as chalcopyrite from the Polish Kupferschiefer and the CACB, whilst Ga is strongly associated with KCB when compared to the other two deposits (Fig. 6). Thus, the Ga and Ag in chalcopyrite concentrations were plotted to test the results of Random Forest analyses (Fig. 7). Gallium, which has the highest Gini value when compared to the other two deposits (Fig. 6 & Appendix P3-3), clearly discriminates the KCB samples. Silver has the highest Gini value only between the Polish Kupferschiefer and the KCB and discriminates these two deposits well (Fig. 7). Silver content between the DOF and KCB has a relative lower Gini value (Fig. 6A; Appendix P3-3), meaning it is not as powerful as a discriminating element (Fig. 7).

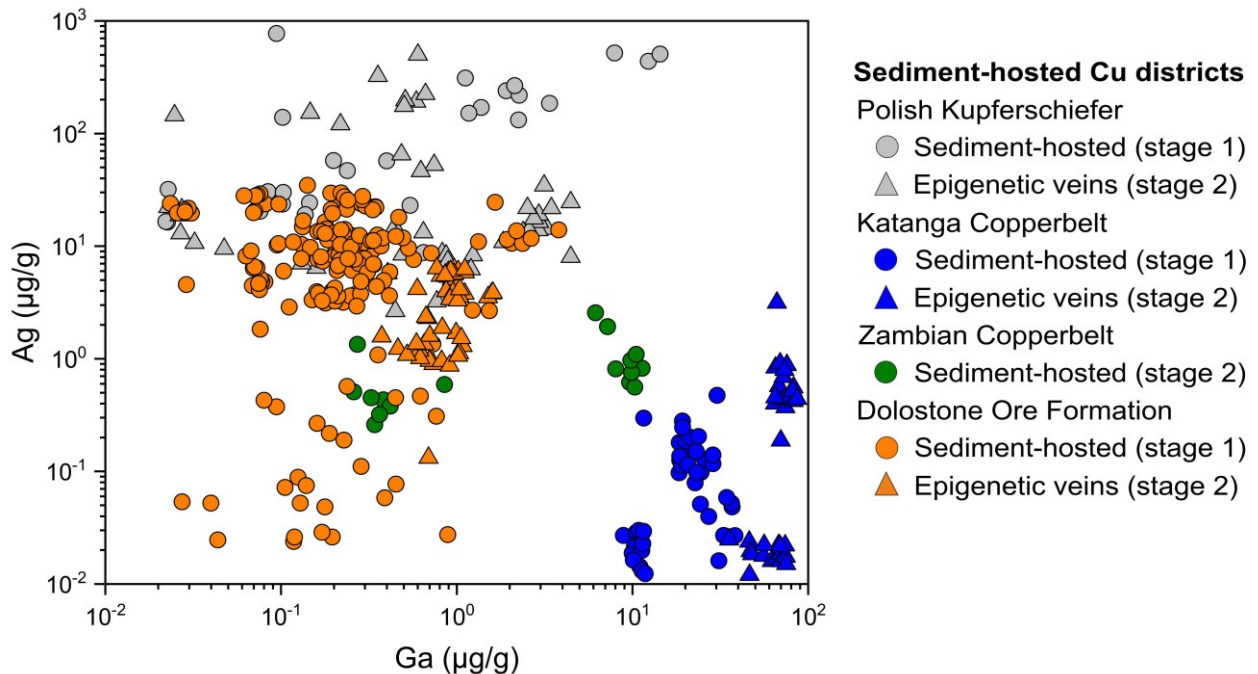


Fig. 7 Binary plot of Ga and Ag concentrations in chalcopyrite from the four sediment-hosted Cu(-Co) districts investigated in this study. Gallium and Ag were used due to both these elements being demonstrated to be good discriminator elements by Random Forest analyses

Chalcopyrite composition variations between mineralization stages

There are obvious differences in geochemistry between stage 1 and 2 sulfides (e.g., Fig. 2). To better compare the geochemistry of the ore stages, the trace element data was divided according to stage and Random Forest analyses were carried out. For chalcopyrite, this was only done on the KCB and DOF datasets due to the risk of overfitting the smaller datasets of the other districts (Fig. 8). Gallium is the best indicator element to distinguish chalcopyrite from the second major Co-ore stage from the first Co-ore stage of the KCB (Fig. 8A); In, V, and Pb are also attributed to the second Co-ore stage. Chalcopyrite from the first Co-ore stage is defined by higher concentrations of Se and Sb. It is important to note that several of these elements have significant variance between samples within one ore stage, which may indicate a more complex formation history than simply two independent stages. Cobalt is the only element with a more significant Mean Gini value for DOF stage 1 chalcopyrite, and where Se is the most distinctive element for DOF stage 2 (Fig. 8B). It is interesting to see that Se is elevated in KCB stage 1 chalcopyrite but in stage 2 chalcopyrite in the DOF.

Although omitted from the Random Forest analyses, the ZCB Ga-Ag concentrations in chalcopyrite show two distinct populations (Fig. 7), the first population plotting with DOF chalcopyrite and the second with KCB stage 1 chalcopyrite. ZCB chalcopyrite plotting with both the DOF and the KCB may be related to the fact that both the ZCB and DOF experienced higher grades of regional metamorphism (Mendelsohn 1961; Annels 1986; Richards et al. 1988; Bertrandsson Erlandsson et al. 2022). Hence, the ZCB data may be reflecting both a stage 1 and 2 population.

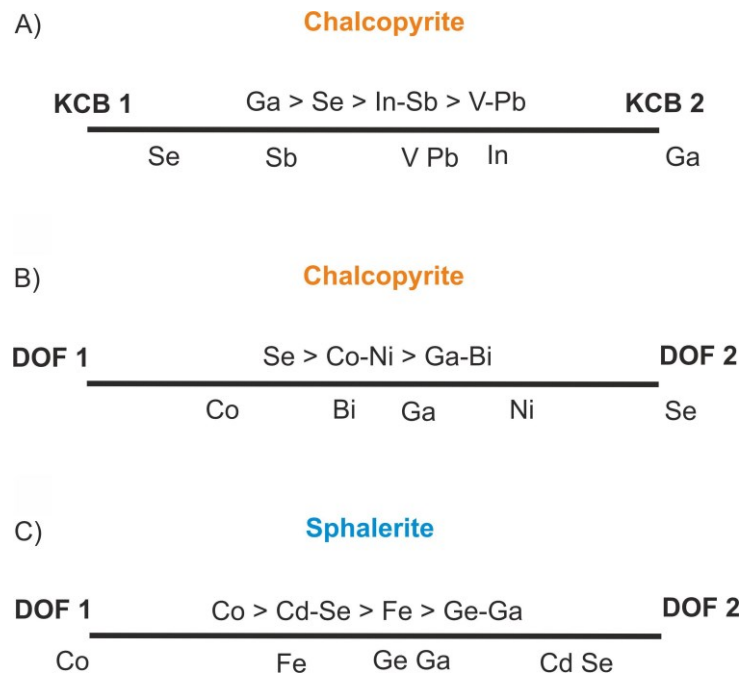


Fig. 8 Binary representation of defining elements, from Random Forest analysis, in chalcopyrite (A and B) between the two main mineralization stages of the Katanga Copperbelt (KCB 1 & 2) and Dolostone Ore Formation (DOF 1 & 2). And in sphalerite (C) between the two main mineralization stages of the DOF deposit. Ore stage 1 (DOF 1) being the main Cu-Co-Zn stage and ore stage 2 (DOF 2) being Cu-Zn mineralization without substantial Co mineralization. The proximity of the element, underneath the thick line, to the deposit name relates to a higher mean Gini value. Relative grouping of the elements, based on higher Gini values, are indicated by >

5.1.2 Trace element characteristics of sphalerite from sediment-hosted Cu deposits

Cadmium and Tl characterize sphalerite from the Polish Kupferschiefer (Fig. 6B), as DOF sphalerite is remarkably Cd-poor (median 175 µg/g for stage 1 and median 1,700 µg/g for stage 2) and Tl predominantly shows values below detection limits. Iron and In are the prime distinguishing elements of the DOF, with Co and Mn at lesser degrees of Gini values. Indium and Tl discriminate the Polish Kupferschiefer from the DOF with regard to both chalcopyrite and sphalerite, where Tl is enriched in chalcopyrite and sphalerite from the Polish Kupferschiefer and In in the DOF sulfides.

Manganese, Fe, and In in sphalerite have been shown to be temperature-dependent by the Ga-Ge-In-Mn-Fe in sphalerite (GGIMFis) geothermometer developed by Frenzel et al. (2016). Manganese and Fe increase with higher temperatures whilst Ga and Ge decrease (Frenzel et al. 2016). The GGIMFis applied on DOF sphalerite revealed that the sphalerite had formed at temperatures above 310 ± 50 °C (Bertrandsson Erlandsson et al. 2022), the closing temperature of the GGIMFis. The GGIMFis on epigenetic sphalerite (stage 2) from the Polish Kupferschiefer yielded formation temperatures of 122 – 123 °C (Foltyn et al. 2022). This is close to temperature maximum 100 – 130 °C for the main-stage sediment-hosted mineralization (Speczik and Puttmann 1987; Bechtel et al. 1995) and 145 – 200 °C for later epigenetic veins (Strengel-Martinez et al. 1993). Taking these observations into account, many of the discriminating elements are probably due to the difference in sphalerite formation temperatures. DOF sphalerites are indeed elevated in Mn, Fe and In whilst being depleted in Ge in comparison to the Polish Kupferschiefer sphalerite

(Fig. 3). Gallium is the only temperature dependent element that does not show a distinct difference between the two deposits, as sphalerite from both deposits are Ga-poor (median <1 $\mu\text{g/g}$).

DOF sphalerite is enriched in Co. Ore stage 1 DOF sphalerite has a median Co concentration of 8,600 $\mu\text{g/g}$, with min and max concentrations of 4,300 and 10,700 $\mu\text{g/g}$ respectively. The later ore stage 2 DOF sphalerite, associated with late orogenic remobilization, has a much wider range of Co concentrations (min 32 and max 10,100 $\mu\text{g/g}$), which is why the Random Forest analyses does not attribute Co a higher Mean Decreasing Gini value. This is demonstrated from Random Forest analyses carried out between the two main DOF ore stages. Nonetheless, Cd and Co are interesting elements for discriminating the deposits, as these are not believed to be directly temperature dependent. A noteworthy point is that Co and Cd were included in the study by Frenzel et al. (2016), but they could not conclude the control of these elements in sphalerite. However, Co and Cd are suitable discriminating elements between the Polish Kupferschiefer and DOF. The Random Forest analyses indicated Fe and Cd to be the two best discrimination elements, which is clearly evident when plotted (Fig. 9). From this it is also evident that stage 2 sphalerite is characterized by lower Fe and higher Cd, compared to their stage 1 equivalent.

Other studies also discuss the possibility of Mn in sphalerite being a relative redox indicator, where higher Mn concentrations are attributed to more reduced formation environments (Kelley et al. 2004; Zhuang et al. 2019). These studies base their conclusions on Mn concentration differences of tens of $\mu\text{g/g}$ (Kelley et al. 2004), not hundreds to thousands of $\mu\text{g/g}$ difference as seen in this study. Kelley et al. (2004) also discredits the impact of temperature in relation to metal concentrations in sphalerite (at their formation temperatures below 150 °C), which seems to be quite contradictory to the study of Frenzel et al. (2016) who has compared the GGIMFis temperatures of sphalerite to that of fluid inclusion data and concluded that Mn in sphalerite is temperature dependent.

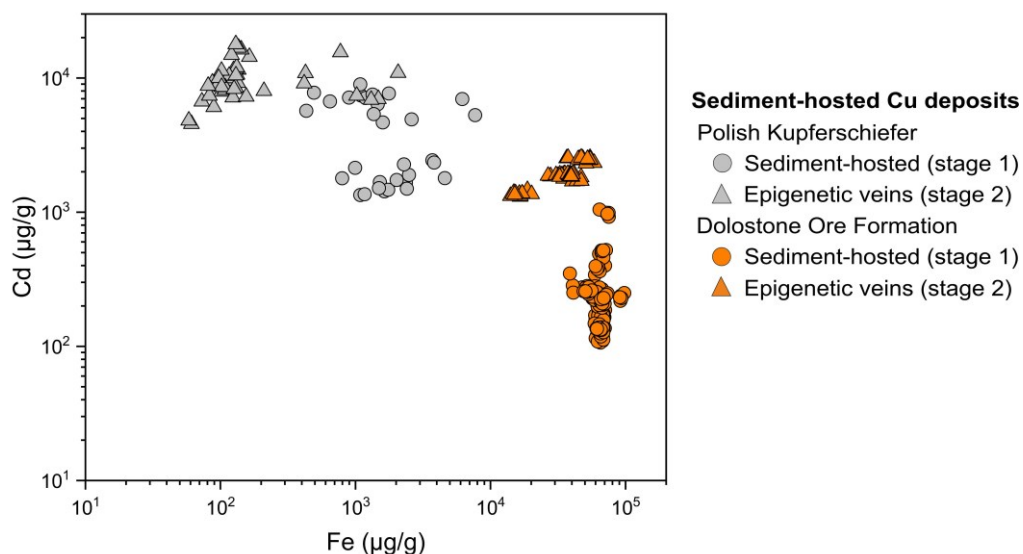


Fig. 9 Binary plot of Fe and Cd concentrations in sphalerite from the Polish Kupferschiefer and the Namibian Dolostone Ore Formation

Sphalerite composition variations between mineralization stages

For the DOF, two main stages of ore mineralization have been proposed, where the first ore stage (DOF stage 1) was responsible for the main Co mineralization associated with Cu-Zn whilst stage 2 (DOF stage 2) lacks substantial Co-phases (Bertrandsson Erlandsson et al. 2022). This is directly evident from the Random Forest analyses of these two stages, where Co is affiliated with both chalcopyrite and sphalerite from the main Co-stage DOF stage 1 (Fig. 8B,C). Nickel in chalcopyrite is associated with stage 2, decoupled from Co (Fig. 8B). This was also indicated for sphalerite by Bertrandsson Erlandsson et al. (2022), although the Random Forest analysis did not indicate Ni as a good discriminator element for DOF sphalerite. Although individual Co-phases are associated with chalcopyrite, sphalerite and pyrite from the main Co-stage, it is evident that the aforementioned sulfides are all enriched in Co.

It has been discussed herein that preexisting sedimentary pyrites may have served as a source of, at least parts, of the Co, indicating host rock interaction and leaching of elements. Host rock limestones have low average Cd concentrations (0.04 $\mu\text{g/g}$), resulting in Cd in sphalerite requiring a magmatic source or some post-magmatic processes (Chon and Shimazaki 1986). Thus, stage 1 DOF sphalerite may have formed as a result of host rock leaching due to the low Cd concentrations in the sphalerite. Schwartz (2000) suggested low Cd concentrations in sphalerite to correlate with high total activity of reduced S, which furthermore points to interaction with the reduced S from the sulfides or microbial S associated with the host sediments. Although having relatively low Mean Gini Values, Ga (and Ge in sphalerite) is associated with the later epigenetic/remobilized DOF stage 2 (Fig. 8C). This is reasonable for sphalerite as Ga and Ge are associated with lower temperature sphalerite (Frenzel et al. 2016), and as the DOF stage 2 was proposed by Bertrandsson Erlandsson et al. (2022) to have formed at slightly lower temperatures. This also explains Fe being attributed to DOF stage 1 sphalerite, as Fe is generally enriched in higher temperature sphalerite (Frenzel et al. 2016) as previously stated.

5.1.3 Trace element characteristics of pyrite from sediment-hosted Cu deposits

Manganese is the best discriminator element for pyrite between the KCB and DOF (Fig. 6C), with DOF pyrite having median 11 $\mu\text{g/g}$ of Mn and KCB pyrite having median 2.7 $\mu\text{g/g}$ Mn. Silver, Tl and As were all assigned similar Gini values of approximately 4.5. Both Ag and Tl are higher in DOF pyrite with median 0.59 and 0.53 $\mu\text{g/g}$ respectively, in comparison to the KCB pyrite that only contains median concentrations below each respective detection limit. Arsenic is enriched in the KCB pyrite with a median 148 $\mu\text{g/g}$, whilst the DOF pyrite contains median 1.8 $\mu\text{g/g}$ of As.

Pyrite from both deposits show high concentrations of Co (Fig. 4), although the KCB has the highest median Co concentrations of 5.6 wt% compared to the median 6,445 $\mu\text{g/g}$ Co in DOF pyrites and 91 $\mu\text{g/g}$ in the Polish Kupferschiefer. It is obvious that pyrite from the Co-rich districts is significantly elevated in Co. This is also reflected in stage 2 DOF pyrite, which contains only 3,699 $\mu\text{g/g}$ Co, whilst DOF stage 1 pyrite has 12,432 $\mu\text{g/g}$ Co. Stage 2 DOF pyrite lacks associated Co-mineralization (Bertrandsson Erlandsson et al. 2022). Pyrite from KCB stage 1 also formed before the formation of stoichiometric Co-minerals (e.g. Cailteux et al. 2005), which would explain the lower Co concentrations in KCB stage 1 pyrite (8,480 $\mu\text{g/g}$) compared to stage 2 (7.6 wt%). As pyrites from these deposits are believed to have formed before the main Co-mineralization, it seems the earlier pyrite-forming fluids were already elevated in Co, and other factors lead to the

eventual formation of stoichiometric Co-phases. Similar trends appear to be true for Cu. Copper seems to be elevated in pyrite from both the Polish Kupferschiefer (median 4,593 $\mu\text{g/g}$) and the stage 1 KAB (median 564 $\mu\text{g/g}$); both these pyrite stage predate first Cu mineralizations. In contrast, stage 2 KAB contains median 10.3 $\mu\text{g/g}$ and both DOF stages have Cu concentrations below or around detection limits (4.9 $\mu\text{g/g}$). The stage 1 ore-forming fluids must hence have been elevated in Cu during pyrite formation. The significantly elevated concentrations of Cu and Ag in the Polish Kupferschiefer may also be attributed to chalcopyrite inclusions, as the chalcopyrite is Ag-rich (Foltyn et al. 2022). It seems pyrite geochemistry tends to mirror the associated metal mineralization, where the Polish Kupferschiefer pyrites are enriched in e.g. Ag whilst the African Co-deposits have pyrite with elevated Co concentrations. Pyrite may thus be an important exploration tool and indicator mineral for sediment-hosted Cu and Co ores.

5.3 Comparison of trace elements compositions to other deposit types

Certain elements show similar concentrations between the investigated deposits for chalcopyrite (Co, Ni, Se, and Bi), sphalerite (Ga, Ge, Se, and Hg) and pyrite (Ni and Se). Thus, trace element compositions may serve to characterize sediment-hosted Cu(-Co) deposits, as these trends comprise both early and late stages of mineralization.

5.3.1 Chalcopyrite trace element signatures in sediment-hosted Cu(-Co) and other deposit types

Most trace elements in chalcopyrite from the four sediment-hosted Cu(-Co) deposits show a wide spread in average concentrations and show little consistency when compared to other genetic types (Fig. 10). Cobalt shows significantly elevated concentrations in chalcopyrite compared to all the other deposit types. This suggests that Co is enriched in chalcopyrite from sediment-hosted Cu deposits with or without major Co mineralization. DOF chalcopyrite shows the highest median Co concentration (7.4 $\mu\text{g/g}$) whilst chalcopyrite from the KCB shows the lowest median Co concentration (2.8 $\mu\text{g/g}$) of the four deposits. This indicates that Co is enriched in sediment-hosted Cu deposits in general. The relatively lower Co concentrations in KCB chalcopyrite, compared to DOF, may be due to contemporaneous crystallization of the Co-phase carrollite (CuCo_2S_4 ; El Desouky et al. 2010). In this case, Co preferably partitions into carrollite rather than into chalcopyrite. In the DOF, the main Co mineralization is believed to pre-date the stage 1 Cu-Zn mineralization, and thus the stage 1 chalcopyrite and sphalerite are more enriched in Co (Bertrandsson Erlandsson et al. 2022). Nickel is generally higher in chalcopyrite from the sediment-hosted Cu(-Co) deposits, SEDEX chalcopyrite being the only genetic type that shows some overlap (Fig. 10).

Selenium shows similar average concentrations between the Polish Kupferschiefer, KCB and DOF (23 – 39 $\mu\text{g/g}$), with ZCB chalcopyrite showing slightly lower median Se concentrations (8.1 $\mu\text{g/g}$). Porphyry copper and skarn chalcopyrite show median Se concentrations between these two intervals. Mercury shows relatively similar concentrations between the stratiform sediment-hosted Cu(-Co) deposits (median 1.8 – 5.2 $\mu\text{g/g}$). This is significantly higher than in other deposit types, except for SEDEX chalcopyrite that is much higher in Se (Fig. 10). SEDEX deposits are also per definition sediment-hosted, may undergo diagenetic processes, and generally form from lower-temperature fluids (Sangster 2002) similarly to SSHCDs. This may be the reason for the generally similar trends in chalcopyrite trace elements such as Mn, Ni, As, Se, Cd, Sn, and Hg between SSHCDs and SEDEX (Fig. 10).

Average chalcopyrite trace element compositions of different ore deposit-types, from overview studies (George et al. 2018), were compared to the four investigated sediment-hosted Cu(-Co) deposits of this study (Fig. 10). Manganese, Ga, As, Ag, Cd, In, Pb, and Bi in chalcopyrite from sediment-hosted Cu(-Co) deposits show wide ranges of concentrations when compared to other genetic deposit types (Fig. 10). The elevated Zn concentrations in DOF chalcopyrite may relate to the strong association with sphalerite, resulting in sphalerite inclusions but furthermore indicating that the ore-forming system of the DOF was Zn-bearing compared to the KCB samples where sphalerite and galena are absent in the investigated samples. This is also evident in the slightly elevated Zn concentrations in Polish Kupferschiefer chalcopyrite (Fig. 10), where sphalerite is also present, although in lesser amounts than in the DOF deposit. Concentrations of Ga in chalcopyrite are relatively low in all compared deposit types, between 0.1 – 1 µg/g, but chalcopyrite from both the KCB and ZCB show elevated concentrations of Ga (32 and 3.5 µg/g respectively). Cobalt, Sn and Hg (Ni and Se to a lesser degree) show good potential for discrimination of chalcopyrite from sediment-hosted Cu(-Co) deposits to chalcopyrite from deposit types such as VMS, SEDEX, skarn, epithermal and porphyry copper. Additionally, As, Ag, In, Sn, Sb, and, to a lesser extent, Bi show median concentrations distinctly separate in chalcopyrite from sediment-hosted Cu deposits (the Polish Kupferschiefer) and the sediment-hosted Cu-Co deposits (Fig. 10). As, Ag, In, Sn, Sb, and Bi may be useful to distinguish sediment-hosted Cu deposits with and without substantial Co.

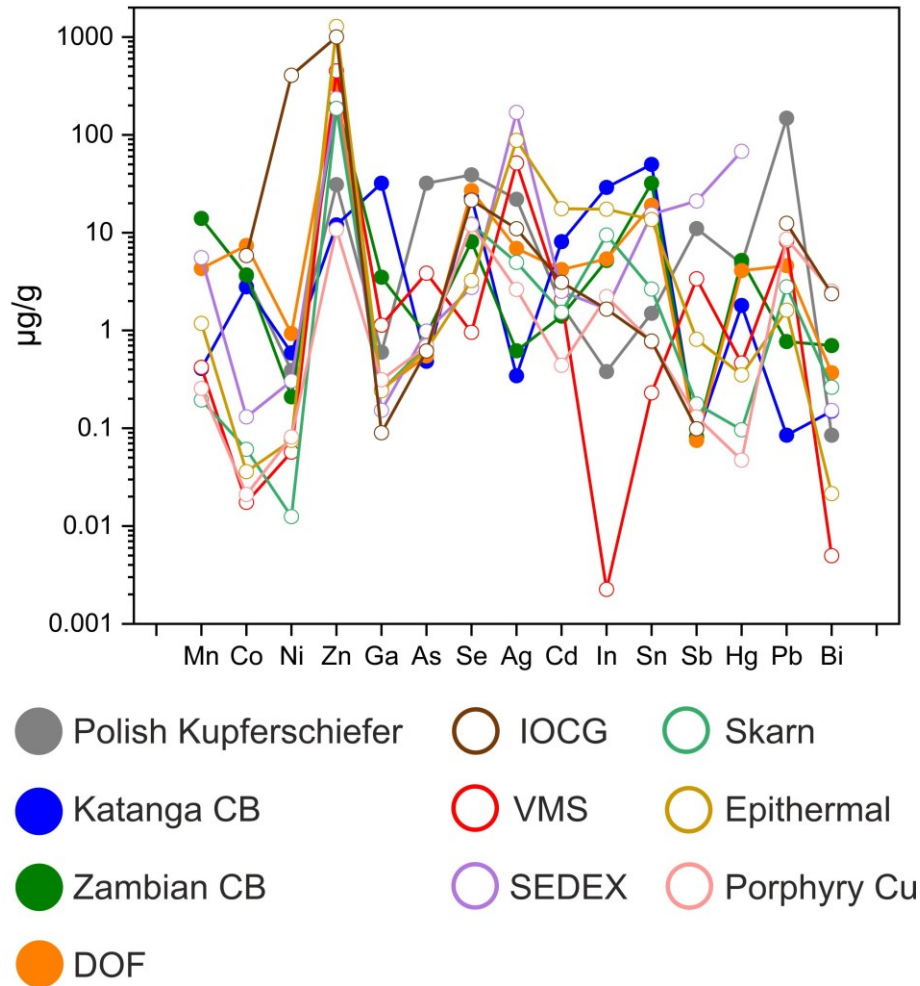


Fig. 10 Comparison of average concentrations of selected elements in chalcopyrite from different ore deposit types. Data for other deposits from George et al. (2018), IOCG data from Mansur et al. (2022). Abbreviations: CB = Copperbelt; DOF = Dolostone Ore Formation; IOCG = Iron-Oxide-Copper-Gold; VMS = volcanogenic massive sulfides; SEDEX = sedimentary exhalative

5.3.2 Sphalerite trace element signatures in sediment-hosted Cu(-Co) and other deposit types

Liu et al. (2022) compiled sphalerite trace element data to develop discrimination plots of MVT, VMS, skarn, and SEDEX sphalerite. Both stage 1 Kupferschiefer and stage 2 DOF sphalerite plots predominantly within the MVT field. Stage 1 DOF sphalerite plots more towards the higher-temperature fields (Fig. 11). It is important to note that the contents of Mn, Fe, and Ge in sphalerite are all temperature dependent, where Mn and Fe are attributed to higher formation temperatures (Frenzel et al. 2016). This is evident in the plots where Mn and Fe are main discriminatory elements of the deposits associated with higher formation temperatures (VMS, skarn, and SEDEX) and the low-temperature MVT field. This helps to explain why DOF stage 1 sphalerite trends towards the higher-temperature fields (Fig. 11), as DOF sphalerite formed at temperatures $>310 \pm 50$ °C (Bertrandsson Erlandsson et al. 2022). Manganese and Fe were also shown by the Random Forest analysis to be reliable distinguishing elements between sphalerite from the Polish Kupferschiefer and DOF, as the formation temperature of the Polish Kupferschiefer has been estimated at 100 - 130 °C (Speczik and Puttmann 1987; Bechtel et al. 1995).

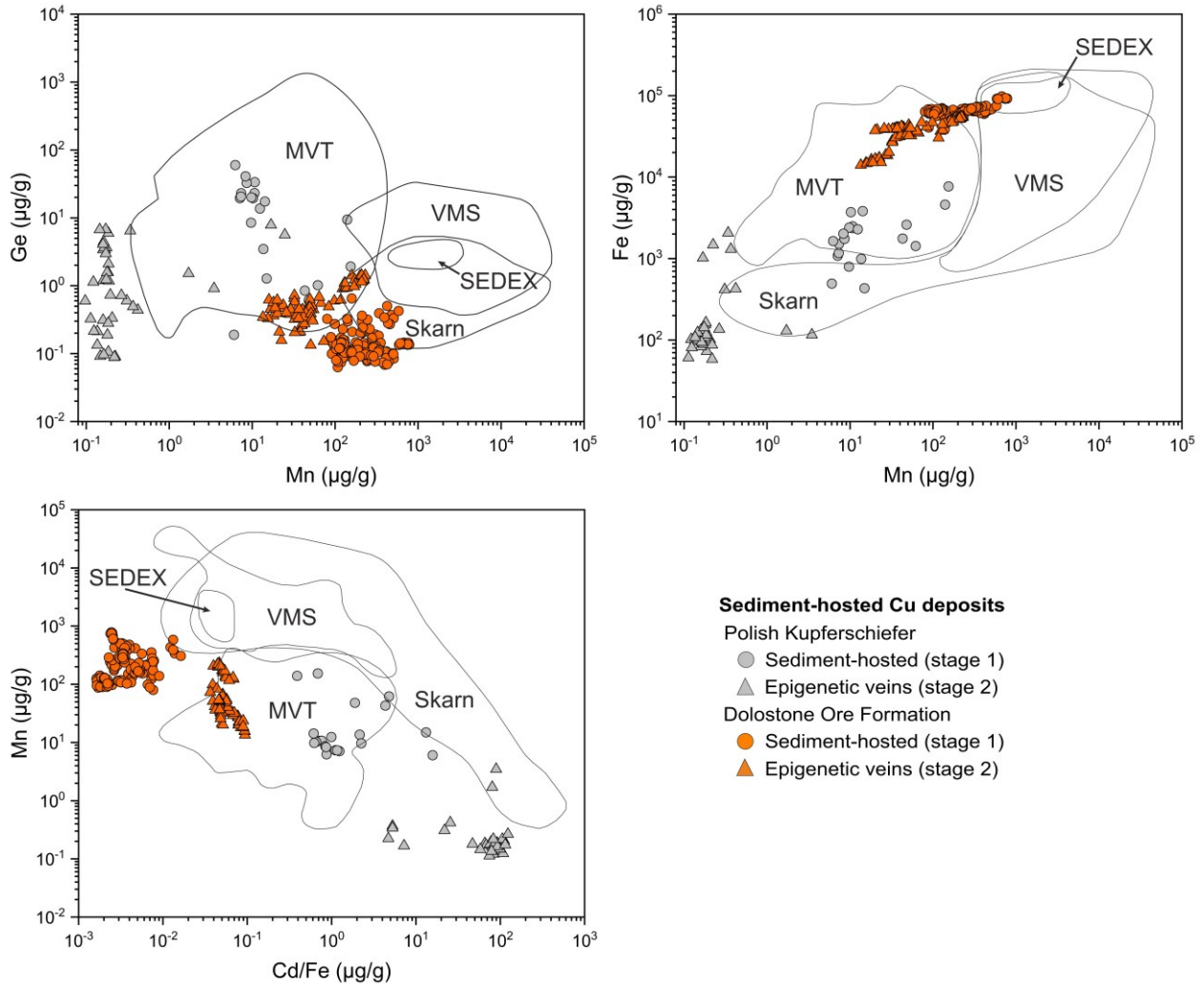


Fig. 11 Binary discrimination plots of (A) Mn vs Ge, (B) Mn vs Fe, and (C) Cd/Fe vs Mn for sphalerite from MVT deposits and higher temperature deposits (VMS, skarn, and SEDEX), fields after Liu et al. (2022) and compiled reference data therein

Sphalerite from DOF shows larger differences in trace element concentrations than the Polish Kupferschiefer sphalerite, when compared to other genetic types of ore deposits (Fig. 12). The DOF sphalerite shows intermediate concentrations of Mn and In, whilst showing elevated concentrations in Fe and Co. Copper, Ge and Cd are all distinctly lower than the averages of other ore deposit types. As aforementioned, DOF sphalerite is significantly enriched in Co and skarn sphalerite is the only other genetic type of sphalerite showing elevated concentrations of Co, although not close to the average concentrations of Co in DOF sphalerite. Gallium and In in DOF sphalerite show similar average concentrations to that of skarn-type sphalerite. Cadmium in sphalerite is indicated by Random Forest as a strong indicator element between the Polish Kupferschiefer and DOF; this is due to the low Cd (median 256 $\mu\text{g/g}$) concentrations in DOF sphalerite (Fig. 12).

The Polish Kupferschiefer sphalerite shows element concentrations similar to most other deposits types in its Co, Cu, Ga, Ge, and Cd concentrations (Fig. 12). Whilst Mn, Fe, and In concentrations

are all lower than in any other genetic type, the Polish Kupferschiefer sphalerite is closest to the MVT sphalerite in these elements (Fig. 12). It thus seems like sphalerite from both the Polish Kupferschiefer and DOF share average concentrations to that of MVT deposits, but with some differences in particular in the temperature-dependent elements. Nonetheless, both SSHC(C)Ds show distinct characteristics in sphalerite trace elements geochemistry and may have good potential for discriminating sphalerite from both sediment-hosted copper and sediment-hosted copper-cobalt deposits both independently and from other deposit types sphalerite.

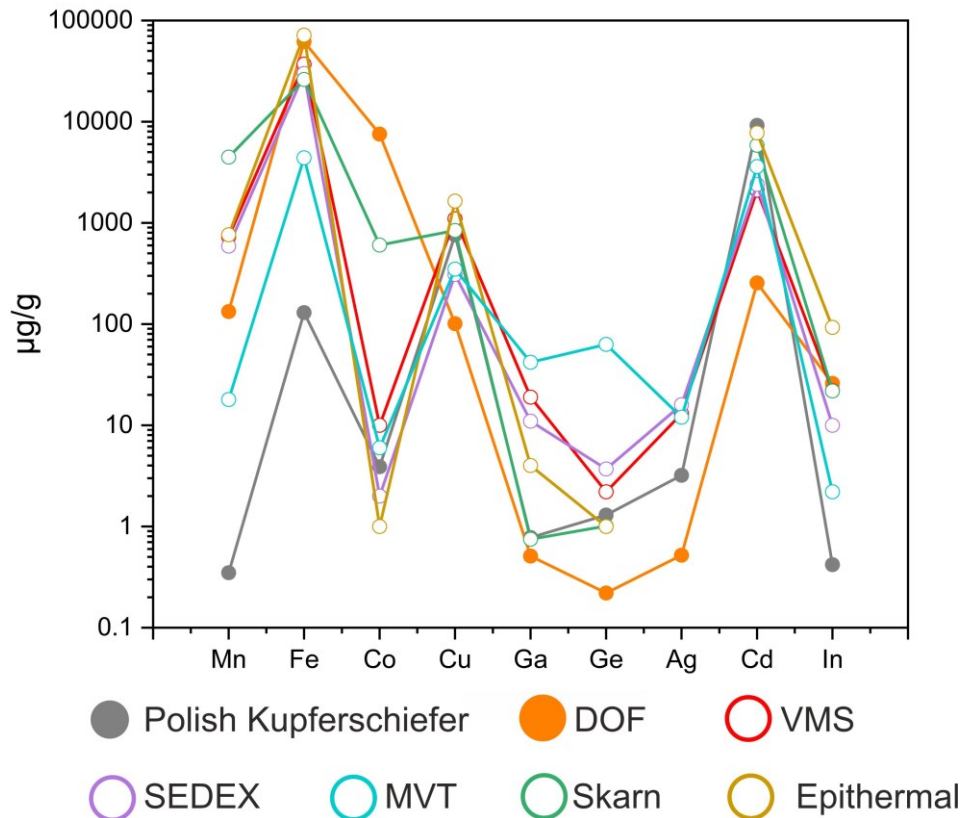


Fig. 12 Average concentrations of selected elements in sphalerite from different ore deposit types. Data for VMS, SEDEX and MVT comes from Frenzel et al. (2016) and references therein; skarn and epithermal deposits comes from Cook et al. (2009) and references therein. Abbreviations: DOF = Dolostone Ore Formation; VMS = volcanogenic massive sulfides; SEDEX = sedimentary exhalative; MVT = Mississippi Valley Type

5.3.3 Pyrite trace element signatures in sediment-hosted Cu-Co and other deposit types

Cobalt-Ni ratios are among the most utilized trace element pairs to determine the origin of pyrite, from the early work of Loftus-Hills and Solomon (1967) discriminating sedimentary, volcanic and magmatic pyrite. Later, Campbell and Ethier (1984) proposed a Co-Ni discrimination plot with fields wherein sedimentary, volcanic and magmatic pyrite plots. The sediment-hosted Cu-Co pyrites of this study cluster in their own separate field when plotted in the Campbell and Ethier (1984) diagram (Fig. 13). This is primarily due to the high Co concentrations of sediment-hosted Cu-Co pyrite, whilst having Ni concentrations lower than the magmatic pyrite field. This is why we herein propose an additional field for pyrite of sedimentary Cu-Co affinity.

It is apparent that there is a wide spread in, predominantly DOF, pyrite Co-Ni data, which is likely the result of early sedimentary pyrite being remobilized in the main ore Cu-Co forming stages in the DOF. Bertrandsson Erlandsson et al. (2022) show that sedimentary pyrite is absent in the main ore horizon of the DOF. They suggest that preexisting sedimentary pyrite was replaced by Cu-Zn sulfides and recycled to form the later pyrite associated with the main ore stage. Thus, this later pyrite could have inherited trace elements from the sedimentary pyrite, resulting in mixed trace elements signatures of e.g., Co and Ni.

Sedimentary pyrite from the DOF shows Co and Ni concentrations in good accordance with the field for sedimentary pyrite (Fig. 13) and average Neoproterozoic sedimentary pyrite from Gregory et al. (2015). Sedimentary DOF pyrite shows slightly elevated Co concentrations compared to both the sedimentary discrimination field and the average Neoproterozoic pyrite. This combined with the model of recycled sedimentary pyrite being part of the formation for the main Cu-Co stage mineralization of the DOF reinforces the idea of early sedimentary pyrite being a partial Co-source for the DOF, as suggested by Bertrandsson Erlandsson et al. (2022). The Cu-Co mineralization-associated pyrite is clearly more Co enriched than the sedimentary DOF pyrite (Fig. 13) and thus it is reasonable that an additional source of Co is required to explain the DOF Co-mineralization.

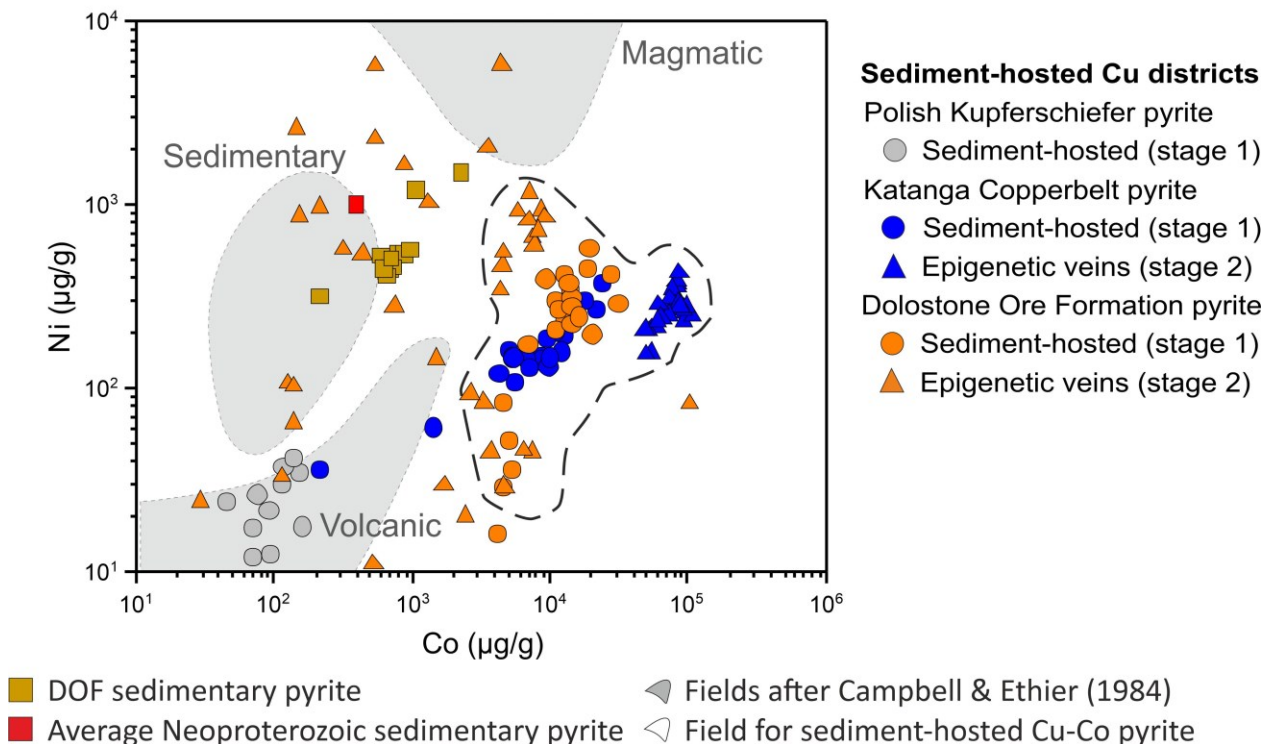


Fig. 13 Binary discrimination plot of sedimentary, volcanic and magmatic pyrite based on Co-Ni concentrations in pyrite (after Campbell and Ethier 1984). A new field for sediment-hosted Cu-Co pyrite is herein proposed. Sedimentary DOF pyrite is shown separate along with a data point for average Neoproterozoic sedimentary pyrite from Gregory et al. (2015) as reference points in the plot. DOF pyrite data includes combined data from this study and Bertrandsson Erlandsson et al. (2022). Abbreviations: DOF = Dolostone Ore Formation

Duran et al. (2015) combined Co, As, Se and Sb trace element data from hydrothermal deposits (Cu-porphyrines, orogenic Au and volcanogenic-hosted massive sulfides) and magmatic deposits to discriminate between hydrothermal and magmatic pyrite. The sediment-hosted Cu-Co pyrites cluster predominantly within the magmatic field of this discrimination plot (Fig. 14). This is due to the high Co concentrations in pyrite from sediment-hosted Cu-Co deposits and not due to the pyrite being magmatic in origin. The separation from magmatic pyrite is demonstrated in the Co-Ni discrimination plot (Fig. 13) of Campbell and Ethier (1984).

The source of Co in sediment-hosted Cu-Co deposits is still enigmatic and several sources have been suggested: mafic volcanoclastics (Unrug 1988), erosion materials of basement-hosted magmatic Cu-Co-Ni ores (Cailteux et al. 2005), or the basement rocks in general (El Desouky et al. 2010; Van Wilderode et al. 2015). These sources could thus explain the magmatic trace element signatures seen in pyrite, as other magmatic affiliated elements might also have been transported in the metal-scavenging fluids, thus resulting in an inherited magmatic trace element signature in the sediment-hosted Cu-Co pyrite. Only one population of DOF samples plots in the more hydrothermal field, notably in the domain where porphyry copper pyrites cluster. These are related to a specific quartz-carbonate vein mineralization of the DOF, the so-called “Event” mineralization style, and thus a hydrothermal trace element signature is proposed.

Thallium is significantly elevated in the Polish Kupferschiefer pyrite (846 $\mu\text{g/g}$) compared to the other districts (Fig. 4), but also contains elevated concentrations of Sb and Hg. Several sediment-hosted Carlin-type Au districts show a positive As-Sb-Hg-Tl trend (e.g., Muntean et al. 2011, Daliran et al. 2018). Another example is the sediment-hosted As-Sb-Tl-Pb \pm Hg \pm Au mineralization of Janjevo, Kosovo, that is attributed to a distant, unknown porphyry system (Mederski et al. 2022). The source of these Carlin-like As-Sb-Tl-Pb + Au mineralizing fluids has been suggested by several authors to be fueled by subduction-related magmatism (e.g., Muntean et al. 2011, Mederski et al. 2022). This again suggests that pyrite geochemistry inherits trends related to the metal-source, without direct proximity to, e.g., a magma chamber. Sedimentary pyrite from both the DOF and the average Neoproterozoic sedimentary pyrite from Gregory et al. (2015) plot in a small gap between the hydrothermal and magmatic fields. This suggests that perhaps there is an additional application of the discrimination plot by Duran et al. (2015) to distinguish sedimentary to diagenetic pyrite from hydrothermal and magmatic pyrite.

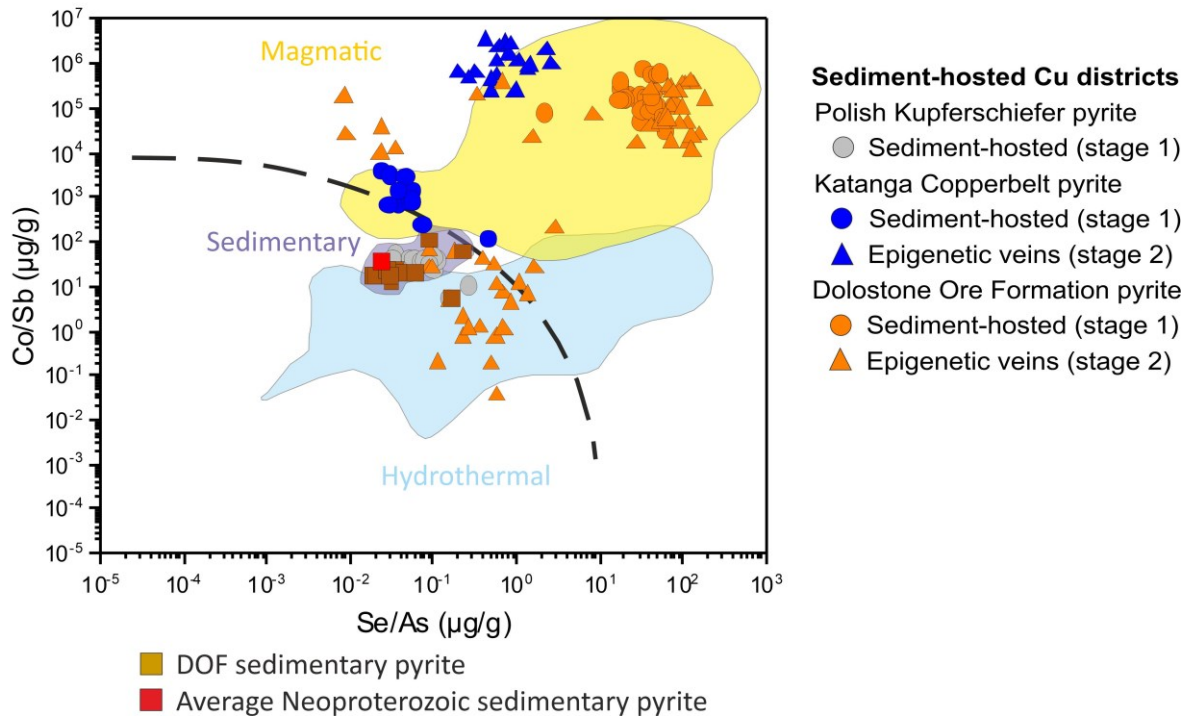


Fig. 14 Binary discrimination plot of hydrothermal and magmatic pyrite based of Se/As and Co/Sb (after Duran et al. 2015). Sedimentary DOF pyrite is shown separate along with a data point for average Neoproterozoic sedimentary pyrite from Gregory et al. (2015) as reference points for sedimentary pyrite field suggested in the study. DOF pyrite data includes combined data from this study and Bertrandsson Erlandsson et al. (2022)

5.4. Impact of metal sources on the sulfide trace element composition in sediment-hosted Cu(-Co) deposits

Trace elements in sulfides can be considered as a proxy for both metal source and mineralizing processes. Although this study has treated the investigated deposits as one deposit type (stratiform sediment-hosted Cu), it is worth keeping in mind that there are significant differences between European and African deposits. Kupferschiefer mineralization in Poland and Germany is Cu-Ag rich and relatively undeformed whilst the African deposits are distinctively Cu-Co rich and underwent significant deformation. Diagenetic mineralization in both districts likely formed in similar temperature, pH and Eh conditions, but the CACB also experienced syn- and post-tectonic mineralizing events, replacing earlier and forming new sulfides at significantly higher temperatures (e.g. El Desouky et al. 2009). This consideration helps to explain why overarching trends in the sulfide trace element geochemistry are not as straightforward. Indeed, the data shows more similarities between the African deposits compared to the Polish Kupferschiefer, and this is very likely due to the difference in metal sources for the metallogenic districts investigated herein. Higher temperature solutions are usually more effective in dissolving minerals and releasing metals as well as are more efficient as transporting agent. This could partially explain why African deposits are enriched in some elements (e.g., Co, In, and Sn) in comparison to the Kupferschiefer but the fact that deposits in Zechstein Basin are enriched in elements such as Ag or Tl indicates that the role of rocks providing the source of metals cannot be neglected.

5.4.1 Metal sources for the Polish Kupferschiefer

One of the main driving forces behind discussion about metal sources is the desire to explain the extraordinary size of the Kupferschiefer Cu-Ag deposit. Wedepohl et al. (1978) investigated Pb isotopes and suggested basement rocks as a major source of Pb in the Kupferschiefer ores but interpreted it in the light of the older syngenetic origin model, where eroded country rocks provide metals transported to the Zechstein Sea by rivers. More recent diagenetic-epigenetic models assume that the Cu and other metals were liberated by highly saline brines from the volcano-sedimentary sequence filling lower Permian basins (the Upper Rotliegendes red beds and bimodal volcanic units in the Lower Rotliegendes) but not exclude the possibility that underlying basement rocks, accessible by fault and shear zones, might also have played a role (Jowett 1986; Oszczepalski 1989; Borg 1991; Cathles et al. 1993; Oszczepalski 1999; Blundell et al. 2003; Hitzman et al. 2005; Brown 2009; Borg et al. 2012). Relative contribution is unclear but Borg (1991) pointed out that early Cisuralian volcanics show clear Cu depletion making them a prime candidate for the source. In addition, the Upper Rotliegendes red beds still have base metal contents at the level of or higher than Clark values (Rentzsch and Kampe 1979). Models might require an unrealistic assumption to account for the transport of up to 350 Mt of Cu in the southwest part of the Polish basin, therefore Cathles et al. (1993) included in the mass-balance calculations not only Permian rocks in the Fore-Sudetic Homocline but also underlying Carboniferous sediments while Blundell et al. (2003) in their deep-seated fault-fracture model favors the crystalline basement as source of metals. Many models assume liberation of metals from rock-forming minerals and also that the basement might have been leached by fluids, but metamorphic Variscan rocks might as well provide fertility in a more subtle way by constituting a source of clastic material supplying Carboniferous and Permian sediments underlying the Cu-Ag deposits in SW Poland. If mineralized, denuded crystalline rocks and hypothetical orebodies could supply certain metals to the Central European Permian Basin. The role of basement is additionally highlighted by the fact that even though red beds and volcanics cover a huge area from England to Lithuania, significant Cu-Ag deposits are conspicuously restricted and confined to the southern edge of the basin. Areas with rich mineralization in Poland and Germany form a curved belt located roughly above the Mid-German Crystalline High (basement rocks of magmatic arc origin) and Rhenohercynian Suture as well as their potential continuation or equivalent in Poland (Borg et al. 2012).

From the broad geotectonical point of view, the Variscan Orogen in the Central European belt was formed by accretion of a series of mainly Gondwana-derived small microplates/terranees which were progressively docked to the Laurussian margin during Devonian. In Carboniferous the amalgamation concluded with the collision of Gondwana with Laurussia and formation of Pangea in a major Himalaya type collisional event (Franke 2006). The assembly of this supercontinent involved closure of smaller ocean basins such as the Saxothuringian and Rhenohercynian oceans in the late Devonian and Mississippian (e.g. Franke et al. 2017). The subduction and plate collision may have provided favorable conditions for the formation of porphyry-epithermal style mineralization analogous to those known in the Tethyan Orogenic Belt in Europe and Asia, Paleozoic Central Asian Orogenic Belt or in the circum-Pacific region. However, porphyry style mineralizations are almost completely unknown/absent from the Variscan Belt at present time, most likely as a result of deep erosion of Variscan igneous rocks (although the possibility of deep burial below younger sediments cannot be excluded). A rare example of a porphyry-style

mineralization, which seems to be spatially and temporally related to the Variscan Orogen, is the Myszków Mo-Cu-W deposit in Poland, synchronous with felsic magmatism at 303.8 – 292.7 Ma (Mikulski and Stein 2012; Mikulski et al. 2019) and located at the Cracow-Lubliniec tectonic zone, aligned with the Middle Odra Fault Zone further to the NW. The Myszków deposit has been proposed to have partly been eroded and then covered by a sequence of Triassic marine rocks (Podemski 2001). Therefore, sediments derived from Myszków and hypothetical Variscan-related porphyry deposits further NW likely contributed to the sedimentation of the Rotliegend strata. Deep erosion of hypothetical epithermal-porphyry mineralization and rapid burial in an arid Permian climate (perhaps analogous to the modern Andes) before or after the collapse of Variscan Orogen had a potential to supply dispersed/diluted, but in terms of total tonnage quite substantial, amount of copper sulfides and products of their weathering. This could explain some of the features of the Kupferschiefer Cu-Ag deposit such as being dominantly Cu-Ag enriched with little Co. Besides copper, mineral deposits along the American Cordillera are also rich in Ag (Peru, Mexico, Chile, Bolivia are all top 10 Ag producers, US Geological Survey 2023), while Cu-Mo deposits there are world's major source of rhenium. Although these thoughts are hypothetical, they pose a reasonable explanation to the metals found in the Polish Kupferschiefer.

5.4.2 Metal sources for the African sediment-hosted Cu-Co deposits

In contrast to the Kupferschiefer, the CACB and DOF have a longer and more complex geological history with different orogenic and metamorphic events, making the true basement association more difficult. There are still several significant aspects to consider in relation to the possible source of metals. Whilst the source for the Cu-Co-Zn in the DOF is still highly uncertain, it is widely believed that the Cu-Co in the CACB is predominantly sourced from mafic volcanics and basement rocks or from the eroded products of basement rocks (e.g., Selley et al. 2005; Van Wilderode et al. 2014). As mafic rocks have more elevated concentrations of elements such as Co and Cu (Faure 1997), this is a more plausible metal source than for the Polish Kupferschiefer.

As the basement in the larger area around the CACB contains Cu-Co-Ni ores, these deposits (and their eroded detrital sediments) have been proposed to be a possible metal source for sediment-hosted Cu-Co deposits in the CACB (Cailteux et al. 2005; Kampunzu et al. 2009). Musongati and Kabanga are two examples of Ni-Cu-Co deposits situated in the Kibara Belt, north of the CACB (Pohl et al. 2013; Fig. 15). The Kibara Belt is a Mesoproterozoic NE-SW trending orogenic belt that stretches from the west of Lake Victoria down south and underneath the Lufilian Arc, wherein the CACB is situated (Fig. 15). The elevated concentrations of Sn in the CACB chalcopyrite (Fig. 2) support this model, as there is a vast amount of post-orogenic granite-related Sn(-W-Ta) mineralization also present in the Kibara Belt (Pohl et al. 2013; Hulsbosch et al. 2014; Fig. 15). The possible occurrence of post-orogenic Sn-granites (Caron et al. 1986) in the basement, could explain the Sn enrichment in CACB chalcopyrite (Fig. 2). A similar source may be present, although unknown, in the Kunene region of the DOF.

Both KCB and ZCB chalcopyrite show elevated concentrations of Ga and the KCB shows elevated Ge compared to the other districts (Fig. 2). The SSHCD are not the only example of ore deposits with elevated Ga and Ge concentrations: the carbonate-hosted Kipushi deposit in Katanga is well known for its Ga- and Ge-phases but these elements also occur within both chalcopyrite and sphalerite (Kelvin et al. 2022). It is evident that, in particular in the Katanga part, the CACB is rich

in Ga and Ge mineralization, which is mirrored in its SSHCDs, although the Kipushi deposit formed much later than the SSHCDs (Schneider et al. 2007; Heijlen et al. 2008). Van Wilderode et al. (2013) suggested that the origin of Ga and Ge in the Kipushi deposit was most probably both mafic and felsic rocks within the basement, and possibly the siliciclastic Roan sediments. Hence, a similar source for Ga and Ge in the SSHCDs may be plausible.

The relation between Cu mineralization and especially the associated metals and different basement rocks in the host basins, suggests that source rocks heavily impact the trace element composition of the sulfides in SHCDs.

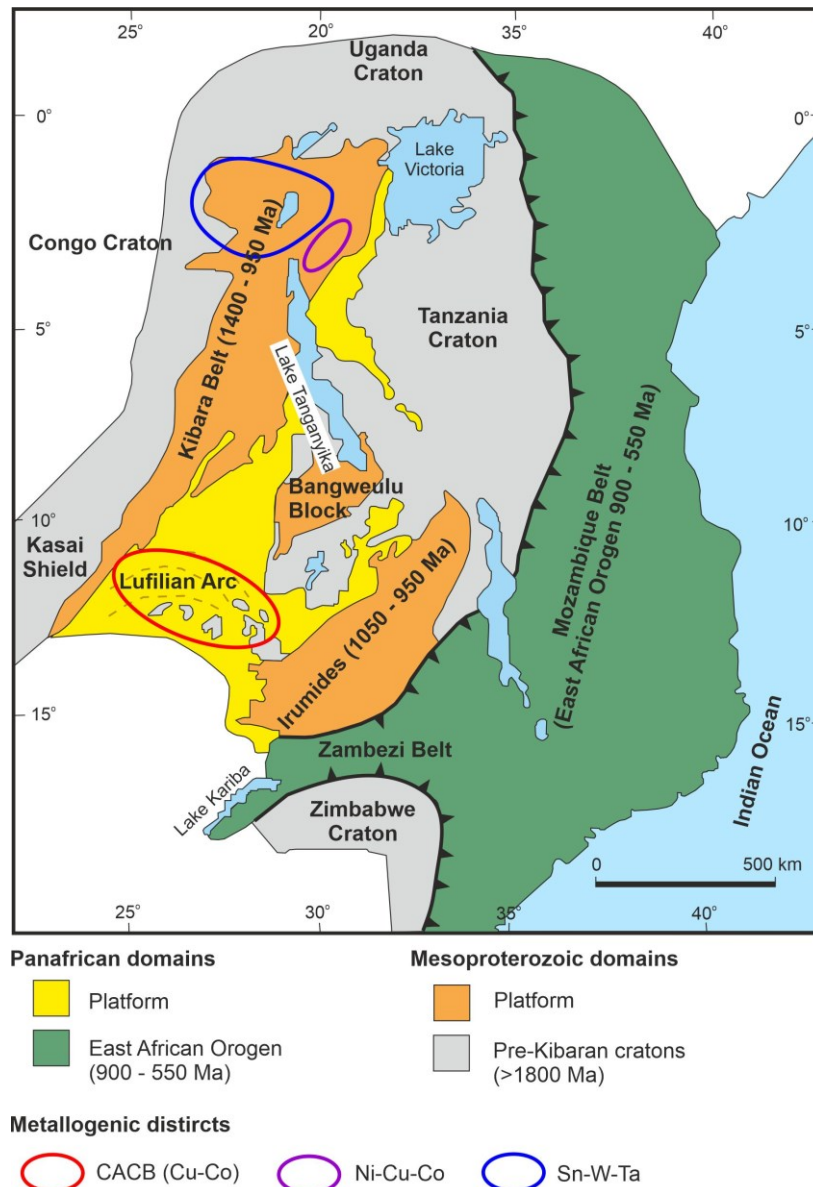


Fig. 15 Metallogenic districts containing elements associated with the sulfide trace element compositions in the sediment-hosted copper deposits of the Central African Copperbelt (CACB). Geological units simplified after De Waele et al. (2008), metallogenic districts after Pohl et al. (2013)

5.5 Trace element distributions between sulfides from different sediment-hosted Cu(-Co) deposits

Chalcopyrite from the Polish Kupferschiefer shows the most elevated trace element concentrations (Mn, Ni, Ge, As, Se, Ag, Tl, and Pb), compared to the Congolese and Zambian Copperbelt deposits and the DOF (Table 2). KCB chalcopyrite also contains high concentrations of Ge along with Ga, In, Sn, and Te. The ZCB chalcopyrite only shows elevated concentrations of Mn and Zn, where the elevated Zn may relate to the elevated formation temperatures. Both Co and Ni are elevated in DOF chalcopyrite. Sphalerite from the Polish Kupferschiefer shows higher concentrations of Ge typically associated with lower-temperature sphalerite, whilst DOF sphalerite contains higher concentrations of elements associated with higher-temperature sphalerite, i.e. Mn, Fe and In. Although Co occurs at high concentrations in pyrite from both the KCB and DOF, pyrite from the KCB contains higher concentrations than DOF pyrite. Sulfides from the Polish Kupferschiefer (chalcopyrite and sphalerite) show elevated concentrations of Ge, Ag, Tl, and Pb. The most noteworthy trace elements in chalcopyrite from the KCB are Ga and Sn. The Namibian DOF shows higher concentrations of both Co and Ni in both chalcopyrite and sphalerite, sphalerite containing significantly high Co concentrations. DOF pyrite is also Co-rich, but not to the same degree as pyrite from the KCB.

Table 2 Significant elements in sulfides from the investigated sediment-hosted Cu(-Co) deposits, based on the element composition and the Random Forest analyses. Elements written in “italics” were not recognized by the Random Forest analyses to have significant Gini values or are relatively low, compared to other more significantly enriched mineralization stages. Abbreviations: CB = Copperbelt; DOF = Dolostone Ore Formation; na = not applicable

		Chalcopyrite	Sphalerite	Pyrite
Polish Kupferschiefer	Stage 1	Mn, <i>Ni</i> , Ag, Tl, Pb	Ni, Ga, Se, Ag, Cd, Hg, Tl, Pb	Mn, Cu, As, <i>Sn</i> , Tl, Pb
	Stage 2	Mn, Ge, As, <i>Ag</i> , Sb, Pb	<i>Ag</i> , Cd, <i>Tl</i>	na
Katanga CB	Stage 1	<i>Ga</i> , In, Sn, <i>Sb</i>	na	Co, Cu, As, Sn
	Stage 2	Ga, In, Sn	na	<i>Co</i> , As, Se
Zambian CB	Stage 1	Mn, Zn, Sn	na	na
Namibian DOF	Stage 1	Co, Zn, Sn	Fe, Co, Ni, In	<i>Co</i>
	Stage 2	Ni, Zn, Se, <i>Sn</i>	<i>Fe</i> , <i>Co</i> , Ni, Se, Cd, In	<i>Pb</i>

6. Conclusions

Random Forest analysis of chalcopyrite attributes Ag and Tl to the Polish Kupferschiefer, Ga and Ge to the KCB and Zn and In to the DOF as top district indicator elements. Cobalt, Ni, Se, and Bi in chalcopyrite show similar concentrations between the four investigated districts. Gallium occurs in relatively low median concentrations in chalcopyrite (<10 µg/g) in all deposits except the KCB that has median Ga concentrations of 32 µg/g. Cobalt, Sn and Hg distinguish chalcopyrite from sediment-hosted Cu(-Co) deposits to that of other ore deposit types, e.g. VMS, SEDEX, skarn, epithermal and porphyry copper. Additionally, As, Ag, In, Sn, and Sb show potential in discriminating chalcopyrite from sediment-hosted Cu deposits to chalcopyrite from sediment-hosted Cu-Co deposits.

Random Forest analysis of sphalerite attributes Cd and Tl along with Fe and In, as top indicator elements for sphalerite from the Polish Kupferschiefer and DOF. Both Fe and In are strongly temperature dependent in sphalerite (Frenzel et al. 2016) which helps to explain this difference. Sphalerite from sediment-hosted Cu(-Co) deposits are poor in Mn, Ga, Ge and Ag when compared to sphalerite from other deposit types. Sphalerite from the Polish Kupferschiefer shows the lowest average concentrations of Mn, Fe and In when compared to other genetic types of sphalerite. Cobalt is only highly enriched in the sediment-hosted Cu-Co DOF sphalerite, in particular when formed during the main Co-phase. Later Cu-Zn-Pb ore stages form sphalerite with significantly lower Co concentrations. Sphalerite trace element geochemistry is different from other ore deposit types for genetic discrimination of sphalerite from both sediment-hosted Cu and Cu-Co deposit independently (Fig. 12).

Random Forest analysis of pyrite attributes As to the KCB and Mn to the DOF, as top indicator elements for pyrite between the two deposits. Cobalt is highly enriched in pyrites from sediment-hosted Cu-Co deposits that dominantly show Co/Ni ratios separate from that of volcanic, magmatic and sedimentary pyrite (Fig. 13). Cobalt occurs as both solid solution and as individual inclusions in pyrite from sediment-hosted Cu-Co deposits. Although the source of cobalt in these types of deposits are enigmatic, it is evident that cobalt is enriched in other sulfides associated with the Co-mineralization, such as sphalerite and pyrite. Sedimentary pyrite trace element compositions from the DOF are in accordance to that of typical sedimentary pyrite (Gregory et al. 2015), but is slightly enriched in Co (Fig. 13). This suggests that the introduction of Co may have started during (early) diagenesis even in the case of the metamorphosed DOF deposit that otherwise show little association to a sedimentary origin of Co-mineralization (Bertrandsson Erlandsson et al. 2022).

From the trace element-based discrimination plots, SSHCDs needs to be included as a deposit type as they plot differently from the pre-existing deposit type fields. Trace element composition clearly shows that there are deposit-dependent differences between the investigated metallogenic Cu(-Co) districts. The African districts show more similarities compared to the Polish Kupferschiefer. This is proposed to primarily be due to the impact of the metal sources in the different host basins. With the African districts being situated in similar tectonostratigraphic settings, it is not surprising that these districts have more similarities than to the Polish Kupferschiefer.

Acknowledgements

The authors acknowledge whole Gecko Namibia exploration team who's time and effort enabled the DOF sample campaign. Philippe Muchez acknowledges the financial support from the research grant C14/21/056 of the KU Leuven Special Research Fund.

Include Conflict of Interest

The authors declare no competing interests.

References

- Alderton DHM, Selby D, Kucha H, Blundell DJ (2016) A multistage origin for Kupferschiefer mineralization. *Ore Geol Rev* (79), pp. 535–543.
- Allen NK (2016) Structurally controlled Cu-Zn-(Co-Pb) mineralization in the Neoproterozoic Ombombo Subgroup, Kaokoland, Namibia. Master Thesis. Colorado School of Mines.
- Annels AE (1986) Ore genesis in the Zambia copperbelt, with particular reference to the northern sector of the Chambishi basin. *Can Mineral: Mineral Assoc Can. Cityview 78087*. Canada.
- Armstrong RA, Master S, Robb LJ (2005) Geochronology of the Nchanga Granite, and constraints on the maximum age of the Katanga Supergroup, Zambian Copperbelt. In *Journal of African Earth Sciences* 42 (1-5), pp. 32–40.
- Barra F, Broughton D, Ruiz J, Hitzman M (2004) Multi-stage mineralization in the Zambian Copperbelt based on Re-Os isotope constraints. *Geolo Soc Am Abstr Progrs* (Vol. 36, No. 5, p. 516).
- Bartholomé P, Evrard P, Katekesha F, Lopez-Ruiz J, Ngongo M (1972) Diagenetic ore-forming processes at Kamoto, Katanga, Republic of the Congo. In Amstutz GC, Bernard AJ, *Ore sediments*. Springer-Verlag, New York, p 21-41.
- Bartholomé P, Katekesha F, Ruiz J, López (1971) Cobalt zoning in microscopic pyrite from Kamoto, Republic of the Congo (Kinshasa). *Miner Deposita* 6 (3), pp. 167–176.
- Bechtel A, Elliott WC, Wampler JM, Oszczepalski S (1999) Clay mineralogy, crystallinity, and K-Ar ages of illites within the Polish Zechstein Basin; implications for the age of Kupferschiefer mineralization. *Econ Geol* 94 (2), pp. 261–272.
- Bechtel A, Püttmann W, Hoernes S (1995) Reconstruction of the thermal history of the Kupferschiefer within the Zechstein basin of central Europe: A stable isotope and organic geochemical approach. *Ore Geol Rev* 9 (5), pp. 371–389.
- Belissant R, Boiron MC, Luais B, Cathelineau M (2014) LA-ICP-MS analyses of minor and trace elements and bulk Ge isotopes in zoned Ge-rich sphalerites from the Noailhac–Saint-Salvy deposit (France): Insights into incorporation mechanisms and ore deposition processes. *Geochim Cosmochim Acta* (126), pp. 518–540.
- Bertrandsson Erlandsson V, Wallner D, Ellmies R, Raith JG, Melcher F (2022) Trace element composition of base metal sulfides from the sediment-hosted Dolostone Ore Formation (DOF) Cu-Co deposit in northwestern Namibia: Implications for ore genesis. *J Geochem Explo*, p. 107105.
- Blundell DJ, Karnkowski PH, Alderton DHM, Oszczepalski S, Kucha H (2003) Copper mineralization of the Polish Kupferschiefer: a proposed basement fault-fracture system of fluid flow. *Econ Geol* 98 (7), pp. 1487–1495.
- Borg G (1991) The significance of Rotliegend volcanics for the metal provinces of the Kupferschiefer Basin. *Zbl. Geol. Paläont. Teil I, H 4*, pp. 929–943.
- Borg G, Piestrzyński AB, Gerhard H, Püttmann W, Walther S, Fiedler M (2012) An Overview of the European Kupferschiefer Deposits.
- Breiman L (2001) Random forests. *Machine learning* 45 (1), pp. 5–32.
- Brems D, Muchez P, Sikazwe O, Mukumba W (2009) Metallogenesis of the Nkana copper–cobalt south orebody, Zambia. *J Afri Earth Sci* (55), 3-4, pp. 185–196.

Brown AC (2009) A process-based approach to estimating the copper derived from red beds in the sediment-hosted stratiform copper deposit model. *Econ Geol* (104), 6, pp. 857–868.

Cailteux JLH, Kampunzu AB, Lerouge C, Kaputo AK, Milesi JP (2005) Genesis of sediment-hosted stratiform copper–cobalt deposits, central African Copperbelt. *J Afri Earth Sci* (42), 1-5, pp. 134–158.

Cailteux JLH, Muchez P, Cuyper J, Dewaele S, Putter T (2018) Origin of the megabreccias in the Katanga Copperbelt (DR Congo). *J Afri Earth Sci* 140, pp. 76–93.

Campbell FA, Ethier VG (1984) Nickel and cobalt in pyrrhotite and pyrite from the Faro and Sullivan orebodies. *Can Mineral* (22), 3, pp. 503–506.

Caron JPH, Kampunzu AB, Lwango LB, Manteka B, Nkanika WR (1986) Les ressources minérales d'âge protérozoïque moyen en Afrique équatoriale et l'évolution géodynamique de la chaîne Kibarienne.

Cathles LM, Oszczepalski S, Jowett EC (1993) Mass balance evaluation of the late diagenetic hypothesis for Kupferschiefer Cu mineralization in the Lubin Basin of southwestern Poland. *Econ Geol* 88. doi: <https://doi.org/10.2113/gsecongeo.88.4.948>, pp. 948–956

Celsius Resources Limited (2021) ASX Release 1 July 2021 Celsius doubles mineral resource at Opuwo cobalt-copper project.

Chen F, Deng J, Wang Q, Huizenga JM, Li G, Gu Y (2020) LA-ICP-MS trace element analysis of magnetite and pyrite from the Hetaoping Fe-Zn-Pb skarn deposit in Baoshan block, SW China: Implications for ore-forming processes. *Ore Geol Rev* 117, p. 103309.

Chon HT, Shimazaki H (1986) Iron, manganese and cadmium contents of sphalerites and their genetical implications to hydrothermal metallic ore deposits in Korea. *Econo Enviro Geol* 19 (spc), pp. 139–149.

Cook NJ, Ciobanu CL, George LL, Zhu ZY, Wade B, Ehrig K (2016) Trace element analysis of minerals in magmatic-hydrothermal ores by laser ablation inductively-coupled plasma mass spectrometry: Approaches and opportunities. *Minerals* (6), 4, p. 111.

Cook NJ, Ciobanu CL, Pring A, Skinner W, Shimizu M, Danyushevsky LV et al. (2009) Trace and minor elements in sphalerite: A LA-ICPMS study. *Geochim Cosmochim Acta* (73), 16, pp. 4761–4791.

Daliran F, Hofstra A, Walther J, Topa D (2018) Ore genesis constraints on the Agdarreh and Zarshouran Carlin-style gold deposits in the Takab region of northwestern Iran.

Daly MC, Chakraborty SK, Kasolo P, Musiwa M, Mumba P, Naidu B et al (1984) The Lufilian arc and Irumide belt of Zambia: results of a geotraverse across their intersection. *J Afri Earth Sci* (1983) 2 (4), pp. 311–318.

Development Core Team R (2013) R: A language and environment for statistical computing.

Dewaele S, Muchez P, Vets J, Fernandez-Alonzo M, Tack L (2006) Multiphase origin of the Cu–Co ore deposits in the western part of the Lufilian fold-and-thrust belt, Katanga (Democratic Republic of Congo). *J Afri Earth Sci* (46), 5, pp. 455–469.

Duran CJ, Barnes SJ, Corkery JT (2015) Chalcophile and platinum-group element distribution in pyrites from the sulfide-rich pods of the Lac des Iles Pd deposits, Western Ontario, Canada: Implications for post-cumulus re-equilibration of the ore and the use of pyrite compositions in exploration. *J Geochem Explo* 158, pp. 223–242.

Duran CJ, Dubé-Loubert H, Pagé P, Barnes SJ, Roy M, Savard D et al (2019) Applications of trace element chemistry of pyrite and chalcopyrite in glacial sediments to mineral exploration targeting: Example from the Churchill Province, northern Quebec, Canada. *J Geochem Explo* (196), pp. 105–130.

El Desouky HA, Muchez P, Boyce AJ, Schneider J, Cailteux JHL, Dewaele S, Quadt A (2010) Genesis of sediment-hosted stratiform copper–cobalt mineralization at Luiswishi and Kamoto, Katanga Copperbelt (Democratic Republic of Congo). *Miner Deposita* 45 (8), pp. 735–763.

El Desouky HA, Muchez P, Cailteux J (2009) Two Cu–Co sulfide phases and contrasting fluid systems in the Katanga Copperbelt, Democratic Republic of Congo. *Ore Geol Rev* 36 (4), pp. 315–332.

Esri (2018) OpenStreetMap contributors, and the GIS user community. Software: ArcGIS, ArcMap.

Faure G (1997) Principles and applications of geochemistry: Prentice Hall Upper Saddle River, NJ.

Foltyn K, Bertrandsson Erlandsson V, Zygo W, Melcher F, Pieczonka J, (2022) New perspective on trace element (Re, Ge, Ag) hosts in the Cu-Ag Kupferschiefer deposit, Poland: insight from a LA-ICP-MS trace element study. *Ore Geol Rev*, p. 104768.

Foster DA, Goscombe BD, Gray DR (2009) Rapid exhumation of deep crust in an obliquely convergent orogen: The Kaoko Belt of the Damara Orogen. *Tectonics* (28), 4, 1-24.

Franchini M, McFarlane C, Maydagán L, Reich M, Lentz DR, Meinert L, Bouhier V (2015) Trace metals in pyrite and marcasite from the Agua Rica porphyry-high sulfidation epithermal deposit, Catamarca, Argentina: Textural features and metal zoning at the porphyry to epithermal transition. *Ore Geol Rev* 66, pp. 366–387.

Franke W (2006) The Variscan orogen in Central Europe: construction and collapse. *Geol Soc, London, Memoirs* 32 (1), pp. 333–343.

Franke W, Cocks L, Robin M, Torsvik TH, (2017) The palaeozoic variscan oceans revisited. *Gondwana Research* 48, pp. 257–284. doi: <https://doi.org/10.1016/j.gr.2017.03.005>

Frenzel M, Hirsch T, Gutzmer J (2016) Gallium, germanium, indium, and other trace and minor elements in sphalerite as a function of deposit type - A meta-analysis. *Ore Geol Rev* (76), pp. 52–78.

George LL, Cook NJ, Crowe BBP, Ciobanu CL (2018) Trace elements in hydrothermal chalcopyrite. *Mineral Mag* (82), 1, pp. 59–88.

Glennie KW, Buller AT (1983) The Permian Weissliegendes of NW Europe: the partial deformation of aeolian dune sands caused by the Zechstein transgression. *Sediment Geol* 35 (1), pp. 43–81.

Goscombe BD (1999) Geological report on magnetic and radiometric anomalies mapped in the region south of the Kunene Igneous Complex, Namibia. Company exploration reports, Geolo Surv Namibia.

Goscombe BD, Gray DR, Hand M (2005) Extrusional Tectonics in the Core of a Transpressional Orogen; the Kaoko Belt, Namibia. *J Petro* (46), 6, pp. 1203–1241.

Goscombe BD, Hand M, Gray DR (2003) Structure of the Kaoko Belt, Namibia: progressive evolution of a classic transpressional orogen. *J Struct Geol* (25), 7, pp. 1049–1081.

Gregory DD, Large RR, Halpin JA, Baturina EL, Lyons TW, Wu S et al (2015) Trace element content of sedimentary pyrite in black shales. *Soc Econ Geol Spec Pub* 16 (110), 6, pp. 1389–1410.

Gregory DD, Cracknell MJ, Large RR, McGoldrick P, Kuhn S, Maslennikov VV et al (2019) Distinguishing ore deposit type and barren sedimentary pyrite using laser ablation-inductively coupled plasma-mass spectrometry trace element data and statistical analysis of large data sets. *Econ Geol* 114 (4), pp. 771–786.

Guj P (1970) The Damara Mobile Belt in the south-western Kaokoveld South West Africa. PhD Thesis. University of Cape Town / Precambrian Research Unit, Cape Town, South Africa.

Hanson RE, Wardlaw MS, Wilson TJ, Mwale G (1993) U/Pb zircon ages from the Hook granite massif and Mwembeshi dislocation: Constraints on Pan-African deformation, plutonism, and transcurrent shearing in central Zambia. *Precambrian Research* 63 (3-4), pp. 189–209.

Heijlen W, Banks DA, Muchez P, Stensgard BM, Yardley BWD (2008) The nature of mineralizing fluids of the Kipushi Zn-Cu deposit, Katanga, Democratic Republic of Congo: Quantitative fluid inclusion analysis using laser ablation ICP-MS and bulk crush-leach methods. *Econ Geol* 103 (7), pp. 1459–1482.

Hitzman MW, Broughton D, Selley D, Woodhead J, Wood D, Bull S (2012) The Central African Copperbelt: diverse stratigraphic, structural, and temporal settings in the world's largest sedimentary copper district. *Soc of Econ Geol Spec Publ* (16), pp. 487–514.

Hitzman MW, Kirkham R, Broughton D, Thorson J, Selley D (2005) The sediment-hosted stratiform copper ore system. *Econ Geol* (100).

Hoffman PF, Halverson GP (2008) Otavi Group of the western Northern Platform, the Eastern Kaoko Zone and the western Northern Margin Zone. R. McG. Miller: The Geology of Namibia: Neoproterozoic to Lower Palaeozoic. 2nd ed. Windhoek, Namibia: *Geolo Surv* (2), 13-69–13-136.

Hu Y, Wei C, Ye L, Huang Z, Danyushevsky Leonid WH (2021) LA-ICP-MS sphalerite and galena trace element chemistry and mineralization-style fingerprinting for carbonate-hosted Pb-Zn deposits: Perspective from Early Devonian Huodehong deposit in Yunnan, South China. *Ore Geol Rev*, p. 104253.

Hulsbosch N, Hertogen J, Dewaele S, André L, Muchez P (2014) Alkali metal and rare earth element evolution of rock-forming minerals from the Gatumba area pegmatites (Rwanda): Quantitative assessment of crystal-melt fractionation in the regional zonation of pegmatite groups. *Geochim Cosmochim Acta* 132, pp. 349–374.

John T, Schenk V, Mezger K, Tembo F (2004) Timing and PT evolution of whiteschist metamorphism in the Lufilian Arc–Zambezi Belt orogen (Zambia): implications for the assembly of Gondwana. *J Geol* 112 (1), pp. 71–90.

Jowett EC (1987) Formation of sulfide-calcite veinlets in the Kupferschiefer Cu-Ag deposits in Poland by natural hydrofracturing during basin subsidence. *J Geol* (95), 4, pp. 513–526.

Jowett EC (1986) Genesis of Kupferschiefer Cu-Ag deposits by convective flow of Rotliegendes brines during Triassic rifting. *Econ Geol* 81 (8), pp. 1823–1837.

Jowett EC, Pearce GW, Rydzewski A (1987) A Mid-Triassic paleomagnetic age of the Kupferschiefer mineralization in Poland, based on a revised apparent polar wander path for Europe and Russia. *J Geophysical Research: Solid Earth* 92 (B1), pp. 581–598.

Kamunzu AB, Cailteux JLH, af Kamona, Intiomale MM, Melcher F (2009) Sediment-hosted Zn–Pb–Cu deposits in the Central African Copperbelt. *Ore Geol Rev* (35), 3-4, pp. 263–297.

Karnkowski PH (1999) Origin and evolution of the Polish Rotliegend Basin. *Polish Geol Inst Spec Papers* 3, pp. 1–93.

Kelley KD, Leach L, Johnson CA, Clark JL, Fayek M, Slack JF et al (2004) Textural, compositional, and sulfur isotope variations of sulfide minerals in the Red Dog Zn-Pb-Ag deposits, Brooks Range, Alaska: Implications for ore formation. *Econ Geol* 99 (7), pp. 1509–1532.

Kelvin M, Whiteman E, Petrus J, Leybourne M, Nkuna V (2022) Application of LA-ICP-MS to process mineralogy: Gallium and germanium recovery at Kipushi copper-zinc deposit. *Minerals Eng* 176, p. 107322.

Kiersnowski H, Buniak A (2006) Evolution of the Rotliegend Basin of northwestern Poland. *Geol Quart* 50 (1), pp. 119–138.

Kłapciński J, Peryt TM (2007) Budowa geologiczna monokliny przedsudeckiej. *Monografia KGHM Polska Miedź SA*, pp. 69–77.

Kłapciński J (1971) Lithology, fauna, stratigraphy, and paleogeography of the Permian in the Fore-Sudetic monocline. *Geologia Sudetica* 5, pp. 77–135.

Large RR, Halpin JA, Danyushevsky LV, Maslennikov VV, Bull SW, Long JA et al (2014) Trace element content of sedimentary pyrite as a new proxy for deep-time ocean–atmosphere evolution. *Earth and Planetary Sci Letters* (389), pp. 209–220.

Large RR, Maslennikov VV, Robert F, Danyushevsky LV, Chang Z (2007) Multistage sedimentary and metamorphic origin of pyrite and gold in the giant Sukhoi Log deposit, Lena gold province, Russia. *Econ Geol* (102), 7, pp. 1233–1267.

Large RR, Danyushevsky L, Hollit C, Maslennikov V, Meffre S, Gilbert S et al (2009) Gold and trace element zonation in pyrite using a laser imaging technique: Implications for the timing of gold in orogenic and Carlin-style sediment-hosted deposits. *Econ Geol* 104 (5), pp. 635–668.

Liu S, Zhang Y, Ai G, Xue X, Li H, Shah SA et al (2022) LA-ICP-MS trace element geochemistry of sphalerite: Metallogenic constraints on the Qingshuitang Pb–Zn deposit in the Qinhang Ore Belt, South China. *Ore Geol Rev* 141, p. 104659.

Loftus-Hills G, Solomon M (1967) Cobalt, nickel and selenium in sulphides as indicators of ore genesis. *Miner Deposita* (2), 3, pp. 228–242.

Mambwe P, Swennen R, Cailteux J, Mumba C, Dewaele S, Muchez P (2023) Review of the origin of breccias and their resource potential in the Central Africa Copperbelt. *Ore Geol Rev*, p. 105389.

Mansur ET, Dare SAS, Ferreira Filho CF, Miranda ACR, Monteiro LVS (2022) The distribution of trace elements in sulfides and magnetite from the Jaguar hydrothermal nickel deposit: exploring the link with IOA and IOCG deposits within the Carajás Mineral Province, Brazil. *Ore Geol Rev*, p. 105256.

Marsh EE, Hitzman MW, Leach David L (2016) Critical elements in sediment-hosted deposits (clastic-dominated Zn-Pb-Ag, Mississippi Valley-type Zn-Pb, sedimentary rock-hosted Stratiform Cu, and carbonate-hosted Polymetallic Deposits): A review.

Master S, Rainaud C, Armstrong RA, Phillips D, Robb LJ (2005) Provenance ages of the Neoproterozoic Katanga Supergroup (Central African Copperbelt), with implications for basin evolution. *J Afri Earth Sci* 42 (1-5), pp. 41–60.

McCann T, Pascal C, Timmerman MJ, Krzywiec P, López-Gómez J, Wetzel L et al (2006) Post-Variscan (end Carboniferous–Early Permian) basin evolution in western and central Europe. *Geol Soc Lon, Memoirs* 32 (1), pp. 355–388.

McGowan RR, Roberts S, Boyce AJ (2006) Origin of the Nchanga copper–cobalt deposits of the Zambian Copperbelt. *Miner Deposita* (40), 6-7, p. 617.

McGowan RR, Roberts S, Foster RP, Boyce AJ, Coller D (2003) Origin of the copper-cobalt deposits of the Zambian Copperbelt: An epigenetic view from Nchanga. *Geology* 31 (6), pp. 497–500.

Mederski S, Pršek J, Majzlan J, Kiefer S, Dimitrova D, Milovský R et al (2022) Geochemistry and textural evolution of As-Tl-Sb-Hg-rich pyrite from a sediment-hosted As-Sb-Tl-Pb±Hg±Au mineralization in Janjevo, Kosovo. *Ore Geol Rev*, p. 105221.

Mendelsohn F (1961) The geology of the northern Rhodesian copperbelt: Macdonald.

Menning M, Alekseev AS, Chuvashov BI, Davydov VI, Devuyt FX, Forke HC et al (2006) Global time scale and regional stratigraphic reference scales of central and west Europe, east Europe, Tethys, south China, and North America as used in the Devonian–Carboniferous–Permian Correlation Chart 2003 (DCP 2003). *Palaeogeography, palaeoclimatology, palaeoecology* 240 (1-2), pp. 318–372.

Michalik M, Sawłowicz Z (2001) Multi-stage and long-term origin of the Kupferschiefer copper deposits in Poland. *Mineral Deposits at the Beginning of the 21st Century: CRC Press*, pp. 235–238.

Mikulski SZ, Stein HJ (2012) The age of molybdenites in Poland in the light of Re-Os isotopic studies. *Biul Państ Inst Geol* 452, pp. 199–216.

Mikulski SZ, Stein HJ (2015) Re-Os ages for Ag-bearing Cu sulphide ores from the Kupferschiefer in Poland. *Proc 13th Biennial SGA Meeting*.

Mikulski SZ, Stein HJ (2017) Re-Os isotopic age of the Cu-Ag sulphide ore and its mineralogical and geochemical characteristic from the Lubin-Polkowice mining area (SW Poland). *Biuletyn–Panstwowego Instytutu Geologicznego* 468, pp. 79–96.

Mikulski SZ, Williams IS, Markowiak M (2019) Carboniferous–Permian magmatism and Mo–Cu (W) mineralization in the contact zone between the Małopolska and Upper Silesia Blocks (south Poland): An echo of the Baltica–Gondwana collision. *Int J Earth Sci* 108, pp. 1467–1492.

Miller RMG (2008) *The Geology of Namibia: Neoproterozoic to Lower Palaeozoic*. 2nd ed. Windhoek, Namibia: *Geol Surv* (2).

Molak B (1995) Some structural and petrological aspects of the Cu (Co) mineralization in the Copperbelt and northwestern provinces of Zambia. *Annales des Sciences Géologiques: Royal Museum of Central Africa, Tervuren Belgium*.

Muntean JL, Cline JS, Simon AC, Longo AA (2011) Magmatic–hydrothermal origin of Nevada’s Carlin-type gold deposits. *Nature geosci* 4 (2), pp. 122–127.

Nawrocki J (2000) Clay mineralogy, crystallinity, and K-Ar ages of illites within the Polish Zechstein Basin: Implications for the age of Kupferschiefer mineralization—A discussion. *Econ Geol* 95 (1), pp. 241–242.

Nawrocki J (2017) O wieku paleomagnetycznym mineralizacji miedziowej, uranowej i cynkowo-olowiowej w Polsce określanym metodą porównania charakterystycznych namagnesowań z krzywą referencyjną pozornej wędrówki bieguna paleomagnetycznego. *Przegląd Geologiczny* 65 (2).

Onuk P, Melcher F, Mertz-Kraus R, Gäbler HE, Goldmann S (2017) Development of a Matrix-Matched Sphalerite Reference Material (MUL -ZnS-1) for Calibration of In Situ Trace Element Measurements by Laser Ablation-Inductively Coupled Plasma-Mass Spectrometry. *Geostandards and Geoanalytical Research* (41), 2, pp. 263–272.

Oszczepalski S (1999) Origin of the Kupferschiefer polymetallic mineralization in Poland. *Miner Deposita* 34 (5), pp. 599–613.

Oszczepalski S (1989) Kupferschiefer in southwestern Poland: sedimentary environments, metal zoning, and ore controls. *GAC Spec. Paper* 36, pp. 571–600.

Paton C, Hellstrom J, Paul B, Woodhead J, Hergt J (2011) Iolite: Freeware for the visualisation and processing of mass spectrometric data. *J Analytical Atomic Spectrometry* (26), 12, pp. 2508–2518.

Paul J (2006) Der Kupferschiefer: Lithologie, Stratigraphie, Fazies und Metallogenese eines Schwarzschiefers. *Zeitschrift der deutschen Gesellschaft für Geowissenschaften* 157 (1), pp. 57–76.

Peryt TM, Durakiewicz T, Kotarba MJ, Oszczepalski S, Peryt D (2012) Carbon isotope stratigraphy of the basal Zechstein (Lopingian) strata in Northern Poland and its global correlation. *Geol Quart* 56 (2), 285–298, doi: <http://dx.doi.org/10.7306/gq.1022>.

PGI, Państwowy Instytut Geologiczny (2021) The balance of mineral resources deposits in Poland (in Polish). *Bilansu zasobów złóż kopalin w Polsce. Stanu na 31 XII*. ISSN 2299-4459.

Podemski M (2001) Palaeozoic porphyry molybdenum-tungsten deposit in the Myszków area, Southern Poland. *Polish Geol Inst Spec Papers* 6, pp. 1–88.

Pohl WL, Biryabarema M, Lehmann B (2013) Early Neoproterozoic rare metal (Sn, Ta, W) and gold metallogeny of the Central Africa Region: a review. *Appl Earth Sci* 122 (2), pp. 66–82.

Porada H (1989) Pan-African rifting and orogenesis in southern to equatorial Africa and eastern Brazil. *Precambrian Research* (44), 2, pp. 103–136.

Rainaud C, Master S, Armstrong RA, Phillips D, Robb LJ (2005) Monazite U–Pb dating and ⁴⁰Ar–³⁹Ar thermochronology of metamorphic events in the Central African Copperbelt during the Pan-African Lufilian Orogeny. *J Afri Earth Sci* 42 (1–5), pp. 183–199.

Rentzsch J, Kampe A (1979) Zur geochemie der sedimentite des Permosiles im Südteil der DDR. *Physics and Chem Earth* 11, pp. 751–766.

Richards JP, Krogh TE, Spooner ETC (1988) Fluid inclusion characteristics and U–Pb rutile age of late hydrothermal alteration and veining at the Musoshi stratiform copper deposit, Central African copper belt, Zaire. *Econ Geol* 83 (1), pp. 118–139.

Sangster DF (2002) The role of dense brines in the formation of vent-distal sedimentary-exhalative (SEDEX) lead–zinc deposits: field and laboratory evidence. *Miner Deposita* 37 (2), pp. 149–157.

Schneider J, Melcher F, Brauns M (2007) Concordant ages for the giant Kipushi base metal deposit (DR Congo) from direct Rb–Sr and Re–Os dating of sulfides. *Miner Deposita* 42, pp. 791–797.

Schwartz MO (2000) Cadmium in zinc deposits: Econ Geol of a polluting element. *Int Geol Rev* 42 (5), pp. 445–469.

Selley D, Broughton D, Scott RJ, Hitzman M, Bull SW, Large RR et al (2005) A new look at the geology of the Zambian Copperbelt. *Soc Econ Geol*, p. 100.

Speczik S, Puttmann W (1987) Origin of Kupferschiefer mineralization as suggested by coal petrology and organic geochemical studies. *Acta Geologica Polonica* 37 (3–4), pp. 167–188.

Strengel-Martinez M, Speczik S, Jankowski J (1993) Epigenetic veins in Kupferschiefer deposits of SW Poland. *Archiwum mineralogiczne* 49 (1), pp. 203–204.

Swardt AM (1962) Structural relationships in the N. Rhodesian Copperbelt: an alternative explanation. *Northern Rhodesia Geol Surv Occasional Paper* (30, 15–28).

Sykora S, Cooke DR, Meffre S, Stephanov AS, Gardner K, Scott R et al (2018) Evolution of pyrite trace element compositions from porphyry-style and epithermal conditions at the Lihir gold deposit: Implications for ore genesis and mineral processing. *Econ Geol* 113 (1), pp. 193–208.

Symons DTA, Kawasaki K, Walther S, Borg G (2011) Paleomagnetism of the Cu–Zn–Pb-bearing Kupferschiefer black shale (Upper Permian) at Sangerhausen, Germany. *Miner Deposita* 46 (2), pp. 137–152.

Taylor CD, Causey JD, Denning P, Hammarstrom JM, Hayes TS, Horton JD et al (2013) Descriptive models, grade-tonnage relations, and databases for the assessment of sediment-hosted copper deposits: with emphasis on deposits in the Central Africa Copperbelt, Democratic Republic of the Congo and Zambia: Chapter J in *Global mineral resource assessment*. US Geol Surv.

Tomaszewski JB (1978) The geological structure of the Lubin-Sierszowice region (Lower Silesia). *Geologia Sudetica* 13, pp. 85–132.

Unrug R (1988) Mineralization controls and source of metals in the Lufilian fold belt, Shaba (Zaire), Zambia, and Angola. *Econ Geol* 83 (6), pp. 1247–1258.

US Geological Survey (2023) Mineral commodity summaries 2023. U.S. Geological Survey, p. 210. doi: <https://doi.org/10.3133/mcs2023>

USGS (2020) Mineral commodity summaries 2020. DOI: 10.3133/mcs2020.

Van Wilderode J, Debruyne D, Torremans K, Elburg MA, Vanhaecke F, Muchez P (2015) Metal sources for the Nkana and Konkola stratiform Cu–Co deposits (Zambian Copperbelt): Insights from Sr and Nd isotope ratios. *Ore Geol Rev* 97 (127–138).

Van Wilderode J, El Desouky HA, Elburg MA, Vanhaecke F, Muchez P (2014) Metal sources for the Katanga Copperbelt deposits (DRC): insights from Sr and Nd isotope ratios. *Geologica Belgica* (17), 2, pp. 137–147.

Van Wilderode J, Heijlen W, Muynck D, Schneider J, Vanhaecke F, Muchez P (2013) The Kipushi Cu–Zn deposit (DR Congo) and its host rocks: A petrographical, stable isotope (O, C) and radiogenic isotope (Sr, Nd) study. *J Afri Earth Sci* 79, pp. 143–156.

Vaughan DJ, Sweeney MA, Friedrich G, Diedel R, Haranczyk C (1989) The Kupferschiefer; an overview with an appraisal of the different types of mineralization. *Econ Geol* 84 (5), pp. 1003–1027.

Velojić M, Bertrandsson Erlandsson V, Melcher F, Onuk P, Jelenković R, Cvetković V (2022) Trace elements in pyrite from the Čukaru Peki porphyry Cu–high-sulfidation deposit, Serbia: implications for ore evolution in a polyphase hydrothermal system. *Geologia Croatica* 75 (Special issue), pp. 303–316.

Waele B, Johnson SP, Pisarevsky SA (2008) Palaeoproterozoic to Neoproterozoic growth and evolution of the eastern Congo Craton: Its role in the Rodinia puzzle. *Precambrian Research* (160), 1, pp. 127–141.

Wedepohl KH, Delevaux MH, Doe BR (1978) The potential source of lead in the Permian Kupferschiefer bed of Europe and some selected Paleozoic mineral deposits in the Federal Republic of Germany. *Contributions to Mineralogy and Petrology* 65 (3), pp. 273–281. doi: <https://doi.org/10.1007/BF00375513>

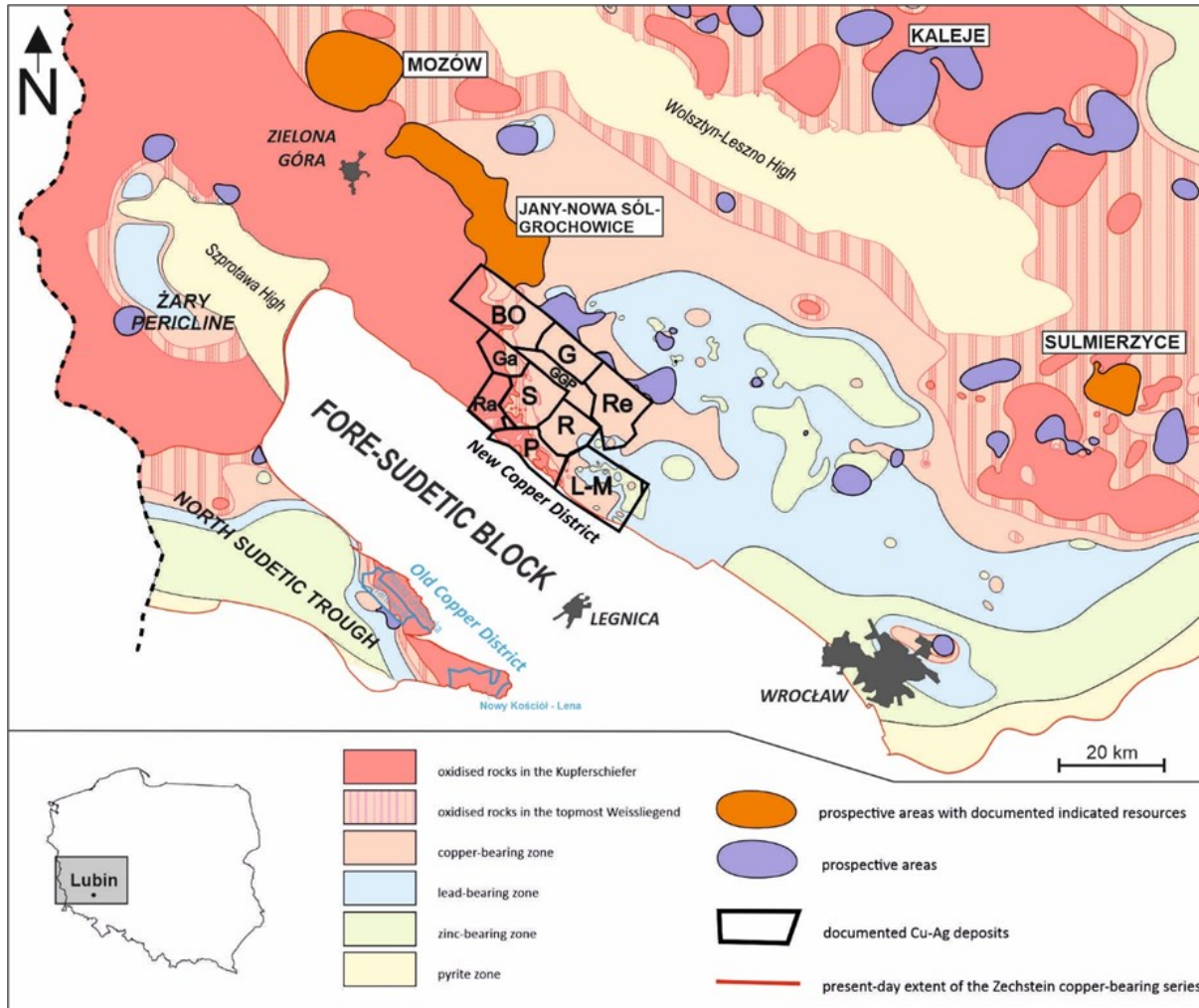
Wilson SA, Ridley WI, Koenig AE (2002) Development of sulfide calibration standards for the laser ablation inductively-coupled plasma mass spectrometry technique. *J Analytical Atomic Spectrometry* (17), 4, pp. 406–409.

Wodzicki A, Piestrzyński A (1994) An ore genetic model for the Lubin—Sierszowice mining district, Poland. *Miner Deposita* 29 (1), pp. 30–43.

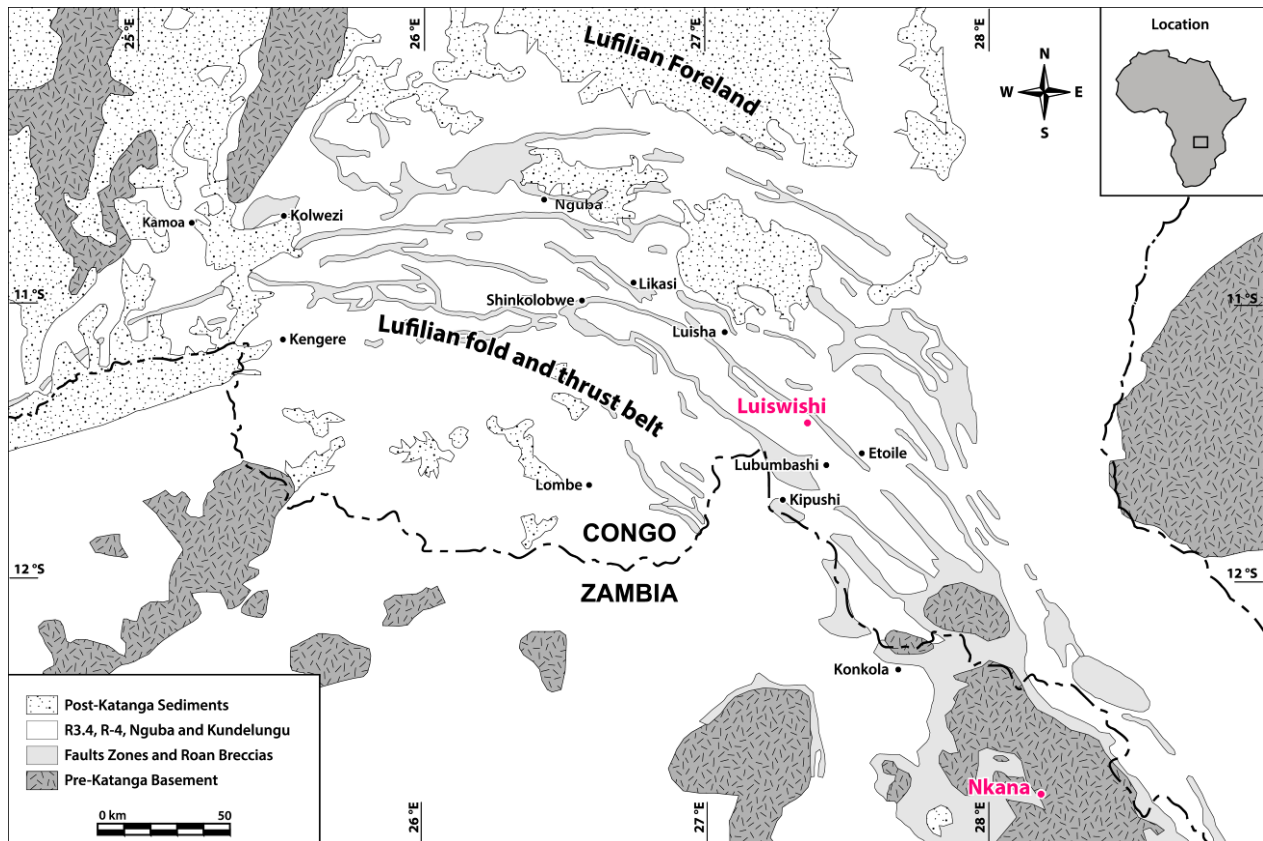
Zhuang L, Song Y, Liu Y, Fard M, Hou Z (2019) Major and trace elements and sulfur isotopes in two stages of sphalerite from the world-class Angouran Zn–Pb deposit, Iran: Implications for mineralization conditions and type. *Ore Geol Rev* 109, pp. 184–200.

Appendix P3 (Publication III)

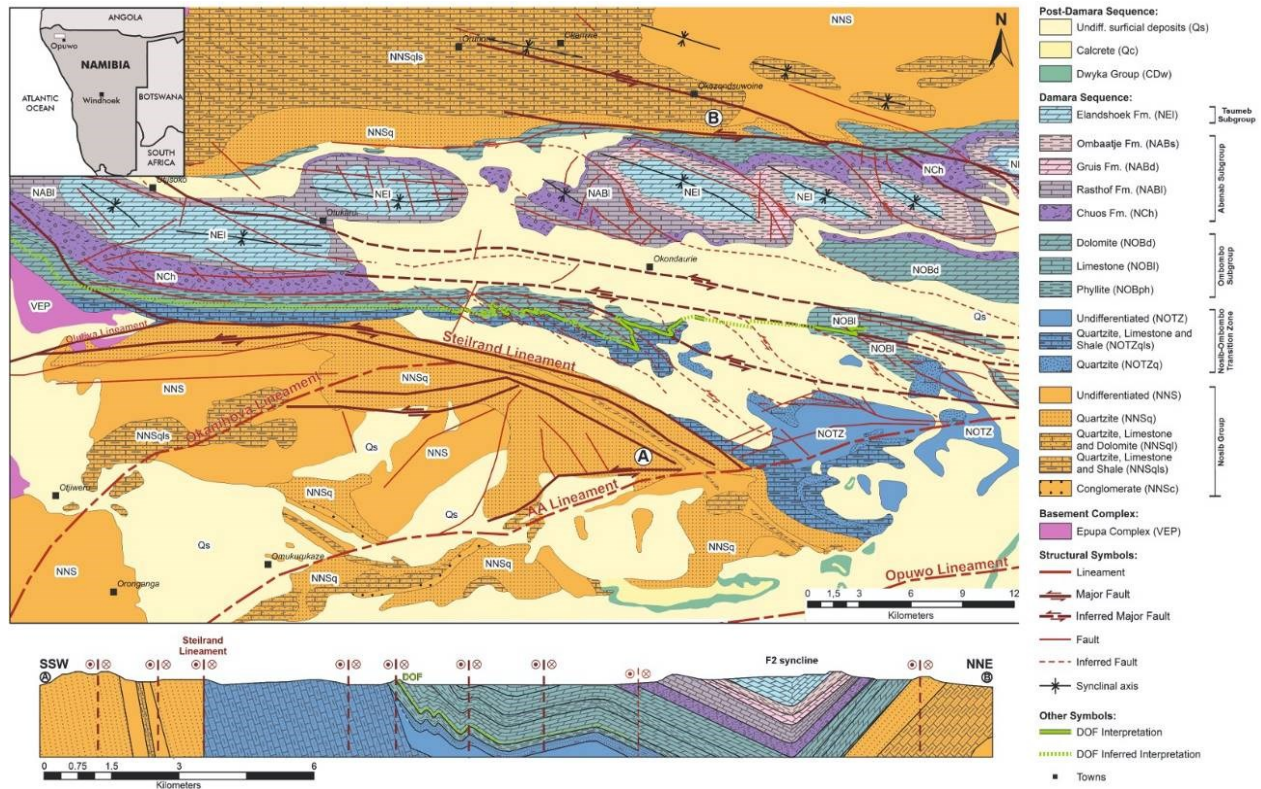
Appendix P3-1



AppendixP3 Figure 1. The Lubin-Głogów copper district and prospective copper areas in SW Poland in relation to Rote Fäule areas and metal zonation (modified after Oszczepalski et al. 2019). BO – Bytom Odrzański, G – Głogów, Ga – Gaworzyce, GGP – Głogów Głęboki Przemysłowy, L-M – Lubin-Małomice, P – Polkowice, R - Rudna, Ra – Radwanice, Re – Retków, S – Sierszowice.



AppendixP3 Figure 2. Simplified geological map of the Central African Copperbelt with the locations of the Luiswishi and Nchanga (Nkana) deposits, included in this study, marked out (modified after Mambwe et al. 2019).



AppendixP3 Figure 3. Geological map of the local geology of the Dolostone Ore Formation (DOF) area and schematic geological cross-section through the DOF, marked out by A and B (modified by Bertrandsson Erlandsson et al. 2022 from sources therein).

Appendix P3-2

AppendixP3 Table 1. Statistical summary of chalcopyrite LA-ICP-MS trace element data. Data for the Polish Kupferschiefer and ZCB is from Foltyn et al. (2022); the Dolostone Ore Formation is from this study and Bertrandsson Erlandsson et al. (2022). N = number of LA-ICP-MS analyses for each element; n = number of spot analyses with below detection limit values (bdl); DL = average detection limit.

Polish Kupferschiefer												
	Stage 1						Stage 2					
	Median	Min	Max	N	n	DL	Median	Min	Max	N	n	DL
V	14	0.71	1394	29	0	0.079	<0.071	<0.071	<0.071	46	39	0.071
Cr				na	na					na	na	
Mn	24	14	640	29	0	0.43	13	3.9	51	48	0	0.42
Co	0.57	0.15	49	29	0	0.055	3.7	<0.054	33	46	5	0.054
Ni	9.7	1.5	210	29	0	0.27	<0.24	<0.24	3.7	42	35	0.24
Zn	<13	<13	50	26	22	13	50.1	<15	4614	47	10	15
Ga	0.32	<0.63	14	28	5	0.063	0.64	<0.051	4.5	48	6	0.051
Ge	0.42	<0.17	7.8	29	4	0.17	1240	0.19	4806	48	0	0.18
As	<1.9	<1.9	36	27	15	1.9	307	<1.6	1045	45	5	1.6
Se	36	15	69	29	0	9.3	40	<9.4	192	46	11	9.4
Mo	5.7	<0.082	828	29	6	0.082	0.077	<0.064	3.0	47	26	0.064
Ag	57	8.8	773	29	0	0.017	14	2.3	500	48	0	0.014
Cd	<1.8	<1.8	<1.8	25	25	1.8	<1.7	<1.7	99	44	36	1.7
In	1.5	0.019	2.8	27	0	0.020	0.37	0.021	222	48	0	0.016
Sn	1.1	0.30	9.4	29	0	0.23	1.6	<0.18	544	47	1	0.18
Sb	1.8	0.75	18	29	0	0.082	30	<0.087	395	47	5	0.087
Te	<0.018	<0.018	1.1	29	21	0.18	<0.21	<0.21	1.5	47	43	0.21
Au	<0.028	<0.028	0.029	29	27	0.028	<0.028	<0.028	0.31	47	39	0.028
Hg	7.9	<4.9	59	29	13	4.9	4.2	<1.5	121	48	13	1.5
Tl	1.5	0.40	13	29	0	0.017	0.60	<0.018	1.9	48	1	0.018
Pb	137	46	1614	29	0	0.068	152	18	4441	46	0	0.079
Bi	0.054	<0.018	2.8	26	3	0.018	0.10	<0.014	4784	46	4	0.014

Katanga Copperbelt												
	Stage 1						Stage 2					
	Median	Min	Max	N	n	DL	Median	Min	Max	N	n	DL
V	<0.058	<0.058	20	42	24	0.058	<0.044	<0.044	0.49	38	36	0.044
Cr	<2.7	<2.7	26	48	37	2.7	<1.3	<1.3	<1.3	42	42	1.3
Mn	<0.48	<0.48	33	40	21	0.48	<0.34	<0.34	22	33	32	0.34
Co	2.9	1.5	10	44	0	0.13	2.7	1.9	11	43	0	0.093
Ni	<0.64	<0.64	1.8	43	33	0.64	<0.49	<0.49	<0.49	41	41	0.49
Zn	<16	<16	95	46	30	16	<11	<11	<11	37	37	11
Ga	19	7.4	38	53	0	0.15	70	36	86	43	0	0.10
Ge	6.4	4.5	12	53	0	0.32	3.8	3.0	9.6	43	0	0.25
As	<1.0	<1.0	5.9	51	30	1.0	<0.86	<0.86	<0.86	43	43	0.86
Se	31	<13	45	53	1	13	13	<8.9	23	43	14	8.9
Mo	0.660	<0.17	8.3	44	31	0.17	<0.13	<0.13	<0.13	43	43	0.13
Ag	<0.057	<0.057	0.47	45	26	0.057	0.37	<0.044	3.1	37	18	0.044
Cd	<7.2	<7.2	<7.2	52	52	7.2	<9.6	<9.6	<9.6	43	43	9.6
In	19	2.5	43	53	0	0.040	31	24	39	43	0	0.037
Sn	50	35	157	53	0	1.6	49	43	64	43	0	1.3
Sb	0.44	<0.17	126	52	16	0.17	<0.14	<0.14	1.5	41	40	0.14
Te	<4.8	<4.8	<4.8	50	50	4.8	<4.4	<4.4	<4.4	43	43	4.4
Au	<0.23	<0.23	1.9	53	29	0.23	<0.023	<0.023	<0.023	40	40	0.023
Hg	2.4	<1.2	6.2	53	6	1.2	1.6	<1.0	5.5	42	7	1.0
Tl	0.055	<0.030	1.2	52	24	0.030	<0.030	<0.030	<0.030	41	41	0.030
Pb	1.8	<0.10	67	48	19	0.10	<0.067	<0.067	0.48	30	23	0.067
Bi	25	<0.031	222	44	8	0.031	0.088	0.0073	0.86	32	0	0.018

Zambian Copperbelt						
	Median	Min	Max	N	n	DL
V	<0.058	<0.058	1.2	18	15	0.058
Cr				na	na	
Mn	14	14	20	18	0	0.35
Co	3.7	2.0	71	18	0	0.035
Ni	<0.21	<0.21	10	18	16	0.21
Zn	222	<12	2273	17	5	12
Ga	3.5	0.26	11	18	0	0.035
Ge	0.80	<0.15	2.0	18	3	0.15
As	<1.8	<1.8	<1.8	18	18	1.8
Se	<8.1	<8.1	19	18	9	8.1
Mo	<0.060	<0.060	0.24	18	16	0.060
Ag	0.62	0.26	2.6	17	0	0.012
Cd	<1.4	<1.4	3.3	17	10	1.4
In	5.2	3.7	5.7	18	0	0.019
Sn	32	14	70	18	0	0.22
Sb	<0.077	<0.077	0.32	18	10	0.077
Te	0.20	<0.17	0.41	18	9	0.17
Au	<0.014	<0.014	0.057	18	12	0.014
Hg	5.2	<1.6	26	18	3	1.6
Tl	<0.010	<0.010	0.021	18	12	0.010
Pb	0.76	0.13	9.7	17	0	0.044
Bi	0.70	0.25	2.4	15	0	0.017

Dolostone Ore Formation												
	Stage 1						Stage 2					
	Median	Min	Max	N	n	DL	Median	Min	Max	N	n	DL
V	<0.074	<0.074	2.7	132	109	0.074	<0.98	<0.98	0.15	47	45	0.098
Cr	<0.95	<0.95	10	168	157	0.95	<0.74	<0.74	<0.74	47	47	0.74
Mn	4.2	<0.50	22	126	43	0.50	4.4	3.8	5.2	47	0	0.60
Co	8.6	<0.091	164	138	1	0.091	0.17	<0.080	0.74	47	11	0.080
Ni	0.66	<0.47	62	156	57	0.47	54	<0.40	62	47	1	0.40
Zn	339	112	821	149	0	25	137	45	514	36	0	31
Ga	0.22	<0.080	3.8	172	30	0.080	0.90	0.37	1.6	46	0	0.061
Ge	0.41	<0.24	7.0	178	44	0.24	0.80	0.44	1.6	47	0	0.23
As	<1.3	<1.3	<1.3	188	188	1.3	<0.90	<0.90	<0.90	46	46	0.90
Se	23	<13	135	177	20	13	104	73	137	47	0	14
Mo	<0.12	<0.12	2.2	185	184	0.12	<0.096	<0.096	1.1	47	40	0.096
Ag	8.3	<0.039	35	195	7	0.039	3.8	0.13	6.4	47	0	0.032
Cd	<4.1	<4.1	5.1	192	190	4.1	<5.5	<5.5	11	46	33	5.5
In	6.5	0.097	70	195	0	0.030	4.3	1.6	31	47	0	0.016
Sn	18	0.44	131	194	0	1.1	59	1.3	95	47	0	0.50
Sb	<0.16	<0.16	1.0	187	163	0.16	<0.12	<0.12	1.5	47	30	0.12
Te	<0.40	<0.40	7.1	193	127	0.40	<0.36	<0.36	1.0	47	44	0.36
Au	<0.040	<0.040	0.31	195	157	0.040	<0.032	<0.032	<0.032	47	47	0.032
Hg	5.2	<1.3	42	189	17	1.3	3.2	<1.2	12	47	1	1.2
Tl	<0.030	<0.030	2.5	161	122	0.030	<0.028	<0.028	0.053	47	47	0.028
Pb	5.7	<0.077	138	164	1	0.077	0.89	0.11	31	46	0	0.067
Bi	0.65	<0.021	24	174	3	0.021	0.028	<0.017	0.27	47	15	0.017

Appendix P3 Table 2. Statistical summary of sphalerite LA-ICP-MS trace element data. Data for the Polish Kupferschiefer is from Foltyn et al. (2022) and this study; the Dolostone Ore Formation is from this study and Bertrandsson Erlandsson et al. (2022). N = number of LA-ICP-MS analyses for each element; n = number of spot analyses with below detection limit values (bdl); DL = average detection limit.

Polish Kupferschiefer												
	Median	Min	Max	N	n	DL	Median	Min	Max	N	n	DL
V	0.60	0.22	47	11	0	0.046	<0.056	<0.056	0.13	32	23	0.059
Cr	<0.93	<0.93	12	15	9	0.93	0.57	<0.58	1.7	32	10	0.58
Mn	11	6.0	154	22	0	0.51	<0.34	<0.34	25	32	22	0.34
Fe	1502	432	7688	32	0	20	125	58	2069	32	0	9.5
Co	<0.13	<0.13	7.5	28	13	0.13	4.2	0.58	49	32	0	0.051
Ni	3.0	<0.69	40	30	11	0.69	<0.22	<0.22	0.35	32	20	0.22
Cu	2317	<5.2	4810	26	1	5.2	266	22	11095	32	0	1.8
Ga	18	1.5	108	33	0	0.16	0.58	0.053	7.1	32	0	0.032
Ge	3.5	<0.38	60	33	1	0.38	1.2	<0.17	7.9	32	6	0.17
As	<1.2	<1.2	19	33	23	1.2	0.69	<0.69	16	32	4	0.69
Se	15	8.7	398	29	0	8.6	15	2.3	23	32	0	6.0
Mo	10	<0.16	99	33	8	0.16	<0.071	<0.071	14	32	17	0.071
Ag	33	21	201	33	0	0.082	2.7	0.277356	29	32	1	0.023
Cd	4673	1341.6	8974	33	0	1.9	9175	4540	17835	32	0	2.1
In	<0.038	<0.038	0.39	33	20	0.038	0.039	<0.017	22	32	3	0.017
Sn	3.6	<1.2	11	32	1	1.2	1.2	<0.27	208	32	2	0.27
Sb	1.1	<0.10	8.9	33	2	0.10	0.20	<0.085	2.6	32	14	0.085
Te	<0.54	<0.54	0.82	33	32	0.54	<0.13	<0.13	<0.13	32	32	0.13
Au	<0.59	<0.59	<0.59	28	28	0.59	<0.35	<0.35	<0.35	18	18	0.35
Hg	130	<2.9	225	33	1	2.9	54	9.2	175	32	0	2.7
Tl	2.4	0.73	4.4	33	0	0.067	1.1	<0.019	15	32	1	0.019
Pb	102	24	42681	26	0	0.13	25	<0.24	325	32	2	0.24
Bi	<0.022	<0.022	0.37	31	26	0.022	<0.012	<0.012	0.075	32	17	0.012

Dolostone Ore Formation												
	Median	Min	Max	N	n	DL	Median	Min	Max	N	n	DL
V	<0.053	<0.053	0.18	118	108	0.053	<0.064	<0.064	<0.064	75	75	0.064
Cr	<0.70	<0.70	0.99	138	135	0.70	<0.63	<0.63	<0.63	75	75	0.63
Mn	201	80	339	142	0	0.39	44	13	230	75	0	0.42
Fe	65268	38664	73529	147	0	17	38599	14043	58622	74	0	21
Co	8672	4311	9496	151	0	0.091	799	32	1637	75	0	0.072
Ni	0.86	<0.38	8.5	146	22	0.38	19	1.1	37	74	0	0.40
Cu	104	12	88	85	0	3.0	97	26	974	69	0	2.7
Ga	0.36	<0.067	1.3	148	2	0.067	1.5	0.56	7.7	75	0	0.055
Ge	<0.22	<0.22	0.65	149	118	0.22	0.48	<0.21	1.4	75	3	0.21
As	<0.94	<0.94	8.8	148	83	0.94	<0.74	<0.74	<0.74	74	74	0.74
Se	28	15	32	151	0	8.2	99	53	241	75	0	10
Mo	<0.067	<0.067	0.65	149	148	0.067	<0.0067	<0.0067	<0.0067	75	75	0.067
Ag	0.60	<0.028	1.6	138	5	0.028	0.27	0.049	7.2	75	0	0.026
Cd	222	107	349	151	0	3.5	1865	1285	2550	75	0	3.9
In	34	5.3	11	151	0	0.021	21	17	152	75	0	0.016
Sn	1.4	<0.54	2.8	149	42	0.54	<0.45	<0.45	7.024698	75	46	0.45
Sb	<0.11	<0.11	0.070	150	149	0.11	<0.11	<0.11	<0.11	74	74	0.11
Te	<0.35	<0.35	2.9	151	146	0.35	<0.31	<0.31	<0.31	75	75	0.31
Au	<0.23	<0.23	0.38	127	124	0.023	<0.020	<0.020	<0.020	75	75	0.020
Hg	68	29	159	151	0	1.0	100	59	153	75	0	1.0
Tl	<0.021	<0.021	0.016	150	136	0.021	<0.022	<0.022	<0.022	74	74	0.022
Pb	1.2	<0.052	0.82	128	17	0.052	0.11	<0.063	5.8	73	19	0.063
Bi	0.13	<0.011	0.043	137	26	0.011	<0.013	<0.013	0.040	73	62	0.013

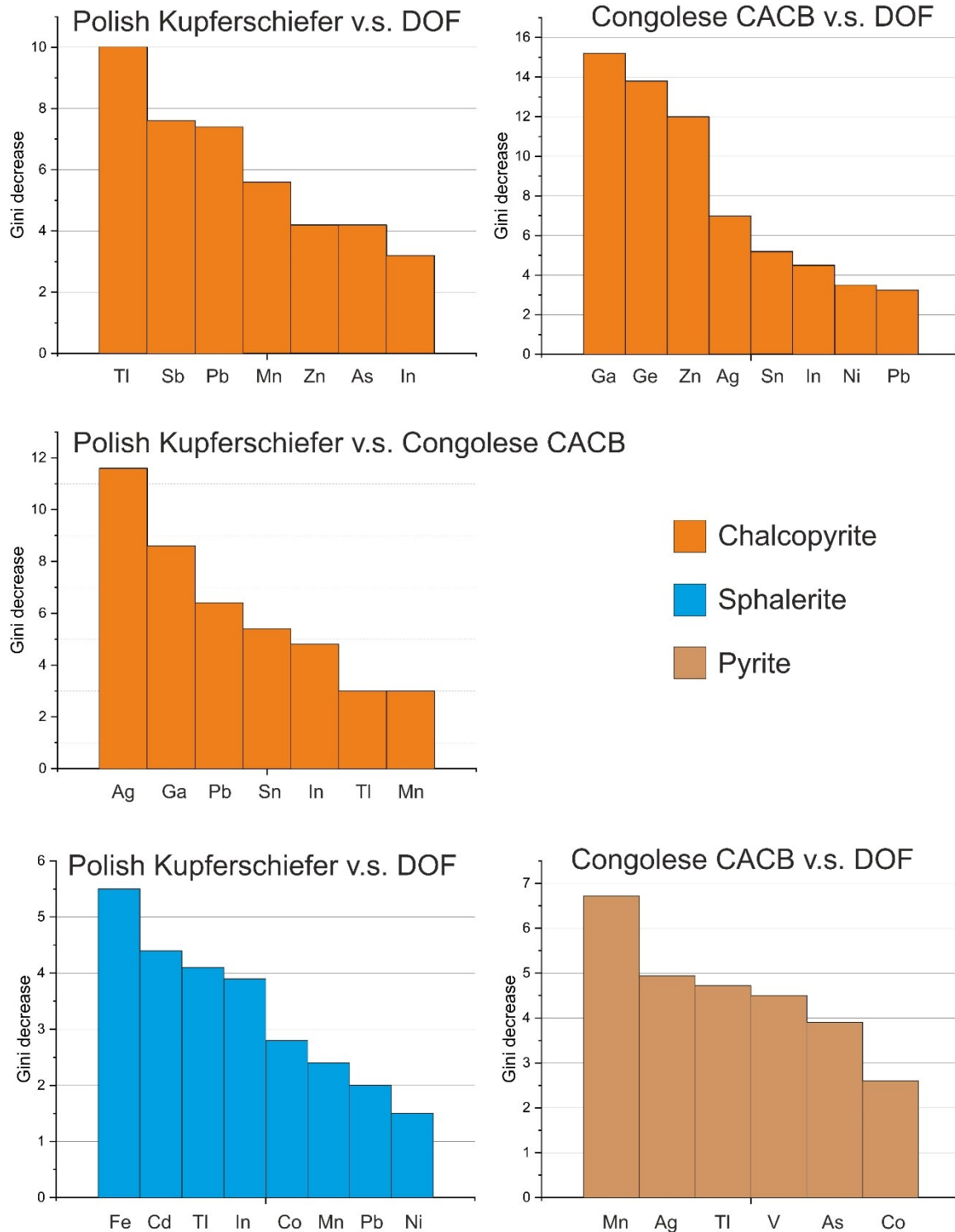
AppendixP3 Table 3. Statistical summary of pyrite LA-ICP-MS trace element data. Data for the Dolostone Ore Formation is from this study and Bertrandsson Erlandsson et al. (2022). N = number of LA-ICP-MS analyses for each element; n = number of spot analyses with below detection limit values (bdl); DL = average detection limit.

Polish Kupferschiefer						
	Stage 1					
	Median	Min	Max	N	n	DL
V	4.4	1.6	6.5	11	0	0.017
Cr	1.0	0.57	2.0	14	0	0.33
Mn	260	164	787	17	0	0.17
Co	91	14	154	14	0	0.041
Ni	25	12	67	13	0	0.16
Cu	4593	786	7047	8	0	1.1
Zn	33	23	73	18	0	4.0
Ga	<0.051	<0.051	0.059	8	6	0.051
Ge	0.14	<0.12	0.24	14	6	0.12
As	137	64	235	14	0	0.41
Se	10	3.1	17	18	0	2.9
Mo	25	8.7	116	18	0	0.61
Ag	13	2.7	29	7	0	0.016
Cd	19	13	27	18	0	0.67
In	0.095	0.028	0.15	18	0	0.015
Sn	1.5	0.84	1.9	18	0	0.30
Sb	2.4	1.4	4.2	18	0	0.050
Te	bdl	bdl	bdl	18	18	
Au	<0.17	<0.17	<0.17	18	18	0.17
Hg	2.7	1.7	6.9	18	0	0.85
Tl	846	612	1254	17	0	0.019
Pb	1706	249	2861	18	0	0.063
Bi	0.036	<0.0048	0.12	18	3	0.0048

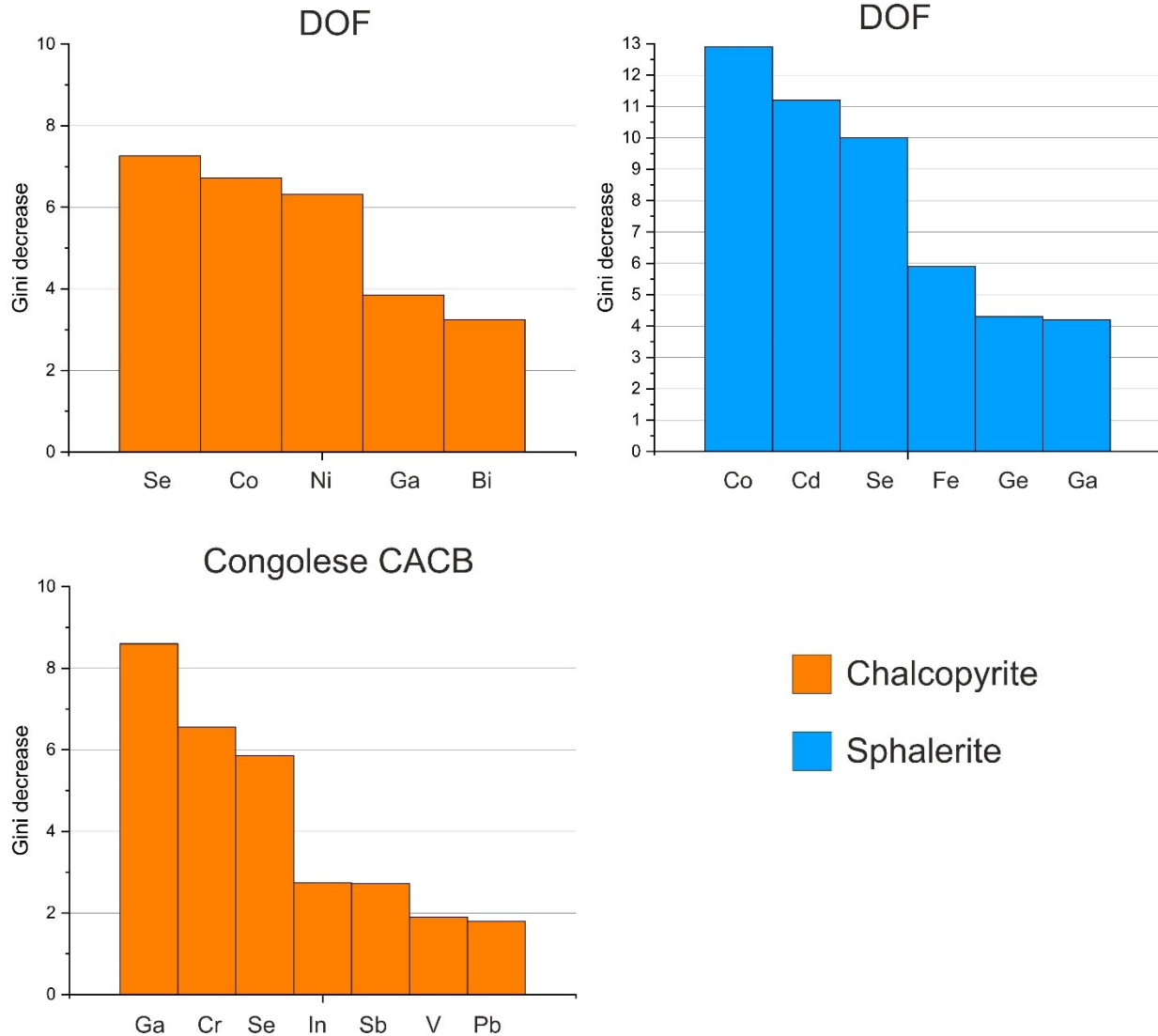
Katanga Coppberbelt													
	Stage 1							Stage 1					
	Median	Min	Max	N	n	DL		Median	Min	Max	N	n	DL
V	1.4	0.94	1.8	2	0	0.022		<0.023	<0.023	<0.023	16	14	0.023
Cr	3.2	1.1	4.7	16	0	0.52		<0.38	<0.38	<0.38	29	29	0.38
Mn	7.9	2.7	17	10	0	0.23		0.64	0.30	3.7	11	0	0.21
Co	8480	206	23153	21	0	0.16		77058	48968	108174	31	0	0.19
Ni	154	37	384	22	0	0.31		277	155	434	30	0	0.31
Cu	564	101	855	8	0	2.8		9.2	2.8	26	16	0	1.1
Zn	11	<8.5	106	11	5	8.5		<6.4	<6.4	<6.4	29	29	6.4
Ga	0.61	0.32	1.5	6	0	0.088		<0.070	<0.070	<0.070	18	18	0.070
Ge	1.2	0.61	3.2	7	0	0.21		0.33	<0.14	0.79	29	2	0.14
As	367	20	643	10	0	0.89		90	25	198	22	0	0.67
Se	15	8.8	25	18	0	5.8		55	25	140	31	0	4.8
Mo	<0.049	<0.049	0.67	12	11	0.049		<0.076	<0.076	<0.076	31	31	0.076
Ag	0.16	<0.15	0.22	15	6	0.15		<0.034	<0.034	<0.034	31	31	0.034
Cd	<2.2	<2.2	<2.2	18	18	2.2		<1.4	<1.4	<1.4	31	31	1.4
In	0.73	<0.024	1.8	15	1	0.024		<0.016	<0.016	0.034	26	22	0.016
Sn	3.2	<0.55	8.7	16	1	0.55		<0.50	<0.50	0.52	27	27	0.50
Sb	5.3	0.73	13	16	0	0.091		0.065	<0.044	0.39	28	9	0.044
Te	bdl	bdl	bdl	18	18	4.0		<3.5	<3.5	2.6	31	30	3.5
Au	<0.015	<0.015	0.042	18	14	0.015		<0.014	<0.014	0.14	29	17	0.014
Hg	1.3	<0.89	3.7	18	6	0.89		<1.0	<1.0	<1.0	30	30	1.0
Tl	0.061	0.019	0.17	16	0	0.016		<0.010	<0.010	<0.010	31	31	0.010
Pb	11	3.9	46	15	0	0.020		0.034	<0.016	0.14	17	4	0.016
Bi	8.6	1.5	16	14	0	0.0066		0.64	0.15	3.1	12	0	0.0060

	Dolostone Ore Formation											
	Stage 1						Stage 2					
	Median	Min	Max	N	n	DL	Median	Min	Max	N	n	DL
V	0.10	0.037	0.52	13	0	0.030	0.027	<0.025	0.25	49	22	0.025
Cr	0.29	<0.23	0.76	34	14	0.23	0.67	<0.30	0.97	56	47	0.30
Mn	21	9.9	136	14	0	0.19	9.2	0.79	319	40	0	0.18
Co	12432	4031	30380	34	0	0.053	3699	1.3	102748	57	0	0.038
Ni	246	16	2054	32	0	0.21	181	<0.23	5893	56	1	0.23
Cu	<1.56	<1.56	230	19	10	1.6	1.9	<1.4	183	53	22	1.4
Zn	<4.9	<4.9	<4.9	11	11	4.9	<4.9	<4.88	18	56	50	4.9
Ga	0.090	<0.027	1.0	25	3	0.027	0.044	<0.24	1.2	63	15	0.024
Ge	0.36	<0.082	1.7	32	1	0.082	0.38	<0.11	1.5	63	6	0.11
As	0.60	<0.34	2.9	29	14	0.34	5.2	<0.47	9917	61	16	0.47
Se	23	6.0	60	33	0	3.4	31	<4.0	175	64	3	4.0
Mo	<0.034	<0.034	0.12	30	18	0.034	0.077	<0.031	3.1	62	37	0.031
Ag	0.53	<0.011	1.5	25	2	0.011	0.61	0.002779	3.4	62	13	0.012
Cd	<1.5	<1.5	<1.5	34	34	1.5	<1.5	<1.5	<1.5	62	62	1.5
In	<0.017	<0.017	0.032	28	18	0.017	<0.010	<0.010	0.26	62	41	0.010
Sn	<0.27	<0.27	1.6	34	20	0.26	<0.23	<0.23	26	63	38	0.23
Sb	0.076	<0.054	0.67	32	13	0.054	0.15	<0.057	235	64	24	0.057
Te	0.25	<0.10	1.8	23	4	0.10	0.15	<0.12	2.6	47	22	0.12
Au	<0.10	<0.10	<0.10	14	14	0.10	<0.013	<0.013	0.12	64	46	0.013
Hg	<0.36	<0.36	1.5	30	18	0.36	0.70	<0.51	22	63	27	0.51
Tl	3.7	0.019	10.9	24	0	0.010	0.26	<0.0090	3.8	64	10	0.0090
Pb	25	2.4	117	27	0	0.068	18	<0.17	4404	62	6	0.17
Bi	1.5	0.31	4.3	23	0	0.0076	0.28	<0.0086	29	62	9	0.0086

Appendix P3-3



AppendixP3 Figure 4. Average decrease Gini value for the most relevant elements for chalcopyrite, sphalerite and pyrite. Averages were calculated from five independent Random Forest analyses for each mineral. Abbreviations: CACB = Central African Copperbelt; DOF = Dolostone Ore Formation.



AppendixP3 Figure 5. Average decrease Gini value for the most relevant elements for chalcopyrite and sphalerite. Averages were calculated from five independent Random Forest analyses for each mineral. Abbreviations: CACB = Central African Copperbelt; DOF = Dolostone Ore Formation.

Publication IV

New perspective on trace element (Re, Ge, Ag) hosts in the Cu-Ag Kupferschiefer deposit, Poland: Insight from a LA-ICP-MS trace element study

Krzysztof Foltyn¹, Viktor Bertrandsson Erlandsson², Władysław Zygo¹, Frank Melcher², Jadwiga Pieczonka¹

¹AGH University of Science and Technology, Faculty of Geology, Geophysics and Environmental Protection, Krakow, Poland

²Montanuniversität Leoben, Department of Applied Geosciences and Geophysics, Leoben, Austria

Ore geology Reviews, 143 (2022) 104768

The publication version in this thesis is the latest version, which was accepted and published.

Abstract

The Kupferschiefer deposit in SW Poland provides an opportunity to study an ore system where besides factors such as temperature, salinity and pH, redox conditions play a major role in controlling trace element incorporation in sulphides. Chalcocite, djurleite, bornite, chalcopyrite, sphalerite, covellite and pyrite from the Cu-Ag deposits in the Lubin-Sieroszowice district were analysed with laser ablation inductively coupled plasma mass spectrometry (LA-ICP-MS) to study the distribution of trace elements and to identify the main carriers of by-products such as silver and rhenium. Trace element anomalies are not only associated with certain minerals but also linked to specific mineralization styles. Chalcopyrite in epigenetic veins has significantly higher content of Ge, As and Sb while sulphides adjacent to hematitic “red spots” are enriched in redox sensitive elements: djurleite is enriched in V, Se, Re, Au, Hg and Tl, chalcopyrite in V, Se, Hg and Tl, and pyrite in Tl in comparison with bulk Cu-Ag mineralization. Elevated and substantially more variable data for V, Mn, Ni, Co, Ga, Mo, Sn in shale hosted sulphides can be attributed to submicron inclusions of Kupferschiefer silicate matrix which might skew low concentrations values even if careful petrographic observations and precise spot selection are applied. Silver concentrations form a linear pattern from chalcocite/djurleite > bornite > chalcopyrite > sphalerite. Silver distribution in the deposit on a broad scale could be linked to the general Fe³⁺-Cu-Pb-Zn-Fe²⁺ zonation as well as mineral sequence (hematite-chalcocite-bornite-chalcopyrite-galena-sphalerite-pyrite) observed in the majority of sediment hosted stratiform copper deposits. Epigenetic sulphide-calcite veins crosscutting lithologies and associated with local faults and tectonic zones contain chalcopyrite exceptionally rich in germanium (up to 4806 µg/g of Ge) suggesting that the potential of Kupferschiefer Cu-Ag ores in terms of Ge grades and resources could be underestimated. The majority of analysed sulphides do not contain rhenium above detection limits (0.1 µg/g Re) with measurable quantities found almost exclusively in djurleite (up to 3.9 µg/g Re). This indicates that copper sulphides, in particular djurleite, could be a preferred host and an important carrier of rhenium in the deposit.

Highlights

Silver concentrations exhibit a pattern of chalcocite/djurleite > bornite > chalcopyrite > sphalerite, similar to the mineral sequence and the general Fe³⁺-Cu-Pb-Zn-Fe²⁺ zonation.

Germanium enriched chalcopyrite (up to 4806 µg/g of Ge) was found in veins from the Lubin-Sieroszowice ore district.

Djurleite has been identified as the major host of rhenium among sulphides from the Cu-Ag Kupferschiefer deposit

1. Introduction

Rhenium is one of the rarest and most dispersed elements in the Earth's upper crust and its annual production does not exceed 50 tons. This element has a strong affinity for sulphur and occurs mainly as a substitute for molybdenum in molybdenite (MoS₂) which makes it the principal source of Re. Molybdenites from porphyry copper deposits usually contain 100-3000 ppm of Re but in some cases, high concentrations up to 4.7% of Re were reported (Voudouris et al. 2009; John et al. 2017). Currently nearly all of the primary production of rhenium is a by-product of copper mining, with porphyry copper-molybdenum-gold deposits supplying about 80 % of its

primary production (Polyak, 2017, USGS 2020). The rest is extracted from sediment hosted stratabound copper deposits (SSC) in Poland and Kazakhstan. Cu-Ag deposits in the Lubin-Sieroszowice district are operated by KGHM PM S.A. and were responsible for around 18% of the annual Re production in 2018 (USGS 2020). In contrast to molybdenite present in porphyry copper deposits, which have been extensively studied due to Re-Os dating being one of the "gold standards" of geochronology (e.g. Berzina et al. 2005, Voudouris et al. 2013, Pašava et al. 2016, Barra et al. 2017), there is a surprisingly large gap in knowledge regarding the occurrence of rhenium in SSC deposits. Although copper mineralization in Poland, Germany and Kazakhstan is strongly enriched in Re compared to the average crustal value, geological processes responsible for this phenomenon remain not fully understood. A longstanding, unresolved question regarding Kupferschiefer mineralization in Poland is the mineralogical host of Re. Copper minerals (Kijewski, Jarosz 1987), molybdenum phases (Kucha 1990) and organic matter (Kijewski, Jarosz 1987) were suggested as Re carriers but low abundances (at ppb-ppm levels) and low resolution of available analytical methods in the past, made more precise investigations tremendously difficult.

Laser ablation inductively-coupled plasma mass spectrometry (LA-ICP-MS) emerged as a solution to the problem of measuring low-concentrations of trace elements in-situ in minerals at the micron-scale and has been successfully implemented to a broad range of ore minerals, such as sphalerite (e.g. Cook et al. 2009, Frenzel et al. 2016), chalcopyrite (e.g. Wohlgemuth-Ueberwasser et al. 2015, George et al. 2018), pyrite (Large et al. 2009, Gregory et al. 2015), tetrahedrite-tennantite (George et al. 2017), bornite, chalcocite (Cook et al. 2011), pyrrhotite (Duran et al. 2016), galena (George et al. 2015), arsenopyrite (Lawley et al. 2015) and magnetite (Dare et al. 2014). The method was applied to samples representing virtually all major types of magmatic and hydrothermal mineral deposits (see e.g. Cook et al. 2016 and references therein) with a notable omission: sediment rock hosted stratiform copper deposits (SSC). They account for approximately 23% of the world's copper production and known reserves (Singer 1995), but are also world's largest producing deposit type for cobalt and fourth largest producing deposit type for silver (Hayes et al. 2015), primarily on account of two supergiants: the Central African Copperbelt and the European Kupferschiefer, respectively (Hitzman et al. 2005).

Formation of SSC deposits in general seems to be rather well understood: they form by precipitation of sulphides at the redox interface by oxidation-reduction reactions and show broad similarities in terms of mineralization style and mineralogy. They usually form stratabound to stratiform disseminations in siltstones, shales, sandstones and carbonates with ore minerals usually occurring as cements, replacements and veinlets. These deposits are commonly characterized by lateral and vertical metal (and mineral) zonation with the general sequence: Fe³⁺ zone (hematite) – redox proximal Cu zone (chalcocite, bornite, chalcopyrite) – Pb and Zn zone (galena and sphalerite) – distal Fe²⁺ (pyrite) (Hitzman et al. 2005).

At the first glance, this group of deposits might not seem to be an attractive target for in-situ trace element studies. These ores are widely considered to form at low temperatures (75–200°C) from oxidizing brines circulating through red beds without involvement of magmatic fluids or direct link to magmatism (Wodzicki and Piestrzyński 1994; Oszczepalski 1999). Redox conditions can separate metals quite efficiently, leaving little trace elements available for incorporation into major sulphides. Moreover, their features cause several obstacles for LA-ICP-MS measurements:

mineralization is often fine-grained, disseminated and non-homogenous; intergrowths and aggregates with gangue minerals are common so spot selection for laser ablation is challenging.

Despite these obstacles, LA-ICP-MS might provide an important insight into formation of the SSC deposits. Substantial size, variety of ore textures and multistage origin adds considerable variation to apparent simplicity. In the case of the Kupferschiefer, hematization is the only extensive alteration and with scarcity of fluid inclusions data it is more difficult to characterize ore forming fluids and untie the evolution of the hydrothermal system responsible for deposit formation. Although there is a plethora of whole rock data for the Cu-Ag deposits in the Fore-Sudetic Monocline in Poland, detailed mineral chemistry data are scarce. Investigating trace elements in sulphides with much greater detail than available with electron microprobe, can potentially help to paint a more detailed picture of the ore forming processes. Additionally, although copper and silver are the main commodities, mines in Poland exploiting SSC deposits also produce significant amount of by-products (Pb, Re, Pt, Pd, Au, Ni, Se). Mineralogical hosts for some of these elements (most notably rhenium) are not well understood and LA-ICP-MS studies can shed a new light on this matter.

Despite some challenges, the lack of LA-ICP-MS data for this group of deposits in the literature is baffling, especially as they provide an opportunity to study ore systems where redox conditions play a dominant role and can overshadow factors such as temperature, salinity and pH of hydrothermal fluids in controlling trace element partitioning. Therefore, the aim of this paper is to demonstrate the feasibility of such investigations, to provide in-situ trace element data for common sulphides from the Cu-Ag Lubin-Sieroszowice district and to determine whether they can constitute a major rhenium carrier.

2. Geological settings

The Kupferschiefer (copper bearing shale) strata occurs in the Southern Permian Basin in Europe, which extends from the United Kingdom through North Sea, northern Germany to Poland. It gave name to one of the subtypes of SSC deposits, where the reduced sediments containing organic matter overlie oxidized, hematite-bearing sandstone, siltstone, and (or) conglomerate (red beds) deposited in an arid climate (Zientek et al. 2015). The world-class Lubin-Sieroszowice copper district in southwestern Poland is a classic example of this type of mineralization and as such its geological settings has been extensively studied and described in numerous papers (e.g. Tomaszewski 1978; Oszczepalski 1999; Kłapciński and Peryt, 2007; Pieczonka et al. 2008). It is located in the SW part of the Fore-Sudetic Monocline, adjacent to the northern boundary of the Fore-Sudetic Block (Fig 1). The basement of the Monocline is composed mainly of Proterozoic and early Paleozoic gneisses, schists, phyllites, granitoids and deformed Carboniferous conglomerates, sandstones and mudstones. They are overlain by Permian sediments which are part of the European Permian sedimentary basin formed in the final stages of the Variscan Orogeny (McCann et al. 2006). The Variscan foreland in Europe was subjected to extensive rift-related tectonism and related magmatic activity resulting in Lower Rotliegend (“Autunian”) beds composed of red-colored clastic sediments and bi-modal volcanics composed of rhyolites, rhyolitic tuffs and trachybasalts. The Upper Rotliegend (“Saxonian”) are essentially terrestrial beds composed of aeolian sandstones interbedded with deposits of alluvial fans, braided rivers and playas characteristic of fluvial, aeolian and lacustrine sedimentary environments in a land-

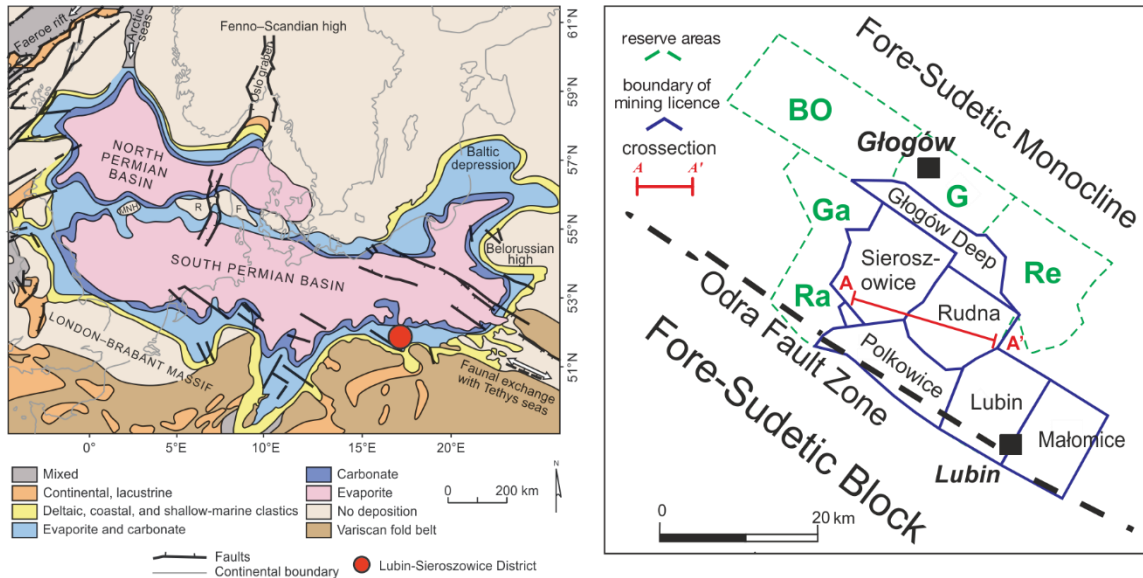
locked basin and arid climate (Karnkowski 1999, Kiersnowski and Buniak 2006, McCann et al. 2006). In the Late Permian, the continental Rotliegend Basin has been rapidly flooded in a catastrophic sea transgression (Gast et al. 2010), an event analogous to the Zanclean flood which rapidly refilled the Mediterranean Sea after the Messinian salinity crisis 5.33 Ma ago (Garcia-Castellanos et al. 2009). As a result of transgression, the uppermost part of the Rotliegend was reworked and redeposited forming gray white sandstone called Weissliegend (Glennie and Buller 1983). Its thickness varies from less than 1 meter up to 40 meters. Locally, mainly in the south-eastern part of the district, the Basal Limestone, in the mine district called “boundary dolomite”, overlies the Weissliegend and is up to 0.3 meters thick (Kłapciński 1971, Kłapciński and Peryt 2007).

The Kupferschiefer is a thin (average 0.3 m-thick) layer of black, marine, organic-bearing shale, forming the base of the Zechstein succession (Fig 2). It was formed under anoxic, euxinic bottom waters (Paul et al. 2006) and represents a change of the deposition conditions from oxidized to reduced sediments. The Zechstein sediments in the South Permian Basin are subdivided into carbonate-evaporite cyclothem series reflecting progressive evaporation and chemical precipitation in a large saline basin. Marine carbonate sediments (limestones or marls) form the base of each cycle and are followed by layers of evaporates, mainly of anhydrite and halite. Zechstein rocks in Poland are subdivided into four evaporitic cycles, referred to as PZ1 (Z1 Werra), PZ2 (Z2 Stassfurt), PZ3 (Z3 Leine), and PZ4 (Z4 Aller) (Kłapciński and Peryt 2007). The Kupferschiefer is overlain by the Zechstein Limestone (Z1) which grades upwards from dolomitic to calcitic and is followed by the Lower Anhydrite (A1d), the Oldest Halite (Na1), and the Upper Anhydrite (A1g) constituting the first cyclothem series (Z1 Werra).

The Cu-Ag sulphide mineralization occurs in the contact zone between the Zechstein and Rotliegend groups and is not restricted to the Kupferschiefer layer. It occurs in the Weissliegend, the Basal Limestone, the Kupferschiefer and the Zechstein Limestone units (Fig 1) and the majority of the reserves is in fact hosted in the sandstone units. An important feature is the presence of a red coloured hematitic footwall alteration zone (“red spots”, “red stains”) closely associated with ore-grade mineralization of the Kupferschiefer and called the “Rote Fäule”. It is usually considered to form by secondary oxidation (e.g. Oszczepalski 1989, 1999) resulting from the flow of oxidizing fluids through the Kupferschiefer, probably during diagenesis. Other papers suggest the existence of more than one “Rote Fäule” facies with only some of them linked with ore-grade mineralization. Kucha (1995) distinguished 4 types of syngenetic “red spots” and 4 types of epigenetic “red spots” although differentiation criteria are not precisely defined. Differences between two separate phases of “red spots”, i.e. older spots originated from synsedimentary or early diagenetic processes, named “diagenetic oxidation stage (DOS)” and younger, epigenetic “secondary oxidation stage (SOS)” overprinting earlier DOS and associated with enrichment in precious metals, were highlighted by Pieczonka (2000), Pieczonka and Piestrzyński (2000), Piestrzyński et al. (2002), Pieczonka et al. (2008). These authors suggest that oxidizing brines responsible for deposition of noble metals and epigenetic “red spots” (SOS system) postdate the formation of economic-grade copper mineralization and should be treated separately from the DOS system. Samples with hematite alteration investigated in this study represent the epigenetic variety of “red spots” related to noble metals mineralization.

The depositional age of the Kupferschiefer is generally accepted as 258 Ma (Menning et al. 2006, Peryt et al. 2012) but age of the mineralization proved to be more difficult to constrain. Different geochronological methods point toward Late Permian-Early Triassic (Jowett et al. 1987, Nawrocki et al. 2000, Alderton et al. 2016, Nawrocki 2017), Late Triassic (Mikulski and Stein 2015, 2017), Late Triassic-Early Jurassic (Bechtel 1999, Alderton et al. 2016) and Late Jurassic (Symons et al. 2011) time periods. Most authors agree that mineralization processes were long-term and took place in several stages (Wodzicki and Piestrzyński 1994, Alderton et al. 2016, Michalik and Sawłowicz 2001). The main mineralizing process was the migration of low-temperature, oxidizing, metalliferous chloride brines sourced from the paleo-depressions filled with Rotliegend red bed sediments, through the anoxic basal sediments of the Zechstein Group (Jowett 1986).

Six mining areas (Deep Głogów, Lubin-Małomice, Polkowice, Radwanice-Gaworzyce, Rudna, and Sieroszowice, Fig 1) have been established in the district and are operated by KGHM PM S.A. In recent years, the exploration drilling program of Miedzi Copper Corporation (MCC) allowed preliminary documentation of three new “deep” Cu-Ag deposits in the Fore-Sudetic Monocline: Nowa Sól, Mozów and Sulmierzyce North (Zieliński and Speczik 2017, Oszczepalski et al. 2019).



WSW

Sieroszowice Mine

Rudna Mine

ENE

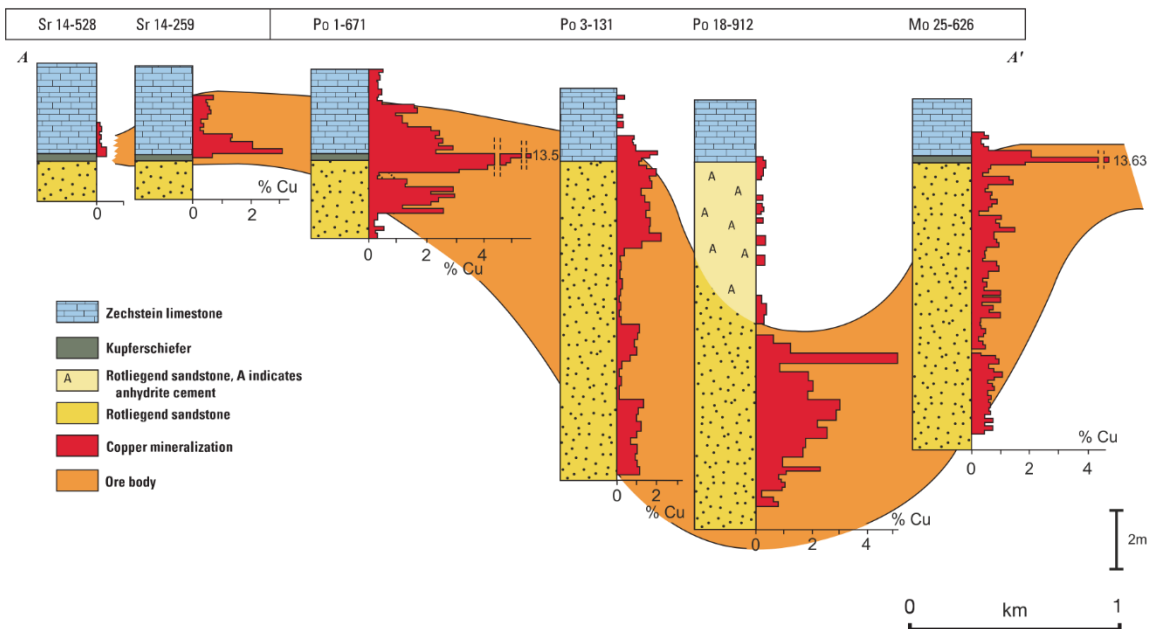


Fig. 1. Extend of the Zechstein Basin in Europe with location of the Lubin-Sieroszowice district (modified from Jackson and Hudec 2017 after Ziegler 2005). Cu-Ag deposits in the Fore-Sudetic Monocline in Poland and stratigraphic columns through the Kupferschiefer in the Sieroszowice and Rudna Mine areas with histograms of copper content. Modified after Wodzicki and Piestrzyński 1994, and Borg et al. 2012.

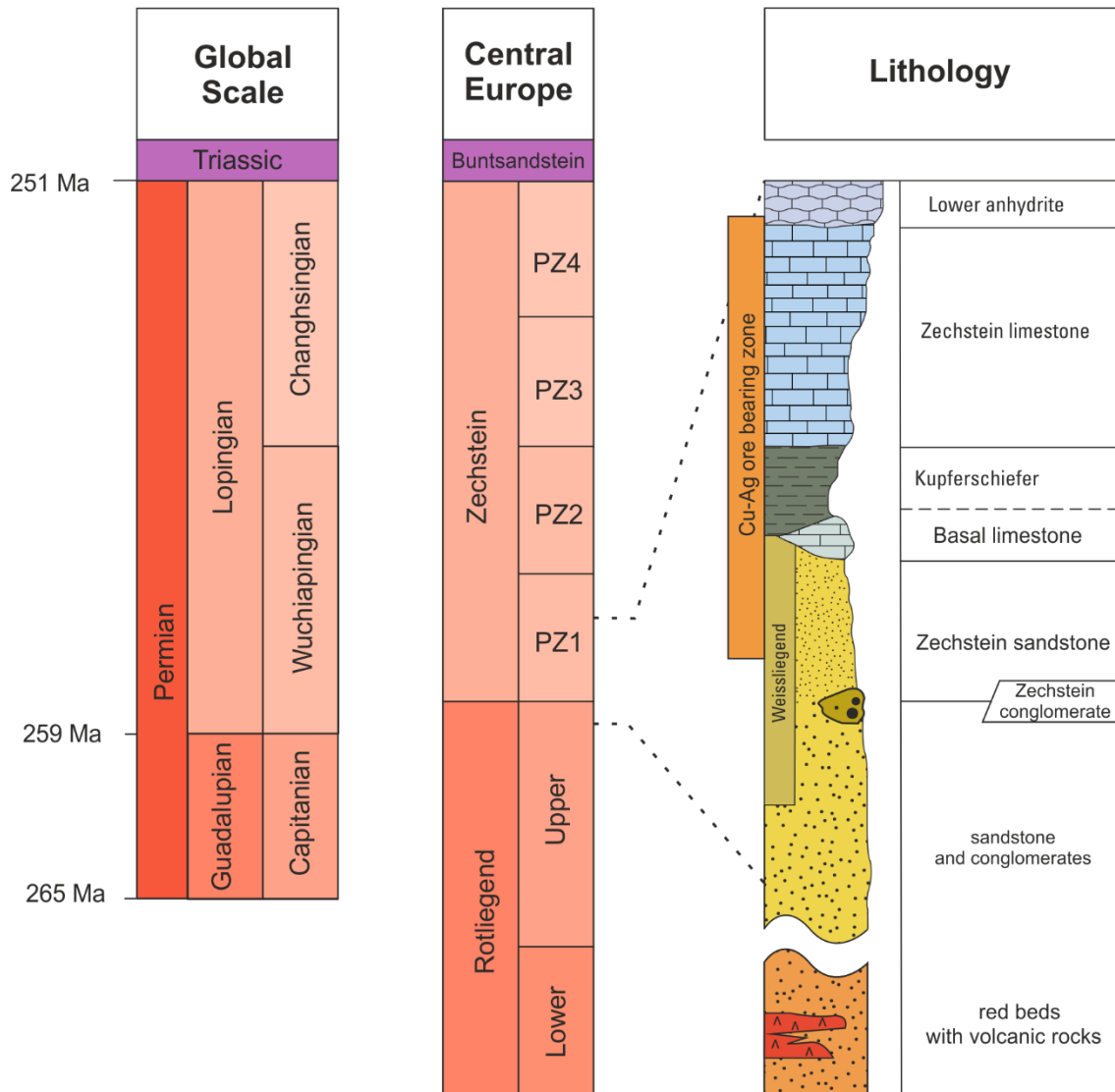


Fig. 2. Generalized stratigraphic column of the lowermost part of Zechstein Group and underlying Upper Rotliegend Group in the Southern Permian Basin. After Zientek et al. 2015 and Borg et al. 2012, modified.

3. Samples and methods

Samples used for this study, representing typical mineral assemblages and the most common ore textures of the Cu-Ag deposit in the Fore-Sudetic Monocline, come from the collection of Department of Economic Geology, AGH University of Science and Technology, consisting of samples collected over the past 45 years in the Lubin, Rudna and Sieroszowice-Polkowice underground mines.

Samples considered suitable for measurements can be divided into 4 major groups:

- a) Sulphide veinlets and thin veins (up to 1 cm) in the shale, concordant with lamination and often associated with finely disseminated sulphides; represented by chalcopyrite (Fig 3a, Fig 4a-c), bornite, sphalerite (Fig 3b, Fig 4d) and chalcocite. Two of these samples, Ko11-2339-103 and Sr10-3484-104 (consisting of chalcopyrite veinlets in shale with chalcocite, digenite (Cu₉S₅), djurleite (Cu₃₁S₁₆) and bornite disseminations) were added due to bulk

- rock geochemistry data indicating rhenium enrichment (1.85 and 18.4 ppm of Re respectively).
- More irregular and massive mineralization represented by massive djurleite lens/vein at the boundary between shale and carbonates (Fig 3c); by chalcocite (Fig 3d, Fig 4e) and covellite (Fig 3e, Fig 4f) in the Weisslied sandstone; and by massive collomorphic bornite and chalcocite in organogenic limestone.
 - Epigenetic massive sulphide (\pm carbonates) veins, up to 10 cm thick, usually steep and commonly fault-related, in some cases cementing and impregnating breccia zones. Ore assemblage consists mainly of chalcopyrite (Fig 3f), with minor bornite, sphalerite (Fig 4g), galena and tennantite.
 - Sulphide mineralization inside or in the vicinity of the secondary oxidation zones (SOS system, not to be confused with supergene processes) characterized by the widespread presence of disseminated hematite (“red spots”), locally associated with noble metals mineralization. They are represented by chalcopyrite (Fig 4h), pyrite (Fig 3g, Fig 4i), and djurleite (Fig 3h).

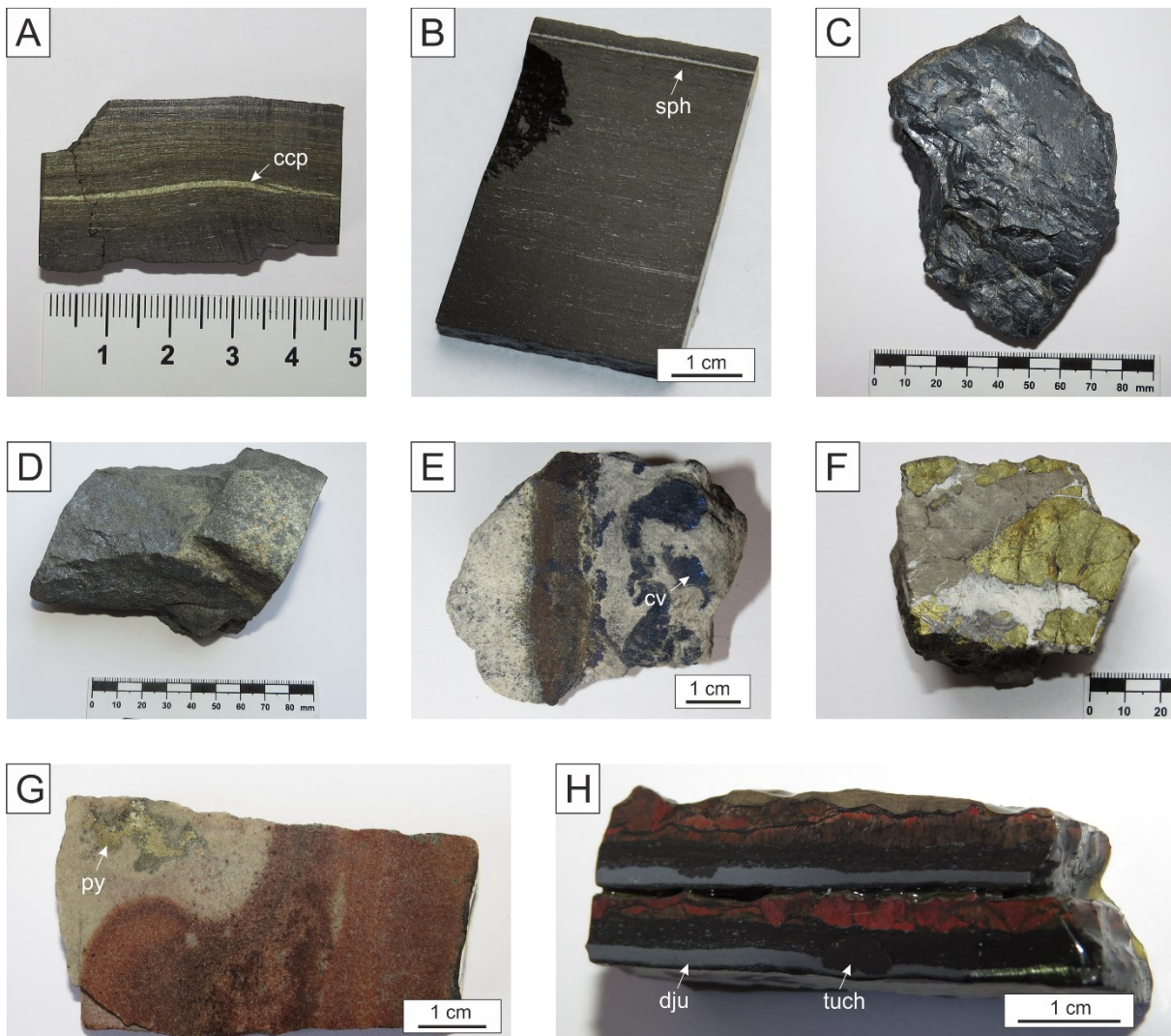


Fig. 3. A – chalcopyrite (ccp) vein, veinlets and disseminations in the Kupferschiefer, parallel to shale lamination (sample B-1-2); B – sphalerite (sph) veinlet in the Kupferschiefer, parallel to shale lamination

(sample SPH-S1); C – massive djurleite lens from the contact between shale and carbonates (sample WZ-14); D – massive chalcocite ore in sandstone from the “sandstone elevation” (sample WZ-17); E – covellite (cv) in the Weisslied sandstone (sample WZ-16); F – part of chalcopyrite-calcite epigenetic vein in carbonate lithology (sample SPW9, the same sampling location as sample WZ 20); G – pyrite (py) aggregates in the Weisslied sandstone near red coloured hematite stained “red spots” zone (sample RU-CP-1); H – djurleite (dju) veinlets and thucholite (tuch) concretion in shale adjacent to hematite “red spots” alteration (sample CC-P-1, picture show two rock pieces glued on top of each other).

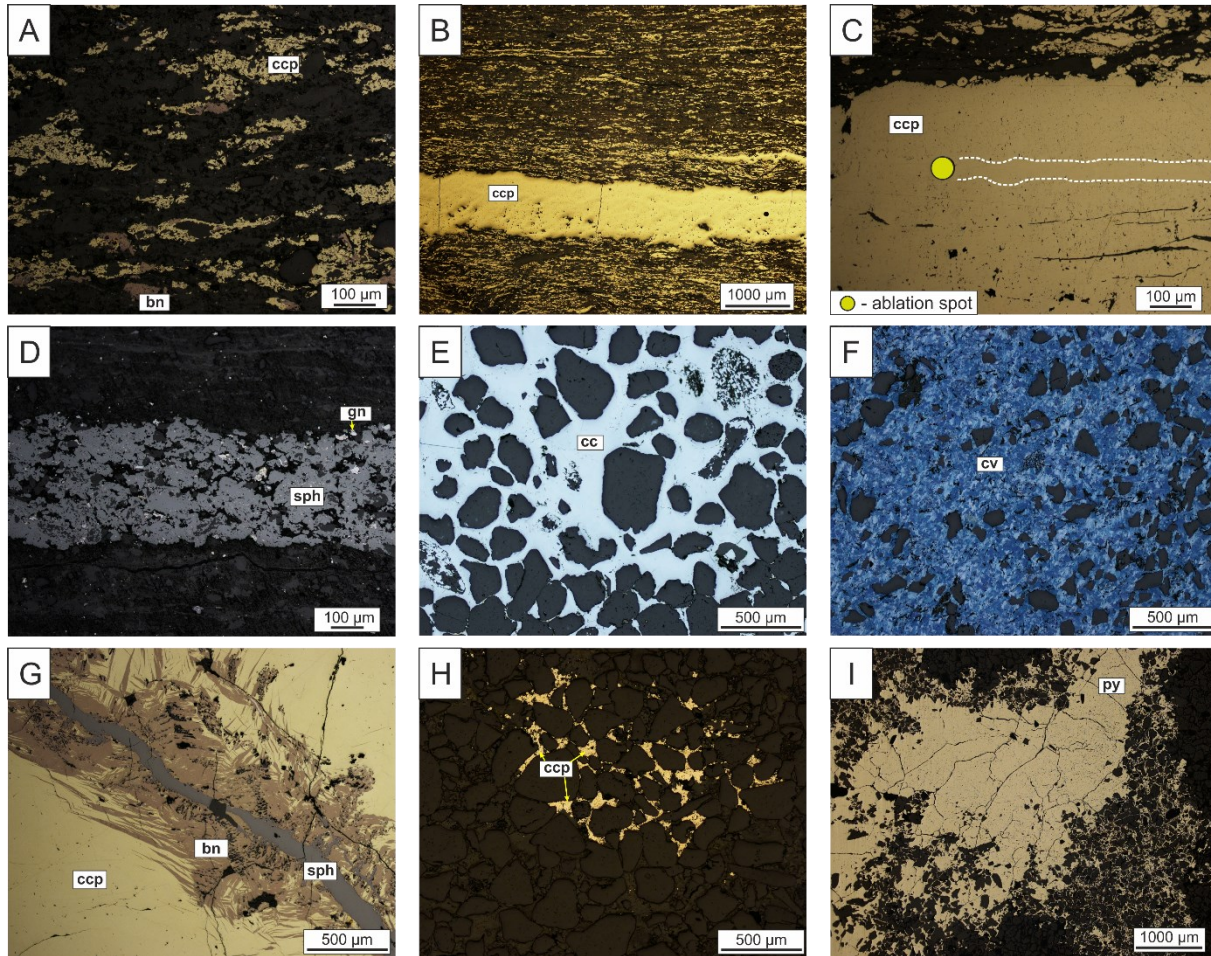


Fig. 4. A – typical chalcopyrite and bornite disseminations in the Kupferschiefer (too fine-grained to be analysed with LA-ICP-MS); B – bedding-parallel chalcopyrite vein and veinlets in the Kupferschiefer (sample B-1-2); C – chalcopyrite vein in the shale, note the variability in the amount of gangue mineral inclusions in the vein, white line indicates the border between relatively inclusion free and inclusion rich zones (sample B-1-2), D – bedding-parallel sphalerite vein in the Kupferschiefer, with visible inclusions of galena (sample SPH-S1); E – massive chalcocite ore replacing matrix in the Weisslied sandstone (sample WZ-17); F – massive covellite in the Weisslied sandstone (sample WZ-16); G – massive chalcopyrite in epigenetic vein cut by sphalerite veinlet and with bornite replacement at the contact (sample WZ-20); H – chalcopyrite replacing matrix in red coloured sandstone (caused by hematite alteration related to the SOS system) (sample CP-1); I – pyrite in sandstone near hematite alteration zone (SOS system) (sample RU-CP-1). Bn – bornite, cc – chalcocite, ccp – chalcopyrite, cv – covellite, gn – galena, py – pyrite, sph – sphalerite.

Additionally, two representative samples of chalcopyrite from the Nchanga deposit (Zambian Copperbelt) were analysed for reference. The suite of samples was biased towards coarse-grained, inclusion-free sulphides, disseminated mineralization was not analysed. Additionally, they tend to be rather monomineralic with the exception of fault-related epigenetic sulphide-carbonate veins (chalcopyrite-bornite-sphalerite) and sample WZ-18 with collomorphic bornite and chalcocite. Optical light microscopy was used to characterize ore minerals and select spots for further analyses, paying particular attention to mineral inclusions, intergrowths, zoning, cracks or other textural aspects, all of which may impact on trace element distribution. Nonetheless, even relatively thick sulphide veinlets in the Kupferschiefer contain numerous inclusions of shale matrix (Fig. 4c-d) and in these cases, multiple spots were picked and analysed to minimize their influence (e.g. prioritizing sectors with less inclusions, see Fig. 4c as an example). Samples were studied by electron microprobe to assess the content of major element, which would be used as the internal standard during LA-ICP-MS measurements. In cases where the EPMA data was not available, stoichiometric concentrations of Cu for copper sulphides and S for sphalerite and pyrite were assumed and used as the internal standard. Microprobe analyses (EPMA) of chalcopyrite, djurleite, sphalerite, covellite, bornite and chalcocite were carried out using a JEOL JXA-8230 SuperProbe at the Laboratory of Critical Elements AGH-KGHM in Kraków. The electron microprobe was operated in the wavelength-dispersive mode at an accelerating voltage of 20kV and a probe current of 20 nA. Counting times of 20 s on peak, and of 10 s on both (-) and (+) backgrounds were used for all elements except In and Ge where 40 s on peak and 20 s on both (-) and (+) backgrounds were used. The following standards and spectral lines were used for sulphides: FeS₂ (FeK α , SK α), chalcopyrite (CuK α), ZnS (ZnK α), Ag (AgL α), stibnite (SbL α), CdS (CdL α), GaAs (AsL α), Sb₂Se₃ (SeL α), GeS (GeL α) and HgS (HgM α). Data were corrected by the ZAF procedure using JEOL software for electron microprobe. Presence of djurleite, suggested by Cu/S atomic ratios in measured phases, was confirmed by X-ray powder diffraction (XRD).

Trace element contents were measured at the Department of Applied Geosciences and Geophysics, Montanuniversität Leoben, Austria, using an ESI NWR213 Nd:YAG laser ablation system coupled to an Agilent 8800[®] triple quadrupole ICP-MS. Helium was used as carrier gas with a flow rate of 0.75 L/min. Fluency was set between 2-3 J/cm². For sphalerite and pyrite analyses, the matrix-matched sintered pressed powder pellet reference material MUL-ZnS 1 (Onuk et al., 2017) was used as the external standard for quantification of the element content and the USGS powder pressed polysulphide reference material MASS-1 (Wilson et al., 2002) was used for quality control of the analyses. The MASS-1 reference material was used as the external standard for quantification of chalcopyrite, bornite, chalcocite and djurleite. Data reduction was done using the Lolite V4.0 software. Integration intervals for calculating absolute concentrations in $\mu\text{g/g}$ were chosen on smooth spectra concordant with the signals of the internal standard and other major elements of the different sulphides. The following isotopes were analysed: ⁵¹V, ⁵⁵Mn, ⁵⁷Fe, ⁵⁹Co, ⁶⁰Ni, ⁶³Cu, ⁷¹Ga, ⁷⁴Ge, ⁷⁵As, ⁸²Se, ⁹⁵Mo, ¹⁰⁷Ag, ¹¹¹Cd, ¹¹⁵In, ¹¹⁸Sn, ¹²¹Sb, ¹²⁵Te, ¹⁸⁵Re, ¹⁹⁵Pt, ¹⁹⁷Au, ²⁰¹Hg, ²⁰⁵Tl, ²⁰⁸Pb, ²⁰⁹Bi. Sphalerite (MUL-ZnS1) and sulphide (MASS-1) reference materials were periodically analysed (every 14 spots) for quality control. As MASS-1 contains little Re (0 $\mu\text{g/g}$ according to Feng et al. 2018 and 0.504 $\mu\text{g/g}$ according to Sen et al. 2010) and Pt, NIST-612 reference material was used to quantify the content of these elements. Ablation spots were carefully selected in an effort to analyse sulphides free of obvious inclusions or cracks;

nevertheless, samples locally display inhomogeneity on the scale of the ablation spot. A consistent 50 μm diameter spot size was used for all measurements.

Due to the isobaric interference between ^{113}In and ^{113}Cd , ^{115}In was primarily used to estimate the concentration of In. The interference of ^{115}Sn on ^{115}In was insignificant as Sn content in analysed sulphides was sufficiently low and the ^{115}Sn isotope abundance is just 0.34%. Ge suffers from various interferences on its isotopes (e.g. ^{72}Ge with $^{40}\text{Ar}^{32}\text{S}$ and $^{56}\text{Fe}^{16}\text{O}$; ^{73}Ge with $^{40}\text{Ar}^{33}\text{S}$, $^{57}\text{Fe}^{16}\text{O}$, and $^{56}\text{Fe}^{16}\text{O}^1\text{H}$; ^{74}Ge with $^{40}\text{Ar}^{34}\text{S}$ and $^{58}\text{Ni}^{16}\text{O}$; Belissont et al. 2014) while measured with ICP-MS and thus provides a challenge for confident determination of low concentrations (Cook et al. 2009). The ^{74}Ge isotope was chosen for this study to minimize potential interferences in Cu-Fe sulphides following Belissont et al. (2014) who have shown that at least in the case of sphalerite, the ^{74}Ge isotope seems to be the most suitable one due to relative isotopic abundance and negligible interferences. Despite potential interference contributions of TmO^+ in ^{185}Re , HfO^+ in ^{195}Pt and TaO^+ in ^{197}Au determination, the lithophile nature of Tm, Hf and Ta suggest their concentrations in sulphides would be sufficiently low to not affect results in a meaningful way. ^{185}Re isotope was preferred as ^{187}Re has a potential isobaric interference not only with YbO^+ but also with ^{187}Os . In the majority of samples, no signal was detected for ^{185}Re , ^{195}Pt and ^{197}Au suggesting concentrations below detection limit (in most cases below 0.1 $\mu\text{g/g}$). The non-matrix matched reference material (NIST 612) used for Re and Pt might decrease the confidence in the low concentration values reported here and can be considered as semiquantitative; nonetheless, the presence or lack of signals for ^{185}Re , ^{195}Pt and ^{197}Au itself is considered an important information.

Due to intergrowths and inhomogeneity, data for 21 samples (7 from the Rudna, 6 from the Sieroszowice-Polkowice and 6 from the Lubin mine) were considered to be of sufficiently good quality to be presented here. Data for 5 chalcocite/djurleite, 1 covellite, 2 bornite, 3 sphalerite, 1 pyrite and 12 chalcopyrite samples amounts to a total of 225 in situ LA-ICP-MS spots. A complete list of samples with the location (mine), host rock and mineralization style can be found in Table 1.

4. Results

4.1 Overview

Results of the measurements are presented in the Table 1 and Appendix A with an overview provided as box and whisker plots on Figures 5 and 6. When compared with other measured sulphides, chalcocite/djurleite shows enrichment in Ag and Bi but also depletion in V, Co, As, Sn; in the case of covellite higher content of Mn, Ga, Mo, Tl, Pb, Bi is noticeable; bornite has higher Sn, higher and more variable Co; chalcopyrite is enriched in Ge and Sb while sphalerite is characterized by increased content of Cd and Hg with simultaneous depletion in As, Ag and Pb (Fig. 5). Data for V, Co, Ni, Ga, Ge, As, Mo show significant variation within given mineral which could be explained by two factors. Firstly, distinct trace elements composition within one mineral species reflects different mineralizing fluids and/or processes. Data for chalcopyrite split according to ore texture (Fig. 6) show clear contrast. Epigenetic chalcopyrite veins have high concentrations of Ge and As (or In, Sb and Bi instead of Ge and As in sample LB-6) while chalcopyrite found in the zone of “red spots” (sample CP-1) is enriched in Ge, Se, Hg, Tl, Pb, Bi (Fig. 6, Fig 7b-f) in comparison to its counterpart occurring as concordant, shale-hosted veinlets.

In fact, “red spots” chalcopyrite is characterized by the highest contents of selenium (median 4207 $\mu\text{g/g}$) and Hg (median 614 $\mu\text{g/g}$) among all measured sulphides. Djurleite associated with the “red spots” (sample CC-P-1) is enriched in V, Co, Ni, As, Se, Hg, Tl, Pb and Bi when compared with other chalcocite/djurleite samples. Pyrite near the “red spots” zone is rich in Tl (median 130 $\mu\text{g/g}$) and As (median 5333 $\mu\text{g/g}$). Additionally, “red spots” associated djurleite (but not chalcopyrite or pyrite) is unique due to consistently detectable signal of Au and Re (up to 0.5 and 0.9 $\mu\text{g/g}$ respectively, Fig. 7b, Tab. 1). Enrichment in Hg, Tl, V, Se with occasional Re and Au seems to be a characteristic feature of sulphides found in the “red spots” areas, clearly differentiating them from the bulk Cu-Ag ore.

Secondly, the dataset for chalcocite, bornite, chalcopyrite and sphalerite can be split into two distinct groups: the first consists of more massive mineralization (e.g. epigenetic veins, massive chalcocite in sandstone) while the second is represented by shale hosted, bedding parallel veins and veinlets, often rich in inclusions of gangue minerals. The latter group is characterized by higher concentration and substantially more variable data for some elements (e.g. V, Ni, Co), which in turn are often absent in the samples from the “massive mineralization” group (Fig. 6, Tab. 1). This variation suggest that trace elements content can be related to the host rock, more specifically it might be affected by micro- and/or nano-inclusions associated with them. Tiny Kupferschiefer-matrix inclusions (predominantly a mixture of clay minerals, silica, organic matter and carbonates in various proportions) enclosed by crystallizing ore minerals, could be enriched in many metals (e.g. Co, Ni, Mo) in contrast to remnants of either Weissliegend sandstone matrix or Zechstein carbonates. Although we did our best to minimize the effect of inclusions, their influence cannot be completely excluded. Figure 7 presents selected time-resolved downhole ablation spectra where subparallel and smooth lines are generally indicative of lattice-bound elements or evenly distributed nano-scale inclusions while “rugged” patterns suggest the presence of micro-inclusions (Pb in Fig. 7d is a clear example of microinclusions). Si, Al and Ca should be used in the future studies as a proxy for tiny shale-matrix inclusions, nonetheless it can be hard to unambiguously distinguish them in time-resolved spectra, especially in case of less abundant elements with multiple possible hosts (e.g. Mn, Co, Ni). Some of the spots were unsuitable for data reduction because ablated material turned out to contain a significant portion of shale matrix, but in return they could provide clues how to interpret results affected by non-sulphide material. Stepanov et al. (2020) present a method of measuring fine-grained pyrite intergrowth with silicate matrix in sedimentary rocks, involving analysis of both pyrite and pyrite-free sediment matrix and regression of time-resolved LA-ICP-MS data. While quantification of trace element requires several steps, for our purpose we can simply use raw counts along single ablation spot to assess whether the trace elements in this particular area are hosted within the copper sulphides (strong correlation with Cu and S) or other phases interpreted as shale matrix (elements strongly correlated with each other but not with Cu and S). Especially useful are samples with a clear transition between sulphide and shale, e.g. ablation of a relatively large inclusion just below the sulphide surface (Fig. 8). Visual inspection of the time resolved downhole spectra, coupled with calculation of statistical correlation between counts (Appendix B), allow to prepare a provisional classification of elements. Two clusters of elements stand out: one with affinity to chalcopyrite (Cu, Fe, S) including Ag, Tl, Sb, Pb (+Ge, As, Hg) and a second one consisting of Ni, V, Ga, Sn, Co, Mo (+Mn) which can be associated with Kupferschiefer matrix. Despite exceptions (e.g. strong Mo enrichment in sulphide in sample LZ 03), it seems that variation in V,

Ni, Co, Ga, Mo, Sn in chalcopyrite (Fig. 6) can be attributed to shale matrix inclusions. Not enough data was available for similar analysis regarding chalcocite, bornite and sphalerite but analogous explanation for high variations of these elements seems to be plausible. Elements with no clear preference include Se, In, Cd and Bi. Se and Cd have relatively high detection limits which might generate apparent inert characteristic but a noticeable feature is very low content of indium in almost all measured sulphides (Fig. 5, Tab. 1, Appendix A). Almost 55% of all spots have below 0.1 µg/g of In, while only 15% has >1 µg/g of In (chalcopyrite sample LB6 with up to 222 µg/g In being the exception and outlier).

*Tab. 1. Summary statistics for trace element concentrations (µg/g) in ore minerals. SD = Standard deviation, ADL (%) = Percentage of analyses above the lower detection limit, * - weak signal, na = not measured, samples with high background values for Se and Hg are marked in red. bn – bornite, cc – chalcocite, ccp – chalcopyrite, cth – clausthalite, cv – covellite, dig – digenite, dju – djurleite, gn – galena, py – pyrite, sph – sphalerite, tnt – tennantite, tuch – tucholite.*

All min, max, median, mean and SD data are in µg/g

Mineral	Texture	Sample name (n = no. of analyses)	V	Cr	Ni	Cu	Zn	Ga	Ge	As	Se	Mo	Ag	Cd	In	Sn	Sb	Te	Re	Pt	Au	Hg	Tl	Pb	Bi	Lithology/Mine/Ore mineral assemblage
djurleite	massive mineralization	WZ-14	Max 1.19	160	1603	4.66	1.35	-	0.42	7.48	13.01	3474	0.29	0.33	0.15	3.06	7.73	1.40	165	1.14	0.86	0.06	1.7	0.40	carbonates/shale	
		n=13	Min 0.17	0.93	103	0.29	0.80	-	0.09	1.20	0.13	3088	0.23	0.65	1.90	0.49	35	0.54	Lubin							
chalcoite	massive mineralization	Mean	11.7	199	0.44	-	-	5.55	1.80	3214	1.14	2.69	0.52	45	0.67	dju, minor py										
		SD	32.3	411	1.40	-	-	4.56	2.80	3234	1.27	2.12	0.45	47	0.25											
		ADL	54%	85%	100%	38%	31%	0%	17%	0%	62%	0%	85%	100%	100%	100%	100%									
		Max 19.0	1837	5164	0.70	2.09	-	1.19	2.44	5.01	453	20.65	0.27	0.73	1.50	0.19	10.21	25.9	3553	85						
chalcoite	massive mineralization	Min	0.17	33.8	140	0.16	0.77	-	0.19	1.25	0.67	208	0.23	<2	0.46	94	2.69	sandstone								
		Median	0.96	136	340	0.22	-	-	239	4.18	4.02	511	13.47	Rudina												
		Mean	3.62	308	857	0.33	-	-	258	4.81	5.81	777	20.34	cc												
		SD	6.36	542	1527	0.20	-	-	70	2.53	7.26	998	23.41													
chalcoite	massive mineralization	ADL	90%	100%	100%	80%	30%	0%	30%	0%	20%	100%	10%	20%	20%	50%	0%	10%	0%	0%	80%	100%	100%	100%		
		Max 0.36	726	1376	0.69	-	28	0.39	7.90	4.81	1070	0.42	5.59	2.47	8.30	45.5	1169	112								
chalcoite	massive mineralization	Min	0.29	3.09	<50	-	-	1.26	0.26	792	0.23	0.27	1.63	0.10	3.8	0.51	organogenic limestone									
		Median	4.15	-	-	-	-	0.39	833	0.53	23.5	2.16	5.52	154	12.91	cc, bn										
chalcoite	concordant vein in shale	Mean	151	-	-	-	-	1.24	865	0.20	81	14.99	381	34.8	5.52	154	12.91	cc, bn								
		SD	322	-	-	-	-	2.00	81	0.20	81	14.99	381	34.8	5.52	154	12.91	cc, bn								
		ADL	20%	50%	80%	8%	0%	10%	10%	0%	20%	40%	0%	30%	0%	0%	20%	70%	90%	100%	100%					
		Max 2.70	1.21	101	0.71	0.38	-	0.63	25.09	20.01	3814	2.22	0.8	0.05	0.03	17.67	0.54	17.8	0.04							
djurleite	adjacent to oxidized lithologies	Min	0.37	0.91	<50	0.06	0.24	-	0.05	17.23	0.46	3600	0.36	0.1	4.1	0.5	27	0.52	shale							
		Median	1.02	-	-	0.23	-	0.16	2.36	3704	0.06	6.0	0.11	6.7	0.15	4.7										
		Mean	1.41	-	-	0.22	-	0.21	5.01	3704	0.33%	42%	100%	100%	8%	0%	8%	0%	33%	42%	50%	100%	42%			
		SD	1.05	-	-	0.19	-	0.19	5.72	67	0.96	0.3	0.2	16.5	10.3	372	9.29									
djurleite	adjacent to oxidized lithologies	ADL	67%	17%	17%	83%	17%	0%	25%	0%	0%	42%	100%	100%	8%	0%	8%	0%	33%	42%	50%	100%	42%			
		Max 258	220	inclusions	195	275	-	1.10	0.96	794	101	34.45	566	0.03	2.63	0.56	0.9	0.5	37	24.5	972	24.54				
covellite	massive mineralization	Min	3.03	18.6	0.13	1.16	-	0.05	0.29	2.58	32.8	0.35	289	0.36	0.1	4.1	0.5	27	0.52	shale						
		Median	65.7	42.9	28.3	46.4	-	0.53	0.49	86.7	58.3	5.65	382	0.96	0.3	0.2	16.5	10.3	372	9.29						
		Mean	77.1	78.4	49.6	79.9	-	0.49	0.55	208	61.8	7.75	379	1.23	0.3	0.2	16.9	9.4	353	8.99						
		SD	68.0	72.8	61.6	90.9	-	0.39	0.25	248	19.8	9.41	84	0.74	0.3	0.1	10.5	7.5	292	7.62						
covellite	massive mineralization	ADL	100%	100%	83%	83%	-	0%	92%	58%	83%	100%	100%	100%	0%	8%	0%	75%	8%	75%	0%	100%	100%	100%	100%	
		Max 43.2	436	10269	22.1	14.65	-	75.5	38.5	2.27	179	191	692	0.02	1.52	1.28	0.37	*	na	16.81	10.31	1476	93.6			
covellite	massive mineralization	Min	12.25	8.67	2811	3.25	4.10	-	19.52	1.65	0.36	27.4	1.82	4.62	0.43	0.21	0.23	*	na	2.53	4.98	572	40.4	sandstone		
		Max 12.25	8.67	2811	3.25	4.10	-	19.52	1.65	0.36	27.4	1.82	4.62	0.43	0.21	0.23	*	na	2.53	4.98	572	40.4	sandstone			

(continued on next page)

Table 1 (continued)

		All min, max, median, mean and SD data are in µg/g																												
Mineral	Texture	Sample name (n = no. of analyses)	V	Mn	Fe	Co	Ni	Cu	Zn	Ga	Ge	As	Se	Mo	Ag	Cd	In	Sn	Sb	Te	Re	Pt	Au	Hg	Tl	Pb	Bi	Lithology/ Mine/Ore mineral assemblage		
bornite	concordant vein/veinlets in shale	BRN-1	Median 14.95	114	4061	11.47	9.51	-	3.77	34.9	34.9	63.0	20.1	564	1.06	0.71	1.06	0.71	0.71	*	na	na	6.23	7.13	701	59.0	Rudna			
			Mean 19.81	143	5282	12.02	9.42	-	9.44	63.0	63.0	42.6	569	42.6	569	1.07	0.67	1.07	0.67	*	na	na	7.95	7.23	804	58.7	cv, traces of ccp			
			SD 10.76	137	2731	7.73	4.26	-	15.97	65.4	65.4	67.1	87.0	67.1	87.0	0.47	0.38	0.47	0.38	*	na	na	6.69	2.16	311	18.15				
			ADL 86%	100%	100%	86%	71%	-	29%	43%	71%	0%	100%	100%	0%	14%	71%	86%	29%	*	na	na	0%	57%	100%	100%	100%	100%		
	Max 34.7	30.9	-	1.15	14.23	-	3.06	1.07	63	16.19	479	63	16.19	479	0.25	0.40	0.25	0.40	*	na	na	3.97	0.60	83.2	0.12					
bornite	fault-related epigenetic veins	n=11	Min 1.12	4.34	-	0.16	0.73	-	0.24	0.33	391	0.24	0.33	391	0.24	0.24	0.24	0.24	0.24	*	na	na	1.62	0.02	5.10	0.05	shale			
			Median 4.21	6.53	-	0.32	3.55	-	0.31	51	1.34	407	51	1.34	407	0.31	0.31	0.31	0.31	*	na	na	2.65	0.28	40.2	0.07	Polkowice-Sierozowice			
			Mean 9.90	10.81	-	0.47	4.36	-	0.90	46	3.42	420	46	3.42	420	0.90	0.90	0.90	0.90	*	na	na	2.80	0.34	36.7	0.08	bn, traces of ccp, cc, dig			
			SD 10.94	9.34	-	0.41	3.99	-	1.39	13.8	4.56	26.0	13.8	4.56	26.0	1.39	1.39	1.39	1.39	*	na	na	0.72	0.22	26.4	0.02				
	ADL 100%	100%	-	45%	82%	-	0%	36%	9%	0%	100%	100%	0%	0%	9%	36%	0%	*	na	na	0%	91%	91%	100%	91%	100%				
	Max 0.18	24.2	-	345	319	-	0%	3.66	870	3.31	175	3.31	175	0.08	22.81	4.04	0.08	22.81	4.04	*	na	na	2.05	1.38	388	0.18				
chalcopyrite	concordant vein/veinlets in shale	n=11	Min 4.5	-	0.0	0.0	-	2.98	8.45	2.98	8.45	4.10	206	0.20	83.0	0.05	2.02	0.19	0.05	2.02	0.19	*	na	na	0.85	0.84	133	0.14	carbonates	
			Median 5.6	-	67	42	-	4.10	206	4.10	206	0.71	120	0.71	120	7.44	0.62	7.44	0.62	*	na	na	1.25	1.18	242	0.15	Polkowice-Sierozowice			
			Mean 7.2	-	92	74	-	4.40	229	4.40	229	1.21	110	1.21	110	8.82	1.07	8.82	1.07	*	na	na	1.26	1.11	252	0.16	ccp, minor bn, sph, gn			
			SD 5.7	-	94	60	-	1.52	233	1.52	233	1.17	25.5	1.17	25.5	6.40	1.10	6.40	1.10	*	na	na	0.30	0.17	72.0	0.03				
	ADL 9%	100%	-	100%	100%	-	0%	100%	100%	0%	73%	100%	0%	36%	100%	100%	0%	36%	100%	100%	0%	0%	91%	100%	100%	91%	100%			
	Max 1394	640	-	7.45	210	-	49.9	14.36	7.84	4.40	62.3	192	520	0.10	3.79	4.49	0.10	3.79	4.49	*	na	na	0.02	58.6	6.16	317	0.07			
chalcopyrite	concordant vein/veinlets in shale	n=4	Min 33.2	16.3	-	0.57	11.01	-	24.2	1.12	2.49	3.52	32.8	9.10	311	0.02	0.63	0.99	0.02	0.63	0.99	*	na	na	15.95	4.26	248		shale	
			Median 797	200	-	4.98	86.9	-	49.8	10.12	6.54	3.97	43.5	119	473	0.08	2.55	3.29	0.08	2.55	3.29	*	na	na	25.7	4.91	284		Rudna	
			Mean 755	264	-	4.50	98.6	-	41.3	8.93	5.85	3.96	45.5	110	445	0.07	2.38	3.02	0.07	2.38	3.02	*	na	na	31.5	5.06	283		ccp	
			SD 592	266	-	3.02	84.1	-	14.80	5.86	2.53	0.44	13.88	78.7	95.8	0.04	1.37	1.52	0.04	1.37	1.52	*	na	na	18.79	0.82	33.1			
	ADL 100%	100%	-	100%	100%	-	75%	100%	100%	75%	100%	100%	100%	0%	100%	100%	0%	100%	100%	100%	0%	na	25%	100%	100%	100%	25%			
	Max 1.40	15.33	-	0.42	7.32	-	0.08	0.21	26.7	0.12	31.9	26.7	0.12	31.9	2.83	1.23	1.66	2.83	1.23	1.66	*	na	na	22.0	1.84	137	0.03			
chalcopyrite	concordant vein/veinlets in shale	n=7	Min 0.71	14.01	-	0.19	3.31	-	0.08	0.15	14.56	16.35	14.56	16.35	1.88	0.95	1.46	1.88	0.95	1.46	*	na	na	5.16	0.98	96.8	0.02	shale		
			Median 0.90	14.44	-	0.29	4.93	-	18.51	20.4	18.51	20.4	20.3	22.7	1.92	1.15	1.63	1.92	1.15	1.63	*	na	na	10.19	1.42	116	0.02	Lubina		
			Mean 1.03	14.40	-	0.31	5.42	-	20.3	22.7	20.3	22.7	2.25	1.11	1.61	2.25	1.11	1.61	2.25	1.11	1.61	*	na	na	11.01	1.43	116	0.02	ccp, minor bn	
			SD 0.26	0.42	-	0.08	1.32	-	4.70	6.40	4.70	6.40	100%	100%	100%	0%	100%	100%	100%	0%	0%	0%	0%	45%	100%	100%	71%			
	ADL 100%	100%	-	100%	100%	-	0%	29%	43%	0%	100%	14%	100%	0%	0%	0%	0%	0%	0%	0%	0%	0%	0%	0%	0%	0%	0%			
	Max 47.9	269	-	4.41	39.3	-	0.65	1.36	5.84	69.4	22.4	773	69.4	22.4	0.09	0.66	3.25	0.09	0.66	3.25	0.10	na	0.01	28.7	2.04	285	0.08			
chalcopyrite	concordant vein/veinlets in shale	n=11	Min 5.20	15.83	-	0.15	1.54	-	0.09	0.25	3.27	27.2	0.64	8.79	0.02	0.30	0.75	0.02	0.30	0.75	*	na	na	7.92	0.40	45.6	0.02	shale		
			Median 8.26	23.1	-	0.49	6.99	-	0.20	0.37	43.5	3.23	30.0	43.5	3.23	30.0	0.04	0.43	1.70	0.04	0.43	1.70	*	na	na	10.70	1.01	113	0.05	Rudna
			Mean 16.70	44.6	-	1.10	9.64	-	0.26	0.49	41.9	5.39	108	41.9	5.39	108	0.05	0.44	1.92	0.05	0.44	1.92	*	na	na	13.10	1.11	135	0.05	ccp
			SD 16.15	74.7	-	1.45	10.55	-	0.20	0.34	12.69	6.19	224	12.69	6.19	224	0.02	0.10	0.66	0.02	0.10	0.66	*	na	na	7.15	0.52	78.0	0.02	
	ADL 100%	100%	-	100%	100%	-	0%	91%	100%	18%	100%	100%	100%	0%	82%	100%	100%	9%	82%	100%	100%	9%	na	9%	64%	100%	100%	91%		

(continued on next page)

Table 1 (continued)

Mineral	Texture	Sample name (n = no. of analyses)	All min, max, median, mean and SD data are in µg/g																												Lithology/ Mine/Ore mineral assemblage
			V	Mn	Fe	Co	Ni	Cu	Zn	Ga	Ge	As	Se	Mo	Ag	Cd	In	Sn	Sb	Te	Re	Pt	Au	Hg	Tl	Pb	Bi				
chalcopyrite	concordant vein/veinlets in chalc	LZ 03	Max	200	185	-	49.0	22.1	-	17.2	3.37	1.79	35.8	55.3	828	266	1.73	9.39	17.61	1.13	*	na	na	na	na	13.4	1614	2.75			
		n=7	Min	80.0	62.0	-	24.8	12.28	-	1.17	0.77	14.88	31.2	472	132			1.51	2.81	9.47	0.67	*	na	na	na	5.52	973	1.31	chalc		
			Median	159	123	-	42.4	20.4	-	2.13	1.11	27.5	51.9	665	185			1.55	7.31	12.79	0.75	*	na	na	na	8.55	1205	1.85	Lubin		
			Mean	148	126	-	39.3	17.81	-	2.07	1.23	26.3	47.8	645	195			1.59	6.58	12.87	0.88	*	na	na	na	8.98	1217	1.84	ccp, traces of bn		
chalcopyrite	fault related epigenetic veins	WZ-20	SD	39.0	43.4	-	9.41	4.03	-	0.72	0.39	7.87	6.47	151	48.7			0.09	2.15	2.88	0.21	*	na	na	na	2.81	214	0.51			
		n=11	ADL	100%	100%	-	100%	100%	-	14%	100%	100%	100%	100%	100%	0%			100%	100%	100%	100%	*	na	na	na	0%	100%	100%	100%	
			Max	0.07	10.38	-	19.07	-	-	1.41	0.89	2403	415	31.4	0.10	13.59			0.57	32.6	59.5		na	na	na	na	6.22	1.03	138	0.16	
			Min	9.29	-	-	0.39	-	-	36.6	0.13	11.38	26.7	10.45	0.08	2.30			0.10	0.55	11.28		na	na	na	na	0.63	0.05	26	0.02	
chalcopyrite	fault related epigenetic veins	RUG-3a	Median	9.68	-	-	5.16	-	-	46.7	0.44	1106	55.2	6.42				0.36	1.55	20.9		na	na	na	na	1.89	0.66	118	0.05		
		n=10	Mean	9.73	-	-	6.30	-	-	60.3	0.51	920	163	6.42				0.31	8.91	22.8		na	na	na	na	2.77	0.49	176	0.07		
			SD	0.31	-	-	6.02	-	-	34.6	0.28	735	157	3.23				0.18	12.48	13.77		na	na	na	na	1.85	0.38	124	0.05		
			ADL	9%	100%	-	100%	0%	-	73%	91%	100%	100%	45%	27%	100%	0%		100%	91%	100%	0%	na	na	na	na	100%	100%	91%	73%	
chalcopyrite	fault related epigenetic veins	RU-W2	Max	4.90	-	-	5.78	-	-	214	1.34	2726	1045	192	3.00	65.3			0.25	17.97	73.0		na	na	na	na	121	1.91	379	1.73	
		n=10	Min	3.93	-	-	2.17	-	-	45.8	0.44	948	115	53.7	0.11	6.22			0.09	1.91	30.5		na	na	na	na	26.2	0.17	42	0.12	carbonates
			Median	4.22	-	-	3.43	-	-	94.8	0.69	1609	571	80.9	0.63	10.95			0.16	7.55	48.3		na	na	na	na	33.9	0.66	133	0.36	Rudha
			Mean	4.23	-	-	3.55	-	-	96.8	0.76	1646	571	97.3	1.00	23.2			0.16	8.66	50.6		na	na	na	na	51.9	0.84	365	0.58	ccp, minor bn and sph, gn inclusions
chalcopyrite	fault related epigenetic veins	RU-W2	SD	0.28	-	-	1.24	-	-	50.2	0.28	530	415	48.8	0.92	22.4			0.06	6.51	14.82		na	na	na	na	31.8	0.62	609	0.55	
		n=13	ADL	0%	100%	-	100%	0%	-	90%	100%	100%	100%	100%	100%	0%			100%	100%	100%	0%	0%	0%	0%	0%	100%	100%	90%	100%	
			Max	13.75	-	-	8.90	0.97	-	186	4.46	4806	969	15.52	0.80	34.5			0.62	1.94	395		na	na	na	na	0.02	2.27	1.29	458	0.11
			Min	12.90	-	-	2.47	-	-	22.4	1.84	1288	337	10.62	0.04	8.03			0.24	0.14	104		na	na	na	na	0.39	0.28	126	0.02	carbonates
chalcopyrite	epigenetic veins	LB6	Median	13.32	-	-	3.93	-	-	39.4	2.93	2236	705	12.97	16.39			0.45	1.16	299		na	na	na	na	1.06	0.66	258	0.07	Rudha	
		n=8	Mean	13.30	-	-	4.93	-	-	66.1	3.05	2581	688	12.89	17.66			0.45	1.01	267		na	na	na	na	1.19	0.66	262	0.07	ccp, minor bn and sph	
			SD	0.24	-	-	2.28	-	-	54.6	0.75	897	239	1.90	6.87			0.09	0.61	107		na	na	na	na	0.63	0.30	103	0.03		
			ADL	0%	100%	-	92%	8%	-	92%	100%	100%	100%	46%	38%	100%	0%		100%	92%	100%	0%	0%	0%	0%	8%	77%	92%	100%	85%	
chalcopyrite	epigenetic veins	LZ 2 VII	Max	0.49	51.0	-	32.8	3.72	-	4614	0.66	1.01	307	142	1.79	500	91.3	222	544	5.57	1.50	*	na	na	na	na	0.17	1.23	4441	4784	
		n=8	Min	0.11	14.91	-	3.04	0.34	-	413	0.15	0.19	15.56	21.1	0.09	121	12.52	140	100	0.34	0.36	*	na	na	na	na	0.07	0.27	490	127	carbonates
			Median	0.20	20.1	-	5.05	0.74	-	1467	0.51	0.60	98.7	194	43.5	180	333	2.17					na	na	na	na	0.10	0.45	1269	304	Lubin
			Mean	0.23	23.2	-	8.63	1.08	-	1962	0.45	0.64	93.8	236	47.2	178	307	2.58					na	na	na	na	0.11	0.65	1869	993	ccp
chalcopyrite	epigenetic veins	LZ 2 VII	SD	0.14	11.61	-	9.88	1.09	-	1404	0.19	0.29	37.7	123	27.9	33.4	153	1.87				na	na	na	na	0.04	0.38	1538	1576		
		n=6	ADL	63%	100%	-	100%	75%	-	100%	100%	100%	38%	100%	38%	100%	100%	100%	100%	100%	50%	*	na	na	na	na	88%	0%	100%	100%	100%
			Max	0.03	12.96	-	-	-	-	0.03	0.42	4.84	56.4	145				0.06	0.85			na	na	na	na	27.9	0.89	378	0.22		
			Min	12.40	-	-	-	-	-	0.25	1.00	44.5	10.68				0.02	0.34				na	na	na	na	14.25	0.09	18.01	0.04	carbonates	
chalcopyrite	epigenetic veins	LZ 2 VII	Median	12.91	-	-	-	-	0.30	3.16	47.8	20.0				0.04	0.61				na	na	na	na	15.78	0.22	38.7	0.06	Lubin		
			Mean	12.83	-	-	-	-	0.31	3.04	48.8	38.5				0.04	0.60				na	na	na	na	18.43	0.31	91.8	0.02	ccp, tint, minor bn		
			SD	0.14	11.61	-	9.88	1.09	-	1404	0.19	0.29	37.7	123	27.9	33.4	153	1.87				na	na	na	na	0.04	0.38	1538	1576		

(continued on next page)

Table 1 (continued)

Mineral	Texture	Sample name (n = no. of analyses)	V	Mn	Fe	Co	Ni	Cu	Zn	Ga	Ge	As	Se	Mo	Ag	Cd	In	Sn	Sb	Tc	Rc	Pt	Au	Hg	Tl	Pb	Bi	Lithology/ Mine/Ore mineral assemblage	
chalcopyrite	near oxidized lithologies	SD	0.21	-	-	-	-	-	-	0.06	1.62	4.80	52.3	-	-	-	0.01	0.17	-	-	*	na	na	6.37	0.29	1.41	0.08		
		ADL	17%	100%	-	0%	0%	-	0%	17%	100%	67%	100%	0%	100%	0%	0%	100%	100%	0%	0%	*	na	0%	67%	100%	100%	83%	
		Max	285	169	-	1.47	3.47	-	1.45	35.1	10.38	5085	5.59	27.5	-	-	-	0.09	1.72	71.6	2.24	0.05	0.09	738	55.4	1386	4.91		
		n=3	Min	50.6	29.2	-	0.40	0.77	-	0.29	6.26	1090	0.95	14.15	-	-	-	0.04	0.41	12.15	0.51	-	0.04	246	30.2	513	0.87	sandstone	
pyrite	near oxidized lithologies	Median	222	31.5	-	1.29	3.45	-	0.82	21.2	4207	5.20	35.2	-	-	-	0.08	1.53	20.6	1.45	-	614	49.0	1048	2.26		Polkowice-Sieroszowice		
		Mean	186	76.4	-	1.05	2.56	-	0.86	17.51	3461	3.91	22.3	-	-	-	0.07	1.22	34.8	1.40	-	533	44.9	963	2.68	disseminated hem			
		SD	121	79.8	-	0.57	1.55	-	0.58	9.93	2100	2.57	7.11	-	-	-	0.02	0.71	32.1	0.87	-	256	13.12	440	2.05				
sphalerite	concordant vein/veinlets in shale	ADL	100%	100%	-	100%	100%	-	0%	100%	100%	67%	100%	100%	100%	0%	100%	100%	100%	100%	0%	100%	100%	100%	100%	100%	100%		
		Max	0.16	274	-	34.2	32.3	693	27.6	0.07	0.35	18181	45.2	18	108	1.15	0.01	6.7	-	-	-	0.02	4.79	398	686	<0.1			
		n=14	Min	0.04	17.25	-	1.11	1.03	11.4	20.58	0.04	0.11	422	7.19	0.44	3.2	-	-	0.3	-	-	-	0.01	0.11	102	95		sandstone	
		Median	0.08	156	-	7.66	3.28	203.4	-	0.05	0.19	1263	22.4	1.69	28	-	-	0.6	-	-	-	-	158	339	-		Rudna		
sphalerite	fault-related epigenetic veins	Mean	0.09	137	-	12.18	6.32	211	-	0.05	0.20	4436	20.9	5.62	37	-	-	1.4	-	-	-	-	199	321	-		py		
		SD	0.04	89	-	11.35	9.92	185.9	-	0.01	0.06	5809	12.26	6.46	35	-	-	1.9	-	-	-	-	102	171	-				
		ADL	71%	100%	-	100%	100%	100%	14%	100%	86%	100%	93%	100%	100%	7%	14%	0%	100%	0%	0%	0%	14%	64%	100%	100%	36%		
		Max	46.5	154	7688	7.54	25.1	4810	-	18.45	9.40	18.84	398	95.8	56.2	7667	0.12	11.06	2.34	0.5	na	na	na	na	168	3.57	779	0.37	
sphalerite	fault-related epigenetic veins	Min	7.53	43.1	1764	0.40	6.56	2401	-	3.21	0.61	1.98	45	10.61	22.8	1796	0.07	5.37	0.54	-	-	-	na	na	126	1.86	0.06	shale	
		Median	35.2	93.9	4589	2.84	12.62	3169	-	10.05	1.33	11.20	83	42.6	33.4	5281	0.10	7.05	1.11	-	-	-	na	na	144	2.76	0.18	Lubin	
		Mean	28.6	96.1	4566	3.00	15.24	3245	-	11.68	2.82	9.58	135	50.4	35.5	5326	0.10	7.63	1.26	-	-	-	na	na	146	2.57	0.18	sph, minor gn and py	
		n=5	SD	19.18	58.7	2453	2.75	6.86	950	-	6.36	3.71	6.74	148	38.2	12.95	2280	0.02	2.42	0.69	-	-	-	na	na	19.76	0.72	0.13	
sphalerite	fault-related epigenetic veins	ADL	100%	80%	100%	100%	100%	100%	-	100%	100%	100%	100%	100%	100%	80%	80%	100%	20%	na	na	na	na	na	80%	100%	20%	100%	
		Max	3.46	1479	-	14.91	0.17	11095	-	7.11	6.72	1.13	20.1	2.74	24.3	10384	1.55	36.4	0.20	-	-	-	na	na	175	2.94	325		
		n=12	Min	0.14	56.3	-	3.76	0.11	22.1	-	0.07	0.13	0.14	14.1	0.02	0.28	4540	0.01	0.39	0.06	-	-	-	na	na	45.0	0.05	1.01	carbonates
		Median	116	-	5.81	69.7	-	0.20	0.49	0.63	17.3	0.07	1.50	8521	0.05	0.75	-	-	-	-	-	-	na	na	112	0.38	10.56	Rudna	
sphalerite	fault-related epigenetic veins	Mean	301	-	6.31	1579	-	0.88	1.72	0.77	16.9	0.41	4.04	8071	0.24	4.10	-	-	-	-	-	na	na	116	1.04	40.6		ccp, minor bn, sph, gn	
		SD	486	-	2.99	3626	-	1.94	2.81	0.29	2.1	0.94	7.09	1887	0.48	10.74	-	-	-	-	-	na	na	35.4	1.08	90.7			
		ADL	0%	25%	100%	100%	17%	100%	-	100%	50%	75%	100%	58%	92%	100%	80%	75%	83%	25%	0%	na	na	na	100%	100%	92%	0%	
		Max	1.71	2069	-	48.6	0.29	3716	-	0.84	6.46	0.74	17.4	0.36	2.76	17835	21.6	22.3	1.36	-	-	-	na	na	113	9.67	70.5	0.01	
chalcopyrite	aggregate in Feldspathic Quartzite	Min	0.17	121	-	38.3	91.8	-	0.24	0.30	0.37	13.5	0.06	0.48	10454	0.70	0.74	0.40	-	-	-	na	na	na	53.2	1.01	10.56	carbonates	
		Median	136	-	41.1	346	-	0.49	1.51	0.64	15.6	1.63	15547	3.73	5.68	0.68	-	-	-	-	-	na	na	na	95.3	2.24	36.0	Polkowice-Sieroszowice	
		Mean	500	-	42.7	1200	-	0.56	2.38	0.61	15.4	1.75	14675	6.42	7.44	0.74	-	-	-	-	-	na	na	na	86.0	3.49	32.6	Sieroszowice	
		n=7	SD	732	-	3.67	1560	-	0.24	2.29	0.15	1.4	0.81	2887	7.42	7.83	0.35	-	-	-	-	-	na	na	na	23.2	3.14	20.4	ccp, minor bn, sph, gn
chalcopyrite	aggregate in Feldspathic Quartzite	ADL	0%	43%	100%	100%	14%	100%	-	100%	100%	71%	100%	49%	100%	100%	100%	100%	0%	na	na	na	na	na	100%	100%	100%	29%	
		Max	0.06	15.92	-	70.8	10.40	-	2273	11.35	2.04	18.90	2.56	3.28	5.11	69.8	0.32	0.41	*	na	na	na	0.06	5.65	0.02	2.43	2.44		

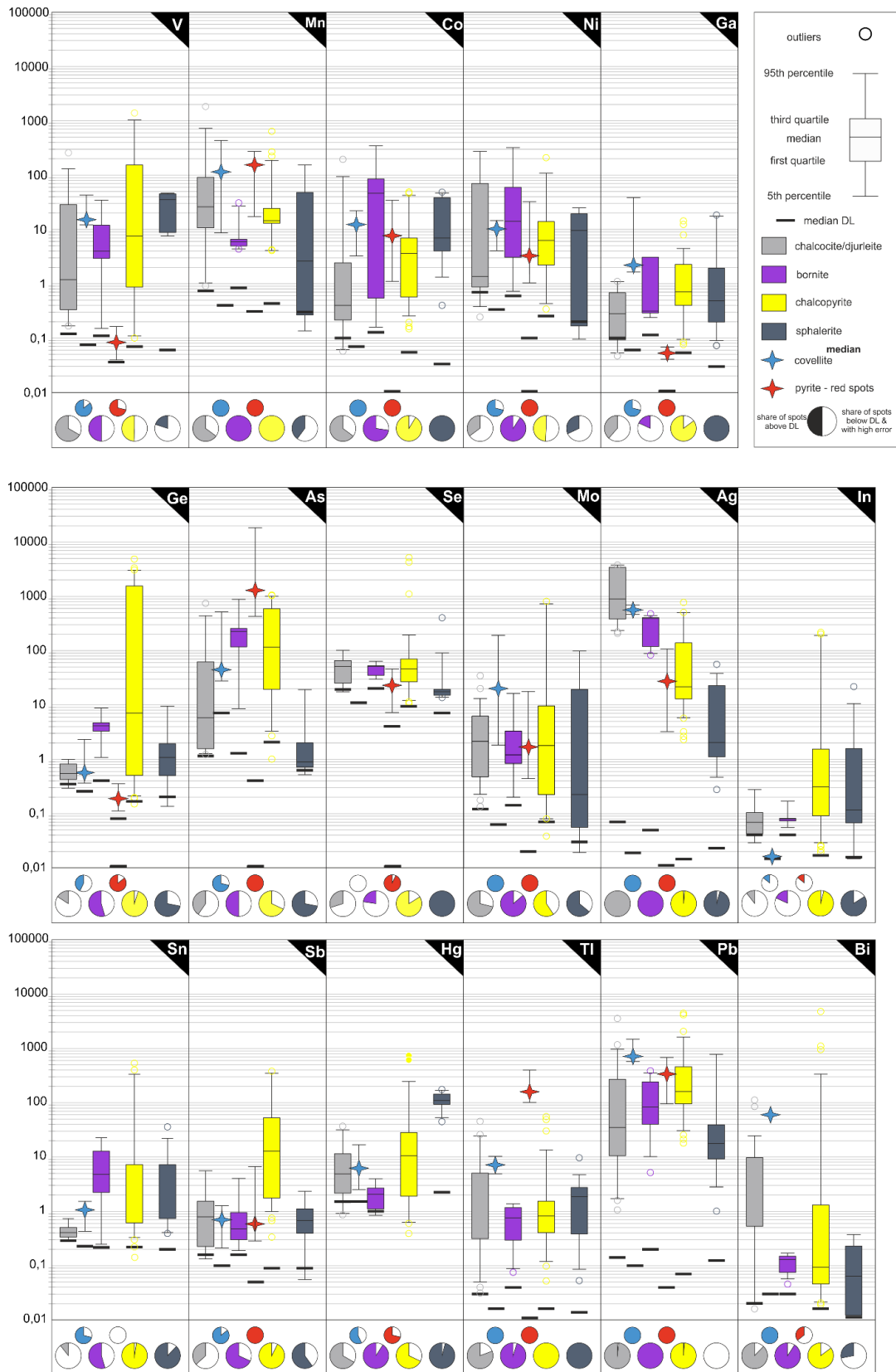


Fig. 5. Box and whisker diagrams of selected trace elements in main ore minerals from the Lubin-Sieroszowice district, logarithmic scale in $\mu\text{g/g}$, values below detection limit are not included in the plot and calculations.

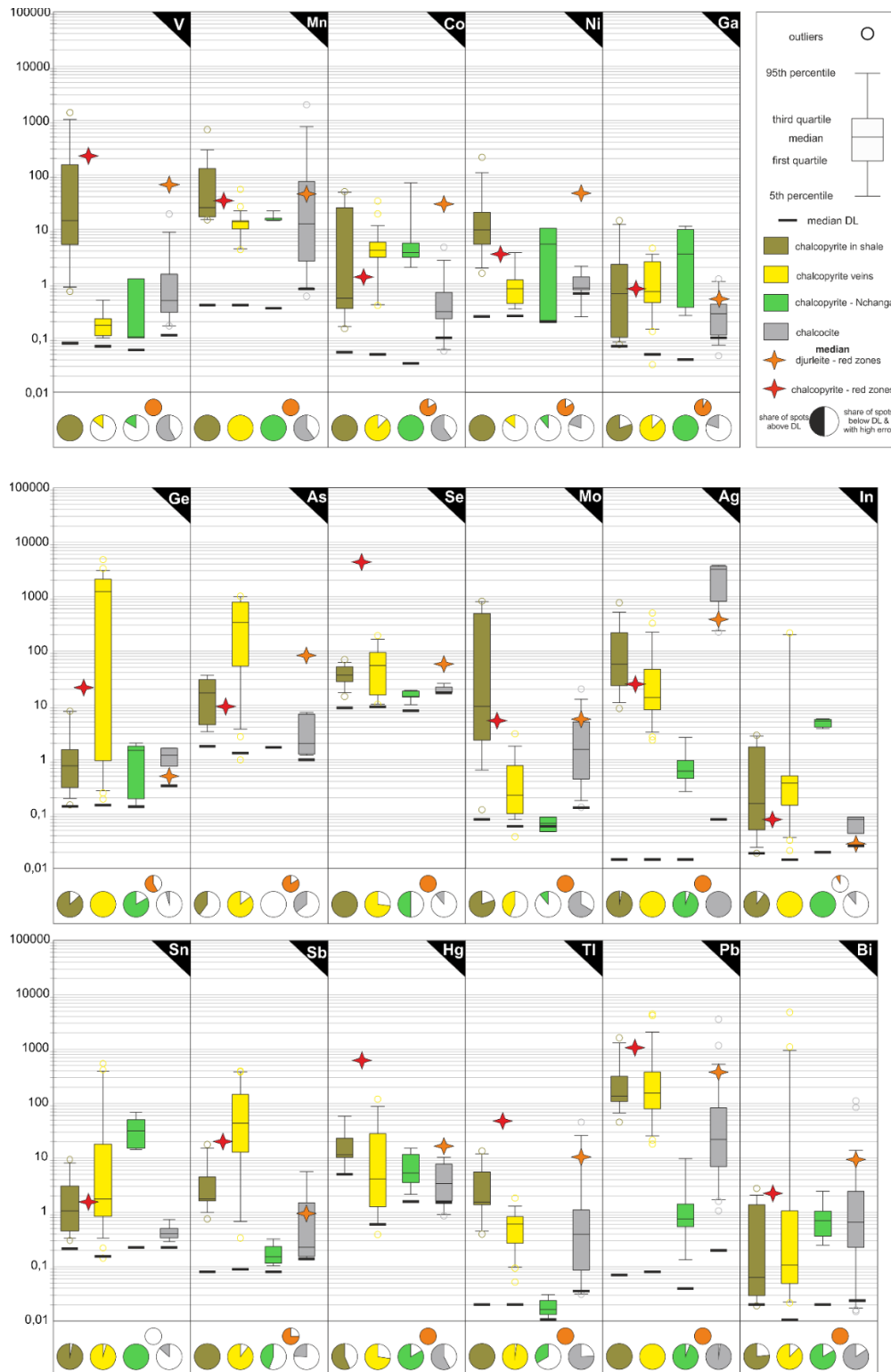


Fig. 6. Box and whisker diagrams of selected trace elements in main ore minerals from the Lubin-Sieroszowice district break down by the mode of occurrence (veinlets in shale, non-shale hosted veins, red spots). Results for two chalcopyrite samples from Nchanga deposit are added for comparison. Logarithmic scale in $\mu\text{g/g}$, values below detection limit are not included in the plot and calculations.

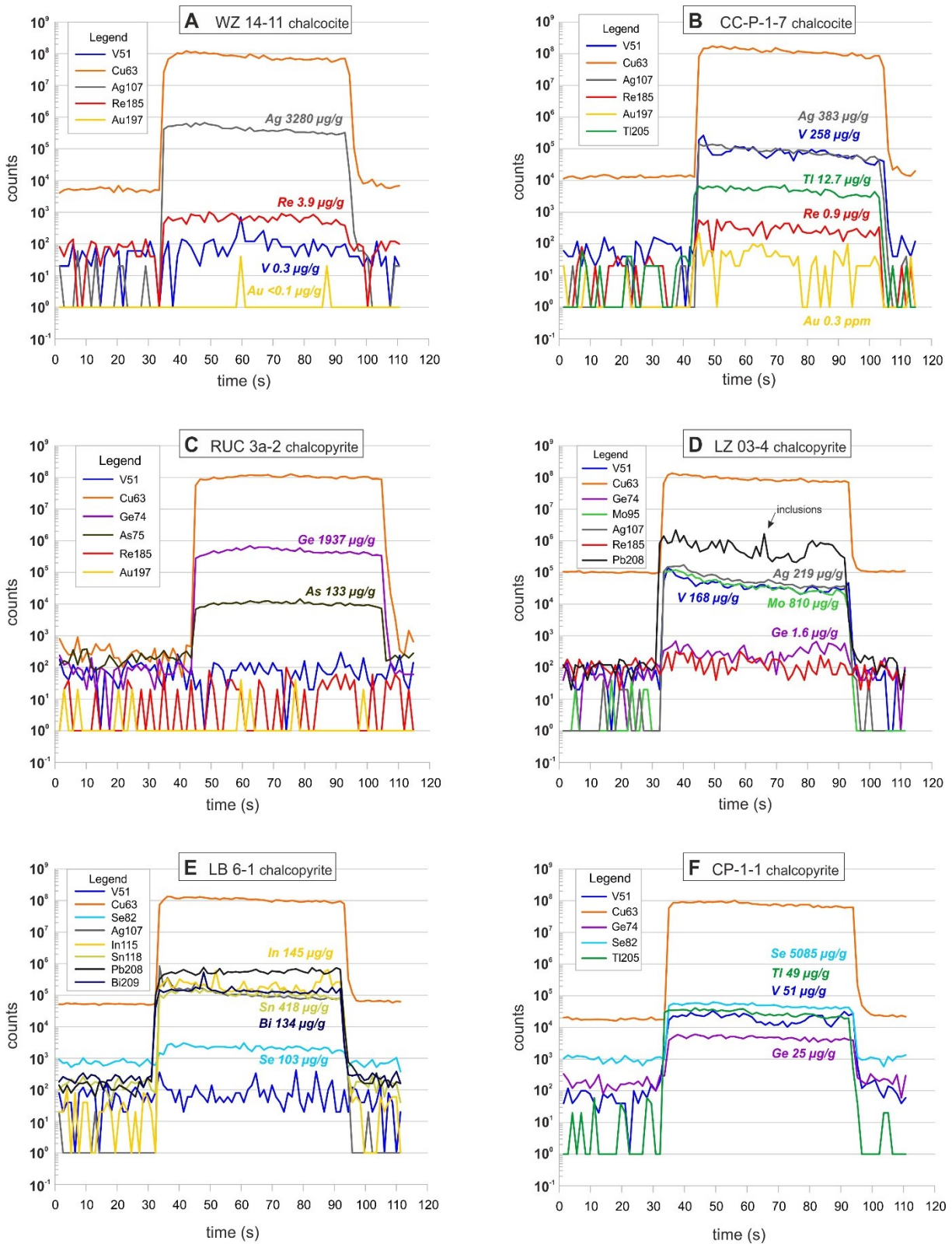


Fig. 7. Time-resolved downhole ablation spectra for selected samples.

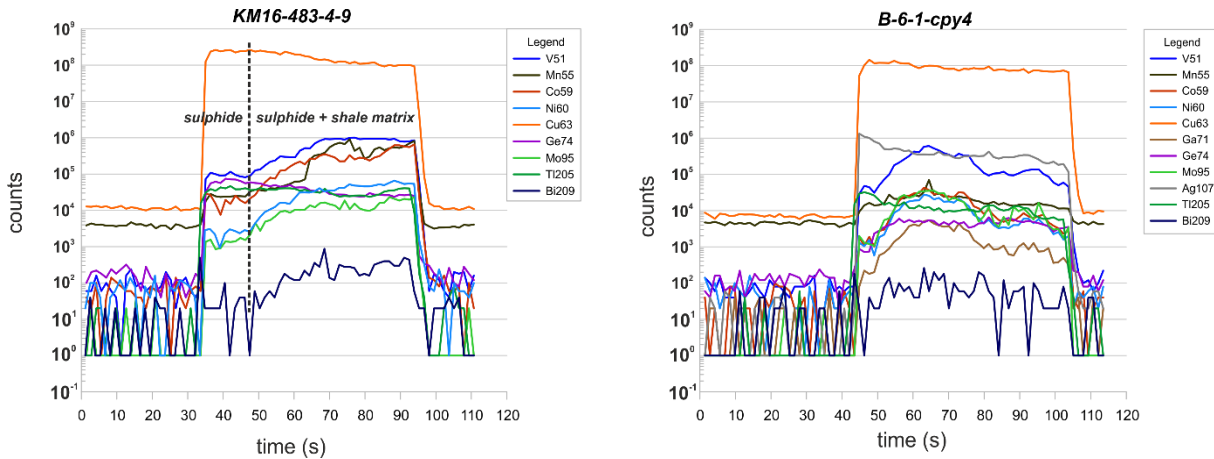


Fig. 8. Examples of time resolved diagrams with significant input of shale matrix material in the ablation spot. In the case of A, shale material was beneath a thin cover of sulphide while in the case of B it occurred as an inclusion.

4.2 Rhenium, silver and germanium

^{185}Re signals were consistently detected only in djurleite (WZ-14, CC-P-1); after data reduction most spots gave values above detection limits (up to $3.9 \mu\text{g/g}$ in sample WZ-14, Fig. 7a-b, Fig. 9, Appendix A). This indicates that djurleite is a preferential host for Re among all analysed Cu sulphides, thus, processes responsible for its formation could be also linked with Re enrichment. Djurleite in the vicinity of the “red spot” zone (Fig. 9) is quite distinct: in comparison with chalcocite samples it is enriched in V, Co, Ni, Se, Tl, Pb, Bi (Fig. 6, Fig. 7b; although shale matrix inclusions could be a source of V, Co and Ni). Copper sulphides in Re-enriched, shale hosted samples Ko11-2339-103 and Sr10-3484-104 were too fine-grained and contained too many inclusions to quantify trace element content with sufficient confidence. Therefore, the data were not included in the results presented in the Appendix A. Semiquantitative measurements of 10 spots in a chalcopyrite vein from sample Sr10-3484-104 (Fig. 10) suggest that the Re content does not exceed $1.6 \mu\text{g/g}$ of Re and cannot account for 18.4 ppm Re revealed in bulk-rock geochemistry. Potential candidates for Re hosts include disseminated Cu-S sulphides or shale matrix/organic matter related phases.

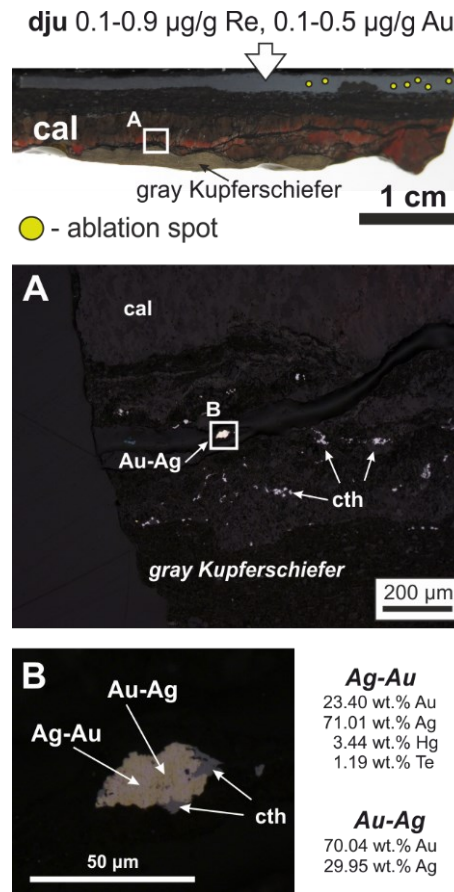


Fig. 9. CC-P-1 shale sample containing djurleite adjacent to hematite “red spots” alteration characterized by presence of native gold (SOS system). Dju-djurleite, cal – calcite, cth – clausthalite.

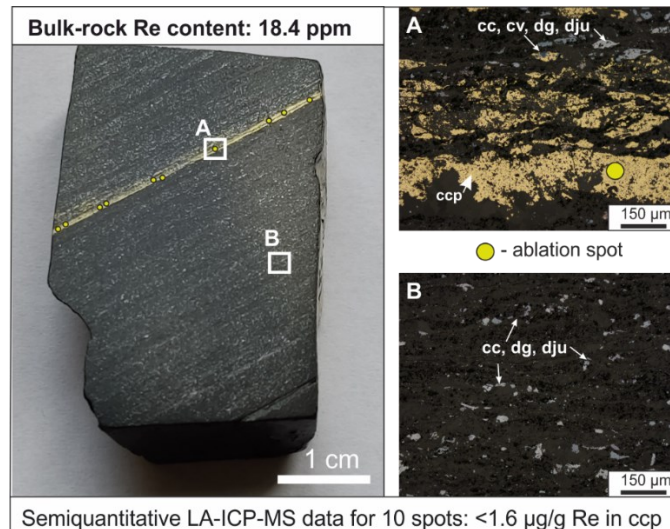


Fig. 10. Sample Sr10-3484-104 enriched in rhenium and consisting of chalcopyrite (ccp) veinlets in shale with chalcocite (cc), digenite (dg), djurleite (dju), covellite (cv) and bornite disseminations. LA-ICP-MS analyses suggest that bulk of the Re is not hosted in the chalcopyrite veinlet, leaving disseminated Cu-S sulphides or shale matrix/organic matter related phases as possible hosts for rhenium.

Tab. 2. Representative EPMA analysis of samples investigated with LA-ICP-MS. Abbreviations: cv = covellite; dju = djurelite; ccp = chalcopyrite; bn = bornite; sph = sphalerite.

Sample	Mineral	Ag	Cu	S	Fe	Sb	Cd	Hg	As	Se	Zn	Ge	Total	Atm. Cu/S
WZ-16	cv	0.09	67.12	33.42	0.25	<0.02	na	<0.05	<0.07	<0.07	na	na	100.88	-
WZ-17	cc	0.03	80.77	19.99	<0.02	<0.02	na	0.05	<0.07	<0.07	na	na	100.83	2.04
WZ-18	cc	0.35	80.52	20.11	<0.02	<0.02	na	<0.05	<0.07	<0.07	na	na	100.98	2.02
CC-P-1	dju	0.07	79.53	20.59	<0.02	<0.02	na	na	<0.07	<0.07	0.08	na	100.26	1.95
CC-P-1	dju	0.07	80.08	20.57	<0.02	<0.02	na	na	<0.07	<0.07	0.07	na	100.78	1.96
CC-P-1	dju	0.10	80.02	20.56	<0.02	<0.02	na	na	<0.07	<0.07	0.11	na	100.79	1.96
WZ_14	dju	0.46	79.42	20.85	<0.02	<0.02	na	na	<0.07	0.12	0.12	na	100.97	1.92
WZ_14	dju	0.43	78.87	20.69	<0.02	<0.02	na	na	<0.07	<0.07	0.06	na	100.04	1.92
WZ_14	dju	0.44	79.67	20.74	<0.02	<0.02	na	na	<0.07	<0.07	0.08	na	100.92	1.94
WZ-20	ccp	<0.01	34.27	35.25	29.48	na	na	na	na	na	<0.03	0.15	99.15	-
WZ-20	ccp	<0.01	34.25	35.60	29.87	na	na	na	na	na	0.03	<0.03	99.75	-
WZ-20	ccp	<0.01	34.34	34.98	29.40	na	na	na	na	na	<0.03	0.13	98.85	-
WZ-20	bn	0.04	63.38	25.60	11.06	<0.02	na	<0.05	<0.07	<0.07	na	na	100.08	-
WZ-20	sph	<0.01	0.22	32.74	0.21	na	0.61	0.06	na	na	67.96	<0.03	101.79	-

Silver is the most important by-product in the Lubin-Sierszowice district and the highest silver content has been measured in djurleite and chalcocite (Fig. 5 & 7a), with values up to 3814 $\mu\text{g/g}$, in agreement with the results obtained with EPMA (Tab. 2). Hundreds $\mu\text{g/g}$ of Ag were also measured in bornite and covellite, while chalcopyrite shows a lot of variation: some of them contain hundreds of $\mu\text{g/g}$ of Ag (median 473 $\mu\text{g/g}$ in sample B-1-1) while others contain only single $\mu\text{g/g}$ of Ag (median 6.4 $\mu\text{g/g}$, sample WZ-20). Kozub-Budzyń and Piestrzyński (2017) report EPMA determined concentrations of Ag in copper minerals from the Lubin-Sierszowice district as follows: chalcocite 0.40-11.97 wt.%, bornite 0.13-8.66 wt.%, digenite 0.06-3.21 wt.%, covellite 0.21-0.40 wt.% and <0.14 wt.% in chalcopyrite. Mikulski et al. (2020) present Ag contents for chalcocite (2.54-6.28 wt.%), bornite (up to 3.30 wt.%), digenite (up to 3.55 wt.%), djurleite (up to 0.91 wt.%), geerite (Cu_8S_5 , 0.34-10.1 wt.%), yarrowite (Cu_9S_8 , 0.18-0.66 wt.%), and chalcopyrite (up to 0.08 wt.%). Although silver minerals (native silver, silver amalgams, stromeyerite, naumannite) have been identified in the deposit, their abundance is significantly lower and the bulk of the Ag enrichment in the copper ore is hosted by common copper sulphides (Ag-bearing bornite and chalcocite) (Kozub-Budzyń and Piestrzyński 2017).

High concentrations of Ge (up to 4806 $\mu\text{g/g}$), accompanied by increased concentrations of As (up to 1045 $\mu\text{g/g}$) have been measured in chalcopyrite from the epigenetic sulphide-calcite veins (samples WZ-20, RU-W2, RUG 3a; Fig 7c). EPMA confirms the high Ge content in sample WZ-20; results of Ge analyses also reveal significant variation (Tab. 2, <0.03- 0.15 wt.% Ge while LA-ICP-MS data for this sample fall in the range 11.38-2402 $\mu\text{g/g}$). Ge-As-Sb rich chalcopyrite has been found in samples from both the Sierszowice-Polkowice and Rudna mines and likely represents a more common phenomenon. Slightly elevated Ge content is also observed in chalcopyrite near “red spots” (sample CP-1, up to 25 $\mu\text{g/g}$ of Ge). Fe-low sphalerite crosscutting Ge-rich chalcopyrite is not particularly rich in Ge (up to 6.5 $\mu\text{g/g}$ of Ge), similarly to sphalerite forming veinlet in a shale (sample SPH-S1, up to 9.4 $\mu\text{g/g}$ of Ge).

5. Discussion

An element zonation sequence of Fe^{3+} -Cu-Pb-Zn- Fe^{2+} as well as mineral zonation (hematite-chalcocite-bornite-chalcopyrite-galena-sphalerite-pyrite) from the contact with the red beds into the reduced, ore-bearing sediments is a common feature of sedimentary rock hosted stratiform copper systems (e.g. Hitzman et al. 2005). This raises the question whether similar zonation patterns can be observed for trace elements. While for most of the measured elements this is not the case, Fig. 5 reveals a clear pattern for Ag (almost linear decrease from chalcocite/djurleite > covellite > bornite > chalcopyrite > sphalerite when concentrations are shown in log scale) and Pb (increase from chalcocite < bornite < chalcopyrite followed by sharp drop for sphalerite). It suggests that Ag distribution on a scale of the district, could be controlled by the redox conditions and follow general mineral zonation in SSC deposits. Among copper sulphides, chalcocite/djurleite seems to be a favourable host for Bi and Re, while chalcopyrite for Sb (Fig. 5). Trace elements in Kupferschiefer ores also vary depending on the location in the district (e.g. Kijewski and Jarosz 1987; Banaś et al. 2007; Kijewski and Wirth 2011; Kozub-Budzyn and Piestrzynski 2017; Mikulski et al. 2020, with references therein), mineral assemblage, and texture (e.g. Pieczonka et al. 2008; Wodzicki and Piestrzynski 1994; Kucha 2007) and data presented in this paper imply that particular trace element signatures seem to be linked to a certain mineralization style (Fig. 11).

	Stratiform/stratabound					SOS system	Epigenetic veins
	Rote Fäule zone	Transition zone	Copper zone	Lead-zinc zone	Pyrite zone		
Selenides						■	
Au, Pt, Pd						■	
hematite	■	■				■	
covellite		■					
chalcocite			■			■	
djurleite		■?				■	
bornite			■				■
chalcopyrite			■			■?	■
galena				■			■
sphalerite				■			■
pyrite				■		■?	
calcite							■
Elements enriched in sulphides	Ag Re?					Re ± Au, Se, Hg, Tl	Ge ± As, In, Bi, Sn
Germanium concentrations in chalcopyrite	0.15-7.84 µg/g					6.26-25.1 µg/g	fault related: 11.38-4806 µg/g other veins: 0.19-1.01 µg/g

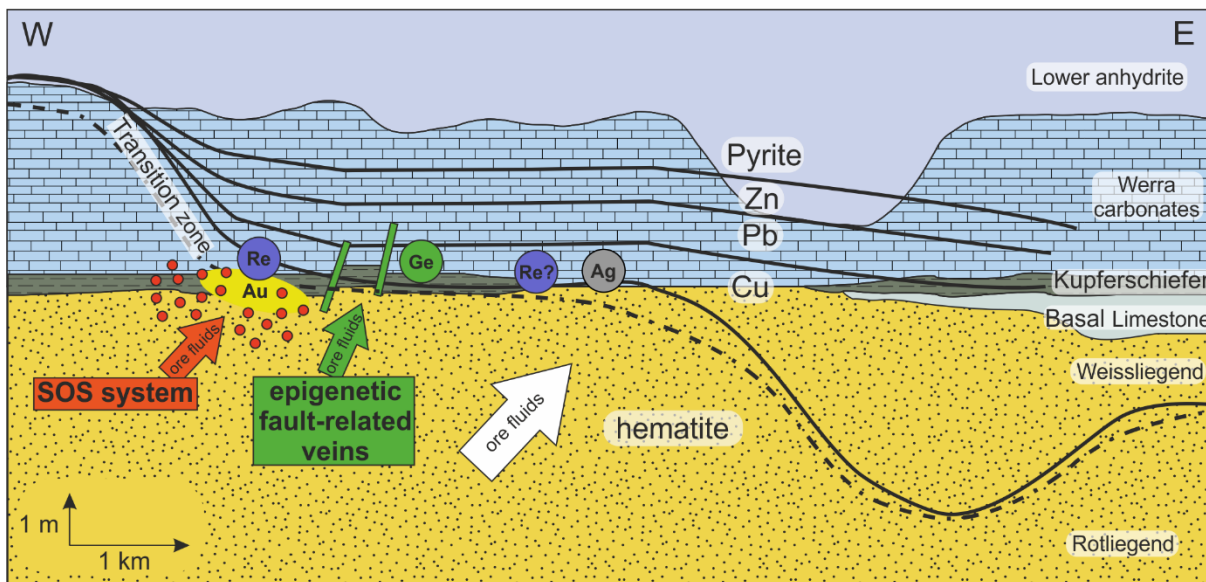


Fig. 11. Spatial sequence of hematite and sulphides from stratiform/stratabound mineralization (after Oszczepalski 1999) with simplified paragenetic sequence for the mineral assemblage in SOS system and epigenetic veins. Below schematic section of the Kupferschiefer ore series (modified after Oszczepalski 1999 and Alderton et al. 2016) with different mineralization styles discussed in the text.

5.1 Stages of mineralization

5.1.1 Reduced vs oxidized (SOS) facies

The ore-bearing series can be subdivided into two contrasting facies: reduced (dark grey, rich in organic matter, containing sulphides) and oxidized zones (red, organic matter deficient, hematite-bearing, usually Cu-Ag barren but in some cases enriched in Au-Pt-Pd), with the highest Cu grades usually surrounding oxidized areas. Organic geochemistry, especially parameters such as S₂/S₃ (HI/OI) ratio, total organic carbon (TOC) and oxygen index (OI) obtained during Rock-Eval pyrolysis (Oszczepalski and Rydzewski 1991, Oszczepalski 1999, Bechtel et al. 2002, Więclaw et al. 2007) reveal a third, transitional zone. Two episodes of oxidation have been postulated by Pieczonka (2000), Pieczonka and Piestrzyński (2000), Piestrzyński et al. (2002), Pieczonka et al. (2008). The first one is related to the bulk of the copper accumulation (DOS, diagenetic oxidation stage) and

the second one, at higher temperatures, is responsible for Au-Pt-Pd enrichment (SOS, secondary oxidation stage). Although sulphide accumulations in the oxidized strata (both DOS and SOS), are usually finely disseminated and rarely sufficiently large for LA-ICP-MS measurements, we were able to obtain data for pyrite, chalcopyrite and djurleite associated with the “red spots” and the SOS system. Although the set of samples is limited, results show distinct contrast between them and their counterparts in areas without hematitic alteration (Fig. 5 and 6). Those from the “red spots” are particularly enriched in certain elements: chalcopyrite and djurleite in V, Se, Hg and Tl, while pyrite in Tl and As. In general, sulphides from both reduced and SOS zones, do not contain measurable quantities of Re, Au and Pt with the exception of sample CC-P-1 (djurleite in shale adjacent to “red spots”; both Re and Au are indicated with sufficient confidence). Application of a matrix-matched reference material might result in different values, but it will most likely fall within the same order of magnitude as reported here. We consider sample CC-P-1 to represent high grade Cu mineralization adjacent to the oxidized (SOS) areas and formed by remobilization of copper ore via influx of oxidizing fluids and a moving redox front. These results are consistent with increasing U, Co, V, Bi, Hg, Se and Tl in the direction of the oxidized zone (Oszczepalski and Rydzewski 1997). Electron microprobe data presented by Chmielewski (2014) and Oszczepalski et al. (2017) show that sulphides in the oxidized and transition zone tend to contain Hg (up to 1.02 wt. % in chalcopyrite) and Se (for example up to 0.78 wt.% in bornite, up to 0.61 wt.% in chalcopyrite, up to 0.16 wt.% in pyrite and up to 1.14 wt.% in covellite). EPMA data for sulphides from the Sieroszowice-1 borehole, which was recently reinvestigated by Oszczepalski and Chmielewski (2017), reveal that while chalcopyrite and pyrite in Zechstein limestone and Kupferschiefer contain 0.00-0.03 wt.% Se (only one out of 37 measurements gave 0.08 wt.% Se), selenium content rapidly increases in sulphides from the Weissliegend sandstone (0.15-0.17 wt. % Se). While minerals such as clausthalite PbSe, naumannite Ag₂Se (Pieczonka et al. 2008), tiemannite HgSe (Salamon 1976), eugenite Ag₁₁Hg₂ (Kucha 1986), thalcosite Tl₂Cu₃FeS₄ (Oszczepalski and Chmielewski 2017, Pieczonka et al. 2019) have been found in the mineralization from the Fore-Sudetic Monocline (usually in the “red spots” zones and areas enriched in Au-Pt-Pd, although PbSe also in galena-rich zones), high values of Se and Tl in sulphides measured by other authors via EPMA not necessarily are caused by intergrowths with these phases. Our data prove that elevated content of Se, Tl, Hg is also hosted in the structure of sulphides or as evenly distributed nano-inclusions rather than microinclusions (Fig. 7f). In this regard sulphides from oxidized areas (SOS) are remarkably different from those found in reduced part of ore-bearing series (Fig. 6).

One of the interesting topics regarding SSC deposits is how they are related to and affected by tectonic evolution, i.e. from the basin initiation and rifting, up to basin inversion. Kupferschiefer deposits in Central Europe are of special interest in this regard, because in contrast to other “giants” such as African Copperbelt or Udokan, they are undeformed and not metamorphosed. Trace elements can record the chemistry of hydrothermal fluids depending on parameters such as temperature (e.g. Frenzel et al. 2016), pH, and oxygen fugacity, and therefore can be a useful proxy for fluids and their sources. While some authors link both Cu-Ag as well as Au-Pt-Pd mineralization to the same fluids forming single mineralizing system (e.g. Oszczepalski et al. 1999, Cathles 2019), others suggest that the precious metals enrichment associated with “red spots” formed in a separate phase, overprinting earlier copper mineralization (Pieczonka 2000, Pieczonka and Piestrzyński 2000, Piestrzyński et al. 2002, Pieczonka et al. 2008). Results presented

here indicate that sulphides in the “red spots” zones exhibit a trace elements pattern that is clearly distinct from the bulk Cu-Ag mineralization (Fig. 6) and support the idea that these two types should be treated separately.

5.1.2 Epigenetic ores

While ore minerals present as disseminations and veinlets appears to have occurred early in the mineralization history, epigenetic veins crosscutting lithology indicate overpressure and formation after lithification. Clear differences in trace element data between these two styles of mineralization (Fig. 6) are due to the group of epigenetic Ge-As-Sb rich chalcopyrite veins (samples RUG-3a, RU-W2, WZ-20) and epigenetic vein with chalcopyrite enriched in Zn (median 1467 µg/g), Sn (median 334 µg/g), Bi (median 304 µg/g) and In (median 180 µg/g) (sample LB-6, Fig. 7e). These veins likely represent a distinct and separate, later stage of deposit formation (fig. 11) and could represent a promising target for “high-technology” metal such as Ge and In. However, whether these differences in trace elements point to a different fluid source or different formation mechanism remains unknown. Although a four point isochron Re-Os age of chalcopyrite veinlets parallel to shale lamination has been determined by Mikulski and Stein (2015) as 212 ± 7 Ma, model Re-Os ages for these four samples (concordant veins and veinlets in the shale) range from 268 to 256 Ma (Mikulski and Stein 2017). Crosscutting veinlet perpendicular to lamination gave a model age of 217 ± 2 Ma (Mikulski and Stein 2010). This might suggest the presence of a crosscutting phase of mineralization overprinting an earlier stage of Permian mineralization (240–255 Ma), at least in the case of shale-hosted thin veinlets. However, the problem of fault-related, thicker chalcopyrite veins as well as the question of how much metals have been introduced during epigenetic phase and how much has just been remobilized from existing material remains open for discussion and further investigation.

5.1.3 Temperature estimations

Temperature estimation for the formation of Cu-Ag Kupferschiefer deposit are typically based on the parameters of organic matter (e.g. up to 130°C, Bechtel et al. 1995). Results of vitrinite reflectance (Speczik and Puttmann 1987) indicate that the temperature of mineralizing fluids in most cases did not exceed 100°C but higher temperatures are correlated with a second major maturation process which took place after the main stage of mineralization. Djurleite is stable at low temperatures, and on heating above 93°C it reverts reversibly to high digenite and hexagonal “high chalcocite” (Roseboom 1966, Potter 1977, Evans 1979), similar to the “low chalcocite” & “high-chalcocite” transition at 103.5°C (Roseboom 1966). As organic matter maturation cannot be reversed, only the maximum temperature can be documented and any later or prior cooler fluids are not recorded. Due to the lack of suitable host minerals, few data on fluid inclusions from the Lubin-Sieroszowice district is available in literature. Measurements on the epigenetic ore veins continuing below and above the stratabound Kupferschiefer orebody gave homogenization temperatures of 145° - 160°C for smaller gas liquid inclusions and 180° - 200°C for larger ones which often contain solid phases and liquid carbon dioxide (Strengel-Martinez et al. 1993). Fluid inclusions incorporated in the carbonate cement of the clastic Weissliegend point to homogenization temperature of about 120°C (Vaughan et al. 1989). The Ga-Ge-In-Mn-Fe-in-sphalerite geothermometer (GGIMFis, Frenzel et al. 2016) utilizing trace elements concentrations may provide new independent data on temperature estimation. Unfortunately, due to inclusions as well as In and Mn values below detection limit, only 2 spots (both in sample RUG - 3a,

epigenetic vein) could be used, giving 122-123°C. For a provisional estimation, substituting Mn and In with the detection limit value into GGIMFis, gave temperatures in the range 79 - 113°C. Due to the fact that both Mn and In are denominators in the GGIMFis formula, these values are likely overestimated. Future studies are needed to determine whether the apparent difference between temperatures estimation for bulk mineralization and epigenetic veins represent real phenomena or is just an artefact caused by limited number of samples and limitations of analytical methods. Except for Fe, the LA-ICP-MS data for sphalerite presented here resemble those from deeply seated, carbonate-hosted (Zechstein - Ca₂) MVT-alike Zn-Fe-Pb-sulphide mineralization in the Lower Saxony Basin (NW Germany), formed by fluids expelled from an over-pressurized system during Late Cretaceous basin inversion (Nadoll et al. 2019, Sośnicka and Lüders 2019). Similarities include significant Cd values in the range of X000 µg/g and low median values (<1 µg/g) of Ga, In, Tl (Knorsch et al. 2020) but preliminary data presented here might indicate lower range of temperatures (Lower Saxony Basin: GGIMFis temperatures 148 ± 55°C, Knorsch et al. 2020; homogenization temperatures of sphalerite-hosted inclusions: 125° - 208 °C, Sośnicka and Lüders 2019). Chemical composition of sphalerites from the Kupferschiefer also show strong similarities (Cd in the X000 µg/g range, Fe-low, low values of Ga, Ge, In) to those from the Ghanzi-Chobe Belt portion of the Kalahari Copper Belt (Kelepile et al. 2020) where fluid inclusion studies suggest trapping temperatures of the mineralizing fluids between 150° and 350°C (Hall et al. 2018).

5.2 Germanium

Germanium does not form specific deposits but is found in minor and trace amounts in various types of mineralization, with economic concentrations in only a handful of them (see extensive reviews by Bernstein et al. 1985, Höll et al. 2007, Melcher and Buchholz 2014). Most of the Ge-bearing sulphide ore originates from low temperature, epigenetic zinc deposits, hosted predominantly in carbonate rocks (Bernstein et al. 1985, Höll et al. 2007) where it occurs as substitution in the structure of sphalerite and wurtzite with discrete germanium minerals usually absent (Melcher and Buchholz 2014). Scarcity and selectivity of germanium data in sediment hosted stratiform copper deposit makes their potential difficult to assess but Melcher and Buchholz (2014) evaluated it as “medium”, the same evaluation as Volcanic-hosted Kuroko-type Cu-Zn(-Pb) (-Ba), porphyry and vein-stockwork Sn-Ag and Kipushi-type polymetallic deposits. Germanium was recovered from the Kupferschiefer ore containing 8–15 ppm of Ge prior to mine closure in the Mansfeld area (Harz mountains, Germany), but more detailed information is lacking (Höll et al. 2007, Melcher and Buchholz 2014). According to Banaś et al. (2007), copper ores in the Lubin-Sieroszowice district contain on average 1 ppm of Ge, but locally it can be enriched up to 10 ppm. Despite such low concentrations, Van Nhan (1970) reported a possible occurrence of argyrodite in chalcocite-bornite ore, containing abundant native Ag found in dolomitic shale samples from the Lubin East field, while Harańczyk (1975) described two new germanium minerals, morozeviczite $Pb_3Ge_{1-x}S_4$ and polkovicite $(Fe,Pb)_3(Ge,Fe)_{1-x}S_4$. These minerals were found in epigenetic veins occurring in a zone of tectonic cracks within sandstone below Zechstein sediments but since the time of their discovery, they have not been found anywhere else. According to an overview on trace elements in the copper ore in the Fore Sudetic Monocline by Kijewski and Jarosz (1987), chemical assays from the stage of deposit documentation show germanium in the range of 0.1-5 ppm, present as substitution in stromeyerite (up to 0.38%), in digenite, bornite, chalcopyrite (0.15-0.18%), in covellite and in galena but they do not specify

what analytical method was used for these measurements, nor what was the location, stratigraphic position or texture. Data presented here show even higher enrichment in germanium (up to 4806 $\mu\text{g/g}$) coupled with high content of arsenic (up to 1045 $\mu\text{g/g}$) in chalcopyrites from the carbonate hosted epigenetic sulphide-calcite veins, associated with local faults and tectonic zones. Time resolved ablation profiles reveal that germanium in chalcopyrite probably occurs as substitution in the crystal lattice or is present as evenly distributed nano-inclusions rather than micro-inclusions of Ge-bearing phases (Fig. 7c). Such high levels of Ge content in chalcopyrite, coupled with additional enrichment in Sn, have been reported in the remobilized Barrigão copper vein deposit from the Iberian Pyrite Belt where up to 0.64% of Ge in chalcopyrite has been determined with EPMA (Reiser et al. 2011) and up to 6260 $\mu\text{g/g}$ with LA-ICP-MS (Belissont et al. 2019). LA-ICP-MS measurements of chalcopyrites from the Kipushi deposit (D.R. Congo) gave 180–647 $\mu\text{g/g}$ Ge (Belissont et al. 2019). With the exception of a “red spots” sample with a median of 21.2 $\mu\text{g/g}$ Ge, the Ge content in remaining Kupferschiefer chalcopyrites is low, usually below 1 $\mu\text{g/g}$ and only slightly higher in sample B-1-1 (stratiform, concordant chalcopyrite; median 6,5 $\mu\text{g/g}$ of Ge). Notably, bornite from the epigenetic vein, replacing Ge-rich chalcopyrite (sample WZ-20), contains on average 4.1 $\mu\text{g/g}$ of Ge (up to 8.7 $\mu\text{g/g}$) while sphalerite veins, crosscutting the same Ge-rich chalcopyrite, contain no more than 1.5 $\mu\text{g/g}$ Ge. Kupferschiefer-hosted stratiform sphalerite has a median value of 1.3 $\mu\text{g/g}$ and contains no more than 10 $\mu\text{g/g}$ of Ge. Therefore, in Kupferschiefer ores, chalcopyrite and Cu phases might be more favourable hosts for Ge than sphalerite. It’s worth to point out that Ge-enrichment appears to be a more widespread phenomenon in the Lubin-Głogów Copper District as it occurs in several samples from both the Sieroszowice-Polkowice and Rudna mines. Germanium is not reported in chemical assays of Kupferschiefer samples (e.g. Mikulski et al. 2020), partly due to analytical problems (Dulski et al. 1999). Therefore, germanium might have been overlooked in the past and the potential in terms of Ge grades and resources is in fact underestimated while data presented here clearly show that these copper ores should be regarded as potential perspective target for germanium. The origin of such enrichment remains enigmatic and requires further studies; at this stage of research we can only speculate whether fluids responsible for formation of epigenetic veins might be enriched in germanium relative to fluids responsible for the majority of stratiform mineralization and/or the process of vein formation itself (involving overpressure and hydraulic fracturing) might play a role.

5.3 Rhenium

The first important investigation focused on rhenium occurrence in mineralization from the Fore-Sudetic monocline in Poland, utilized a self-devised spectrographic method (Gralikowski, 1967). The highlights included association of rhenium with high grade, organic matter-rich copper ore; the notion that the correlation between Re and Cu is stronger than between Re and Mo ($R^2 = 0.738$ and 0.34 respectively) and a speculation that Re enrichment might be connected with chalcocite. Gralikowski (1967) also reported the variability in Re content in terms of the ore type: 0.7-4 ppm for the sandstone ore, 1.4-3.7 ppm for the shale ore and 0-0.8 ppm for the carbonate ore. The main focus of his paper was on the analytical method and unfortunately geological aspects have been neglected. Kanasiewicz (1966, 1967) investigated rocks in the North-Sudetic Trough in Poland and concluded that while there is no significant rhenium - molybdenum correlation, a strong correlation with copper exists. His interpretation was that metals precipitated from seawater, rejecting hypotheses that late hydrothermal fluids were responsible

for the rhenium enrichment in the copper bearing shales. Mikulski et al. (2020) report bulk-rock Re concentrations in the range of <0.05 to 68.7 ppm ($n = 71$) with an arithmetic mean of 5.8 ppm. They confirm that the correlation of rhenium with molybdenum ($r = 0.36$) is weaker than rhenium and copper ($r = 0.55$). Interestingly, they also showed a strong correlation between rhenium and bismuth ($r = 0.74$).

Kijewski and Jarosz (1987) summarized unpublished studies and reports. The highest rhenium concentrations occur in the footwall of the bituminous shale where rhenium is found as substitutions in minerals of molybdenum (0.2-1.2% of Re admixture), copper and iron. According to them, rhenium admixture in chalcocite, pyrite, djurleite, chalcopyrite and bornite can be surprisingly high (up to 1 wt%). The second most important carriers of rhenium are organometallic complexes and kerogen (concentrations 5-35 ppm of Re) which host around 10% of the total rhenium budget (Kijewski and Jarosz 1987). In contrast to previous papers, Kucha (1990) claims that molybdenum phases, mainly castaingite ((Cu,Fe)Mo₂S₅), are the principal host of rhenium in the deposit with an average Mo/Re ratio of 70:1. This opinion was repeated by Alderton et al (2016) where they declare that castaingite accounts for about 75% of the Mo content, and thus is the main host for by-product Re and Mo. These assertions seem to be based on results presented in Kucha et al. (1994), where PIXE analyses showed 1030 ppm of Re in castaingite, as well as data in Kucha (2007) where (K,Cu)Mo₂S₄ and (Pb,Cu)Mo₂S₄ phases are shown to contain 0.18-0.43 % of Re. These results are limited to few samples of rare Mo-phases so their extrapolation to the entire deposit needs to be taken with caution. More recently, Kijewski and Wirth (2011) provided a summary of rhenium occurrence and production in the Lubin-Sieroszowice district with a focus on shale unit, as data for other lithologies are fragmental. They point out that on the scale of the entire deposit operated by KGHM PM S.A., there is no definitive connection between molybdenum and rhenium in the copper bearing shale. Molybdenum is found in the entire area of the documented orebody while the rhenium occurs mainly in the southern part of the deposit. The northern, much deeper part of the orebody, contains significantly less rhenium. This is also indicated by the data presented here, where chalcopyrite in sample LZ 03 is rich in Mo (median value 665 µg/g) but contains no detectable Re. Kupferschiefer-type copper deposits in the Mansfeld-Sangerhausen district in Germany are also known to be enriched in rhenium (0.25-27 ppm, highest in the copper facies of Kupferschiefer; Hammer et al. 1990) but there is no detailed report regarding its mineralogy (Jankowski 1995, John et al. 2017).

There is a limited number of papers tackling rhenium occurrence in other sediment rock hosted copper deposits, in rare exception Box et al. (2012) cover the Dzezkazghan deposit (Kazakhstan). Nevertheless, additional data can be obtained as a by-product of papers focused on Re-Os dating (e.g. Schneider et al. 2007, Tristá-Aguilera et al. 2006, Mikulski and Stein 2015, 2017, Pašava et al. 2007a, Selby et al. 2009). In general, chalcopyrite contains little rhenium (at ppt-ppb level) but in some cases, chalcopyrite, bornite and chalcocite can contain up to a few ppm of rhenium (e.g. Selby et al. 2009, Box et al. 2012).

Pašava et al. (2010) analysed unmineralized Kupferschiefer samples from the Zdrada IG-8 borehole (northern Poland) and obtained concentrations of Re between 64 and 1376 ppb (isochron age of the rock 247±20 Ma). In these samples, rhenium strongly correlates with

molybdenum and is concentrated in the lower part of the black shale. Analyses of mineralized bulk-rock samples (Pašava et al. 2007a) show rhenium concentrations between 249–22174 ppb (age 240 ± 3.8 Ma). Re–Os dating of the mineralization from the Mansfeld area in Germany (Patzold et al. 2002) revealed 3–956 ppb of Re in the Kupferschiefer sample and 5–130 ppb of Re in the underlying conglomerates. According to the authors, a Re–Os age of 204.3 ± 0.5 Ma favours an epigenetic origin of the Kupferschiefer mineralization in this area. Alderton et al. (2016) reported a distinct Re enrichment in the sulphide samples (1.1 to 8.8 ppm), demonstrating that Mo-bearing phases cannot be the only Re carrier and based on the results of Re–Os dating, they presented a multistage model of ore precipitation. Publications by Mikulski and Stein (2010, 2015, 2017) focus on measuring isotopes directly in the separated copper minerals (chalcopyrite, bornite and chalcocite) instead of whole rock samples. Chalcopyrite and bornite analysed by them contains very little rhenium (5.71–12.12 ppb Re), two orders of magnitude lower than the usual rhenium content in the deposit.

Highly oxidized and PGE enriched samples of the Kupferschiefer contain between 212 and 558 ppb Re and show isochron ages of the mineralization older than the age of the host rock (Pašava et al. 2007b). It is not surprising that oxidizing fluids related to the mineralizing processes can disturb the Re–Os system as rhenium and osmium are highly soluble under oxidizing conditions. Xiong et al. (2006) conducted experiments and analysed the solubility of rhenium in hydrothermal conditions, updating earlier studies on this topic. The most favourable conditions for rhenium transport under subcritical conditions are in the hematite stability field with redox conditions as controlling factor. If the oxygen fugacity is only 0.97 log units lower than that of the boundary between $\text{ReS}_2(\text{s})$ and $\text{ReO}_2(\text{s})$, the concentration of rhenium that is transportable in the stability field of $\text{ReS}_2(\text{s})$ drops by 4 orders of magnitude. The authors concluded that rhenium in the SSC could be transported by highly oxidizing hydrothermal fluids regardless of pH. They also speculate that the reduced part of the weathering zone in porphyry deposits might be enriched in Re due to the leaching of this metal from the sulphides by oxidizing fluids.

LA-ICP-MS data show lack of or very low counts of ^{185}Re (if monitored), indicating Re content below detection limit in almost all sulphide samples reported here. However, there are two notable exceptions where Cu–S sulphides seem to be a preferential host for rhenium. Carbonate-hosted massive djurleite and chalcocite (WZ-14 and WZ-18) reveal a median value of $0.67 \mu\text{g/g}$ Re (up to $3.86 \mu\text{g/g}$ Re), while sample CC-P-1 where shale-hosted djurleite is adjacent to “red spots” gave a median value of $0.3 \mu\text{g/g}$ (up to $0.9 \mu\text{g/g}$) (Table 1, Appendix A). Either the structure of djurleite might be favourable for Re incorporation or the processes responsible for djurleite formation could be also linked with Re enrichment. Reversible phase transitions from djurleite to high digenite and hexagonal “high chalcocite” at 93°C (Roseboom 1966, Potter 1977, Evans 1979) might play a role. Although red spot chalcopyrite or pyrite do not contain any measurable Re, our results suggest that djurleite located right at the redox front might constitute a favourable host for rhenium, especially in areas where oxygen fugacity increases enough to rapidly decrease rhenium solubility as described by Xiong et al. (2006). Although more data is necessary for confirmation, we suggest that rhenium enrichment in the deposit might be at least partially controlled by influxes of oxidizing fluids into the Kupferschiefer unit and linked with copper ore remobilization. These fluids were responsible for formation of the high grade Cu ore and Au–Pt–Pd mineralization (SOS system), explaining why Re enrichment is found mainly in the southern

part of the deposit (Wirth and Kijewski 2011). Although rhenium in SSC deposits such as the Kupferschiefer might be present in rare phases such as rheniite, tarkianite, castaingite and dzhezkazganite, the majority of this metal is likely dispersed in much more common copper sulphides.

5.4 Regional specificity?

Question to what degree common ore-forming processes control trace elements concentrations and how significant in comparison is local “flavour” (e.g. source rock and host rock) provides an interesting problem. In the case of sediment hosted stratiform copper deposits it boils down to the question which TE patterns are common worldwide and reflect universal features of mineralizing fluids and which are specific for given sedimentary basin and can vary between districts. So far there is little available literature providing LA-ICP-MS trace element data for SSC deposits such as Central African Copperbelt, White Pine or Udokan, most notably Kelepile et al. (2020) present data from the Ghanzi-Chobe Belt portion of the Kalahari Copper Belt. Therefore, we included in the investigated samples chalcopyrite from the Nchanga deposit (Zambian Copperbelt) and the most obvious differences in comparison to Kupferschiefer samples are much lower content of Ag, Mo, Sb, Tl, and Pb coupled with higher contents of In and Sn (Tab. 3). More data is necessary to assess whether this pattern is just a result of local variation or maybe it represents more fundamental feature, basin-specific trait of the mineralization dependant on source rocks or/and parameters of mineralizing fluids in the Southern Permian Basin and Katangan Basin respectively. When compared with the Kupferschiefer, mean TE concentrations in chalcopyrite reported by Kelepile et al. (2020) are lower in the case of Mo (in almost all samples mean Mo <1.2 µg/g with an exceptional value of 2241 µg/g in one sample) and Sb (0.02-5.9 µg/g), comparable for Ag (1.3-99 µg/g) and Tl (0.01-3.7 µg/g) while slightly higher for In (0.5-27 µg/g) and Sn (0.55-19 µg/g) making structurally controlled mineralization in the Ghanzi-Chobe Belt more similar to Nchanga than to Lubin-Sieroszowice district in this regard. Future studies need to pay particular attention to mineral paragenesis as coexisting phases could constitute a sink for selected trace elements and affect the trace element partitioning into copper sulphides.

Tab. 3. Median concentration of selected elements with the highest divergence between chalcopyrite from the Nchanga and Lubin-Sieroszowice. Due to the quartzite matrix, chalcopyrite samples from the Nchanga deposit should be free from the effect of micro shale inclusions skewing low concentrations data.

	Median content in chalcopyrite (in µg/g)						
	Mo	Ag	In	Sn	Sb	Tl	Pb
Lubin-Sieroszowice district	1.7	22	0.31	1.5	13	0.83	189
Nchanga deposit	<0.1	0.62	5.2	32	0.15	0.01	0.8

6. Conclusions

Sulphides from the Cu-Ag Kupferschiefer deposit present certain challenges for LA-ICP-MS measurements. In contrast to carbonate- and sandstone-hosted massive and vein mineralization, shale-hosted veins, veinlets and replacements contain numerous inclusions of shale matrix (clay minerals, organic matter and carbonates) which can affect the results and need to be taken into account. Even though careful petrographic observations, precise spot selection and repeating spots within a given sample help to minimize the effects of inclusions, they still might cause variations in TE content for elements such as V, Mn, Ni, Co, Ga, Mo, Sn. Time resolved spectra for

non-homogenous spots, where significant portions of ablated material turns out to be shale matrix, help to assess if measured signal for given trace element come from sulphide or shale. The data evaluation leads to the following provisional classification of elements: Cu, Fe, S, Ag, Tl, Sb, Pb are strongly affiliated with chalcopyrite; Ni, V, Ga, Sn, Co, Mo are strongly affiliated with Kupferschiefer matrix; In, Cd are indifferent, while Hg, Se, Bi, Ge, Mn and As are somewhere in between these extremes.

Results of LA-ICP-MS investigation of sulphides from the Cu-Ag Kupferschiefer deposit can be summarized by the following conclusions:

- 1) Trace element signatures are linked to a specific mineralization style (Fig. 11) and therefore assist in petrographic observations in distinguishing separate stages of ore formation.
- 2) Sulphides adjacent to or surrounded by hematitic “red spot” zones are particularly enriched in some of the redox sensitive elements: djurleite in V, Se, Re, Au, Hg and Tl, chalcopyrite in V, Se, Hg and Tl, while pyrite in Tl.
- 3) Clear pattern in Ag concentrations is observed, results presented on a log scale reveal almost linear decrease from chalcocite/djurleite > bornite > chalcopyrite > sphalerite. It suggests that Ag distribution on a scale of the district could be controlled by the redox conditions and might be linked to general zonation of Fe^{3+} -Cu-Pb-Zn- Fe^{2+} as well as mineral zonation sequence (hematite-chalcocite-bornite-chalcopyrite-galena-sphalerite-pyrite).
- 4) A group of sulphide-calcite epigenetic veins crosscutting lithologies and associated with local faults and tectonic zones contains chalcopyrite exceptionally enriched in germanium (up to 4806 $\mu\text{g/g}$ of Ge). The potential of Kupferschiefer Cu-Ag ore in terms of Ge grades and resources could be heavily underestimated.
- 5) The majority of sulphides analysed in the present study do not contain rhenium above detection limits (0.1 $\mu\text{g/g}$ Re), but measurable quantities were found in two types of djurleite. The first one (up to 0.9 $\mu\text{g/g}$ Re) is adjacent to red spots while carbonate hosted djurleite constitutes the second group (up to 3.9 $\mu\text{g/g}$ Re). This suggest that djurleite could be a preferential host for rhenium in the orebody.
- 6) Comparison with samples from the Nchanga deposit indicate that some of the trace element signatures might be basin specific, as chalcopyrite from the Zambian Copperbelt has much lower contents of Mo, Ag, Sb, Tl, Pb but higher contents of In and Sn.
- 7) Results show the great potential of the LA-ICP-MS method in investigating SSC deposits, especially with regards to their critical metal inventory, and emphasize the need for further studies.

Acknowledgement

This work was supported and partially funded by the Society of Economic Geologists through a Hugh McKinstry Fund grant to KF and by statutory funds of the Faculty of Geology, Geophysics and Environmental Protection, AGH University of Science and Technology, Kraków, Poland (No. 16.16.140.315). KF would like to acknowledge support from the OEAD Scholarships of the Scholarship Foundation of the Republic of Austria for Undergraduates, Graduates und Postgraduates. Gabriela Kozub-Budzyń from the Laboratory of Critical Elements at AGH-UST is gratefully acknowledge for assistance with electron microprobe analyses.

Supplementary material

The Supplementary Material for this article can be found online at:

<https://www.sciencedirect.com/science/article/pii/S0169136822000762#s0090>

References

- Alderton, D.H., Selby, D., Kucha, H., Blundell, D.J., 2016. A multistage origin for Kupferschiefer mineralization. *Ore Geol. Rev.* 79, 535-543. <https://doi.org/10.1016/j.oregeorev.2016.05.007>
- Banaś, M., Kijewski, P., Salamon, W., Pieczonka J., Piestrzyński A., 2007. Metale towarzyszące w złożu rud miedzi. In: Piestrzyński, A. (Ed.), *Monografia Polskiej Miedzi*. KGHM S.A., Lubin, pp. 214-228 (in Polish).
- Barra, F., Deditius, A., Roberts, M.P., Reich, M., Kilburn, M.R., Guagliardo, P., 2017. Dissecting the Re-Os molybdenite geochronometer. *Sci. Rep.* 7, 16054. <https://doi.org/10.1038/s41598-017-16380-8>
- Bechtel, A., Elliott, W.C., Wampler, J.M., Oszczepalski, S., 1999. Clay mineralogy, crystallinity, and K-Ar ages of illites within the Polish Zechstein Basin; implications for the age of Kupferschiefer mineralization. *Econ. Geol.* 94, 261-272. <https://doi.org/10.2113/gsecongeo.94.2.261>
- Bechtel, A., Püttmann, W., Hoernes, S., 1995. Reconstruction of the thermal history of the Kupferschiefer within the Zechstein basin of central Europe: A stable isotope and organic geochemical approach. *Ore Geol. Rev.* 9, 371-389. [https://doi.org/10.1016/0169-1368\(94\)00020-0](https://doi.org/10.1016/0169-1368(94)00020-0)
- Bechtel, A., Gratzer, R., Püttmann, W., Oszczepalski, S., 2002. Geochemical characteristics across the oxic/anoxic interface (Rote Fäule front) within the Kupferschiefer of the Lubin-Sieroszowice mining district (SW Poland). *Chem. Geol.* 185, 9-31. [https://doi.org/10.1016/S0009-2541\(01\)00395-3](https://doi.org/10.1016/S0009-2541(01)00395-3)
- Belissant, R., Boiron, M.C., Luais, B., Cathelineau, M., 2014. LA-ICP-MS analyses of minor and trace elements and bulk Ge isotopes in zoned Ge-rich sphalerites from the Noailhac–Saint-Salvy deposit (France): Insights into incorporation mechanisms and ore deposition processes. *Geochim. Cosmochim. Acta* 126, 518-540. <https://doi.org/10.1016/j.gca.2013.10.052>
- Belissant, R., Munoz, M., Boiron, M.C., Luais, B., Mathon, O., 2019. Germanium crystal chemistry in Cu-bearing sulfides from micro-xrf mapping and micro-xanes spectroscopy. *Minerals* 9(4), 227. <https://doi.org/10.3390/min9040227>
- Bernstein, L.R., 1985. Germanium geochemistry and mineralogy. *Geochim. Cosmochim. Acta* 49, 2409-2422. [https://doi.org/10.1016/0016-7037\(85\)90241-8](https://doi.org/10.1016/0016-7037(85)90241-8)
- Berzina, A.N., Sotnikov, V.I., Economou-Eliopoulos, M., Eliopoulos, D.G., 2005. Distribution of rhenium in molybdenite from porphyry Cu–Mo and Mo–Cu deposits of Russia (Siberia) and Mongolia. *Ore Geol. Rev.* 26, 91-113. <https://doi.org/10.1016/j.oregeorev.2004.12.002>
- Borg, G., Piestrzynski, A., Bachmann, G.H., Püttmann, W., Walther, S., Fiedler, M., 2012. An overview of the European Kupferschiefer deposits. *Society of Economic Geologists Special Publication* 16, 455-486.
- Box, S.E., Syusyura, B., Seltmann, R., Creaser, R.A., Dolgoplova, A., Zientek, M.L., 2012. Dzhezkazgan and associated sandstone copper deposits of the Chu-Sarysu basin, central Kazakhstan. *Society of Economic Geologists Special Publications* 16, 303-328.
- Cathles, L., 2019. On the Processes that Produce Hydrocarbon and Mineral Resources in Sedimentary Basins. *Geosciences* 9(12), 520. <https://doi.org/10.3390/geosciences9120520>
- Chmielewski, A. 2014. Characteristic of relict mineralization in the northern part of Radwanice copper field (SW part of Lubin-Sieroszowice deposit). *Biul. Państw. Inst. Geol.* 458, 1-24 (in Polish with English abstract).
- Cook, N.J., Ciobanu, C.L., Pring, A., Skinner, W., Shimizu, M., Danyushevsky, L., Saini-Eidukat, B., Melcher, F., 2009. Trace and minor elements in sphalerite: A LA-ICPMS study. *Geochim. Cosmochim. Acta* 73, 4761-4791. <https://doi.org/10.1016/j.gca.2009.05.045>

Cook, N.J., Ciobanu, C.L., Danyushevsky, L.V., Gilbert, S., 2011. Minor and trace elements in bornite and associated Cu–(Fe)-sulfides: A LA-ICP-MS study Bornite mineral chemistry. *Geochim. Cosmochim. Acta* 75, 6473-6496. <https://doi.org/10.1016/j.gca.2011.08.021>

Cook, N., Ciobanu, C.L., George, L., Zhu, Z.Y., Wade, B., Ehrig, K., 2016. Trace element analysis of minerals in magmatic-hydrothermal ores by laser ablation inductively-coupled plasma mass spectrometry: Approaches and opportunities. *Minerals* 6(4), 111. <https://doi.org/10.3390/min6040111>

Dare, S.A.S., Barnes, S.J., Beaudoin, G., Méric, J., Boutroy, E., Potvin-Doucet, C., 2014. Trace elements in magnetite as petrogenetic indicators. *Mineralium Deposita* 49, 785-796. <https://doi.org/10.1007/s00126-014-0529-0>

Dulski, T.R., 1999. Trace elemental analysis of metals: methods and techniques. CRC Press, Boca Raton. <https://doi.org/10.1201/9780203735299>

Duran, C.J., Barnes, S.J., Corkery, J.T., 2016. Trace element distribution in primary sulfides and Fe–Ti oxides from the sulfide-rich pods of the Lac des Iles Pd deposits, Western Ontario, Canada: constraints on processes controlling the composition of the ore and the use of pentlandite compositions in exploration. *J. Geochem. Explor.* 166, 45-63. <https://doi.org/10.1016/j.gexplo.2016.04.005>

Evans, H.T., 1979. The crystal structures of low chalcocite and djurleite. *Z. Kristallogr. Cryst. Mater.* 150, 299-320. <https://doi.org/10.1524/zkri.1979.150.14.299>

Feng, Y., Zhang, W., Hu, Z., Liu, Y., Chen, K., Fu, J., Xie, J., Shi, Q., 2018. Development of sulfide reference materials for in situ platinum group elements and S–Pb isotope analyses by LA-(MC)-ICP-MS. *J. Anal. At. Spectrom.* 33, 2172-2183. <https://doi.org/10.1039/C8JA00305J>

Frenzel, M., Hirsch, T., Gutzmer, J., 2016. Gallium, germanium, indium, and other trace and minor elements in sphalerite as a function of deposit type - A meta-analysis. *Ore Geol. Rev.* 76, 52-78. <https://doi.org/10.1016/j.oregeorev.2015.12.017>

Garcia-Castellanos, D., Estrada, F., Jiménez-Munt, I., Gorini, C., Fernández, M., Vergés, J., De Vicente, R., 2009. Catastrophic flood of the Mediterranean after the Messinian salinity crisis. *Nature*, 462, 778-781. <https://doi.org/10.1038/nature08555>

Gast, R.E., Dusar, M., Breikreuz, C., Gaupp, R., Schneider, J.W., Stemmerik, L., Geluk, M.C., Geissler, M., Kiersnowski, H., Glennie, K.W., Kabel, S., Jones, N.S., 2010. Rotliegend. In: Doornenbal, J.C., Stevenson, A.G. (Eds.), *Petroleum Geological Atlas of the Southern Permian Basin Area*, Eage Publications B.V., Houten, pp. 101-121.

George, L.L., Cook, N.J., Crowe, B.B., Ciobanu, C.L., 2018. Trace elements in hydrothermal chalcopyrite. *Mineral. Mag.* 82, 59-88. <https://doi.org/10.1180/minmag.2017.081.021>

George, L.L., Cook, N.J., Ciobanu, C.L., 2017. Minor and trace elements in natural tetrahedrite-tennantite: Effects on element partitioning among base metal sulphides. *Minerals* 7(2), 17. <https://doi.org/10.3390/min7020017>

George, L., Cook, N.J., Ciobanu, C.L., Wade, B.P., 2015. Trace and minor elements in galena: A reconnaissance LA-ICP-MS study. *Am. Mineral.* 100, 548-569. <https://doi.org/10.2138/am-2015-4862>

Gralikowski M., 1967. Regularities in geochemical occurrence of rhenium in the zechstein ores from the Lower Silesia (Doctoral dissertation, in Polish). AGH University of Science and Technology, Kraków.

Gregory, D.D., Large, R.R., Halpin, J.A., Baturina, E.L., Lyons, T.W., Wu, S., Danyushevsky, L., Sack, P.J., Chappaz, A., Maslennikov, V.V., Bull, S.W., 2015. Trace element content of sedimentary pyrite in black shales. *Econ. Geol.* 110, 1389-1410. <https://doi.org/10.2113/econgeo.110.6.1389>

Glennie, K.W., Buller, A.T., 1983. The Permian Weisliedend of NW Europe: the partial deformation of aeolian dune sands caused by the Zechstein transgression. *Sediment. Geol.* 35, 43-81. [https://doi.org/10.1016/0037-0738\(83\)90069-6](https://doi.org/10.1016/0037-0738(83)90069-6)

Hall, W.S., Knight, C., Catterall, D.J., Augenstein, C., Davies, B.M., Deane, J., Muyoba, B., Disang, O., Emsbo, P., Li, Y., Enders, M.S., Hitzman, M.W., 2018. Regional- to deposit-scale geologic controls on copper-silver mineralization in the Kalahari Copperbelt, Botswana. *Society of Economic Geologists Special Publications* 21, 207-236. <https://doi.org/10.5382/SP.21.10>

Hammer, J., Junge, F., Rösler, H.J., Niese, S., Gleisberg, B., Stiehl, G., 1990. Element and isotope geochemical investigations of the Kupferschiefer in the vicinity of "Rote Fäule", indicating copper mineralization (Sangerhausen basin, GDR). *Chem. Geol.* 85, 345-360. [https://doi.org/10.1016/0009-2541\(90\)90012-V](https://doi.org/10.1016/0009-2541(90)90012-V)

Harańczyk, C., 1975: Morozewiczite and polkovicite, typochemical minerals of Mesozoic mineralization of the Fore-Sudeten monocline. *Rudy i Metale Nieżelazne* 20, 288-293 (in Polish with English abstract).

Hayes, T.S., Cox, D.P., Piatak, N.M., Seal, R.R., 2015. Sediment-hosted stratabound copper deposit model. Scientific Investigations Report 2010–5070–M. U.S. Geological Survey, Reston, Virginia <https://doi.org/10.3133/sir20105070M>

Hitzman, M., Kirkham, R., Broughton, D., Thorson, J., Selley, D., 2005. The sediment-hosted stratiform copper ore system. *Econ. Geol.* 609–642 (100th Anniversary volume).

Höll, R., Kling, M., Schroll, E., 2007. Metallogenesis of germanium - A review. *Ore Geol. Rev.* 30, 145-180. <https://doi.org/10.1016/j.oregeorev.2005.07.034>

Jackson, M.P.A., Hudec, M.R., 2017. *Salt tectonics: Principles and practice*. Cambridge University Press.

Jankowski, G., 1995. Zur Geschichte des Mansfelder Kupferschieferbergbaus. GDMB-Informationsgesellschaft, Clausthal-Zellerfeld.

John, D., 2015. Rhenium - a rare metal critical to modern transportation: U.S. Geological Survey Fact Sheet 2014–3101, <https://doi.org/10.3133/fs20143101>

John, D.A., Seal, R.R., Polyak, D.E., 2017, Rhenium. In: Schulz, K.J., DeYoung, J.H., Seal, R.R., Bradley, D.C. (Eds.), *Critical mineral resources of the United States - Economic and environmental geology and prospects for future supply*. U.S. Geological Survey Professional Paper 1802, P1-P49, <https://doi.org/10.3133/pp1802P>.

Jowett, E.C., Pearce, G.W., Rydzewski, A., 1987. A Mid-Triassic paleomagnetic age of the Kupferschiefer mineralization in Poland, based on a revised apparent polar wander path for Europe and Russia. *J. Geophys. Res. Solid Earth* 92, 581-598. <https://doi.org/10.1029/JB092iB01p00581>

Jowett, E.C., 1986. Genesis of Kupferschiefer Cu-Ag deposits by convective flow of Rotliegendes brines during Triassic rifting. *Econ. Geol.* 81, 1823-1837. <https://doi.org/10.2113/gsecongeo.81.8.1823>

Kanasiewicz, J., 1966. Geochemical profile of uranium, selenium and rhenium in the Zechstein of the Leszczyzna Trough. *Geological Quarterly* 10, 309-314 (in Polish with english abstract).

Kanasiewicz, J., 1967. Occurrence of rare elements in the copper-bearing marl series of the lower zechstein in the Grodziec Syncline. *Geological Quarterly* 11, 113-117 (in Polish with english abstract).

Karnkowski, P.W., 1999. Origin and evolution of the Polish Rotliegend Basin. *Polish Geological Institute Special Papers* 3, 1-93.

Kelepile, T., Betsi, T.B., Franchi, F., Shemang, E., 2020. Partitioning and distribution of silver in sediment-hosted Cu-Ag deposits: Evidence from the Ghanzi-Chobe Belt portion of the Kalahari Copper Belt. *Ore Geol. Rev.* 124, 103663. <https://doi.org/10.1016/j.oregeorev.2020.103663>

Kiersnowski, H., Buniak, A., 2006. Evolution of the Rotliegend Basin of northwestern Poland. *Geological Quarterly* 50, 119-138.

Kijewski, P., Jarosz, J., 1987. Mineralizacja kruszcowa i formy występowania pierwiastków towarzyszących w złożu rudy miedzi. In: Kijewski, P. (Ed.), *Metale towarzyszące w rudach miedzi, stan badań i perspektywy dalszego ich wykorzystania*, Cuprum, Wrocław, pp. 21-47 (in Polish).

Kijewski, P., Wirth, H., 2011. Rhenium – occurrence in copper ore deposit, the production and its perspectives. *Zesz. Nauk. Inst. Gospod. Surowcami Miner. I Ener. PAN* 81, 103-115 (in Polish with English abstract).

Kłapciński, J., Peryt, T.M., 2007. Budowa geologiczna monokliny przedsudeckiej. In: Piestrzyński, A. (Ed.), *Monografia Polskiej Miedzi*. KGHM S.A., Lubin, pp. 69-77 (in Polish)

Kłapciński, J., 1971. Lithology, fauna, stratigraphy and palaeogeography of the Permian in the fore-Sudetic monocline. *Geologia Sudetica* 5, 77-135 (in Polish with English abstract).

Knorsch, M., Nadoll, P., Klemd, R., 2020. Trace elements and textures of hydrothermal sphalerite and pyrite in Upper Permian (Zechstein) carbonates of the North German Basin. *J. Geochem. Explor.* 209, 106416. <https://doi.org/10.1016/j.gexplo.2019.106416>

Kozub-Budzyń, G.A., Piestrzyński, A., 2017. Geochemical characteristic of Ag-bearing minerals occurring in copper ore deposit at the Fore-Sudetic Monocline. *Biul. Państw. Inst. Geol.* 468, 49-60 (in Polish with English abstract).

Kucha, H., 1995. Redefinition of Rote Fäule, Kupferschiefer, Poland. In: Pasava, J., Kribek, B., Zak, K. (Eds.), *Mineral Deposits: From Their Origin to Their Environmental Impacts*. Balkema, Rotterdam, pp. 953–956.

Kucha, H., 1986. Eugenite, Ag₁₁Hg₂ - A new mineral from Zechstein copper deposits in Poland. *Mineralogia Polonica* 17, 3-12.

Kucha, H., 1990. Geochemistry of the Kupferschiefer, Poland. *Geologische Rundschau* 79, 387-399. <https://doi.org/10.1007/BF01830634>

Kucha, H., 2007. Mineralogy and geochemistry of the Lubin-Sieroszowice orebody. *Biul. Państw. Inst. Geol.* 423, 77-94 (in Polish with English abstract).

Kucha, H., Przybyłowicz, W., Kajfosz, J., Szymczyk, S., 1994. PIXE analysis of Kupferschiefer samples. *Geological Quarterly* 38, 687-700.

Large, R.R., Danyushevsky, L., Hollit, C., Maslennikov, V., Meffre, S., Gilbert, S., Bull, S., Scott, R., Emsbo, P., Thomas, H., Singh, B., Foster, J. (2009). Gold and trace element zonation in pyrite using a laser imaging technique: Implications for the timing of gold in orogenic and Carlin-style sediment-hosted deposits. *Econ. Geol.* 104, 635-668. <https://doi.org/10.2113/gsecongeo.104.5.635>

Lawley, C.J.M., Creaser, R.A., Jackson, S.E., Yang, Z., Davis, B.J., Pehrsson, S.J., Dubé B., Mercier-Langevin, P., Vaillancourt, D., 2015. Unravelling the Western Churchill Province Paleoproterozoic gold metallogeny: Constraints from Re-Os arsenopyrite and U-Pb xenotime geochronology and LA-ICP-MS arsenopyrite trace element chemistry at the BIF-hosted Meliadine Gold District, Nunavut, Canada. *Econ. Geol.* 110, 1425-1454. <https://doi.org/10.2113/econgeo.110.6.1425>

McCann, T., Pascal, C., Timmerman, M.J., Krzywiec, P., López-Gómez, J., Wetzel, L., Krawczyk, C.M., Rieke, H., Lamarche, J., 2006. Post-Variscan (end Carboniferous-Early Permian) basin evolution in western and central Europe. In: Gee, D.G., Stephenson, R.A. (Eds.), *European Lithosphere Dynamics*. Geological Society, London, *Memoirs* 32, pp. 355-388. <https://doi.org/10.1144/GSL.MEM.2006.032.01.22>

Melcher, F., Buchholz, P., 2014. Germanium. In: Gunn, G. (Ed.), *Critical Metals Handbook*. Wiley-Blackwell, Chichester, pp. 177-203. <https://doi.org/10.1002/9781118755341.ch8>

Menning, M., Alekseev, A.S., Chuvashov, B.I., Davydov, V.I., Devuyt, F.X., Forke, H.C., Grunt, T.A., Hance, L., Heckel, P.H., Izokh, N.G., Jin Yugan, Jones, P.J., Kotlyar, G.V., Kozur, H.W., Nemyrovskaya, T.I., Schneider, J.W., Wang, X.D., Weddige, K., Weyer, D., Work, D.M., 2006. Global time scale and regional stratigraphic reference scales of Central and West Europe, East Europe, Tethys, South China, and North America as used in the Devonian-Carboniferous-Permian Correlation Chart 2003 (DCP 2003). *Palaeogeogr. Palaeoclimatol. Palaeoecol.* 240, 318-372. <https://doi.org/10.1016/j.palaeo.2006.03.058>

Michalik, M., Sawłowicz, Z., 2001. Multi-stage and long-term origin of the Kupferschiefer copper deposits in Poland. In: Piestrzyński, A. (Ed.), *Mineral Deposits at the Beginning of the 21st century*. Balkema, pp. 235–238

Mikulski S.Z., Stein H.J., 2010. Re-Os age of a chalcopyrite sample from the Lubin Cu-Ag mine, Kupferschiefer, SW Poland. *Geochim. Cosmochim. Acta*, 74 (12), A708.

Mikulski, S.Z., Stein, H.J., 2015. Re-Os ages for Ag-bearing Cu sulphide ores from the Kupferschiefer in Poland. In: André-Mayer, A.S., Cathelineau, M., Muchez, P., Pirard, E., Sindern, S. (Eds.), *Mineral resources in a sustainable world. 13th Biennial SGA Meeting, Nancy*, pp. 607–610.

Mikulski, S.Z., Stein, H.J., 2017. Re-Os isotopic age of the Cu-Ag sulfide ore and its mineralogical and geochemical characteristic from the Lubin-Polkowice mining area (SW Poland). *Biul. Państw. Inst. Geol.* 468, 79-96 (in Polish with English summary).

Mikulski, S.Z., Oszczepalski, S., Sadłowska, K., Chmielewski, A., Małek, R., 2020. Trace Element Distributions in the Zn-Pb (Mississippi Valley-Type) and Cu-Ag (Kupferschiefer) Sediment-Hosted Deposits in Poland. *Minerals* 10(1), 75. <https://doi.org/10.3390/min10010075>

Nadoll, P., Sośnicka, M., Kraemer, D., Duschl, F., 2019. Post-Variscan structurally-controlled hydrothermal Zn-Fe-Pb sulfide and F-Ba mineralization in deep-seated Paleozoic units of the North German Basin: A review. *Ore Geol. Rev.* 106, 273-299. <https://doi.org/10.1016/j.oregeorev.2019.01.022>

Nawrocki, J., 2017. On the paleomagnetic age of copper, uranium and zinc-lead mineralization in Poland, determined by comparison of characteristic magnetizations with the reference apparent polar wander path. *Przełd Geologiczny* 65, 105-108 (in Polish with English abstract).

Nawrocki, J., 2000. Clay mineralogy, crystallinity, and K-Ar ages of illites within the Polish Zechstein Basin: Implications for the age of Kupferschiefer mineralisation - A discussion. *Econ. Geol.* 95, 241–242. <https://doi.org/10.2113/gsecongeo.95.1.241>

Onuk, P., Melcher, F., Mertz-Kraus, R., Gäbler, H.E., Goldmann, S., 2017. Development of a matrix-matched sphalerite reference material (MUL-ZnS-1) for calibration of in situ trace element measurements by laser ablation-inductively coupled plasma-mass spectrometry. *Geostand. Geoanalytical Res.* 41, 263-272. <https://doi.org/10.1111/ggr.12154>

Oszczepalski, S., 1999. Origin of the Kupferschiefer polymetallic mineralization in Poland. *Miner. Deposita* 34, 599–613

Oszczepalski, S., Rydzewski, A., 1991. The Kupferschiefer mineralization in Poland. *Zentralbl. Geol. Paläontol.* 1, 975–999

Oszczepalski, S., Rydzewski, A., 1997. Rozmieszczenie metali w basenie cechsztyńskim. In: Piestrzyński, A. (Ed.), *Monografia Polskiej Miedzi*. KGHM S.A., Lubin, pp. 115-122 (in Polish).

Oszczepalski, S., Chmielewski, A., 2017. Ore mineralization in the discovery borehole Sieroszowice S-1 in the light of new research. *Przełd Geologiczny* 65, 321-338 (in Polish with English abstract).

Oszczepalski, S., Chmielewski, A., Speczik, S., 2017. Variability of ore mineralization in the north-west-trending extension of the Lubin–Sieroszowice deposit. *Biul. Panstw. Inst. Geol.* 468, 109-141 (in Polish with English abstract).

Oszczepalski, S., Speczik, S., Zieliński, K., Chmielewski, A., 2019. The Kupferschiefer Deposits and Prospects in SW Poland: Past, Present and Future. *Minerals* 9(10), 592. <https://doi.org/10.3390/min9100592>

Pašava, J., Oszczepalski, S., Du, A., 2010. Re-Os age of non-mineralized black shale from the Kupferschiefer, Poland, and implications for metal enrichment. *Miner. Deposita* 45, 189-199. <https://doi.org/10.1007/s00126-009-0269-8>

Pašava, J., Svojtka, M., Veselovský, F., Ďurišová, J., Ackerman, L., Pour, O., Drabek, M., Halodová, P., Haluzová, E., 2016. Laser ablation ICPMS study of trace element chemistry in molybdenite coupled with scanning electron microscopy (SEM) - An important tool for identification of different types of mineralization. *Ore Geol. Rev.* 72, 874-895. <https://doi.org/10.1016/j.oregeorev.2015.09.007>

Pašava, J., Vymazalová, A., Qu, W., Korzekwa, W., 2007a. Re–Os study of the Polish Kupferschiefer; implications for source and timing of metal enrichment. *Geochim. Cosmochim. Acta* 71 (15S), A763.

Pašava, J., Vymazalová, A., Mao, J., Du, A., Qu, W., Korzekwa, W., 2007b. Re-Os study of noble metal-rich blackshales from the Polish Kupferschiefer. In: Andrew, C.J., (Ed.), *Digging Deeper*. Proceedings of the 9th Biennial SGA Meeting, Dublin, Ireland, Irish Association for Economic Geology, pp 221-224.

Pätzold, T., Brauns, C.M., Haack, U., 2002. A Re–Os study bearing on the age of Kupferschiefer mineralization at Mansfeld (Germany). Abstract for Symposium “Highly Siderophile Elements in Terrestrial and Meteoritic Samples: Implications for Planetary Differentiation and Igneous Processes”, Nancy, August 26–28, 2002.

Paul, J., 2006. Der Kupferschiefer: lithologie, stratigraphie, fazies und metallogenese eines schwarzschiefers (The Kupferschiefer: lithology, stratigraphy, facies and metallogeny of a black shale). *Z. Dtsch. Ges. Geowiss.* 157, 57–76. <https://doi.org/10.1127/1860-1804/2006/0157-0057>

Peryt, T.M., Durakiewicz, T., Kotarba, M.J., Oszczepalski, S., Peryt, D., 2012. Carbon isotope stratigraphy of the basal Zechstein (Lopingian) strata in Northern Poland and its global correlation. *Geological Quarterly* 56, 285-298. <http://dx.doi.org/10.7306/gq.1022>

Pieczonka, J., 2000. Strefy utlenienia w złożu rud miedzi na monoklinie przedsudeckiej. *Prace Specjalne Polskiego Towarzystwa Mineralogicznego* 16, 9–54 (in Polish).

Pieczonka, J., Piestrzyński, A., 2000. Model genetyczny koncentracji złota w obszarze występowania złóż rud miedzi na monoklinie przedsudeckiej. *Prace Specjalne Polskiego Towarzystwa Mineralogicznego* 16, 55–82 (in Polish).

Pieczonka, J., Piestrzyński, A., Mucha, J., Głuszek, A., Kotarba, M., Więclaw, D., 2008. The red-bed-type precious metal deposit in the Sieroszowice-Polkowice copper mining district, SW Poland. *Ann. Soc. Geol. Pol.* 78, 151–280.

Pieczonka, J., Piestrzyński, A., Jedlecki, R., 2019. Thalcusite - a new mineral form the Kupferschiefer, Sieroszowice deposit, Poland. In: Smith, D.J., Jenkin, G.R.T., Holwell, D.A., Keith, M. (Eds.), *Life with Ore Deposits on Earth. Proceedings of the 15th Biennial SGA Meeting, Glasgow*, pp. 1879–1882.

Piesterzyński, A., Pieczonka, J., Głuszek, A., 2002. Redbed-type gold mineralisation, Kupferschiefer, south-west Poland. *Miner. Deposita* 37, 512–528. <https://doi.org/10.1007/s00126-002-0256-9>

Polyak, D.E., 2018. Rhenium. In: *Minerals Yearbook: Volume I. Metals and Minerals*. U.S. Geological Survey, Washington, DC. <<https://www.usgs.gov/centers/national-minerals-information-center/rhenium-statistics-and-information>>

Potter, R.W., 1977. An electrochemical investigation of the system copper-sulfur. *Econ. Geol.* 72, 1524-1542. <https://doi.org/10.2113/gsecongeo.72.8.1524>

Reiser, F.K., Rosa, D.R., Pinto, Á.M., Carvalho, J.R., Matos, J.X., Guimarães, F.M., Alves, L.C., de Oliveira, D.P.S., 2011. Mineralogy and geochemistry of tin-and germanium-bearing copper ore, Barrigão re-mobilized vein deposit, Iberian Pyrite Belt, Portugal. *Int. Geol. Rev.* 53, 1212-1238. <https://doi.org/10.1080/00206811003683168>

Roseboom, E.H., 1966. An investigation of the system Cu-S and some natural copper sulfides between 25 degrees and 700 degrees C. *Econ. Geol.* 61, 641-672. <https://doi.org/10.2113/gsecongeo.61.4.641>

Salamon, W., 1976. Metale szlachetne w czarnych łupkach cechsztyńskich na monoklinie przedsudeckiej, Rudy i Metale Nieżelazne 12, 472-477 (in Polish).

Schneider, J., Melcher, F., Brauns, M., 2007. Concordant ages for the giant Kipushi base metal deposit (DR Congo) from direct Rb–Sr and Re–Os dating of sulfides. *Miner. Deposita* 42, 791-797. <https://doi.org/10.1007/s00126-007-0158-y>

Selby, D., Kelley, K.D., Hitzman, M.W., Zieg, J., 2009. Re-Os sulfide (bornite, chalcopyrite, and pyrite) systematics of the carbonate-hosted copper deposits at Ruby Creek, southern Brooks Range, Alaska. *Econ. Geol.* 104, 437-444. <https://doi.org/10.2113/gsecongeo.104.3.437>

Sen, I.S., Bizimis, M., Sen, G., 2010. Geochemistry of sulfides in Hawaiian garnet pyroxenite xenoliths: implications for highly siderophile elements in the oceanic mantle. *Chem. Geol.* 273, 180-192. <https://doi.org/10.1016/j.chemgeo.2010.02.021>

Singer, D.A., 1995. World class base and precious metal deposits; a quantitative analysis. *Econ. Geol.* 90, 88-104. <https://doi.org/10.2113/gsecongeo.90.1.88>

Speczik, S., Puttmann, W., 1987. Origin of Kupferschiefer mineralization as suggested by coal petrology and organic geochemical studies. *Acta Geol. Pol.* 37, 167-188.

Sońnicka, M., Lüders, V., 2019. Super-deep, TSR-controlled Phanerozoic MVT type Zn-Pb deposits hosted by Zechstein-2 gas reservoir carbonate (Ca₂), Lower Saxony Basin, Germany. *Chem. Geol.* 508, 62-77. <https://doi.org/10.1016/j.chemgeo.2018.04.025>

Stepanov, A.S., Danyushevsky, L.V., Large, R.R., Mukherjee, I., Zhukova, I.A., 2020. Deconvolution of the composition of fine-grained pyrite in sedimentary matrix by regression of time-resolved LA-ICP-MS data. *Am. Mineral.* 105, 820-832. <https://doi.org/10.2138/am-2020-7202>

Strengel-Martinez, M., Speczik, S., Jankowski, J., 1993. Epigenetic veins in Kupferschiefer deposits of SW Poland. *Arch. Min.* 49, 203-204.

Symons, D.T., Kawasaki, K., Walther, S., Borg, G., 2011. Paleomagnetism of the Cu–Zn–Pb-bearing Kupferschiefer black shale (Upper Permian) at Sangerhausen, Germany. *Miner. Deposita* 46, 137-152. <https://doi.org/10.1007/s00126-010-0319-2>

Tomaszewski, J.B., 1978. The geological structure of the Lubin-Sieroszowice region (Lower Silesia). *Geol. Sudetica* 13, 85-128 (in Polish with English summary).

Tristá-Aguilera, D., Barra, F., Ruiz, J., Morata, D., Talavera-Mendoza, O., Kojima, S., Ferraris, F., 2006. Re–Os isotope systematics for the Lince–Estefanía deposit: constraints on the timing and source of copper mineralization in a stratabound copper deposit, Coastal Cordillera of Northern Chile. *Miner. Deposita* 41, 99 <https://doi.org/10.1007/s00126-006-0048-8>

U.S. Geological Survey, 2020. Mineral commodity summaries 2020, U.S. Geological Survey, Reston, Virginia <https://doi.org/10.3133/mcs2020>

Van Nhan, N., 1970. New ore minerals of the Lower Silesian Zechstein copper-bearing rocks. *Prace Miner.* 24, 49–60 (in Polish with English summary).

Vaughan, D.J., Sweeney, M.A., Friedrich, G., Diedel, R., Haranczyk, C., 1989. The Kupferschiefer; an overview with an appraisal of the different types of mineralization. *Econ. Geol.* 84, 1003-1027. <https://doi.org/10.2113/gsecongeo.84.5.1003>

Voudouris, P., Melfos, V., Spry, P.G., Bindi, L., Moritz, R., Ortelli, M., Kartal, T., 2013. Extremely Rhenium-rich molybdenite from porphyry Cu-Mo-Au prospects in northeastern Greece: Mode of occurrence, causes of enrichment, and implications for gold exploration. *Minerals* 3(2), 165-191. <https://doi.org/10.3390/min3020165>

Voudouris, P.C., Melfos, V., Spry, P.G., Bindi, L., Kartal, T., Arikas, K., Moritz, R., Ortelli, M., 2009. Rhenium-rich molybdenite and rheniite (ReS₂) in the Pagoni Rachi-Kirki Mo-Cu-Te-Ag-Au deposit, Northern Greece: Implications for the rhenium geochemistry of porphyry style Cu-Mo and Mo mineralization. *Can. Mineral.* 47, 1013-1036. <https://doi.org/10.3749/canmin.47.5.1013>

Wieclaw, D., Kotarba, M.J., Pieczonka, J., Piestrzynski, A., Oszczepalski, S., Marynowski, L., 2007. Reduced, transitional and oxidized zones distribution in the Kupferschiefer in Fore-Sudetic Monocline based on indices of organic matter. *Biul. Państw. Inst. Geol.* 423, 125-138 (in Polish with English abstract).

Wilson, S.A., Ridley, W.I., Koenig, A.E., 2002. Development of sulfide calibration standards for the laser ablation inductively-coupled plasma mass spectrometry technique. *J. Anal. At. Spectrom.* 17, 406-409. <https://doi.org/10.1039/B108787H>

Wodzicki, A., Piestrzyński, A., 1994. An ore genetic model for the Lubin–Sieroszowice mining district, Poland. *Miner. Deposita* 29, 30-43. <https://doi.org/10.1007/BF03326394>

Wohlgemuth-Ueberwasser, C.C., Viljoen, F., Petersen, S., Vorster, C., 2015. Distribution and solubility limits of trace elements in hydrothermal black smoker sulfides: An in-situ LA-ICP-MS study. *Geochim. Cosmochim. Acta* 159, 16-41. <https://doi.org/10.1007/BF03326394>

Ziegler, P.A., 2005. Europe: Permian to recent evolution. In: Selley, R.C., Cocks, L.R.M., Plimer, I.R. (Eds.), *Encyclopedia of geology*. Elsevier, Amsterdam, pp. 102–125.

Zieliński, K., Speczik, S., 2017. Deep copper and silver deposits – a chance for Polish metal mining industry. *Biul. Państw. Inst. Geol.* 468, 153-164 (in Polish with English abstract).

Zientek, M.L., Oszczepalski, S., Parks, H.L., Bliss, J.D., Borg, G., Box, S.E., Taylor, C.D., 2015. Assessment of undiscovered copper resources associated with the Permian Kupferschiefer, Southern Permian Basin, Europe. Scientific Investigations Report 2010-5090-U. U.S. Geological Survey, Reston, Virginia. <https://doi.org/10.3133/sir20105090U>

5. Summary and Conclusions

This PhD dissertation project has broadened the understanding of formation processes of sediment-hosted Cu-Co deposits, through applying a multi-method geochemical approach and a range of microscopic methods on the Cu-Co-Zn DOF deposit. The reflective light and SEM microscopy of the DOF sulfides and gangue phases show that sulfide mineralization occurs in six mineralization styles: (1) disseminated; (2) polysulfide cluster aggregates; (3) polysulfide nodules; (4) veins, both sulfide- and gangue-dominated; (5) mineralized pressure shadows; and (6) “Events”, which is a locally applied term for mineralization which occurs within vein- and/or slump-like structures that portray both ductile and brittle textures.

Although the deposit is named “Dolostone Ore Formation”, the main DOF Cu-Co-Zn horizon is associated with ankerite and siderite. Dolomite and Fe-dolomite are rather present in the wider-DOF Cu-Zn(-Pb) horizon, which does contain host rock-hosted sulfides, but it’s Cu-Zn(-Pb) mineralization is predominantly due to veining. The most abundant sulfides in the DOF deposit are pyrite, pyrrhotite, cobaltpentlandite, chalcopyrite, sphalerite, and linnaeite. Linnaeite and cobaltpentlandite are the main Co-bearing mineral in the DOF. Linnaeite occurs as euhedral crystals in nodules and clusters, partially broken down, whilst cobaltpentlandite occurs as exsolution-like inclusions within pyrite and pyrrhotite. Accessory sulfides include galena, cobaltite, and pentlandite.

Based on the sulfide trace elements, e.g. Fe, Co, Ni, Se, and Cd in sphalerite and Co, Ni, Se, and Bi in chalcopyrite, the disseminated, nodule, cluster, and “Event” sulfides group together, whilst vein- and pressure shadow-hosted sulfides group. Trace element trends of these populations suggest that the vein and pressure shadow mineralization formed at relatively lower temperatures. The sphalerite geothermometer of both populations shows formation temperatures $>310 \pm 50$ °C, indicating a syn-orogenic formation rather than sedimentary to early diagenetic. Sedimentary to early diagenetic formations are common for sediment-hosted Cu(-Co) deposits, e.g. the Polish Kupferschiefer and partially the KCB, which clearly separates the DOF from these other deposits.

The Co in the DOF deposit underwent several stages of remobilization. Cobalt was initially introduced to the DOF through direct substitution ($\text{Fe}^{2+} \leftrightarrow \text{Co}^{2+}$) in hydrothermal pyrite, evident by oscillatory zonation. During later hydrothermal events, possibly related to the Damara Orogen, the physicochemical conditions changed resulting in pyrite not being stable and Co was remobilized to form cobaltpentlandite exsolutions and eventually linnaeite. This process presumably involved a more oxidized fluid, oxidizing the pyrite-hosted Co^{2+} to Co^{3+} , which resulted in the formation of linnaeite ($\text{Co}^{2+}\text{Co}^{3+}_2\text{S}_4$). Later Cu-Zn-rich fluids led to the formation of chalcopyrite and sphalerite which replaces and overgrows the preexisting pyrite and linnaeite. During this stage, the Co was once again remobilized to partition into the chalcopyrite, but foremost sphalerite (up to 1 wt% Co). Such high Co concentrations had yet to be recognized in the published literature. APT of this Co-rich sphalerite showed that the Co occurs through simple substitution ($\text{Zn}^{2+} \leftrightarrow \text{Co}^{2+}$). Although not surprising due to the similar atomic radius and charge of Zn and Co, it is curious that sphalerite does not contain wt% concentrations of Co more commonly, as Fe can commonly occur in several wt% in sphalerite. The Co in the DOF, as

previously mentioned, has experienced several remobilization stages and it is most probably due to this that the DOF sphalerite contains such uniquely high concentrations of Co.

Chalcopyrite, sphalerite, and pyrite geochemistry was compared between the DOF, Polish Kupferschiefer, and the CACB (KCB and ZCB) to investigate the similarities and differences between these sediment-hosted Cu(-Co) deposits. From the sulfide geochemistry it is evident that the African deposits (which are in host rocks of the same age, and have experienced Pan-African metamorphism) share more similarities with their trace element composition, compared to the Polish Kupferschiefer. Random Forest analyses were applied on the trace element data to determine the most distinguishing elements between the deposits. Chalcopyrite from the DOF and KCB were distinguishable by their contents of Ga and Ag. These two elements also distinguished DOF chalcopyrite from Polish Kupferschiefer chalcopyrite rather well, although there were some overlaps. ZCB chalcopyrite could be moderately distinguished with Ga and Ag, one population of ZCB was well distinguishable whilst a second population overlapped with DOF chalcopyrite. Sphalerite was only identified in the DOF and Polish Kupferschiefer, where Random Forest analyses yielded Fe and Cd to be the best distinguishing elements between these deposits. Overall, it was shown that the trace element composition of sulfides from sediment-hosted Cu(-Co) deposits vary greatly due to differences in metal sources, most reasonably relating to different underlying basements and sediment sources of surrounding basement rocks.

The sulfide geochemistry was also compared to other deposit-types to investigate the possibility of deposit-type defining trace element characteristics. Chalcopyrite may be discriminated quite well from other deposit types based on Co, Sn, and Hg. Sphalerite from sediment-hosted Cu(-Co) deposits plots similar to low-temperature MVT deposits, although the DOF trends towards the higher temperature fields in sphalerite discrimination plots. This makes sense as the Kupferschiefer sphalerite formed at lower temperatures than the DOF. Cobalt/Ni of pyrite from both the KCB and DOF plot separately from the pre-established sedimentary, volcanic, and magmatic fields, due to their high Co content. This is also evident in Se/As versus Co/Sb discrimination plots, wherein the KCB and DOF pyrite predominantly plots within the magmatic pyrite field. This may reflect a magmatic source for the Co in pyrite, and consequently these sediment-hosted Cu-Co deposits. Kupferschiefer pyrite tends to plot more into the hydrothermal fields of both discrimination plots.

Appendix 1

List of conference abstracts authored during the time of the PhD

Ten first authored conference abstract contributions have been made to a range of international and local conferences, both at larger and student conferences. All first-authored abstracts have been presented at each respective conference. An additional 13 conference abstracts have been coauthored through direct research involvement.

Bertrandsson Erlandsson, V., Gopon, P., Foltyn, K., Šoster, A., Ellmies, R., & Melcher, F. (2022). More than meets the eye: investigating critical elements in sulfides from different ore deposit types. In PANGEO 2022 Leoben: September 10-13.

Wallner, D., **Bertrandsson Erlandsson, V.**, Raith, J., Rantitsch, G., Melcher, F., & Ellmies, R. (2022). Mineralogical and Geochemical Characterization of the Dolostone Ore Formation, Kunene Region, Namibia. In PANGEO 2022 Leoben: September 10-13.

Niederl, S., Felfer, P., **Bertrandsson Erlandsson, V.**, Mottram, C., Raith, J., & Gopon, P. (2022). Invisible metals for a green future: precious metal associated critical metals in the old mining districts Flatschach, Pusterwald and Kothgraben (Styria). In PANGEO 2022 Leoben: September 10-13.

Mali, H., **Bertrandsson Erlandsson, V.**, Onuk, P., Schuster, R., & Knoll, T. (2022). Spodumene Pegmatite Resource Potential of Austria. In PANGEO 2022 Leoben: September 10-13.

Hiller, J.M., **Bertrandsson Erlandsson, V.**, Bojar, H.P., & Gopon, P. (2022). A green future from a contentious past: gold and critical metals in a historic arsenic mining district Strassegg (Styria). In PANGEO 2022 Leoben: September 10-13.

Gopon, P., Douglas, J., Jenkins, B., **Bertrandsson Erlandsson, V.**, Xie, Z., & Felfer, P. (2022). Hidden in plain sight: using Atom Probe Tomography to understand the formation of invisible gold deposits in North America, China, and Europe. In PANGEO 2022 Leoben: September 10-13.

Gartner, V., **Bertrandsson Erlandsson, V.**, & Melcher, F. Trace elements in sphalerite from the Pb-Zn Raibl deposit (in German). In PANGEO 2022 Leoben: September 10-13.

Bertrandsson Erlandsson, V., Gopon, P., Foltyn, K., Šoster, A., Ellmies, R., & Melcher, F. (2022). Searching for what's within: By-product critical elements in minerals from ore deposits. In ICP-MS User Meeting Leoben 2022 and 14th Mass Spectrometric Methods of Trace Element Analysis Symposium: September 05–08.

Petrovic S., Pacevski A., **Bertrandsson Erlandsson, V.**, & Jelenkovic R., 2022: Origin of Ni, Ag and Sn mineral association in Rudnik polymetallic deposit. Book of abstracts of 18th Serbian Geological Congress "Geology solves the problems". pp 197.

Bertrandsson Erlandsson, V., Wallner, D., Ellmies, R., Melcher, F., & Raith, J. (2021). Applications of sulfide geochemistry for constraining ore-forming processes of the sediment-hosted Cu-Co Dolostone Ore Formation, Namibia. In 3rd European Mineralogical Conference Cracow Poland: EMC2020 (pp. 62).

Bertrandsson Erlandsson, V., Wallner, D., Ellmies, R., Melcher, F., & Raith, J. (2021). Sulfide trace element geochemistry and its implications for metamorphism and ore formation: an example from a sediment-hosted Cu-Co mineralization in northwestern Namibia. In Goldschmidt Virtual 2021: July 4-9, 2021.

Bertrandsson Erlandsson, V., Wallner, D., Ellmies, R., Melcher, F., & Raith, J. (2021). Using sulfide trace element geochemistry for constraining mineralization paragenesis by LA-ICP-MS: an

example from a sediment-hosted Cu-Co deposit in northwestern Namibia. In 2021 PDAC-SEG Student Minerals Colloquium: March 8-11.

Bertrandsson Erlandsson, V., Wallner, D., Ellmies, R., Melcher, F., & Raith, J. (2020). Trace element variations in sulfides between mineralization styles of the sediment-hosted Dolostone Ore Formation copper-cobalt deposit, northwestern Namibia. In Book of Abstracts DMG Virtual Poster Session 2020: 30. November - 03 Dezember 2020 (pp. 8).

Bertrandsson Erlandsson, V., Ellmies, R., Melcher, F., Wallner, D., & Raith, J. (2020). Preliminary results of in situ trace elements analyses of base metal sulfides from the sediment-hosted Dolostone Ore Formation (DOF) copper-cobalt deposit, northwestern Namibia. In GeoUtrecht 2020: 24-26 Aug. 2020.

Foltyn, K., & **Bertrandsson Erlandsson, V.** (2019). Indium in the Stara Kamienica Schist Belt, Poland - Insight from LA-ICPMS. In 1st International Student Conference on Geochemistry and Mineral Deposits, 8-9 November 2019, Prague, Czech Republic (pp. 17-18).

Bertrandsson Erlandsson, V., Wallner, D., Ellmies, R., Melcher, F., & Raith, J. (2019). The sediment-hosted Cu-Co Dolostone Ore Formation mineralization - A continuation of the Central African Copperbelt or a new mineralization process in northwestern Namibia? In 1st International Student Conference on Geochemistry and Mineral Deposits, 8-9 November 2019, Prague, Czech Republic (pp. 7-8).

Velojic, M., & **Bertrandsson Erlandsson, V.** (2019). Trace elements in different veins in Chukaru Peki high sulfidation deposit, Serbia. In 1st International Student Conference on Geochemistry and Mineral Deposits, 8-9 November 2019, Prague, Czech Republic (pp. 15-16).

Bertrandsson Erlandsson, V., Wallner, D., Ellmies, R., Melcher, F., & Raith, J. (2019). Investigating the origins of the sediment-hosted Cu-Co Dolostone Ore Formation mineralization, Kunene Region, Northwestern Namibia. In Abstracts of the 11th Annual Meeting of the SGA Baltic Student Chapter, Kraków, Poland, October 20-25, 2019 (pp. 14).

Foltyn, K., & **Bertrandsson Erlandsson, V.** (2019). Trace elements in sulfides from the Polish Kupferschiefer. In Abstracts of the 11th Annual Meeting of the SGA Baltic Student Chapter, Kraków, Poland, October 20-25, 2019 (pp. 15).

Foltyn, K., Piestrzynski, A., Mochacka, K., **Bertrandsson Erlandsson, V.**, Melcher, F., & Onuk, P. (2019). LA-ICP-MS study of trace elements in sphalerite and chalcopyrite from the Gierczyn mine. In CAGG-AGH-2019, Abstracts.

Bertrandsson Erlandsson, V., Wallner, D., Ellmies, R., Melcher, F., & Raith, J. (2019). A new sediment-hosted Cu-Co deposit in the Kunene Region, northwestern Namibia. In Mitteilungen der Österreichischen Mineralogischen Gesellschaft (2019): MinPet 2019 Graz (165 ed., pp. 30).

Foltyn, K., **Bertrandsson Erlandsson, V.**, Melcher, F., Onuk, P., & Piestrzynski, A. (2019). LA-ICP-MS trace elements study of sphalerite from the MVT Cracow-Silesia district, Poland. In Proceedings of the 15th SGA Biennial Meeting, 27-30 August 2019, Glasgow, Scotland (Vol. 1, pp. 447-450).

Foltyn, K., **Bertrandsson Erlandsson, V.**, Zygo, W., Melcher, F., & Onuk, P. (2019). Ge-enriched chalcopyrite from the Cu-Ag Kupferschiefer deposit. In Goldschmidt Conference 2019 Abstract.

Appendix 2

Drill core sample list

Samples collected from the exploration drill cores. "Sample" indicates quartered drill core sample collected. Depth from and to in (m). Element column notes significant horizons, based on the geochemical assays from Gecko Namibia. Abbreviations: Lith. = lithology; Min. = visible minerals; SSH = argillite; Bx = breccia; EV = DOF Event; VNS = vein; SHR = sheared vein; mDOF = Main DOF horizon; wDOF = Wider DOF horizon; V = vanadium horizon; HW = hanging wall; FW = footwall; lg = low grade; gy = gray; Dgy = dark gray; Lgy = light gray; Sx = unspecified sulfide; Py = pyrite; Po = pyrrhotite; Gn = galena; Sp = sphalerite; Cp = chalcopyrite; Qz = quartz; CL = calcite; Cc = unspecified carbonate mineral; Gr = graphitic; di = disseminated; fg = fine grained; cg = coarse grained. All borehole collar locations are in WGS84.

Borehole-ID: DOFD0277

Borehole collar: Lat = -17.83280233 Long = 13.70853136

Borehole-ID	Date	From	To	Horizon	Color	Lith.	Min.	Sample
DOFD0277	31.03.2019	863.00	869.59	V	Dgy	SSH	low Gr, Sx	DOFD0277-1
DOFD0277	31.03.2019	869.59	869.61	V	Lgy	BA	Sx	DOFD0277-1
DOFD0277	31.03.2019	869.61	870.28	V	gy	SSH	waves, long, Gr M	DOFD0277-2
DOFD0277	31.03.2019	870.28	870.40	V	Dgy	SSH	BH para vns CL - Sx;	DOFD0277-3
DOFD0277	31.03.2019	870.43	871.73	V	Dgy	SSH	BH para vns CL - Sx; Sx	DOFD0277-4
DOFD0277	31.03.2019	872.15	873.25	V	Dgy	SSH	high Gr, Py	DOFD0277-5
DOFD0277	31.03.2019	876.15	876.64	V	Dgy	SSH	Gr, Py	DOFD0277-6
DOFD0277	31.03.2019	877.75	878.20	V	Dgy	SSH	high Gr, Py	DOFD0277-7
DOFD0277	31.03.2019	879.00	880.33	V	gy	SSH	Py	DOFD0277-8
DOFD0277	31.03.2019	890.57	891.55	HW		BX	Py, Po, Sp	DOFD0277-9
DOFD0277	31.03.2019	892.84	894.25	wDOF		BX	Sx	DOFD0277- 10
DOFD0277	31.03.2019	894.25	895.70	wDOF	gy	SSH	Sx	DOFD0277- 11 to -13
DOFD0277	31.03.2019	896.53	897.00	wDOF		VNS- SHR?	Sx	DOFD0277- 14

DOFD0277	31.03.2019	897.00	903.08	wDOF	Dgy	SSH	Sx	DOFD0277-15, -16
DOFD0277	31.03.2019	908.50	909.00	wDOF	Dgy	SSH	Py	DOFD0277-17
DOFD0277	31.03.2019	926.00	926.65	mDOF		BX	Qz, Py, Cp, Gn	DOFD0277-18
DOFD0277	31.03.2019	926.65	927.00	mDOF	gy	SHR	Sx	DOFD0277-18
DOFD0277	31.03.2019	927.30	927.52	mDOF		EV	Qz-FSp in vns/ev, Py, Po, Sx	DOFD0277-19
DOFD0277	31.03.2019	#REF!	928.20	mDOF		EV		DOFD0277-20
DOFD0277	31.03.2019	928.20	928.55	mDOF	Dgy	SSH	Po	DOFD0277-21
DOFD0277	31.03.2019	#REF!	929.58	mDOF		EV		DOFD0277-22
DOFD0277	31.03.2019	929.58	929.67	mDOF		BX	Qz	DOFD0277-22
DOFD0277	31.03.2019	#REF!	931.75	mDOF	gy	SSH	Py, Po, Cp	DOFD0277-23, -24
DOFD0277	31.03.2019	#REF!	933.90	mDOF		EV/BX VNS	Cp, Gn, Py, Po	DOFD0277-25, -26

Borehole-ID: DOFD0202

Borehole collar: Lat = -17.83596269 Long = 13.72365769

Borehole-ID	Date	From	To	Horizon	Color	Lith.	Min.	Sample
DOFD0202	01.04.2019	545.90	547.30	HW	Lgy	SSH		DOFD0202-1
DOFD0202	01.04.2019	547.30	549.10	HW	gy	SSH		DOFD0202-2
DOFD0202	01.04.2019	549.90	568.60	HW	gy	SSH		DOFD0202-3
DOFD0202	01.04.2019	574.70	575.00	V	Dgy	SSH	Py	DOFD0202-4
DOFD0202	01.04.2019	581.42	582.00	wDOF	gy	SSH	Py	DOFD0202-5
DOFD0202	01.04.2019	585.00	585.12	wDOF	Lgy	SSS	Py	DOFD0202-6
DOFD0202	01.04.2019	585.62	586.11	wDOF	Dgy	SSH	Py	DOFD0202-7
DOFD0202	01.04.2019	587.10	587.15	wDOF		VNS	Py, Cp	DOFD0202-8
DOFD0202	01.04.2019	587.15	587.20	wDOF	gy	SSH	Py	DOFD0202-8
DOFD0202	01.04.2019	587.20	587.44	wDOF		BX	Qz, Py, Zn	DOFD0202-8

DOFD0202	01.04.2019	587.85	588.50	wDOF		BX	Qz-CL, littel to no Sx	DOFD0202-9
DOFD0202	01.04.2019	589.93	590.08	mDOF		EV	CL?, Sx	DOFD0202-10
DOFD0202	01.04.2019	590.03	491.17	mDOF		BX/EV	CL, Sx	DOFD0202-11
DOFD0202	01.04.2019	491.17	591.33	mDOF	Dgy	SSH	Sx	DOFD0202-12
DOFD0202	01.04.2019	591.33	591.36	mDOF		EV/VNS		DOFD0202-12
DOFD0202	01.04.2019	591.47	592.50	mDOF	gy	SSH	Sx	DOFD0202-13
DOFD0202	01.04.2019	592.52	592.69	mDOF	gy	SSH	Py	DOFD0202-14
DOFD0202	01.04.2019	592.69	592.87	mDOF		EV	Py, Sx	DOFD0202-15, -16
DOFD0202	01.04.2019	593.80	593.87	mDOF		VNS	Py, Zn	DOFD0202-17
DOFD0202	01.04.2019	594.55	595.43	FW	Dgy	SSH	Min.or Py	DOFD0202-18

Borehole-ID: DOFD0103

Borehole collar: Lat = -17.8410589 Long = 13.74060895

Borehole-ID	Date	From	To	Horizon	Color	Lith.	Min.	Sample
DOFD0103	30.03.2019	235.35	238.50	HW		BX	Pb peak	DOFD0103-25
DOFD0103	30.03.2019	343.00	344.60	HW		SHR+BX		DOFD0103-26
DOFD0103	30.03.2019	344.60	357.00	HW		SSH		DOFD0103-27
DOFD0103	30.03.2019	369.55	428.00	HW		SSH		DOFD0103-28 to -30
DOFD0103	30.03.2019	428.75	431.61	V	Dgy	SSH	Py, Po	DOFD0103-1
DOFD0103	30.03.2019	434.30	434.88	V	Dgy	SSH	Py	DOFD0103-2
DOFD0103	30.03.2019	434.80	435.71	V	Dgy	SSH	Py	DOFD0103-3
DOFD0103	30.03.2019	435.78	436.06	V	gy	SSH	no waves, Py	DOFD0103-4
DOFD0103	30.03.2019	436.33	437.30	V	Dgy	SSH	high gph, Py	DOFD0103-5

DOFD0103	30.03.2019	437.30	437.46	V	gy	SSH	waves, Py	DOFD0103-5
DOFD0103	30.03.2019	442.00	442.54	wDOF	gy	SSH	Py	DOFD0103-6
DOFD0103	30.03.2019	449.20	450.15	mDOF		BX	cc-Qz, Cp, Py	DOFD0103-7, -9 & -10
DOFD0103	30.03.2019	450.15	450.73	mDOF	gy	SSH	Min.or	DOFD0103-8, -11
DOFD0103	30.03.2019	450.73	450.94	mDOF		EV/SHR	Sx	DOFD0103- 12
DOFD0103	30.03.2019	450.94	451.45	mDOF	Dgy	SSH	Py	DOFD0103- 13
DOFD0103	30.03.2019	451.45	451.54	mDOF	Lgy	DEF	Py, Po, Cp	DOFD0103- 14
DOFD0103	30.03.2019	451.90	452.12	mDOF	Dgy	SSH	waves, Py	DOFD0103- 15
DOFD0103	30.03.2019	452.63	452.65	mDOF		EV	Sx	DOFD0103- 16
DOFD0103	30.03.2019	452.65	452.71	mDOF	Dgy	SSH	waves, Py	DOFD0103- 16, -17
DOFD0103	30.03.2019	452.71	453.45	mDOF	Dgy	SSH	Py, Po	DOFD0103- 18
DOFD0103	30.03.2019	453.61	453.66	mDOF	Dgy	SSH	Sx	DOFD0103- 19
DOFD0103	30.03.2019	453.66	454.17	mDOF	Dgy	SSH	Sx	DOFD0103- 20, -21
DOFD0103	30.03.2019	456.51	457.46	FW	gy	SSH	few waves, Py di, euhedral Py, 1 mm di	DOFD0103- 22
DOFD0103	30.03.2019	457.48	458.49	FW	Dgy	SSH	gph, Py	DOFD0103- 23
DOFD0103	30.03.2019	458.49	458.84	FW	gy	SSH	Py	DOFD0103- 24

Borehole-ID: DOFD0173

Borehole collar: Lat = -17.84392202 Long = 13.76278509

Borehole-ID	Date	From	To	Horizon	Color	Lith.	Min.	Sample
DOFD0173	28.03.2019	216.47	222.00	HW	Dgy	SSH	Gr, Py	DOFD0173-2
DOFD0173	28.03.2019	222.00	223.36	V	Dgy	SSH	Gr M, Py	DOFD0173- 3,-4

DOFD0173	28.03.2019	223.35	223.36	HW			Gr M, wave 0.5 cm, Py	DOFD0173-4
DOFD0173	28.03.2019	224.58	224.91	HW	Dgy	SSH	Py	DOFD0173-5
DOFD0173	28.03.2019	227.26	227.45	HW	gy	SSH	Py	DOFD0173-6
DOFD0173	28.03.2019	227.70	228.45	HW		BX		DOFD0173-7
DOFD0173	28.03.2019	228.72	229.38	HW	Dgy	SSH	Py	DOFD0173-8
DOFD0173	28.03.2019	231.82	233.55	HW	Dgy	SSH	Sx	DOFD0173- 9, -10
DOFD0173	28.03.2019	233.56	234.00	HW	Dgy	SSH		DOFD0173- 11
DOFD0173	28.03.2019	236.09	236.59	HW	gy	SSH	bu Gr waves, Sx	DOFD0173- 12
DOFD0173	28.03.2019	237.00	237.53	HW		BX	Qz	DOFD0173- 13
DOFD0173	28.03.2019	237.53	237.56	HW	Dgy	SSH	Sx	DOFD0173- 14
DOFD0173	28.03.2019	237.56	237.57	HW	Lgy	SSH	Sx	DOFD0173- 14
DOFD0173	28.03.2019	237.57	238.00	mDOF	Dgy	SSH	Sx	DOFD0173- 15, -16
DOFD0173	28.03.2019	238.00	238.81	mDOF	Dgy	SSH	Sx	DOFD0173- 16, -17
DOFD0173	28.03.2019	239.46	239.64	mDOF	Lgy	SSH		DOFD0173- 18
DOFD0173	28.03.2019	239.80	240.53	mDOF	Dgy	SSH	waves, Sx	DOFD0173- 19
DOFD0173	28.03.2019	240.68	240.78	mDOF		VNS	Qz-CL-Sx, Sx	DOFD0173- 20
DOFD0173	28.03.2019	250.00	255.00	FW	Dgy	SSH	Sx	DOFD0173- 21
DOFD0173	28.03.2019	261.45	262.35	FW	Lgy	SSS	Gr flakes?, Sx	DOFD0173- 22
DOFD0173	28.03.2019	270.55	270.90	FW		EV/BX	Qz	DOFD0173- 23
DOFD0173	28.03.2019	272.07	272.42	FW		EV	Gr	DOFD0173- 24
DOFD0173	28.03.2019	272.42	296.48	FW	gy	SSH	Sx	DOFD0173- 25

Borehole collar: Lat = -17.84314003 Long = 13.78165097

Borehole-ID	Date	From	To	Horizon	Color	Lith.	Min.	Sample
DOFD0077	26.03.2019	371.40	393.00	HW	Lgy	SSH	Po, Py, Gr	DOFD0077-1
DOFD0077	26.03.2019	393.00	394.00	HW	Lgy	SSH	Py	DOFD0077-2
DOFD0077	26.03.2019	397.16	397.18	HW		BX		DOFD0077-3
DOFD0077	26.03.2019	397.18	444.00	HW	Lgy	SSH	Py	DOFD0077-4
DOFD0077	26.03.2019	459.10	459.20	HW		BX-sed	Py	DOFD0077-5
DOFD0077	26.03.2019	461.34	462.14	HW	Lgy	SSH		DOFD0077-6
DOFD0077	26.03.2019	462.17	463.23	HW	Lgy	SSH	Py	DOFD0077-7, -8
DOFD0077	26.03.2019	463.23	469.37	V	Lgy	SSH	Py	DOFD0077-9, -10
DOFD0077	26.03.2019	470.36	472.12	V	Lgy	SSH	Py, Gr M	DOFD0077- 11
DOFD0077	26.03.2019	472.14	474.90	V	Lgy	SSH	Py, Gr M	DOFD0077- 12
DOFD0077	26.03.2019	474.90	476.43	V	Dgy	SSH	Py, Gr M- H	DOFD0077- 13
DOFD0077	26.03.2019	477.93	478.65	V	Dgy	SSH	Gr	DOFD0077- 14
DOFD0077	26.03.2019	479.75	481.55	lg- wDOF	Dgy	SSH	Py, Gr M- H	DOFD0077- 15
DOFD0077	26.03.2019	481.70	482.58	lg- wDOF	Lgy	SSH	Py	DOFD0077- 16
DOFD0077	26.03.2019	483.41	484.66	wDOF	Dgy	SSH	Py	DOFD0077- 17
DOFD0077	26.03.2019	484.66	485.37	wDOF		BX-like	Py	DOFD0077- 18
DOFD0077	26.03.2019	485.37	486.85	wDOF	Dgy	SSH	Py, Gr M	DOFD0077- 19
DOFD0077	26.03.2019	487.40	488.37	mDOF		BX	Py, Cp, Po, Gn, Qz I	DOFD0077- 20
DOFD0077	26.03.2019	488.37	489.63	mDOF	Dgy	SSH	Py, Gr W ft	DOFD0077- 21
DOFD0077	26.03.2019	489.63	490.05	mDOF		BX-Qz	Py, Cp, Qz	DOFD0077- 22
DOFD0077	26.03.2019	490.05	490.26	mDOF	Lgy	SSH	Py-Po, Gr M	DOFD0077- 23
DOFD0077	26.03.2019	490.26	490.45	mDOF		VNS-QS	Po, Cp	DOFD0077- 24

DOFD0077	26.03.2019	490.45	490.79	mDOF	Dgy	SSH	Po	DOFD0077-25
DOFD0077	26.03.2019	490.84	492.58	mDOF	Dgy	SSH	Po, Py, Cp, di-fg ba	DOFD0077-26 to -30
DOFD0077	26.03.2019	492.58	492.68	mDOF		EV	Po, Cp, Sp, Py, Qz, Gr	DOFD0077-31 to -32
DOFD0077	26.03.2019	493.06	493.12	mDOF		EV/VNS-QS	Po, Py, Sp, Gn, Qz	DOFD0077-33 to -34
DOFD0077	26.03.2019	493.49	493.90	mDOF	Dgy	SSH	Po, Py	DOFD0077-35 to -36
DOFD0077	26.03.2019	493.90	494.38	mDOF	Dgy	SSH	Po>Py	DOFD0077-37
DOFD0077	26.03.2019	494.38	497.00	wDOF	Dgy	SSH	Po>Py, Gr incr downhole	DOFD0077-38
DOFD0077	26.03.2019	497.00	498.88	FW	Dgy	SSH	Py, Gr M	DOFD0077-39 to -40
DOFD0077	26.03.2019	498.88	500.34	FW	Lgy	SSH	Gr	DOFD0077-41

Borehole-ID: DOFD0262

Borehole collar: Lat = -17.84916377 Long = 13.80611918

Borehole-ID	Date	From	To	Horizon	Color	Lith.	Min.	Sample
DOFD0262	02.04.2019	202.54	202.95	HW	Dgy	SSH	little to no Gr.	DOFD0262-1
DOFD0262	02.04.2019	208.26	209.44	HW	Dgy	SSH	Gr M, Py	DOFD0262-2
DOFD0262	02.04.2019	210.53	211.95	HW	Dgy	SSH	little to no Gr, Py	DOFD0262-3
DOFD0262	02.04.2019	212.59	213.30	V	Dgy	SSH	Gr M, Py	DOFD0262-4, -5
DOFD0262	02.04.2019	212.30	212.50	V	Dgy	text	Py	DOFD0262-6
DOFD0262	02.04.2019	212.77	215.00	wDOF	Dgy	SSH	Gr, Py	DOFD0262-7, -8

DOFD0262	02.04.2019	215.00	217.12	wDOF	Dgy	SSH	Py	DOFD0262-9, -10
DOFD0262	02.04.2019	217.12	217.80	wDOF	Lgy	SCB	Py	DOFD0262- 11
DOFD0262	02.04.2019	227.38	227.59	mDOF		BX	Py	DOFD0262- 14
DOFD0262	02.04.2019	227.59	231.03	mDOF	Lgy	SSH	Py	DOFD0262- 12b, -13, -15 to -19
DOFD0262	02.04.2019	231.07	231.68	mDOF	Lgy	SSH	Py	DOFD0262- 20 to -22
DOFD0262	02.04.2019	231.70	232.21	mDOF	Lgy	SSH	Py	DOFD0262- 23
DOFD0262	02.04.2019	231.22	231.85	mDOF	Lgy	SSH	Sx	DOFD0262- 24
DOFD0262	02.04.2019	231.85	231.90	mDOF		SHR	Py	DOFD0262- 24
DOFD0262	02.04.2019	232.10	248.90	FW		SSH		DOFD0262- 25, -26
DOFD0262	02.04.2019	249.10	259.15	FW		EV	Py, Sp?	DOFD0262- 27
DOFD0262	02.04.2019	250.66	250.85	FW		EV	Sx	DOFD0262- 28
DOFD0262	02.04.2019	250.86	263.38	FW		SSH		DOFD0262- 29

Appendix 3

List of prepared sample and analytical methods used

List of prepared samples from the drill core samples in Appendix 2, with notes on analytical methods applied onto sample. Abbreviations: mDOF = Main DOF horizon; wDOF = Wider DOF horizon; HW = hanging wall; FW = footwall; lg = low grade.

Borehole-ID: DOFD0277							
Borehole sample ID	Horizon	Polished mount	Thin section	LA-ICP-MS	$\delta^{34}\text{S}$	Leco	XRF
DOFD0277-1	lg wDOF		1			wDOF	y
DOFD0277-2	lg wDOF						
DOFD0277-3	lg wDOF		1				
DOFD0277-4	lg wDOF		1, 2				
DOFD0277-5	lg wDOF		1			hr	y
DOFD0277-6	lg wDOF		1			wDOF	
DOFD0277-7	lg wDOF	1			mF		
DOFD0277-8	lg wDOF	1	2			wDOF	
DOFD0277-9	HW						
DOFD0277-10	HW		1			hr	y
DOFD0277-11	wDOF						
DOFD0277-12	wDOF	1B	1	1B	C2		
DOFD0277-13	wDOF	1, 2	1				
DOFD0277-14	wDOF						
DOFD0277-15	wDOF	1B, 1C	1, 2	1B, 1C	D1		
DOFD0277-16	wDOF		1				
DOFD0277-17	wDOF		1				
DOFD0277-18	mDOF		1			DOF	y
DOFD0277-19	mDOF						
DOFD0277-20	mDOF	1B	1, 2	1B	mE		
DOFD0277-21	mDOF	1B	1, 2	1B	D2		
DOFD0277-22	mDOF	3B	1, 2, 3	3B	A3		
DOFD0277-23	mDOF		1, 2				
DOFD0277-24	mDOF						
DOFD0277-25	wDOF	1					
DOFD0277-26	wDOF		1			wDOF	

Borehole-ID: DOFD0202

Borehole sample ID	Horizon	Polished mount	Thin section	LA-ICP-MS	$\delta^{34}\text{S}$	Leco	XRF
DOFD0202-1	HW		1				y
DOFD0202-2	HW		1				y
DOFD0202-3	HW		1, 2				
DOFD0202-4	HW		1			hr	y
DOFD0202-5	wDOF	1					
DOFD0202-6	wDOF		1			wDOF	
DOFD0202-7	wDOF		1			DOF	
DOFD0202-8	wDOF						
DOFD0202-9	wDOF						
DOFD0202-10	wDOF		1			DOF	y
DOFD0202-11	wDOF		1, 2				
DOFD0202-12	mDOF		1				
DOFD0202-13	mDOF		1			DOF	
DOFD0202-14	mDOF						
DOFD0202-15	mDOF						
DOFD0202-16	mDOF						
DOFD0202-17	mDOF						
DOFD0202-18	FW		1			hr	y

Borehole-ID: DOFD0103							
Borehole sample ID	Horizon	Polished mount	Thin section	LA-ICP-MS	$\delta^{34}\text{S}$	Leco	XRF
DOFD0103-25	HW						
DOFD0103-26	HW		1				
DOFD0103-27	HW		1				y
DOFD0103-28	HW						
DOFD0103-29	HW				E4		
DOFD0103-30	HW		1				
DOFD0103-1	lg wDOF		1, 2			wDOF	
DOFD0103-2	lg wDOF						
DOFD0103-3	lg wDOF		1			hr	y
DOFD0103-4	lg wDOF		1				
DOFD0103-5	lg wDOF						
DOFD0103-6	wDOF		1			wDOF	y
DOFD0103-7	wDOF		1			wDOF	y
DOFD0103-8	wDOF						
DOFD0103-9	wDOF						
DOFD0103-10	wDOF		1				
DOFD0103-11	mDOF						
DOFD0103-12	mDOF		1, 2			DOF	
DOFD0103-13	mDOF						
DOFD0103-14	mDOF		1			DOF	

DOFDO103-15	mDOF				C4		
DOFDO103-16	mDOF	1, 2, 3	4	2	mF	DOF	
DOFDO103-17	mDOF	1, 2					
DOFDO103-18	mDOF		1			DOF	y
DOFDO103-19	mDOF	1B	1, 2	1B	m		
DOFDO103-20	mDOF		1			DOF	
DOFDO103-21	mDOF						
DOFDO103-22	FW		1			hr	
DOFDO103-23	FW						
DOFDO103-24	FW	1, 1B	2, 3	1B	mE	hr	y

Borehole-ID: DOFDO173							
Borehole sample ID	Horizon	Polished mount	Thin section	LA-ICP-MS	$\delta^{34}\text{S}$	Leco	XRF
DOFDO173-1	HW						
DOFDO173-2	HW		1			hr	y
DOFDO173-3	HW						
DOFDO173-4	wDOF						
DOFDO173-5	wDOF		1, 2			wDOF	y
DOFDO173-6	wDOF						
DOFDO173-7	wDOF		1			wDOF	
DOFDO173-8	wDOF						
DOFDO173-9	wDOF					wDOF	
DOFDO173-10	wDOF						
DOFDO173-11	wDOF						
DOFDO173-12	wDOF		1			wDOF	y
DOFDO173-13	mDOF						
DOFDO173-14	mDOF	1, 2	3(2)	1	C1		
DOFDO173-15	mDOF	1		1	C4		
DOFDO173-16	mDOF						
DOFDO173-17	mDOF	1, 1B		1B	mH		
DOFDO173-18	mDOF		1			DOF	y
DOFDO173-19	mDOF						
DOFDO173-20	wDOF						
DOFDO173-21	FW		1				
DOFDO173-22	FW		1				y
DOFDO173-23	FW						
DOFDO173-24	FW						
DOFDO173-25	FW	2B	1	2B	mD		y

Borehole-ID: DOFDO077

Borehole sample ID	Horizon	Polished mount	Thin section	LA-ICP-MS	$\delta^{34}\text{S}$	Leco	XRF
DOFD0077-1	HW					wDOF	y
DOFD0077-2	HW						
DOFD0077-3	HW					hr	y
DOFD0077-4	HW				-		
DOFD0077-5	HW					hr	y
DOFD0077-6	wDOF				B3	hr	
DOFD0077-7	wDOF		1				
DOFD0077-8	wDOF						
DOFD0077-9	wDOF	1, 2					
DOFD0077-10	wDOF					wDOF	y
DOFD0077-11	wDOF					wDOF	
DOFD0077-12	wDOF					wDOF	y
DOFD0077-13	HW					wDOF	
DOFD0077-14	wDOF					wDOF	y
DOFD0077-15	wDOF						
DOFD0077-16	wDOF						
DOFD0077-17	wDOF						
DOFD0077-18	wDOF						
DOFD0077-19	wDOF						
DOFD0077-20	wDOF						
DOFD0077-21	wDOF						
DOFD0077-22	wDOF					wDOF	y
DOFD0077-23	mDOF						
DOFD0077-24	mDOF						
DOFD0077-25	mDOF						
DOFD0077-26	mDOF					DOF	
DOFD0077-27	mDOF					DOF	
DOFD0077-28	mDOF				A1		
DOFD0077-29	mDOF						
DOFD0077-30	mDOF				B2		
DOFD0077-31	mDOF	1B	1	1B	-		
DOFD0077-32	mDOF				A2		
DOFD0077-33	mDOF						
DOFD0077-34	mDOF					DOF	
DOFD0077-35	mDOF						
DOFD0077-36	mDOF						
DOFD0077-37	wDOF					wDOF	
DOFD0077-38	wDOF					wDOF	
DOFD0077-39	wDOF					wDOF	
DOFD0077-40	FW						
DOFD0077-41	FW					hr	

Borehole-ID: DOFD0262

Borehole sample ID	Horizon	Polished mount	Thin section	LA-ICP-MS	$\delta^{34}\text{S}$	Leco	XRF
DOFD0262-1	HW	1		1	E1		
DOFD0262-2	HW	2		2	E3		
DOFD0262-3	HW		1				
DOFD0262-4	HW					wDOF	y
DOFD0262-5	wDOF						
DOFD0262-6	wDOF	1	2	1			
DOFD0262-7	wDOF						
DOFD0262-8	wDOF						
DOFD0262-9	wDOF		1			wDOF	
DOFD0262-10	wDOF	1		1	B1		
DOFD0262-11	wDOF						
DOFD0262-12b	mDOF						
DOFD0262-13	mDOF						
DOFD0262-14	mDOF	1		1			
DOFD0262-15	mDOF	1		1	B4		
DOFD0262-16	mDOF		1			DOF	
DOFD0262-17	mDOF						
DOFD0262-18	mDOF	1		1	E2		
DOFD0262-19	mDOF			1			
DOFD0262-20	mDOF		1			DOF	y
DOFD0262-21	mDOF	1, 2					
DOFD0262-22	mDOF						
DOFD0262-23	mDOF	1		1	mA		
DOFD0262-24	mDOF		1			DOF	
DOFD0262-25	FW	1		1			
DOFD0262-26	FW		1				
DOFD0262-27	FW	1B	1	1B	mD		
DOFD0262-28	FW	1		1			
DOFD0262-29	FW		1		B5		